

Development of a Quantification Method for various Pronucleotides and their Metabolites in Cell Extracts

- A targeted Approach

Dissertation

to obtain the Scientific Doctoral Degree

by

Michelle Vogts

presented to

of the Faculty of Sciences
at the University of Hamburg

Hamburg

2025

The present work was compiled in the group of Prof. Dr. Chris Meier at the Institute of Organic Chemistry in the Department of Chemistry at the University of Hamburg from January 2021 to May 2025.

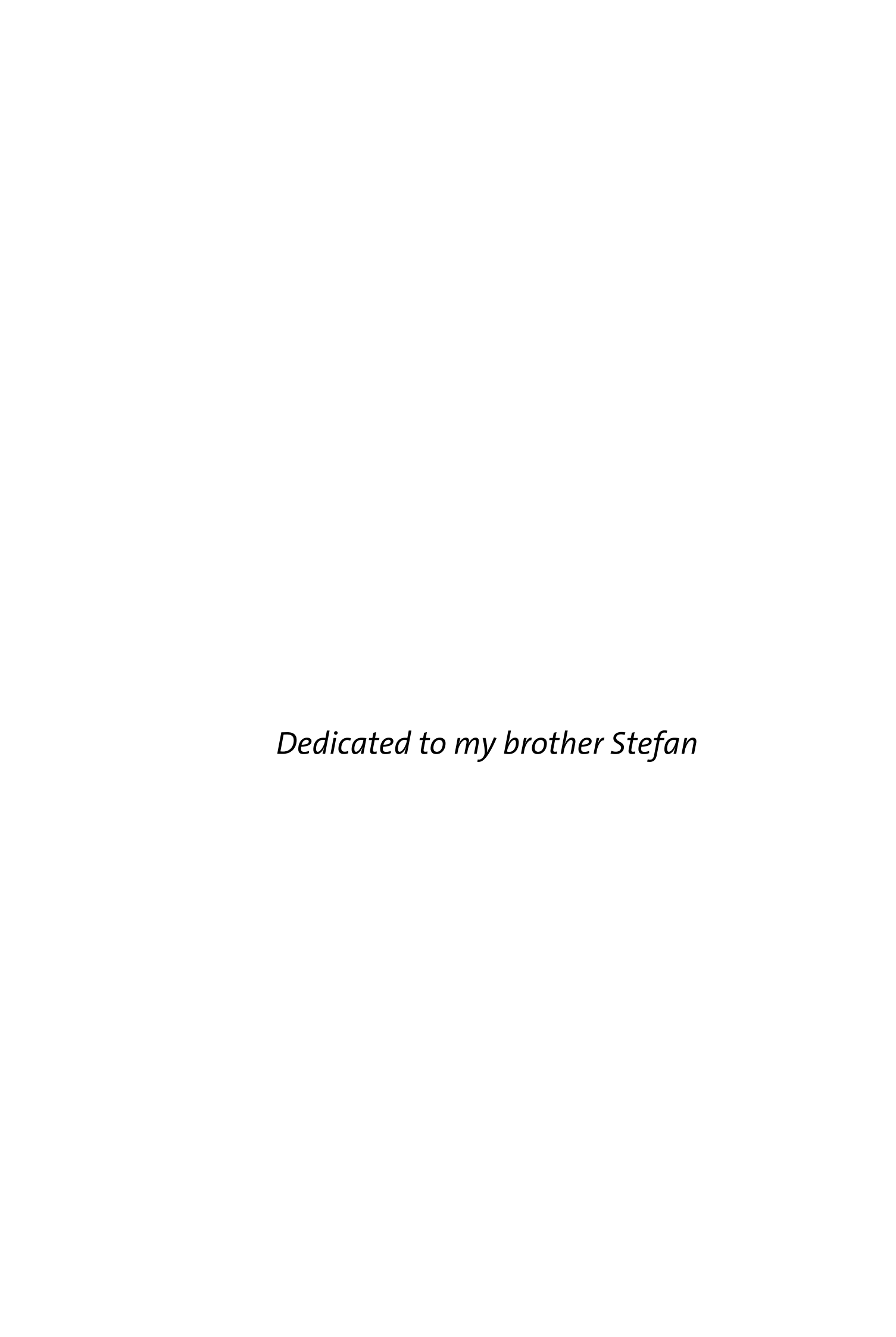
First Reviewer: Prof. Dr. Chris Meier

Second Reviewer: Prof. Dr. Ralph Holl

Third Reviewer: Prof. Dr. Henning J. Jessen

Date of disputation: 24.10.2025

Date of print approval: 04.11.2025





I.	List of publications		
II.	List of	abbreviationsabbreviations	VI
III.	Zusa	ımmenfassung	XI
IV.	. Abst	ract	XIV
1	Introd	uction	1
2	Theore	etical background	3
	2.1 Nı	ucleosides and nucleotides	3
	2.1.1	Structure and function	3
	2.1.2	Use of nucleoside analogues against viral diseases and cancer	5
	2.1.3	Mechanisms of action	7
	2.2 Th	ne Prodrug concept	9
	2.2.1	Design and mechanism of TriPPPro-compounds	11
	2.2.2	Proof of concept and biological data	13
	2.3 Lio	quid chromatography	14
	2.3.1	Hydrophilic interaction liquid chromatography	15
	2.3.1	Mixed-mode chromatography	17
	2.4 O _l	otical detection methods	19
	2.4.1	UV detection	19
	2.4.2	Detection via fluorescence labeling	20
	2.5 M	ass spectrometry as a detection method	21

	2.5.1	Electrospray ionization	23
	2.5.2	The quadrupole as mass analyzer	25
	2.5.3	Tandem mass spectrometry	27
3	Objecti	ve	. 31
4	Results	and discussion	34
4	1.1 Syr	nthesis of the intermediates	37
	4.1.1 R	Retrosynthetic analysis	37
	4.1.2	Synthesis of 5-FdU-monophosphate 9	38
	4.1.3	Synthesis of the intermediate ${\bf 6}$ via the non-symmetric β -cyano eth	hyl
	phosph	onate route	40
	4.1.4	Synthesis of FdU-5'-diphosphate 8	44
	4.1.5	Synthesis of the intermediate ${\bf 6}$ via the non-symmetric β -cyano eth	hyl
	amidite	e route	47
	4.1.6	Synthesis of the intermediate 6 via the non-symmetric F	m-
	phosph	nonate route	49
	4.1.7	Synthesis of the intermediate 11	55
4	1.2 Init	tial MS tuning	60
4	1.3 De	velopment of the HPLC method	63
	4.3.1	Application of a mixed-mode stationary phase	64
	4.3.2	Application of HILIC stationary phases	81
2	1.4 Op	timization studies of the HPLC-MS/MS method	89
	4.4.1	Design of Experiment (DoE)	89
	4.4.2	Evaluation of the DoE	93
	4.4.3	Optimization using FIA1	06
	4.4.4	Evaluation of calibration curves in solvent1	08
4	1.5 Ap _l	plication to d4T derivatives and natural nucleotides1	114
	4.5.1	HPLC-MRM method with d4T derivatives1	114

		4.5.2	HPLC-MRM method with natural nucleotides	116
	4.6	5 E	stablishment of a sample preparation method	118
	4.7	7 V	alidation experiments for different matrices	135
	4	4.7.1	Validation in HT29 cell lysate	138
		4.7.2	Validation in HT29 supernatant	148
		4.7.3	Validation in SW620 cell lysate	156
	4	4.7.4	Validation in SW620 supernatant	162
		4.7.5	Validation in CEM/0 cell lysate	169
		4.7.6	Validation in CEM/0 supernatant	176
	4.8	3 C	uantification of prodrugs and metabolites in cell extracts	183
	4	4.8.1	Cellular uptake studies with HT29 cancer cells	183
	4	4.8.2	Cellular uptake studies with SW620 cancer cells	192
		4.8.3	Cellular uptake studies with CEM/0 virus cells	199
		4.8.4	Conclusion	203
5	ļ	Exper	imental section	
5	5.1	•		206
5	5.1	•	imental section	206
5	5.1	G	imental section	206 206
5	5.1	G 5.1.1	imental sectioneneral Experimental workflow	206206206206
5	5.1	G 5.1.1 5.1.2	imental section eneral Experimental workflow	206206206207
5	5.1	G 5.1.1 5.1.2 5.1.3	imental section eneral Experimental workflow Graphical workflow Starting materials, reagents and solvents	206206206207207
5	5.1	5.1.1 5.1.2 5.1.3 5.1.4 5.1.5	imental section eneral Experimental workflow Graphical workflow Starting materials, reagents and solvents Sample preparation for LC-MS/MS measurements	206206207207209
5	5.1	5.1.1 5.1.2 5.1.3 5.1.4 5.1.5	imental section eneral Experimental workflow Graphical workflow Starting materials, reagents and solvents Sample preparation for LC-MS/MS measurements Preparation of calibration standards and quality controls	206206206207207209209
5	5.1	5.1.1 5.1.2 5.1.3 5.1.4 5.1.5	imental section Experimental workflow Graphical workflow Starting materials, reagents and solvents Sample preparation for LC-MS/MS measurements Preparation of calibration standards and quality controls hromatography	206206206207207209209210
5	5.1 	5.1.1 5.1.2 5.1.3 5.1.4 5.1.5 2 C 5.2.1	imental section eneral Experimental workflow Graphical workflow Starting materials, reagents and solvents Sample preparation for LC-MS/MS measurements Preparation of calibration standards and quality controls hromatography Thin layer chromatography	206206206207209209210210
5	5.1	5.1.1 5.1.2 5.1.3 5.1.4 5.1.5 2 C 5.2.1	imental section eneral Experimental workflow Graphical workflow Starting materials, reagents and solvents Sample preparation for LC-MS/MS measurements Preparation of calibration standards and quality controls hromatography Thin layer chromatography Column chromatography	206206206207207209210210
5	5.1 	5.1.1 5.1.2 5.1.3 5.1.4 5.1.5 2 C 5.2.1 5.2.2	imental section eneral Experimental workflow Graphical workflow Starting materials, reagents and solvents Sample preparation for LC-MS/MS measurements Preparation of calibration standards and quality controls hromatography Thin layer chromatography Column chromatography Ion exchange chromatography	206206206207207209210210211

!	5.4	Mass spectrometry	212
!	5.5	NMR spectroscopy	213
!	5.6	Further devices	213
!	5.7	LC-MS/MS system	214
!	5.8	Bradford assay	215
!	5.9	Cellular uptake studies	216
	5.9.	0.1 Cancer cells	216
	5.9.	0.2 Virus cells	217
!	5.10	Syntheses	218
	5.10	0.1 General procedures	218
	5.10	0.2 Synthesis of 5-FdU monophosphate 9	220
	5.10	0.3 Synthesis of d4T monophosphate 15	223
	5.10	0.4 Synthesis of the non-symmetric <i>H</i> -phosphonates	223
	5.10	0.5 Synthesis of the monomasked triphosphates	227
	5.10	0.6 Synthesis of the non-symmetric amidite 25	230
	5.10	0.7 Synthesis of 5-FdU diphosphate 8	231
6	Bib	oliography	233
7	Λ m.	nondiv	254
,	API	pendix	234
•	7.1	List of hazards and precautionary statements	254
-	7.2	Supplementary data	259
	7.2.	.1 Measurements with the mixed-mode method	259
	7.2.	.2 Diagnostic graphs from the DoE validation	260
	7.2.	.3 Raw data of the validation	266
	7.2.	.4 Calibration curves	280
8	Ack	knowledgement	312
9	Dec	claration on Oath	314

I. List of publications

Publications

- **P1** Vogts, M., Witt, J., Riedner, M., Meier, C. Development of a HILIC-MS/MS method for simultaneous quantification of lipophilic antitumor Tri*PPP*ro-prodrugs and their polar metabolites in HT29 cell extracts, J. Chromatogr. B Analyt. Technol. Biomed. Life Sci. 2025, *1263*, 124673.
- **P2** Nikolova, V., Linnemannstöns, K., Bendel, M., Machado, M., Ganter, B., Budimir, P., Vogts, M., Ganter, M., Meier, C., Dobbelstein, M. Membrane-permeable 5-fluorodeoxyuridine triphosphate derivatives inhibit the proliferation of *Plasmodium falciparum*, ACS Infect. Dis. 2025.

Poster and oral presentations.

- **P3** Vogts, M., Meier, C. HPLC Method Development: Insights into the Analysis of Nucleotide Analogs and their Prodrugs, Oral Presentation at the Waters Seminar 2024. Hamburg, Germany.
- P4 Vogts, M., Meier, C. Development of a targeted HILIC-MRM method for the quantification of Tri*PPP*ro-prodrugs and their metabolites in complex mixtures. Poster presentation at the XXV International Round Table (IRT) on Nucleosides, Nucleotides and Nucleic Acids 2024. Tokyo, Japan.
- **P5** Vogts, M., Witt, J., Meier, C. Analytical mass spectrometry method for quantification of Tri*PPP*ro-prodrugs and their metabolites in cell extracts. Poster presentation at the XXI EuroAnalysis 2023. Geneva, Switzerland.

5-FdU 5-Fluorouridine

5-FU 5-Fluorouracil

A Adenine

AAc Ammonium acetate

AB Acyloxybenzyl

ABC Abacavir

ACB Acyloxy benzyl carbonate

Af Ammonium formate

AIDS Acquired immune deficiency syndrome

AMP Adenosine monophosphate

ANOVA Analysis of variance

ara-C Cytarabine

ATP Adenosine triphosphate

AZT Azidothymidine

BSA Bovine serum albumin

C Cytosine

cAMP Cyclic adenosine monophosphate

CE Collision energy

CID Collision-induced dissociation

CS Calibration standard

CUR Curtain gas

CV Coefficient of variation

CXP Collision cell exit potential

d Doublet (NMR)

d4T Stavudine

DBF Dibenzofulvene

DC Direct current

DCI 4,5-Dicyanoimidazol

ddBCNATP 2',3'-dideoxy-bicyclic nucleoside analogue triphosphate

DMF N,N-Dimethylformamide

DMSO Dimethyl sulfoxide

DNA Deoxyribonucleic acid

dNTP Deoxy nucleoside triphosphate

DoE Design of experiments

DPP Diphenyl phosphite

El Electron impact ionization

EIC Extracted ion chromatogram

EP Entrance potential

ESI Electrospray ionization

ETC Easy-to-change

EtOAc Ethyl acetate

FDA Food and Drug Administration

FIA Flow injection analysis

FLD Fluorescence detection

Fm Flourenylmethyl

FTC Emtricitabine

G Guanine

GC Gas chromatography

GS Ion source gas

HAART Highly active antiretroviral therapy

HBV Hepatitis B virus

HCV Hepatitis C virus

HILIC Hydrophilic interaction liquid chromatography

HIV Human immunodeficiency virus

HPLC High performance liquid chromatography

HSV Herpes simplex virus

HTC Hard-to-change

IE Ionization efficiency

IEX Ion exchange

IS Ion spray voltage

ISD Internal standard

LLE Liquid-liquid extraction

LOD Limit of detection

Log D Decadic logarithm of the distribution coefficient

Log *P* Decadic logarithm of the partition coefficient

LOQ Limit of quantification

m Multiplet (NMR)

m/z Mass-to-charge ratio

MALDI Matrix-assisted laser desorption/ionization

ME Matrix effect

MRM Multiple reaction monitoring

MS Mass spectrometry

MS/MS Tandem mass spectrometry

MTBE Methyl tert-butyl ether

NAD⁺ Nicotinamide adenine dinucleotide

NADP⁺ Nicotinamide adenine dinucleotide phosphate

NDP Nucleoside diphosphate

NMP Nucleoside monophosphate

NMR Nuclear magnetic resonance

NP Normal phase

NRTI Nucleosidic reverse transcriptase inhibitor

NSB Nonspecific binding

NTP Nucleoside triphosphate

OFAT One factor at a time

p Quintet (NMR)

PBS Phosphate buffered saline

PC Phosphocholine

PE Process efficiency

PE Petrol ether

PGC Porous graphitic carbon

pH Potential of hydrogen

Pl Phosphatase inhibitor

PP Polypropylene

ppm Parts per million

PPT Protein precipitation

pyTFA Pyridinium-trifluoroacetate

Q Quadrupole

q Quartet (NMR)

QC Quality control

QqQ Triple quadrupole

*R*² Coefficient of determination

RE Recovery rate

REML Restricted maximum likelihood

RF Radio frequency

RNA Ribonucleic acid

RP Reversed phase

RSM Response surface methodology

RT Reverse transcriptase

s Singlet (NMR)

S/N Signal-to-noise

SPE Solid phase extraction

t Triplet (NMR)

T Thymine

TBA Tetrabutylammonium

TBDMS tert-Butyl dimethyl silyl

TEM Temperature

TFAA Trifluoroacetic anhydride

THF Tetrahydrofuran

TIC Total ion current

TLC Thin layer chromatography

ToF Time-of-flight

U Uracil

UV Ultraviolet

III. Zusammenfassung

Die Anwendung von Nucleosid- und Nucleotidanaloga als antivirale und antitumorale Wirkstoffe ist weit verbreitet. Sie zählen zu den wichtigsten Wirkstoffklassen im Kampf gegen Virusinfektionen, wie beispielsweise HIV, werden aber auch in der chemotherapeutischen Behandlung eingesetzt (Kapitel 2.1.2, S. 5 ff.). Dabei kommen bei den antiviral aktiven Substanzen meist die Nucleosidischen Reverse Transkriptase-Inhibitoren (NRTIs) zum Einsatz, welche intrazellulär metabolisiert werden. Hierbei werden sie in ihre biologisch aktive Form, das Nucleosidtriphosphat (NTP), umgewandelt. Nucleosidanaloga, die antitumorale Aktivität zeigen, gehören zu den Antimetaboliten, die das Zellwachstum der Krebszellen hemmen können. Diese sind jedoch ebenfalls hauptsächlich wirksam als NTP (Kapitel 2.1.3, S. 7 ff.). Für beide Verbindungsklassen gilt, dass sie eine schlechte Membrangängigkeit aufweisen und ihre Bioverfügbarkeit grundlegend von der intrazellulären Phosphorylierungskaskade durch hoch substratspezifische Kinasen abhängig ist. Aus diesen beiden Gründen ist die Konzentration des aktiven Metaboliten innerhalb der Zelle oftmals sehr gering. Allerdings ist es auch nicht möglich, das NTP direkt zu verabreichen, da es sich bedingt durch die negativ geladenen Phosphatgruppen um eine sehr hydrophile Verbindung handelt, die die Membran durch passiven Transport nicht durchdringen kann (Kapitel 2.1.3, S. 7 ff.). Um die NTPs direkt in die Zelle einbringen zu können, hat MEIER spezielle Triphosphat-Prodrugs entwickelt, bei denen die γ-Phosphatgruppe des NTPs lipophil maskiert wird. Dies ist das sogenannte TriPPPro-Konzept. Dadurch wird eine passive Diffusion des Prodrugs in die Zelle ermöglicht. Innerhalb der Zelle werden die lipophilen Maskierungen enzymatisch gespalten und liefern direkt den biologisch aktiven Metaboliten, das Triphosphat (Kapitel 2.2, S. 9 ff.). Dieses Konzept wurde vielfältig bei antiviralen Nucleosiden, wie zum Beispiel Stavudin (d4T), angewendet weiterentwickelt. Neben Acyloxybenzylgruppen (AB) Maskierungseinheiten kamen auch die chemisch stabileren Alkoxycarbonyloxybenzylgruppen (ACB) oder nicht-spaltbare Alkylreste zum Einsatz, welche auf Arbeiten und JιΑ basieren. Dabei wurde die von ZHAO γ -Phosphatgruppe sowohl mit symmetrischen als auch asymmetrischen Maskierungen versehen und deren chemische Stabilität sowie biologische Aktivität evaluiert (Kapitel 2.2.1, S. 11 ff.). WITT erweiterte das TriPPPro-Konzept zudem erstmalig auf antitumorale Nucleosidanaloga und konnte erfolgreich potente TriPPPro-Verbindungen darstellen, die unter anderem Derivate des Zytostatikums 5-Fluorouracil (5-FU) sind. Als Nachweis für die erfolgreiche Zellaufnahme von TriPPPro-Verbindungen, synthetisierte Gollnest fluoreszente TriPPPro-Derivate, die zwar keine antivirale Aktivität zeigten, jedoch als Modellsystem dazu dienten, die sowie die Freisetzung des NTPs in der Zelle Zellaufnahme Fluoreszenzdetektion (FLD) per Hochleistungsflüssigkeitschromatographie (HPLC) zu verfolgen. Dabei konnten bisher allerdings nur qualitative Aussagen über die erfolgreiche Zellaufnahme sowie die Freisetzung des NTPs getroffen werden. Es fehlt bisher noch an quantitativen Daten, die nachweisen, welche Menge an Prodrug in die Zelle diffundiert und wie hoch die Konzentration der intrazellulären Metabolite ist (Kapitel 2.2.2, S. 13 ff.). lm Rahmen dieser Arbeit sollte Quantifizierungsmethode für verschiedenen TriPPPro-Verbindungen und deren Metabolite aus Zellextrakten erarbeitet werden. Hierbei sollte eine HPLC-Methode entwickelt werden, die eine simultane Retention aller Analyten erlaubt und an eine massenspektrometrische (MS) Detektion gekoppelt ist. Dabei wurden erstmalig Zellaufnahmestudien mit aktiven TriPPPro-Verbindungen durchgeführt. Bei diesen Verbindungen handelte es sich zum einen um d4T-Derivate mit verschiedenen Maskierungseinheiten, die eine hohe Aktivität gegenüber HIV-1 und HIV-2 in infizierten Kulturen humaner T-Lymphoblasten (Wildtyp CEM/0-Zellen) zeigten. Zum anderen wurden ebenfalls zwei potente FdU-TriPPPro-Verbindungen untersucht, die in Proliferationsstudien in humanen Kolorektalkrebs-Zellen (HT29

und SW620) erfolgsversprechende Ergebnisse lieferten. Der Fokus dieser Arbeit lag dabei auf der Methodenentwicklung und -optimierung sowie der erfolgreichen Anwendung der Methode zur Quantifizierung von vier Prodrugs und allen zugehörigen Metaboliten aus Zellextrakt. Ein kleiner Teil der Arbeit beschäftigte sich außerdem mit der Darstellung zweier Analyten, die für die Entwicklung der Quantifizierungsmethode benötigt wurden. Wenn die TriPPPro-Verbindungen metabolisiert werden, entsteht ein Intermediat, welches an der γ -Phosphatgruppe nur noch eine Maskierungseinheit trägt. Diese sogenannten monomaskierten Triphosphate stellen wichtige Metabolite dar und sind bei der Betrachtung und Quantifizierung von Zellaufnahmestudien essenziell. Im Rahmen dieser Arbeit wurden zwei monomaskierte Derivate unter Verwendung der von MEIER und GOLLNEST etablierten H-Phosphonatroute synthetisiert (Kapitel 4.1.6, S. 49 ff. und Kapitel 4.1.7, S. 55 ff). Anschließend wurde eine HPLC-Methode entwickelt, die in der Lage ist, sowohl lipophile Prodrug-Verbindungen als auch deren hydrophile Metabolite (Triphosphate, Diphosphate, Monophosphate und Nucleoside) zu eluieren und zu separieren. Dabei wurden verschiedene Chromatographiemethoden (Kapitel 2.3, S. 14 ff.) evaluiert und auf dieser Grundlage eine hydrophile Interaktionsflüssigkeitschromatographie (HILIC) Methode entwickelt (Kapitel 4.3, S. 63 ff.). Diese wurde außerdem mittels statistischer Versuchsplanung (DoE) optimiert, sodass alle Analyten in Bezug auf die Signalintensität bestmögliche Ergebnisse zeigten (Kapitel 4.4, S. 89 ff.). Für eine sensitive und selektive Detektion der Analyten im fmol-Bereich wurde eine Multiple Reaction Monitoring (MRM) Methode (Kapitel 2.5.3, S. 27 ff.) entwickelt. Anschließend erfolgte die Validierung der Methode unter Einbezug verschiedener Parameter, wie Linearität, Genauigkeit, Selektivität, Carry-Over und Stabilität für alle verwendeten Matrices (Kapitel 4.7, S. 135 ff.). Durch die entwickelte robuste Methode war es somit erstmalig möglich, vier verschiedene TriPPPro-Verbindungen sowie deren Metabolite in Zellextrakten in einem Bereich von 0.5 – 1000 ng/mL zu quantifizieren und damit Daten über die Zellaufnahme der Prodrugs und deren intrazellulärer Verstoffwechselung zu sammeln (Kapitel 4.8, S. 183 ff.)

IV. Abstract

The use of nucleoside and nucleotide analogues as antiviral and antitumor agents is widespread. They are among the most important classes of active substances in the fight against viral infections such as HIV but are also used in chemotherapeutic treatment (chapter 2.1.2, p. 5 ff.). Nucleoside reverse transcriptase inhibitors (NRTIs), which are metabolized intracellularly, are usually used as antivirally active substances. In the process, they are converted into their bioactive form, the nucleoside triphosphate (NTP). Nucleoside analogues with antitumor activity act as antimetabolites that can inhibit the growth of cancer cells. However, these are also mainly effective as NTPs (chapter 2.1.3, p. 7 ff.). Both classes of compounds exhibit poor membrane permeability, and their stepwise intracellular phosphorylation is catalyzed by highly substrate-specific kinases. For these two reasons, the concentration of the active metabolites within the cell is often very low. However, it is not possible to administer the NTP directly, as it is very hydrophilic due to the negatively charged phosphate groups thus preventing passive diffusion through the cellular membrane (chapter 2.1.3, p. 7 ff.). To introduce the NTPs directly into the cell, MEIER has developed triphosphate-prodrugs in which the γ -phosphate group of the NTP is lipophilically masked. This is the so-called TriPPPro concept. This enables passive diffusion of the prodrug into the cell. Within the cell, the lipophilic masking units are enzymatically cleaved and liberate the biologically active metabolite, the triphosphate (chapter 2.2, p. 9 ff.). This concept has already been applied to and further developed for a variety of antiviral nucleosides, such as stavudine (d4T). In addition to acyloxybenzyl (AB) groups as lipophilic masking units, also the chemically more stable alkoxycarbonyloxybenzyl (ACB) moiety or non-cleavable alkyl substituents were introduced, based on work by ZHAO and JIA. Both symmetrical and non-symmetrical substituents at the γ -phosphate were established and their chemical stability and biological activity evaluated (Chapter 2.2.1, p. 11 ff.). WITT also extended the TriPPPro concept to antitumor nucleoside analogues for the first time and was able to successfully synthesize potent TriPPPro-compounds that, among others, were derivatives of the cytostatic drug 5-fluorouracil (5-FU). As proof-ofconcept for the successful cellular uptake of TriPPPro-compounds, GOLLNEST synthesized fluorescent TriPPPro-derivatives, which showed no antiviral activity, but served as a model system for monitoring cellular uptake and the intracellular release of the NTP by means of fluorescence detection (FLD) using high-performance liquid chromatography (HPLC). So far, however, only qualitative statements about the successful cellular uptake and the release of the NTP have been made. There is still a lack of quantitative data showing the amount of prodrug which diffused into the cell and giving a detailed statement about the intracellular concentrations of the metabolites (chapter 2.2.2, p. 13 ff.). Therefore, the objective of this study was the development of a quantification method for various TriPPPro-compounds and their metabolites from cell extracts. The aim was to design an HPLC method that allows for simultaneous retention of all analytes and is coupled to mass spectrometric (MS) detection. For the first time, cellular uptake studies with active TriPPPro-compounds were carried out. These compounds were d4T derivatives with different masking units synthesized by JIA, which proved to be highly active against HIV-1 and HIV-2 in infected cultures of human T lymphoblasts (wild-type CEM/0 cells). On the other hand, two potent FdU-TriPPPro-compounds were also investigated, which showed promising results in proliferation studies in human colorectal cancer cells (HT29 and SW620) and were synthesized by WITT. The focus of this work was on method development and optimization, as well as the successful application of the method to quantify four prodrugs and all their metabolites from cell extracts. A small part of the work also focused on the synthesis of two analytes that were required for the development of the quantification method. When the TriPPPro-compounds are metabolized, an intermediate is formed which has only one masking unit at the γ -phosphate group. These so-called monomasked triphosphates are important

metabolites and, thus, essential for observation and quantification. As part of this work, two monomasked derivatives were synthesized using the H-phosphonate route established by MEIER and GOLLNEST (chapter 4.1.6, p. 49 ff. and chapter 4.1.7, p. 55 ff). An HPLC method was then developed, capable of retarding and separating lipophilic prodrug compounds and their hydrophilic metabolites (triphosphates, diphosphates, monophosphates and nucleosides). Various chromatography methods (chapter 2.3, p. 14 ff.) were evaluated and, on this basis, a hydrophilic interaction liquid chromatography (HILIC) method was developed (chapter 4.3, p. 63 ff.). Further optimization was carried out using statistical design of experiments (DoE), so that all analytes showed the best possible results in terms of signal intensity (chapter 4.4, p. 89 ff.). A Multiple Reaction Monitoring (MRM) method (chapter 2.5.3, p. 27 ff.) has been developed to ensure sensitive and selective detection of the analytes in the fmol range. The method was then validated, considering various parameters such as linearity, accuracy, selectivity, carry-over and stability for all matrices used (chapter 4.7, p. 135 ff.). This robust method enabled quantification of four different TriPPPro-compounds and their metabolites in cell extracts within a concentration range of 0.5 – 1000.0 ng/mL. Consequently, for the first time, quantitative data regarding the cellular uptake of prodrugs and their intracellular metabolism could be obtained (chapter 4.8, p. 183 ff.).

1 Introduction

Nucleosides and nucleotides are among the most important biomolecules and are involved in many biochemical processes. Their synthetic analogues have been used for many decades in antiviral and antitumoral therapies. Nucleoside analogues are key components of the pool of drugs currently used in combination therapy (HAART) to treat people infected with the human immunodeficiency virus (HIV). They are also used to treat several other viral infections due to their antiviral activity against herpes simplex virus (HSV), hepatitis B virus (HBV), or hepatitis C virus (HCV). Nucleoside analogues target virus-encoded deoxyribonucleic acid (DNA) polymerases, such as the HIV reverse transcriptase (RT) or the HCV-encoded ribonucleic acid (RNA)-dependent RNA polymerases, and are therefore also known as nucleoside reverse transcriptase inhibitors (NRTIs).[1,2] Zidovudine (AZT) was the first NRTI approved by the U.S. Food and Drug Administration (FDA) for treating patients with acquired immunodeficiency syndrome (AIDS).[3] Other examples of NRTIs include stavudine (d4T), abacavir (ABC), and emtricitabine (FTC), as displayed in Figure 1-1. As anticancer drugs, nucleoside analogues act as antimetabolites. They produce cytotoxic metabolites, in most cases phosphorylated species that interfere with the synthesis of nucleic acids through a complex metabolic pathway. [4,5]

Figure 1-1: Examples of nucleoside reverse transcriptase inhibitors (NRTIs).

The fluorinated derivative of uracil (5-FU) was the first chemotherapeutic nucleobase analogue approved by the FDA in 1962.[6] Its nucleoside analogue, floxuridine (5-FdU), and other analogues such as cytarabine (ara-C) or cladribine are also widely used as anticancer drugs (Figure 1-2.) The antitumor or antiviral activity of nucleoside analogues is highly dependent on the efficient intracellular conversion of the analogue to the nucleoside monophosphate (NMP), diphosphate (NDP), and ultimately the bioactive triphosphate (NTP) by host cell kinases.^[7,8] In the case of NRTIs, the NTP mimics the building block of the DNA, the natural 2'-deoxyribonucleoside triphosphate (dNTP). Due to the lack of the 3'-hydroxyl group, the following dNTP cannot be attached to the sequence, which leads to transcription impairment and termination of the chain elongation. [9] Because of strong substance specificity of the kinases, the nucleoside analogues are not efficiently converted to the triphosphate. For example, the limiting step for the drug d4T is the first phosphorylation step mediated by thymidine kinase. [10,11] This is called the metabolic bottleneck. While NMPs, NDPs or NTPs are very polar, they exhibit poor cell permeability and cannot cross the cell membrane. Because of that, they are not suitable as drugs to administer. To overcome this issue, the concept of prodrugs was introduced. Prodrugs are non-active derivatives of the bioactive compound, which can be metabolized intracellularly to directly release the active substance. The working group of MEIER developed different approaches to bypass the phosphorylation steps by masking the free charges of the phosphate group with lipophilic moieties to enable cell permeability.[12-16]

Figure 1-2: Examples of chemotherapeutic nucleobase (5-FU) or nucleosidic analogues (5-FdU, ara-C and cladribine).

2 Theoretical background

2.1 Nucleosides and nucleotides

Nucleosides and nucleotides play a crucial role in various cellular processes such as DNA and RNA synthesis, enzyme regulation, cell signaling and metabolism.^[17,18] Due to their importance in several biological events in the human body and as a major group of biochemical molecules, their structure and function as well as the significance of nucleoside analogues including their mechanisms of action are explained in the following sections.

2.1.1 Structure and function

Nucleotides are the phosphate esters of nucleosides and comprise three different components: a heterocyclic nitrogen containing base, a pentose sugar and one or more phosphate residues. As a polymer, they form the ribonucleic acid (RNA) and deoxyribonucleic acid (DNA). The base can be either a monocyclic pyrimidine or a bicyclic purine derivative, whereby the most important purine derivatives found in both DNA and RNA are adenine (A) and guanine (G). In the case of pyrimidines, these are cytosine (C) and thymine (T), which only occurs in DNA and uracil (U), which can only be found in RNA (Figure 2-1). The purine or pyrimidine base forms an N-glycosidic bond to a pentose sugar, more precisely a β -D-ribose.

Figure 2-1: Structures of the five major purine and pyrimidine derivatives, which can be found in the DNA and RNA.

This D-ribose is then forced into a five-membered furanose ring, and they form the four ribonucleosides which are known as adenosine, guanosine, cytidine, and uridine. If the sugar is present as 2'-deoxy-D-ribose, the four major deoxyribonucleosides are the monomers that form the DNA. In this case, the methylated pyrimidine base thymine substitutes uracil in RNA (Figure 2-2).

Figure 2-2: Structures of the four major ribonucleosides (R = OH) and deoxyribonucleosides (R' = H) with numbering of the pentose carbon atoms from 1' to 5'.

Whereas nucleosides only consist of a nucleobase and a pentose sugar, nucleotides are the phosphate esters of the former. The simplest form is the esterification of one hydroxyl group of the pentose by a single phosphate moiety and results in NMPs. A very important 5'-deoxyribonucleotide is adenosine 5'-monophosphate (AMP), which is shown in Figure 2-3. The addition of more phosphate groups results in the formation of NDPs and NTPs. This stepwise phosphorylation process is catalyzed by specific kinases while nucleotides in return can be converted into nucleosides by nucleotidases or phosphatases. In general, nucleotides are involved in numerous biological processes, for example inflammation, cell differentiation or apoptotic cell clearance. AMP occurs as a structural element in several important functional

biomolecules, such as acetyl coenzyme A, the redox cofactors nicotinamide adenine dinucleotide (NAD+), NAD phosphate (NADP+) and flavine adenine dinucleotide (FAD), and certainly in adenosine 5'-triphosphate (ATP).^[19] ATP, which is also shown in Figure 2-3, plays a vital role in cellular metabolism, because it provides chemical energy.^[2]

Figure 2-3: Structures of different nucleotides derived from adenine as nucleoside.

Finally, the last important structure is the cyclic nucleotide in which two neighboring hydroxyl groups of the pentose are esterified by a single phosphate as a diester. An example for a cyclic nucleotide is cAMP (Figure 2-3). It is well known that cAMP plays a significant role in inflammation, sepsis, and vascular tone, as it can regulate the endothelial barrier function.^[20–22]

2.1.2 Use of nucleoside analogues against viral diseases and cancer

When the base or sugar building blocks of nucleosides are chemically modified, they are referred to as nucleoside analogues. Nucleoside analogues have been developed to mimic their physiological counterparts and are recognized by cellular host enzymes in the same way as the natural nucleosides. They are therefore able to inhibit the metabolic pathways and are also known as antimetabolites. Nucleoside analogues can also be incorporated into RNA and DNA and consequently inhibit cellular division and viral replication due to the unnatural conformation of the strand because of the analogue. [9] In addition, they are able to interact with and inhibit certain key enzymes, for example by binding to the active side. These key

enzymes include viral and human polymerases, kinases, DNA methyltransferases, purine and pyrimidine nucleoside phosphorylases, as well as thymidylate synthase. Synthetic nucleosides play a key role as potential drugs for the treatment of viral diseases, for example hepatitis virus infections, herpes and HIV but also cancer. [17] For cancer, the primary standard-of-care treatment includes radiation, chemotherapy, hormone therapy, immune therapy, targeted therapy or surgery. For chemotherapy, which is specific drug treatment for the containment of tumors, there are several main drug classes available: alkylating agents, antimetabolites, antibiotics, topoisomerase inhibitors, mitotic inhibitors, and anti-tumor corticosteroids.[23-28] Chemotherapeutic antimetabolites are analogues of nucleosides, nucleotides, and bases, and they make up a large proportion of the current arsenal of chemotherapeutic agents for cancer. Nucleoside analogues alone rarely cure cancer, but they are a valuable treatment option for cancer patients. Furthermore, other nucleoside analogues are also currently being investigated in clinical trials both as monotherapy and in combination therapy. These trials are attempting to increase the bioavailability or potency of these compounds while reducing the associated dose-limiting toxicity.^[29] With regard to antiviral nucleotide analogues, it can be noted that as of the present date, over 25 therapeutic nucleosides have been approved for use as a means of treating viral infections. Examples include tenofovir against HIV/AIDS^[30,31], acyclovir against herpes infections^[32] or lamivudine against hepatitis B^[33] and sofosbuvir against hepatitis C.[34] For HIV alone, there are eight examples of nucleoside analogues, which are NRTIs. In order to minimize the likelihood of resistance development, two NRTIs are commonly administered in combination with a non-nucleoside reverse transcriptase inhibitor or protease inhibitors.[35]

Antiviral nucleoside or nucleotide analogues target viral enzymes and exhibit low activity on mammalian enzymes, which results in a better tolerance profile that anticancer nucleoside analogues.^[17] A promising target for cancer treatment is the DNA replication, as cancer cells typically undergo replication more frequently than

healthy cells. Nevertheless, the inhibition of DNA replication in healthy tissue can result in the development of toxicity, which may limit the amount of drug that can be administered to the patient.^[36]

2.1.3 Mechanisms of action

Nucleoside analogues can enter cells through specific nucleoside transporters.^[37,38] The nucleoside analogue itself is not active as such and needs to be metabolized. Inside of the cell, they undergo stepwise phosphorylation from the NMP to the NDP and to the corresponding NTP which is mainly catalyzed by host cellular kinases.^[17]

In the case of antiviral nucleoside analogues, or in particular the already mentioned NRTIs, the active NTP analogue competes with the natural dNTP and directly binds to the conserved active site of the viral polymerases which are responsible for the viral genome replication.^[39,40] The mechanism of action of NRTIs is shown schematically in Figure 2-4.

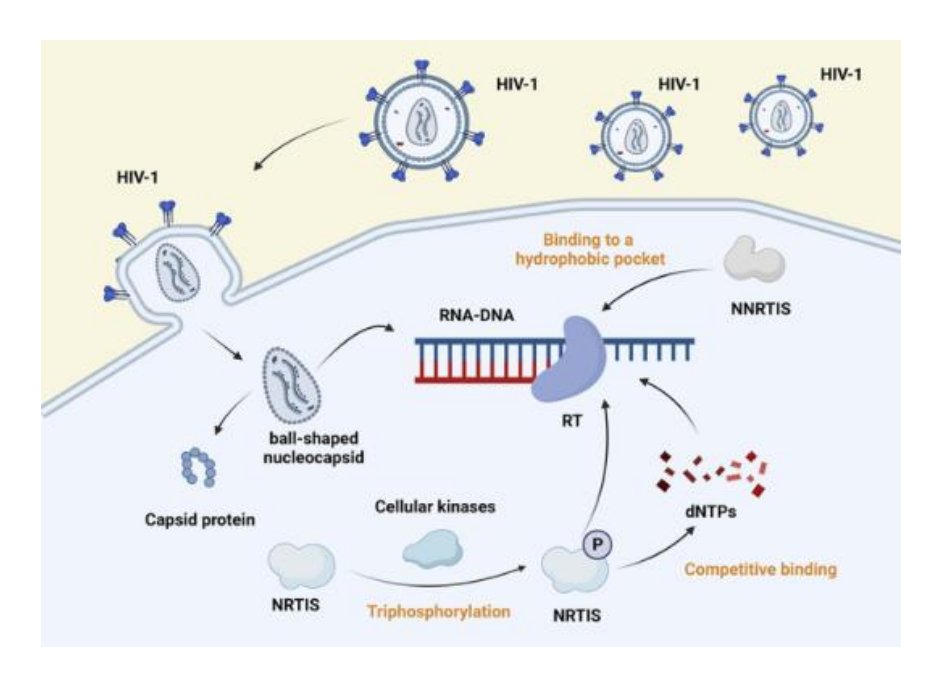


Figure 2-4: Mechanism of action for a NRTI. After phosphorylation of the NRTI by cellular kinases, the NRTI binds competitively to template RNA, which blocks the transcription of viral genes.^[41]

The advantage of this is that human polymerases do not recognize the active substances as substrates, ensuring specific action. After incorporation into the primer strand, they can act as a chain terminator of the DNA synthesis due to the lack of a 3'-hydroxyl group.^[42]

With regard to chemotherapeutics, the objective is, as previously stated in section 2.1.2, to target DNA replication. The nucleoside analogue is capable of inhibiting intracellular enzymes and can also be incorporated into DNA or RNA, which results in the induction of apoptosis. [4,17] As an example, Figure 2-5 shows the mechanism of action for the anticancer drug 5-FU, which emphasizes the different pathways for inhibition. FdU-TP and FdU-MP are considered the key metabolites responsible for the antitumor activity. FdU-TP is incorporated into DNA, resulting in abnormal DNA structures and ultimately triggering cell death. [43] In parallel, FdU-MP inhibits thymidylate synthase (TS), the enzyme responsible for catalyzing the conversion of dUMP to TMP. Inhibition of TS leads to an accumulation of dUTP and a depletion of TTP, creating a nucleotide imbalance that also culminates in cell death. [44]

However, the half-life and pharmacokinetics of nucleoside analogues differ significantly from natural nucleoside properties^[40] and this is mainly due to the fact of the intracellular required activation to the NTP.^[45]

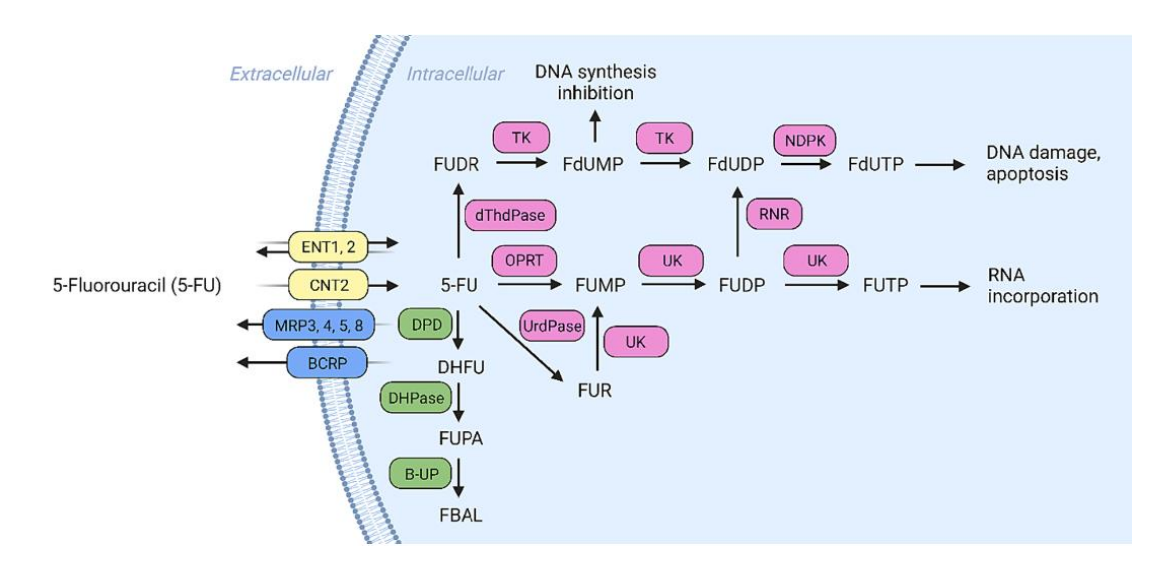


Figure 2-5: Mechanism of action of the anticancer drug 5-FU.^[46]

The first phosphorylation step to the monophosphate is often the rate-limiting step for most nucleoside analogues^[40,47] and also the second phosphorylation step can be critical.^[48,49] Added to this is the substrate specificity of the kinases to natural nucleosides. Nevertheless, the direct administration of nucleotides is not feasible, as the negative charges of the phosphate groups prevent diffusion through the cell membrane, and most cells lack the intrinsic mechanisms necessary for the transport of NTPs.^[17] To overcome this phosphorylation bottleneck, the design of prodrugs of the nucleoside analogues represents a promising approach, which will be discussed in greater detail in the following section.

2.2 The Prodrug concept

As explained in section 2.1.3, in most cases the nucleoside analogue is not active. A general problem with nucleoside analogues is their poor oral bioavailability and low cellular penetration. They also have to undergo stepwise intracellular metabolism to the corresponding active NTP. The concept of a prodrug is based on the derivatization of nucleoside analogues with different chemical groups or functions (so-called masks) that can be cleaved or activated, chemically or through cellular or viral enzymes, to deliver the active nucleotide. These masks can be introduced onto either the base, sugar or phosphate moiety as shown in Figure 2-6.

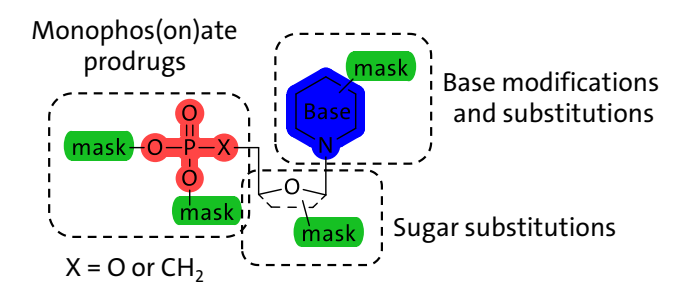


Figure 2-6: General structure of nucleoside prodrugs with possible positions for masking units. Adapted to DE SCHUTTER *et al.*[50]

The prodrug approach led to the FDA approval of various nucleoside and nucleotide analogues such as abacavir or sofosbuvir. [50] As seen in Figure 2-7, the idea of the prodrug concept is to mask the negative charges of the phosphate group of the NMP with lipophilic residues to facilitate cell penetration. Inside the cells, the masks are cleaved by enzymes, releasing the NMP, which then undergoes further phosphorylation to give the active NTP. [2] With this, it is possible to bypass the first and rate-limiting phosphorylation step. It would be highly advantageous to circumvent all phosphorylation steps and develop NTP prodrugs that can directly deliver the active metabolite (NTP) intracellularly. In the literature, it has been suggested that NTP-prodrugs would not be a viable option due to the chemical instability of the compounds. [2] Although the design and synthesis of these prodrugs is very challenging, the working group of MEIER was able to synthesize stable NTP-prodrugs that can enter into the cell and release the bioactive NTP. The so-called TriPPPro-approach will be discussed in the following section.

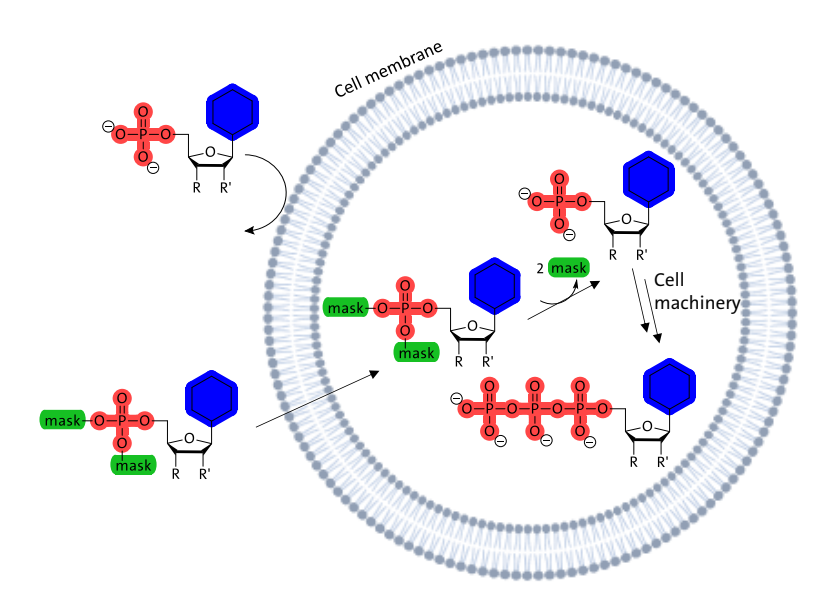


Figure 2-7: Cellular uptake of nucleoside monophosphate prodrugs, release of NMP, and formation of the active metabolite (NTP) by cellular processes. Adapted to CAMARASA *et al.*^[2]

2.2.1 Design and mechanism of TriPPPro-compounds

The initial reports of masked NTPs were synthesized and published by GOLLNEST et al.[1,16] The concept underlying the masking units is the bis-4acyloxybenzyl (BisAB) principle, which was initially developed by Thomson for NMP prodrugs. [51] The negative charges of the γ -phosphate are modified with 4-acyloxylbenzyl (AB) moieties, which can be cleaved off by enzymes. The stability of these compounds can be attributed to the fact that only the terminal phosphate group is masked, while the remaining negative charges on the α and β phosphate groups serve to stabilize the phosphate anhydride bonds. Due to the lipophilic nature of the masking units, the compound is capable of diffusing passively through the cell membrane. Furthermore, the cleavage of the masking units within the cells results in a *lock-in* effect. The mechanism of this enzymatic cleavage is described in Figure 2-8. [14,52] The first step is the hydrolysis of the phenolic acyl ester by esterases. Cleavage destabilizes the acceptor substituent, which becomes a donor substituent. This causes 1,6-elimination, producing 4-hydroxybenzyl alcohol and the monomasked triphosphate, which can so be described as the intermediate. The second AB mask is cleaved similarly, releasing the free nucleoside triphosphate. [14,51]

Figure 2-8: Enzymatic hydrolysis of TriPPPro-compounds and release of the NTP. [14,52]

There is also the possibility of chemical hydrolysis. In general, there are different conceivable mechanisms which are shown in Figure 2-9.[15,52,53] The first mask can be hydrolyzed by nucleophilic substitution at the benzyl position (A). At this stage, it is also possible for the phosphate anhydride bond to be cleaved, which is an unfavorable side reaction, as it results in the formation of NDP or NMP (B). It is not possible for either A or B to occur during the hydrolysis of the second mask due to the presence of the negative charge in the intermediate. Consequently, the cleavage of the acyl ester occurs, which allows for the selective release of the triphosphate (C).[16,52] In recent years, the TriPPPro concept has undergone further development and optimization within the MEIER group. To enhance chemical stability, the AB mask was exchanged to acyloxy benzyl carbonate (ACB) masks. [54,55] There were also TriPPPro-compounds synthesized by ZHAO et al.[56] and JIA et al.[57] bearing nonsymmetrical masking units, for example γ -AB- γ -ACB, γ -AB- γ -alkyl- or even γ -alkyl-TriPPPro-derivatives. The transition from the enzymatic cleavable AB or ACB masking unit to a straightforward alkyl chain maintains an adequate degree of lipophilicity for cellular uptake, while retaining the potential to serve as a substrate for viral polymerases. Additionally, it exhibits remarkable chemical and enzymatic stability as the alkyl moieties cannot be cleaved by nucleophiles or enzymes.^[58,59]

$$\begin{array}{c} O \\ R \\ Nu \\ A \end{array} \begin{array}{c} O \\ \bigcirc P \\ \bigcirc O \\ \bigcirc O$$

Figure 2-9: Chemical hydrolysis of Tri*PPP*ro-compounds. A: First nucleophilic attack at the benzyl position leading to the intermediate, B: nucleophilic attack at the phosphate anhydride bond (unfavorable), C: second nucleophilic attack leading to the formation of the NTP.^[52,53]

2.2.2 Proof of concept and biological data

To confirm the successful cellular uptake of Tri*PPP*ro-compounds and the intracellular delivery of the active NTP, Gollnest *et al.*^[1] conducted cellular uptake studies. As a model system, a fluorescent 2',3'-dideoxy-bicyclic nucleoside analogue triphosphate (ddBCNATP)-prodrug was synthesized and incubated in T-lymphocytes for 60 or 180 min at 37 °C, respectively. Following incubation, the cells were washed, centrifugated and lysed by sonification. The subsequent analysis of the cell extracts via high performance liquid chromatography (HPLC) with fluorescence detection (FLD) employing an ion pair (IP) reagent showed a signal for the fluorescent ddBCNATP, which confirmed the penetration of modified prodrug through the cell membrane.^[1,52]

The antiviral activity determined in CD4⁺ T-lymphocytes of various Tri*PPP*rocompounds derived from the antiviral agent d4T demonstrated, that the synthesized prodrugs were at least similar or often even much more active against HIV-1 and HIV-2 than the nucleoside d4T in wild-type CEM/0 cells.^[60] With regard to Tri*PPP*rocompounds derived from the anticancer drug 5-FU, proliferation assays in different human cancer cell lines indicated that some of the candidates exhibited antitumor activity, given that they demonstrated a proliferation-inhibiting effect that was more pronounced than that observed with 5-FU.^[61] These assays highlight the potential of this antiviral and antitumor prodrug-compounds, while also indicating the necessity for further data concerning cellular uptake, intracellular metabolism and extra- and intracellular concentration levels.

2.3 Liquid chromatography

Following the completion of cellular uptake studies, which were conducted to investigate the successful uptake of the TriPPPro-compound and their subsequent metabolism within the cell, the intracellular metabolites are extracted and subsequently analyzed to determine the concentrations. Cell extracts, as biological matrices, are complex mixtures, and it is not feasible to quantify individual compounds from this without further sample preparation of the resulting extracts. Therefore, this complex mixture must first be separated to facilitate detection. Due to the high peak capacity and simple coupling to various detection methods, column chromatographic separation is the preferred method. Consequently, a significant number of quantification methods are based on HPLC. The most prevalent type of column employed for this purpose is a reversed-phase stationary phase (RP) column. RP columns are defined by the presence of a non-polar stationary phase. The silica particles are covalently bonded to long alkyl moieties (e.g. C18 chains), which render the surface hydrophobic. RP chromatography frequently utilizes aqueous mobile phases for the elution of analytes. The reduction of polarity in the mobile phase facilitates the elution of hydrophobic analytes from the column. [62,63] A disadvantage of this approach is that some drugs, such as nucleotides, are small, hydrophilic compounds that do not interact sufficiently with the stationary phase to allow effective retention without the use of special additives, such as ion-pairing reagents. [64] As a result, these compounds elute in the flow-through peak with many other metabolites as well as salts, which makes a reliable quantification impossible. This issue can be addressed through the implementation of alternative chromatographic techniques, such as ion exchange (IEX) or mixed-mode chromatography, columns with a stationary phase containing porous graphitic carbon (PGC), or hydrophilic interaction liquid chromatography (HILIC).[65] The subsequent section will focus on HILIC and mixed-mode chromatography, given that these two techniques were employed in the course of this work.

2.3.1 Hydrophilic interaction liquid chromatography

For sufficient retention of polar compounds, HILIC has proven to be the most promising approach. Due to the growing field of metabolomics and the increasing development of polar drugs in the pharmaceutical industry, HILIC applications have gained popularity over the last decade. The first time, the HILIC mode of separation was reported in the literature was in the year of 1951, when Gregor et al. [66] described a water-enriched layer on an ion-exchange resin surface. However, it was not until 1990 that HILIC became an acronym, which was first introduced by ALPERT. [67] As already described, the most common HPLC method is RP chromatography and is used in approximately 70 % of LC analyses. Due to the lack of retention of highly hydrophilic compounds, IEX as well as IP chromatography with ion pairing reagents was developed. However, there was a gap concerning compounds that do not have an ionizable functional group. In addition, most of the IP reagents are not volatile and therefore not compatible with mass spectrometric (MS) detection. To overcome this problems, HILIC methods have been developed as an alternative technique for the retention of polar compounds. [68] In comparison to RP chromatography, the stationary phase is mainly polar, whereas the mobile phase contains mostly organic solvent, typically over 70 % acetonitrile and lower amounts of water, at least 2.5 %. [69]

The stationary phases in HILIC often consist of bare silica or modified silica with various polar functional groups such as amino, amide, cyano, diol, zwitterionic, or others. The diversity allows for a wide range of selectivity, making HILIC not only an alternative to normal phase (NP) chromatography but also offering unique selectivity compared to RP chromatography, particularly for the retention of highly polar compounds. [69] A huge advantage of HILIC lies in its compatibility with mass spectrometry, owing to the similarity of solvent used in RP chromatography. The high organic content in the mobile phase, primary acetonitrile, enhances ESI spray formation and ionization efficiency, leading to improved detection sensitivity. Additionally, the low viscosity of organic-rich eluents ensures low operational

column back pressures and high mobile phase velocity, resulting in flatter van Deemter curves and thereby yielding good peak shapes and high column loading capacity.[70,71] Despite its advantages, HILIC presents challenges in method development due to the plethora of column types available, each employing various stationary phase materials. Experimental variables such as the nature of the stationary phase, pH value of the buffer, buffer concentration, organic solvent type and concentration, and temperature further complicate method development. To better understand the influence of the experimental variables and their impact, it is helpful to investigate the retention mechanism of different analytes in HILIC. The retention mechanism remains a subject of debate. The prevailing model is based on a partitioning mechanism between the bulk eluent and a water enriched layer immobilized on the HILIC phase or particles. However, this mechanism alone does not fully explain observed behaviors. Studies have shown that selectivity changes with alterations on organic modifier concentration, buffer concentration, mobile phase pH, and column temperature, suggesting a multimodal retention process involving partitioning of analytes between surface water layers and the bulk mobile phase, as well as adsorption via electrostatic forces between charged ligands and ionized analytes. This is schematically displayed in Figure 2-10 as an example with a zwitterionic stationary phase.^[72] In summary, the retention mechanism in HILIC is highly complex and requires further elucidation through ongoing research efforts.

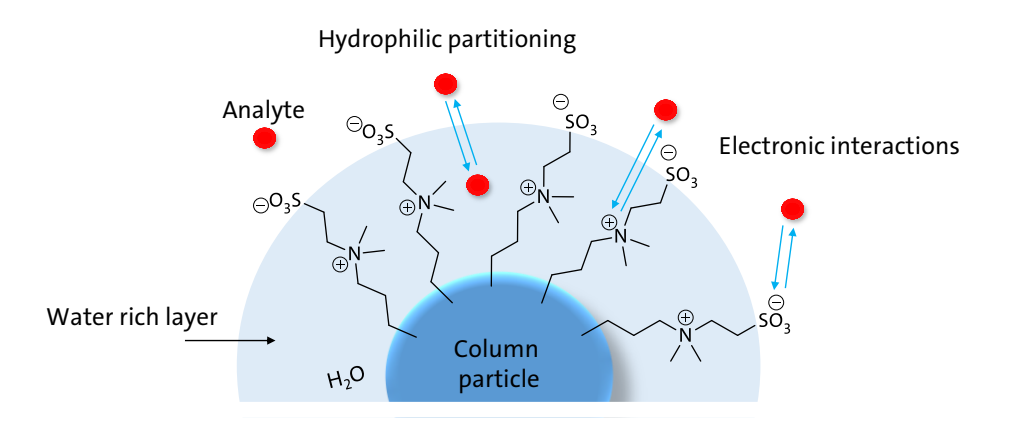


Figure 2-10: HILIC retention mechanism as an example with a zwitterionic stationary phase and the different types of interactions. Adapted to PITENI *et al.*^[72]

2.3.1 Mixed-mode chromatography

Mixed-Mode chromatography has emerged as a versatile tool in chromatographic separations, offering unique advantages for the retention of polar analytes. It was already described by McLaughlin^[73] in 1988 and addresses the limitations encountered in traditional HILIC, notably concerning the retention of ionized polar acids. While HILIC excels at retaining such compounds, challenges remain in finding compatible sample solvents and withstanding long column equilibration times. One of the primary challenges of chromatographic separation lies in retaining highly polar acidic compounds, including metabolites like glucuronides and sulfates, physiological intermediates such as nucleotides, and drugs like peptides and antibiotics particularly when dealing with complex biomatrices.

Mixed-mode chromatography offers a solution by employing an orthogonal separation principle, combining aspects of RP and IEX mechanisms. [74] This approach has gained popularity owing to its ability to simultaneously interact with both polar and non-polar ionic compounds within a single chromatographic run, thus representing a major benefit for the analysis of the lipophilic TriPPPro-compound and its metabolites, the NTP, NDP and NMP. It eliminates the need for separate runs. The pH value of the buffer plays a crucial role in this process, affecting not only the ionization state of the analytes but also that of the stationary phase. Due to its chemical composition, the stationary phase allows for at least two forms of interaction with the analytes. Typically, it features hydrophobic alkyl chains strands alongside hydrophilic domains containing e.g. terminal bicyclic quinuclidine rings with an IEX as seen in Figure 2-11. Therefore, it is an alternative to IP or RP chromatography. As previously mentioned, these modes rely on only one dominant type of interaction, such as hydrophobic or electrostatic forces. In a mixed mode column, the orthogonal combination of RP functionality and ion exchange properties combines both modes of interaction.[73,75,76]

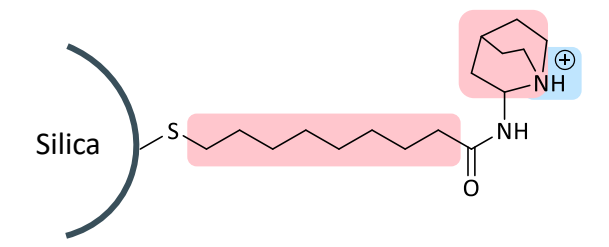


Figure 2-11: Overview of a stationary phase of a mixed mode column (RP/AEX). The regions highlighted in red contribute to the RP functionality, while the tertiary alkylammonium residue highlighted in blue represents an anion exchanger (AEX). Adapted to BICKER *et al.*^[77]

This results in improved retention and separation of small, polar analytes, such as metabolites, which show no retention on a classic RP column. The strength of these interactions can be fine-tuned by adjusting various parameters such as the type of organic modifier, buffer type and concentration, additives, pH value, temperature, and modes of gradient elution. Such flexibility facilitates method development but also introduces complexities, making it more time-consuming and less straightforward compared to traditional chromatographic methods.[77,78] Because many non-volatile substances, such as ion pair reagents, can be omitted, Mixed-Mode chromatography is also well suited for coupling to mass spectrometry. However, when selecting the buffer, buffer concentration and additives, care must be taken to ensure that they are compatible with the subsequent mass spectrometric analysis. Despite its promising features, the separation mechanism underlying mixed-mode chromatography, particularly RP/IEX, remains incompletely understood. A deep understanding is still lacking, mainly because publications have focused on applications rather on the investigation of the separation mechanism.^[76] Furthermore, the method development process itself represents a significant challenge, as it necessitates the exploration of a vast array of parameters, which in turn prolongs the development times and complicates the workflows involved.

A notable success story in the application of mixed-mode chromatography is the development of a method for the highly polar compound ara-C by HSIEH *et al.*^[79] Despite this achievement, the inherent complexity of mixed-mode chromatography

underscores the need for further research to elucidate retention mechanisms fully and streamline method development processes.

2.4 Optical detection methods

The most fundamental quantification methods are often based on RP-HPLC with ultraviolet (UV) or FLD. The following subsections will therefore provide a more detailed examination of these methods, with a particular focus on their limitations in the context of quantifying nucleotide analogues and lipophilic prodrugs.

2.4.1 UV detection

Due to the natural UV absorbance of nucleic bases, UV-based detection is the most straightforward method. This requires that analytes have distinct absorption maxima that do not overlap with other components in the sample. Most studies use a wavelength of 254 nm for analysis. [80,81] Quantification is based on peak area, with concentrations calculated via a calibration curve as an essential part of the method. This approach is suitable for non-volatile, thermally labile, polar or ionic compounds with high molar masses. Non-volatile ion-pairing reagents, such as tetrabutylammonium (TBA) salts, can be added to improve retention and resolution. [82] HUANG *et al.* [83] used RPIP chromatography to analyze intracellular NTP levels in normal and tumor cell lines, achieving detection limits between 1.39 and 15.5 pmol for nine different compound. Other HPLC-UV methods for nucleotides show similar sensitivity in the tens of pmol range. [84,85] However, this method has two main drawbacks: limited sensitivity [81] and specificity. [80,86]

2.4.2 Detection via fluorescence labeling

FLD combined with HPLC can enhance sensitivity and specificity in quantification. Literature reports detection limits in the low fmol range for adenosine derivatives.^[87–89] Fluorescent dyes, also known as fluorophores, are used to study biochemical processes and are excited at specific wavelengths for detection. If an analyte, like nucleotides or TriPPPro-compounds, lack of a natural fluorophore, it can be chemically modified with a fluorescent tag. The ability to distinguish excitation wavelengths from other fluorophores, such as amino acids, is crucial for specificity.^[90,91] Additionally, the derivatization process should not alter the chemical properties of the analyte. The fluorophore must also be chemically stable, exhibit high quantum yield, and resist photobleaching. The analyte can then be quantified by wavelength-selective excitation using fluorescence microscopy in cells or complex biological matrices. [92,93] The pronucleosides or nucleotides are labelled with a dye on the glycone or aglycone. The size of the dye is particularly important because large fluorophores on the analyte molecule affect the diffusion properties of the prodrug, which may make it unsuitable for cell uptake. For these reasons, intrinsically fluorescent nucleoside analogues are used. These contain a nucleoside base that is only slightly modified in its structure and acts as a fluorophore. A good example of this is the use of bicyclic nucleoside analogues (BCNA), which have only a slightly different structural modification of the nucleic base (Figure 2-12) and are therefore well suited as a model system for nucleosides.^[94]

$$R^1$$
 O
 R^4
 O
 O
 R^3
 R^2

Figure 2-12: A schematic display of a bicyclic nucleoside analogue (BCNA).

In the group of MEIER, BCNA derivatives were successfully synthesized by PERTENBREITER^[95], GOLLNEST^[52] and REIMER^[53] for the purpose of investigating the cellular uptake of different prodrugs with FLD-HPLC. By employing the modified Tri*PPP*ro-ddBCNAATP compound, GOLLNEST *et al.*^[16] were able to confirm the successful uptake of the prodrug following incubation in CEM/O cells. However, there remains a lack of data regarding the quantity of compound taken up by cells and insights into the intracellular metabolism of the prodrug-compound.^[96]

Fluorescence detection improves sensitivity and selectivity compared to UV detection. However, derivatization is required if the analyte is not naturally fluorescent.^[5,92,93] Previous research has shown that the fluorescence signal is often weak due to rapid photobleaching of fluorophores when excited at 350 nm, making reliable *in vivo* concentration determinations difficult.^[52,95]

2.5 Mass spectrometry as a detection method

Mass spectrometry (MS) represents the gold standard for the more specific and sensitive detection of analytes. The instrument allows the analysis of compounds present in biological matrices at substance amounts well below the pmol range. [97] In contemporary research, MS is an invaluable analytical instrument for qualitative and quantitative applications and is indispensable for the identification and quantification of analytes. [98] Mass analyzers are utilized for the determination of the specific mass-to-charge ratio (m/z). A mass spectrometer is typically composed of a number of different components. The sample must first be introduced to the spectrometer via the inlet. Subsequently, the analyte must undergo ionization and be transported into the gas phase via the ion source. After that, the ions are separated by a mass analyzer and detected. [97,99] A schematic assembly is displayed in Figure 2-13.

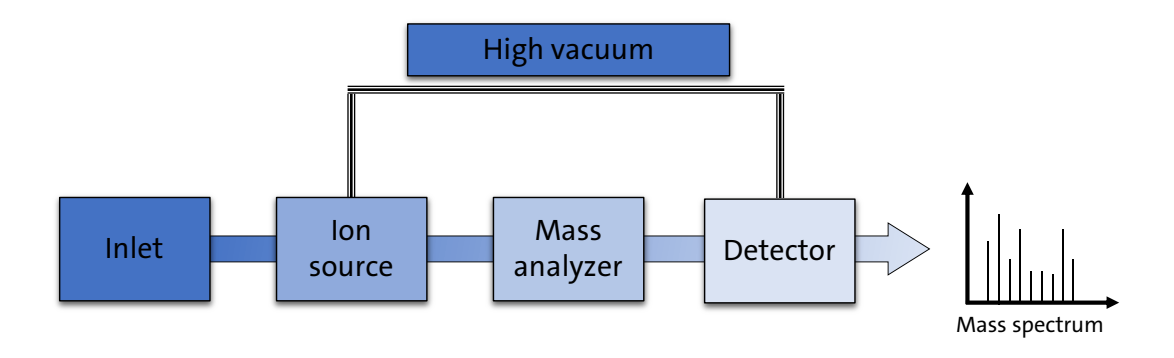


Figure 2-13: Schematic diagram of a mass spectrometer. The sample is introduced through the inlet, followed by ionization in the ion source. The ions produced are then analyzed and detected. The sample inlet and, in some cases, the ion source are not under high vacuum.

Adapted to GRUBER et al.[99]

A variety of ionization methods are available, which can be classified into two main categories: soft and hard ionization techniques. The classification is dependent on the field of application and the properties of the analyte molecule. Hard ionization techniques include electron impact ionization (EI), whereas electrospray ionization (ESI) and matrix-assisted laser desorption/ionization (MALDI) are considered soft ionization techniques.^[97] In EI, highly energetic electrons are employed to generate ions, which results in substantial fragmentation of the analyte of interest. This fragmentation is a valuable tool for identifying the chemical structures of unknown compounds; however, it is most commonly employed for the analysis of small organic molecules with a molecular weight below 600 Da.^[100] For this reason, EI is mainly used in combination with gas chromatography (GC)^[101] and it is not suitable for ionization of Tri*PPP*ro-compounds.

Because of the soft ionization, MALDI is very suitable for the analysis of biomolecules. The analyte is mixed with a certain matrix, applied to a metal plate, and dried. After that, the matrix will be ionized with laser pulses, which results in the formation of a plasma cloud with charged and uncharged matrix and analyte molecules. The analyte molecules are then mainly ionized by proton transfer and analyzed. However, quantitative analysis using MALDI as an ionization technique is very difficult to perform. The main reason for this is that sample morphology can be

very inhomogeneous, leading to poor signal reproducibility. This is known as the sweet spot and coffee ring effects. [102,103] The most suitable ionization technique for the quantification of biomolecules such as nucleotide prodrugs is ESI, and its advantages will be therefore discussed in further detail in the following chapter.

2.5.1 Electrospray ionization

In the mid-1960s, Dole introduced the term ESI. Building on his work, Fenn was able to further develop ESI as ionization technique, and his contribution led to Fenn being awarded the Nobel Prize in Chemistry in 2002. [104,105] In the analysis of biomolecules, including nucleotides and nucleoside analogues, soft ionization methods, such as ESI, are the preferred approach. The degree of fragmentation of the analyte molecule is relatively minimal, with the formation of quasimolecular ions (e.g., [M+H]+, [M-H]-) or adducts with mobile phase ions (e.g., [M+Na]+, [M+NH4]+) observed to a greater extent. Another significant advantage is the ability to readily couple ESI-MS with liquid chromatographic separation techniques, such as HPLC. [106,107]

In ESI, the sample solution is introduced into a narrow metal capillary, which is then subjected to a high voltage. This results in the generation of an electric field, which induces a partial separation of positive and negative electrolyte ions within the solution. [108,109] This results in a spray of droplets that have an excess charge. [110] Ionization can occur in two distinct modes: positive and negative. In the positive ionization mode, the cations are concentrated at the liquid front at the tip of the capillary, while the anions are drawn into the interior of the capillary. When the electric field strength is sufficiently high, the additional repulsion of the positive ions overcomes the surface tension of the liquid, resulting in its expansion into a dynamic cone, known as a Taylor cone. The liquid exits the tip of the capillary in the form of a fine aerosol. [108,109,111] This process is displayed in Figure 2-14.

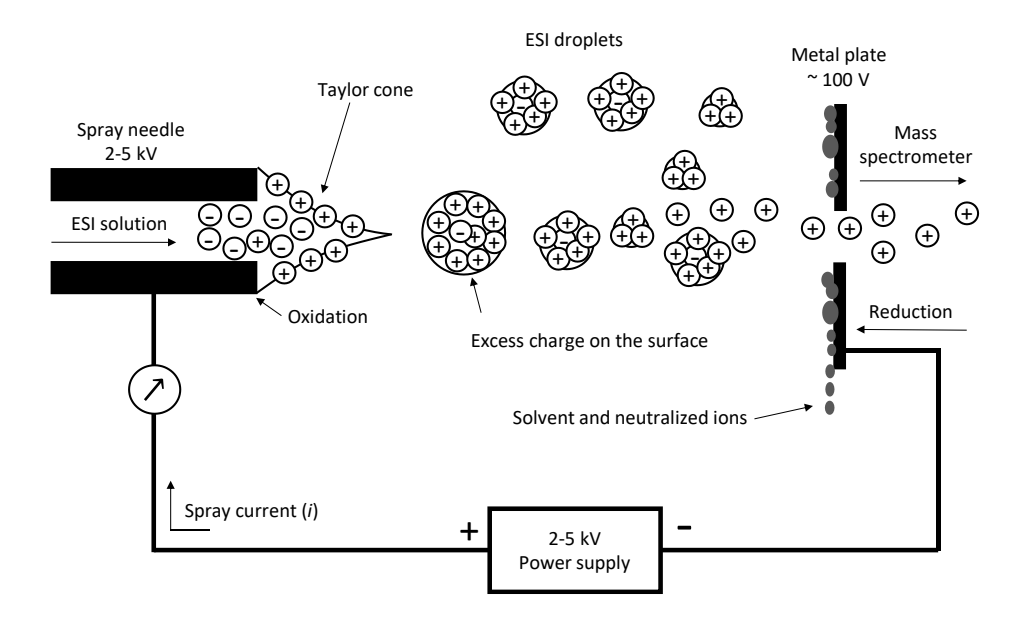


Figure 2-14: Schematic diagram of the ESI process. The sample solution is passed through a capillary to which a high voltage is applied. The electric field between the ESI capillary and the counter electrode creates a gradient that leads to an excess of positive charge on the surface of the liquid. This leads to the formation of a Taylor cone. This results in the formation of charged droplets which evaporate on their way to the mass analyzer, forming individual elementary charge carriers.

Adapted to CECH et al. [106]

In negative ionization mode, the electrophoretic movement of anions and cations is in opposition to the above-described directions. The droplets formed from the Taylor cone diffuse in the direction of the metal plate (counter electrode). Meanwhile, the heat supplied by the electric field evaporates the solvent from the ambient air, reducing the size of the droplets while maintaining their charge. The evaporation of the solvent causes the radii of the charged droplets to reach the Rayleigh limit, where the Coulomb repulsion between the charges on the surface is greater than the cohesive force of the surface tension of the droplets. This leads to a Coulomb explosion and a decay cascade, at the end of which individual charge carriers pass into the gas phase. [106,109–111]

LIIGAND *et al.*^[112] investigated the ionization efficiency (IE), which is defined as the amount of ion generated from a given compound in the ionization source, in ESI. Higher IEs are associated with enhanced sensitivity and, consequently, reduced limits of detection (LOD). Although positive ionization mode is typically the preferred

option, given the expectation of a greater number of compounds being ionized in this mode, negative ionization mode offers a superior overall IE. The primary benefit of negative ESI is the reduction in background noise. [106,111,113] The sensitivity of a mass spectrometer is also dependent upon a number of factors, including the mass analyzers utilized for the separation of individual ions. These mass analyzers can be configured individually or in combination. In this manner, two or more consecutive separations of ions can be conducted, a process known as tandem mass spectrometry (MS/MS).

2.5.2 The quadrupole as mass analyzer

After the ionization of the analyte molecule, the ions are guided into the mass analyzer. Their movement through the electrical field is affected by their m/z and therefore they can be separated.^[114] There are many different types of analyzers used in mass spectrometry, each with its own advantages and disadvantages. The most commonly used mass analyzer is the quadrupole (Q), which consists of four parallel orientated rods that form a square when viewed in horizontal section. This arrangement is shown schematically in Figure 2-15. [97] The rods serve as electrodes, with the opposing pairs being electrically connected to one another. The pairs of electrodes are connected by an alternating radio frequency (RF, ω) potential (U) and a direct current (DC) potential (V). The voltages applied to each pair of electrodes are 180° out of phase.[115,116] The ions, which are initially formed in the ionization chamber, are then pulsed through the quadrupole by an electric field. To illustrate, a positively charged ion will move in the direction of the negatively charged electrode. However, due to the alternation in polarity of the electrodes, the trajectory of the ion will undergo a change before it reaches the electrode. This results in the formation of a complex oscillating trajectory. [97]

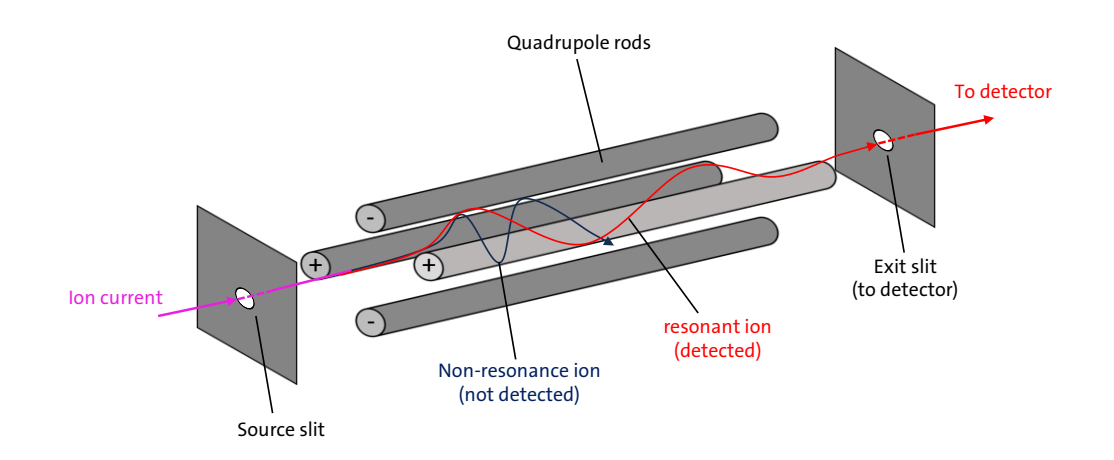


Figure 2-15: Schematic Illustration of a quadrupole. The ion current is passed through four electrodes, from which the opposites are connected to each other by radio frequency and direct current potential. Adapted to EL-ANEED *et al.*^[97]

If V, U and ω are given suitable values, only ions of certain m/z values will have a stable trajectory along the axis of the rod electrodes, while unstable ions will be neutralized as they collide with the walls of the electrodes. [117] As the magnitude of the RF and DC voltages is increased, ions of different m/z values are passed sequentially through the mass filter. [97,116] Although the quadrupole mass analyzer is characterized by a moderate mass range (typically < 4000 Da), low mass resolution and low mass accuracy, the quadrupole has some advantages, such as a high dynamic linear range, low acquisition cost, easy automation, and high sensitivity. [116] Furthermore, the quadrupole is well-suited for coupling to the preceding chromatographic separation (LC-MS) due to its ability to perform rapid scan operations and operate at relatively low voltages, which enables it to withstand comparatively high operating pressures. [97,115] Another advantage of the quadrupole is the characteristic to connect two or more mass analyzer to perform MS/MS experiments.

2.5.3 Tandem mass spectrometry

The fundamental principle of tandem mass spectrometry (MS/MS) is the division of the experiment into two discrete phases, as illustrated in Figure 2-16. In the initial phase of the experiment (MS I), ions with a specific m/z value (precursor ions) generated by the ion source are subjected to mass selection and subsequently focused into a collision cell, where their mass m undergoes a chemical transformation. A product ion and a neutral fragment (or an alternative product ion, in the event that the precursor ion has been charged on multiple occasions) are generated. In the second phase of the experiment (MS II), the mass of the product is analyzed with the objective of establishing a relationship between the precursor and the product ion. This results in the generation of a MS/MS spectrum, which is of great utility for the structural characterization of analyte molecules. [97,116,118] MS/MS experiments are also useful for the analysis of complex mixtures, as the generated spectra are highly specific for a single analyte molecule. Moreover, an advantage of MS/MS experiments is the enhancement of the signal-to-noise ratio (S/N), as the initial step (MS I) functions as a filter for all ions that are not of interest. Such ions will be eliminated, thus preventing any signal from being generated in the spectrum.[119]

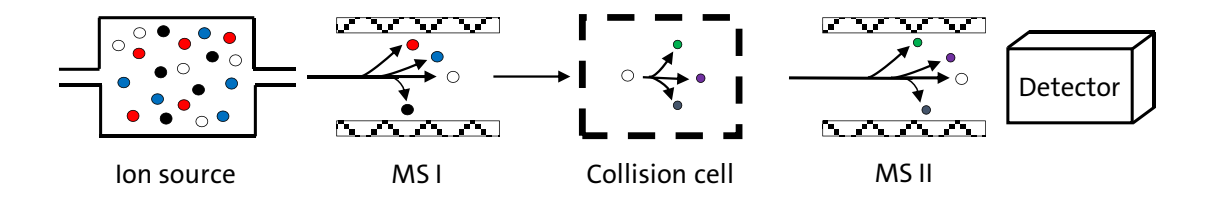


Figure 2-16: Schematic diagram of an MS/MS experiment. After ionization of the analyte in the ion source, the ions enter the first analyzer (MS I) where they are mass selected. The precursor ions are then guided into the collision cell where the collision-induced dissociation (CID) takes place. From there, the product ions are transferred to the second mass analyzer (MS II) where they are analyzed and transferred to the detector. Adapted to EL-ANEED *et al.* [97]

The previously mentioned chemical reactions occur within a collision cell and are, in the majority of cases, unimolecular dissociation reactions initiated by an increase in internal energy. This increase is based on the kinetic energy of the precursor ion, which is released into the environment during the collision with an inert gas (nitrogen, argon, or helium).[120-122] The ions enter an unstable, excited state and subsequently fragment into product ions. This process is referred to as collisioninduced dissociation (CID). The energy transferred during the collision is dependent upon the translational kinetic energy of the precursor ion and its mass. [116,118,120] The majority of existing mass analyzers can be connected in series.^[97,116,118] For example, ions can be isolated in the initial mass analyzer, fragmented in the collision cell, and the resulting fragment ions can be separated in the final mass analyzer based on their m/z values. An illustrative example of an MS/MS instrument is the triple quadrupole mass spectrometer (QqQ), which is a combination of three quadrupole mass analyzers in series.[123] The initial and final quadrupole (Q) stages serve the function of mass filtration, while the second quadrupole (q) represents the collision cell.[115]

A variety of experiments can be performed during an MS/MS measurement, yielding different types of information from the sample. Besides different scans, analyses can be conducted in multiple reaction monitoring (MRM) mode. This method is highly sensitive and selective, rendering it particularly well-suited to quantitative analysis. In MRM mode, a precursor/fragment ion pair is identified that is distinctive for the analyte. This ion pair is called a mass transition. [118] This indicates that for a known analyte, the initial mass analyzer (MS I) is configured to the m/z ratio of its precursor ion, typically the protonated or deprotonated molecule, and only this enters the collision cell. The CID process generates the distinctive fragments, or product ions, of the analyte. The second mass analyzer (MS II) is programmed to selectively filter the m/z ratios of two or more of these known product ions (Figure 2-17). The selectivity for the analyte of interest is therefore markedly high, allowing its detection from complex mixtures. [124]

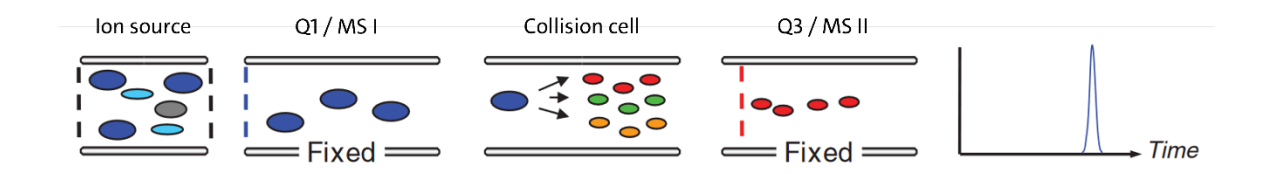


Figure 2-17: Overview of the MRM scan mode. A precursor ion and a specific fragment characteristic for that precursor are selected by MS I and MS II, respectively. The signal, which is the mass transitions, gets recorded as a function of time (chromatographic elution). [124]

The MRM mode is typically performed on QqQ mass spectrometers and is employed in both LC-MS/MS and GC-MS/MS techniques. One such application is the quantification of pharmaceutical compounds in biological matrices.[116,119] By coupling LC and MS/MS, it is possible to obtain both the retention time and the combination of precursor ion and fragment/product ion for each individual compound to be quantified (mass transition). This provides a high selectivity that cannot be achieved by UV or fluorescence detection (see sections 2.4.1 and 2.4.2). Triple quadrupole mass spectrometers generally provide unit mass resolution, meaning that ions differing by one m/z unit can be distinguished. [125] There are numerous examples in the literature of improved sensitivity and specificity compared to UV or fluorescence detection with detection limits in the lower fmol range when quantifying endogenous nucleotides. [126-128] There are also examples available on the quantification of nucleoside analogues. CRAUSTE et al.[129] developed a LC-MS/MS method for the quantification of araCTP, CTP and dCTP in a human cell line using a PGC column for separation. Derissen et al.[130] was able to simultaneously quantify FdU-MP, FdU-DP and FdU-TP in peripheral blood mononuclear cells (PBMCs) using a IEX column.

Given the low substance amounts of metabolites, which range from a few femtomoles to several picomoles, highly sensitive detection is essential.^[65] This is achieved through the use of mass detectors in the LC-MS/MS method. With regard to the LC method, it has been proposed that prior separation of the analytes is a necessary but challenging step to achieve with regular RP columns. In order to achieve accurate and specific quantification in MRM mode, it is necessary to analyze

a minimum of two MRM transitions for each compound. The initial transition is employed for the actual quantification, which is typically the MRM transition exhibiting the greatest intensity. This is referred to as the "quantifier". [131] The second mass transition, which is characteristic of the compound being quantified, is employed to confirm the identity of the compound, thereby enhancing the specificity of the analysis. This mass transition is designated as the "qualifier" for quantification purposes. [131] The peaks of the extracted ion chromatograms (EICs) obtained from the MRM transition are integrated, and the resulting peak area is subjected to comparison. The comparison between two distinct experimental conditions is referred to as relative quantification. In contrast, absolute quantification employs a peak area obtained with an internal standard of known concentration as a reference point. [132,133]

The employment of mixed-mode chromatography or HILIC to separate complex mixtures of the Tri*PPP*ro-compound and the nucleotides after cellular uptake studies in combination with MRM scan mode shows a promising approach to develop a quantification method for intracellular metabolite concentrations.

3 Objective

Nucleoside and nucleotide analogues have been applied in anticancer and antiviral chemotherapy, and they are the frontline of drugs used to combat infections caused by various viruses. Due to the slow and inefficient metabolic conversion of the nucleoside analogue drug to the active NTP analogue, MEIER et al. successfully applied the TriPPPro-approach for direct intracellular delivery of the NTP. This approach has not only been established but also further optimized in recent years. The cellular uptake of various fluorescence-labeled TriPPProcompounds (BCNAs) has been demonstrated by qualitative FLD-HPLC analysis, but cellular uptake studies have only been performed with this model system. TriPPProcompounds without the BCNA motif, which have been tested in biological assays and have shown antiviral or antitumor activity, have never been used for cell uptake studies. Therefore, data on the amount of prodrug taken up by cells and the intracellular concentration of the active metabolite(s) responsible for the antiviral or antitumor activity are still lacking. In order to perform a quantitative analysis, it is necessary to develop a method that is sufficiently sensitive and selective to detect the TriPPPro-compounds within cellular matrices. The objective of this work was to develop an analytical method that meets the sensitivity and selectivity requirements. The selected analytes of interest are four different TriPPProcompounds, which were synthesized within the group of MEIER. Two of these TriPPPro-compounds derived from the anticancer drug 5-FU and synthesized by WITT[61], showed promising cytostatic properties in proliferation assays. The other two TriPPPro-compounds were synthesized by JIA^[55,134] and are potent anti-HIV active pronucleotides of d4T (Figure 3-1).

Figure 3-1: Analytes of interest for cellular uptake studies and subsequent analysis with LC-MS/MS. Compounds **1** and **2** are symmetrical BisAB-FdU-prodrugs and compounds **3** and **4** are asymmetrical d4T-prodrugs.

The two compounds, **1** and **2**, are symmetrical Tri*PPP*ro-derivatives, both bearing two AB masks with different alkyl chain lengths. Compounds **3** and **4** are two different asymmetrical Tri*PPP*ro-derivatives. Compound **3** is an asymmetrical phosphate analogue with one AB mask with a C2 alkyl chain and one ACB mask with a C16 alkyl chain. Compound **4** is a phosphonate analogue with a C18 alkyl chain and an ACB mask with a C4 alkyl chain.

As previously stated, none of the compounds depicted in Figure 3-1 have been subjected to investigation in cellular uptake studies. Following cellular uptake, the compounds will be metabolized by enzymes, as described in section 2.2.1, to release the active NTP. Hydrolysis studies in cellular extracts (CEM/O for d4T-derivatives and different human cancer cell lines for FdU-derivatives) were conducted for all aforementioned compounds to assess stability. These studies revealed the

formation of additional metabolites. Besides the NTP analogue, the formation of NDP and NMP was also observed and the monomasked NTP intermediate is, in the majority of cases, the major product.^[57,61,134] All potential metabolites for the various prodrugs including the Tri*PPP*ro-compounds itself should be evaluated using a quantitative analysis method.

In detail, the aim of this presented work is the development of a HPLC method, which allows for simultaneous retention of both the lipophilic Tri*PPP*ro-compounds and intermediates as well as the hydrophilic metabolites (NTP, NDP, NMP and nucleoside) within a single HPLC run. Due to the complexity of the samples, a targeted approach with MS/MS is desired. Therefore, a MRM method should be developed as well. For the MRM mode, all compounds must be available, and missing compounds need to be synthesized.

In addition to the development of a sensitive and specific LC-MS/MS method, the sample preparation workflow must be adjusted for the quantification of all analytes following cellular uptake studies. The complete analysis workflow should be optimized and validated in terms of the calibration curves' linearity, accuracy and precision, selectivity, carryover, stability, matrix effect, and recovery rate for each analyte.

Possible challenges to be considered are the unknown but likely very large concentration ranges of the analytes, micelle formation of the Tri*PPP*ro-compounds and the different chemical properties of the different analytes of interest.

4 Results and discussion

The development and optimization of an LC-MS/MS method is typically comprised of various steps. This process is iterative and can be highly time-consuming, particularly when confronted with challenging requirements. The key steps are illustrated in Figure 4-1, with the initial MS tuning being the first important step for every MS/MS method. Subsequently, the chromatographic method must be developed, wherein each analyte should exhibit adequate signal intensity and optimal peak shape, given that chromatographic performance impacts sensitivity and selectivity. Following the chromatographic development phase, the MS instrument must undergo optimization with respect to both source parameters and substance-specific parameters. This necessity arises due to the fact that chromatographic conditions, such as flow rate or solvent ratios, have an influence on ionization in the ESI source. Afterwards, the sensitivity and linearity of each analyte will be evaluated.

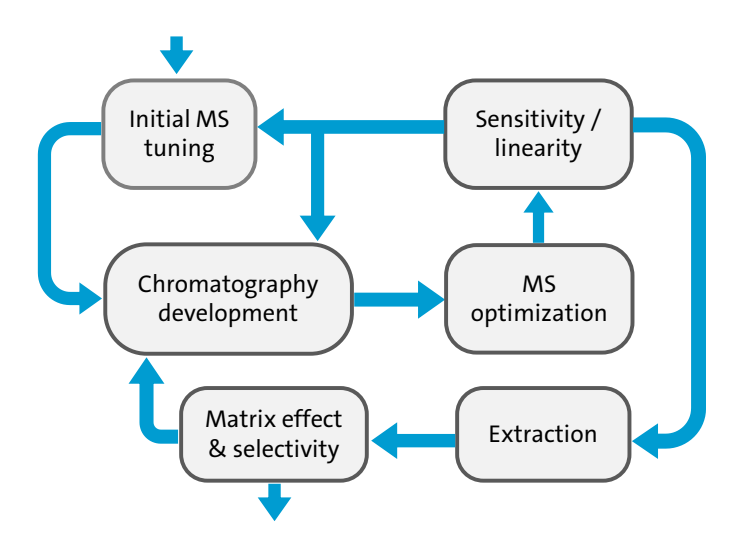


Figure 4-1: Schematic overview of key steps in the development and optimization of an LC-MS/MS method. Adapted to SARGENT *et al.*^[135]

Once these factors are adequately addressed, the extraction of the analyte from the complex matrix must be assessed and optimized. Achieving optimal extraction of the analyte from the complex matrix is crucial, as this sample preparation step significantly impacts the sensitivity and selectivity for the analytes. Subsequently, matrix effects and selectivity must be evaluated. As illustrated in the figure, the key steps exhibit co-dependencies, and, on occasion, it may be necessary to repeat several steps to achieve an optimum result.

Figure 4-2: Tri*PPP*ro-compounds **1** and **2**, along with all possible metabolites derived from them, including their exact masses.

Figure 4-3: Tri*PPP*ro-compounds **3** and **4**, along with all possible metabolites derived from them, including their exact masses.

In the following chapters, a detailed discussion of each step in the method development process will be presented, with Figure 4-1 serving as a schematic overview.

4.1 Synthesis of the intermediates

Prior to the design of the MRM method, the MS instrument must undergo tuning via direct injection of standard solutions comprising the analytes of interest, with the objective of identifying the precursor ion masses. The generated precursor ions are then employed for the fragmentation process, which yields three product ions each. From this, the specific mass transitions are constructed. This is also referred to as initial MS tuning. Two of these mass transitions will be designated as "quantifier" and "qualifier," as outlined in section 2.5.3. Most of the analytes were available as they were synthesized by WITT and JIA and had been characterized by nuclear magnetic resonance (NMR) and MS-ESI-Time-of-flight (ToF) analyses and were also checked for purity via RPIP-UV runs.

Two analytes, the intermediates of the bis[C11AB]-FdU-TP **2** and the intermediate of the [C2AB][C16ACB]-d4T-TP **3** were not accessible and thus required synthesis within the context of this work. The retrosynthetic analysis will be discussed in the next section.

4.1.1 Retrosynthetic analysis

The monomasked compounds **6** and **11** can be synthesized via two different routes, as exemplified in Figure 4-4 for the intermediate **6**. Reimer employed the phosphoramidite route, utilizing a non-symmetrical phosphoramidite bearing a 9-fluorenylmethyl (Fm) moiety as a protecting group for the synthesis of monomasked Di*PP*ro-compounds and successfully extended this approach to TriPPPro-compounds. Jia and Zhao employed the H-phosphonate route, utilizing a non-symmetrical H-phosphonate bearing a β -cyanoethyl moiety as a protecting group. $S^{[58,136]}$

Phosphoramidite route

Phosphoramidite route

Phosphoramidite route

Phosphoramidite route

Phosphoramidite route

$$C_{11}H_{23}$$
 $C_{11}H_{23}$
 $C_{11}H_{$

Figure 4-4: Possible retrosynthetic routes for the synthesis of the monomasked [C11AB]-FdU-TP **6**.^[53,58,136]

In case of the phosphoramidite route, the 5-FdU-DP **8** is coupled to the corresponding non-symmetric amidite **17**, contrasting the H-phosphonate route, in which the FdU-MP **9** is coupled to the corresponding non-symmetric pyrophosphate, which is synthesized from the H-phosphonate **18**. The yields of the final coupling step are comparable for both routes and are found to be between 10-25%. [53,136] The synthesis of nucleoside monophosphates is typically less challenging than that of the corresponding diphosphates, which is why the H-phosphonate route was selected first.

4.1.2 Synthesis of 5-FdU-monophosphate 9

Monophosphates can be obtained via different phosphorylation reactions. Direct phosphorylation of the 5'-hydroxyl group according to conditions of Sowa & Ouchl^[137] and Yoshikawa^[138] are well established within this working group. However, it was known from previous work by WITT^[61] that there were some difficulties with the direct phosphorylation of 5-FdU **10** regarding regioselectivity and formation of byproducts.

Therefore, the phosphoramidite route was selected as phosphorylation reaction. Reaction conditions were applied according to WITT. [61] First, it was necessary to synthesize a 3'-selectively protected nucleoside (Figure 4-5). The 3'-acetyl protected nucleoside 20 could be obtained in a yield of 69 % over two steps. The first step in the synthesis starts from 5-FdU 10, which is commercially available and is stepwise protected with tert-butyl-dimethyl silyl (TBDMS) chloride and acetic acid anhydride. Subsequently, the nucleoside undergoes desilylation using triethylamine trihydrofluoride as the fluoride donor to obtain the 3'-selectively protected nucleoside for phosphorylation with bis(flourenylmethyl)-phosphoramidite (Fmamidite) 21. The Fm-amidite was not synthesized in this work and was gratefully provided within the working group. The phosphorylation was carried out after reaction conditions according to Weinschenk^[139], where the selectively protected nucleoside 20 was reacted with 1.5 equivalents of the Fm-amidite 21 using 1.2 equivalents of 4,5-dicyanoimidazol (DCI) as activator. This was followed by the phosphite-oxidation with 1.5 equivalents of tert-butyl hydroperoxide. Before the deprotection step of the Fm-groups, the protected monophosphorylated product was purified by NP column chromatography. The following deprotection with a mixture of methanol, triethylamine and water with subsequent purification by RP chromatography led to the 5-FdU-MP 9 (Figure 4-6).

Figure 4-5: Synthesis of the 3'-selectively protected FdU 20.[61]

Figure 4-6: Monophosphorylation of 20 using the Fm-amidite 21. [61]

4.1.3 Synthesis of the intermediate $\bf 6$ via the non-symmetric β -cyano ethyl phosphonate route

To synthesize the *H*-phosphonate **18**, the corresponding acyloxybenzyl ester **22** and 3-hydroxypropionnitrile are reacted in an addition-elimination reaction with diphenyl phosphite (DPP). The synthesis of the acyloxybenzyl ester **22** will not be discussed within this thesis since this synthesis is already established within our group and was sufficiently discussed in prior theses^[52,59,61,136] and publications.^[15,16] The reaction conditions are displayed in Figure 4-7 and were employed according to ZHAO.^[58] 1.2 equivalents of DPP were dissolved in pyridine and cooled down to 0 °C. 1.0 equivalents of the acyloxyl benzyl ester **22** were added very slowly and the reaction was stirred at 0 °C until analysis via thin layer chromatography (TLC) showed full consumption of the acyloxy benzyl ester. The reaction mixture was then warmed to room temperature and 1.4 equivalents of 3-hydroxypropionnitrile were added in one portion. The reaction mixture was heated up to 40 °C until the formation of the product was observed via TLC.

Figure 4-7: Synthesis of the asymmetric *H*-phosphonate with β-cyanoethyl moiety as a protecting group **18.**^[58]

The non-symmetric H-phosphonate was obtained in a yield of 47 %. The challenge in the synthesis of asymmetric phosphonates is the likewise formation of the symmetric phosphonates byproducts. Therefore, it is important to add the first alcohol very slowly to the DPP at 0 °C to favor the monosubstitution. Nevertheless, the formation of the symmetric substituted AB- and β -cyanoethyl-H-phosphonates was observed, explaining the moderate yield of 47 %.

The next step was the conversion of the *H*-phosphonate to the corresponding pyrophosphate **23**, which is then activated and coupled to the 5-FdU-MP **9** (Figure 4-8). The synthesis of the pyrophosphate was carried out according to reaction conditions established by Gollnest. The *H*-phosphonate was suspended in acetonitrile and warmed to 50 °C for better solubility of the compound. The addition of *N*-chlorosuccinimide leads to the formation of a chlorophosphate due to an oxidative chlorination. After this activation, the addition of a tetra-*n*-butylammonium dihydrogen phosphate solution resulted in the formation of the pyrophosphate **23**. Pyrophosphates are very unstable and decompose even when stored under inert gas and in non-nucleophilic solvents. Therefore, the residue is only dissolved in dichloromethane and washed twice with aqueous ammonium acetate (1 M) and water. A fast phase separation could be achieved using a centrifuge.

Figure 4-8: Synthesis of the monomasked [C11AB]-FdU-TP 6. [56,61,75,136]

After removing dichloromethane under reduced pressure and co-evaporation with acetonitrile, the pyrophosphate was either stored at -20 °C over night or directly used for the subsequent coupling reaction. A yield of 86 % was determined for the pyrophosphate 23 though it was not subjected to further analysis due to its instability. The following reaction was also established by GOLLNEST [52], who developed the protocol following Mohamady et al.[140] Reaction conditions were applied according to WITT. [61] After dissolving the pyrophosphate 23 in acetonitrile, a mixture of trifluoroacetic anhydride (TFAA) and triethylamine in acetonitrile was added dropwise and the compound 23 was converted to the trifluoro acetyl pyrophosphate 24. After evaporation of all volatile compounds, the residue was dissolved in N,N-dimethylformamide (DMF). After the addition of 1-methylimidazole, the compound reacted to the imidazolidate 25, which acts as a favorable leaving group and enhances the electrophilicity of the phosphorus atom. The last step comprises the addition of the 5-FdU-MP $\bf 9$ to obtain the β -cyanoethyl-protected prodrug 26, which then needs to be deprotected to finally yield the monomasked FdU-triphosphate compound 6 (Figure 4-9). Because of solubility issues of the FdU-MP 9 in acetonitrile, the reaction solvent was changed to DMF before the addition of 1-methylimidazole. The FdU-MP 9 was also added dissolved in DMF.

Figure 4-9: Detailed synthesis of the β -cyanoethyl protected Tri*PPP*ro-compound **26** via formation of the mixed anhydride **24** and the activated imidazolidate **25**. [52]

Unfortunately, following the reaction via RPIP-UV, it was observed that there was no conversion of the FdU-MP **9**. Despite heating the reaction to 40 °C, no conversion could be detected and after purification by automated RP chromatography, only starting material could be re-isolated.

The observation that the FdU-MP **9** did not react may be attributed to the absence of pyrophosphate **23** as a reactant, suggesting a possible issue during its formation or activation. The reaction was conducted again, where the formation of the pyrophosphate was followed by ³¹P-NMR. After the work-up, the dichloromethane was evaporated under reduced pressure and the residue was analyzed by NMR. The NMR spectra did not show any characteristic signals for the pyrophosphate. It was hypothesized that the formation of the pyrophosphate was unsuccessful, although this is considered unlikely given the established reaction conditions within our

group. Alternatively, it was possible that the pyrophosphate was lost during work-up due to micelle formation of the compound or a tendency to diffuse into the aqueous phase due to the low lipophilic character of the β -cyanoethyl moiety. The AB mask alone needs to compensate for the two negative charges on the pyrophosphate. However, isolation of the pyrophosphate from the aqueous phase was not possible, as the separation of the succinimide and the phosphate salt, which were both added in excess, is difficult.

Instead, the monomasked compound should be obtained following the phosphoramidite route as an alternative (Figure 4-4). For that, a non-symmetric phosphoramidite bearing a β -cyano ethyl group needed to be synthesized and subsequently coupled to the FdU-DP **8**.

4.1.4 Synthesis of FdU-5'-diphosphate 8

At first, the FdU-DP **8** was synthesized according to a procedure by Witt.^[61] For the reaction, an activated monophosphate will be coupled to a mono-phosphate salt, which is analogue to the Tri*PPP*ro-synthesis described in chapter 4.1.3. In this case, the monophosphate is the electrophile and will be gradually activated by trifluoroacetic anhydride and 1-methylimidazole, whereas the phosphate salt represents the nucleophile. The exact reaction conditions are displayed in Figure 4-10. After activation of the FdU-MP **9**, it was slowly added to the tetra-*n*-butylammonium phosphate solution. The use of a syringe pump was found to be very useful, since the reaction mixture could be added in a controlled manner with 0.2 mL per min. The formation of by-products was not observed. After one hour of reaction time, the monophosphate was consumed. This finding aligns with the results reported by Witt.^[61]

Figure 4-10: Synthesis of FdU-DP 8.[61]

For the next coupling step with the phosphoramidite, the diphosphate should be available as a tetrabutylammonium salt because it enhances the nucleophilicity of the compound and contributes to the superior solubility of the compound in organic solvents used for phosphoramidite coupling reactions, typically including acetonitrile, tetrahydrofuran or dichloromethane. Therefore, the purification of the diphosphate was modified. After completion of the reaction, aqueous ammonium acetate solution (1 M) was added to the mixture and the aqueous phase was washed twice with chloroform. Within this procedure, the excess of imidazole could be removed. Subsequently, the crude product was purified by automated RP column chromatography. The addition of ammonium acetate solution converted the diphosphate into the ammonium salt, which is very polar and highly water soluble. Thus, the separation of all non-polar contaminants was simple and after lyophilization of the product, the diphosphate was converted into the tetrabutylammonium salt by titration with tetrabutylammonium hydroxide solution (40 %) followed by a second automated RP column chromatography to remove excess ammonium salts. The ³¹P NMR spectrum verified the identity of the diphosphate. As to be expected, two doublet signals for the α - and the β -phosphate were observed (Figure 4-11).

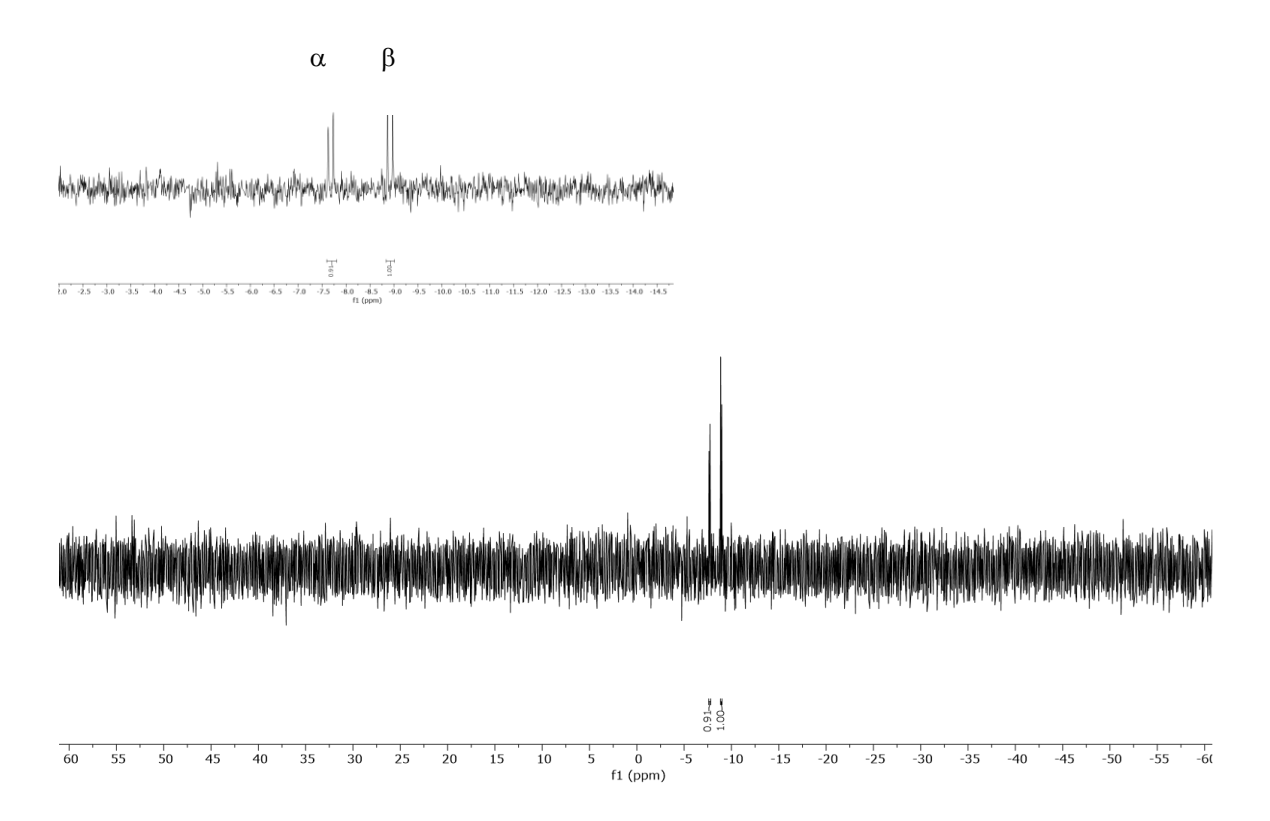


Figure 4-11: ³¹P NMR spectrum of the FdU-diphosphate 8.

The exact number of tetrabutylammonium counterions was determined via 1 H NMR spectroscopy. It was expected to have approximately three counterions as the equivalents of the tetrabutylammonium hydroxide solution were calculated before titration. The number of counterions could then be determined via the ratios of the integrals for the proton signals. Unfortunately, it turned out that the diphosphate contained a disproportionately high number of counterions. Therefore, the RP column chromatography was repeated. After the column chromatography, the diphosphate was insoluble in water and NMR analysis in DMSO- d_6 confirmed, that the diphosphate did exchange the counterions from tetrabutylammonium ions to protons, which was the reason for the sudden insolubility. The titration with 3.5 equivalents of tetrabutylammonium hydroxide solution was repeated, but even after several tries, it was not possible to achieve the correct number of counter ions on the diphosphate. In the end, the compound was obtained with about three tetrabutylammonium counter ions and additionally 6.0 equivalents of tetrabutylammonium salt as an impurity in a yield of 50 %.

4.1.5 Synthesis of the intermediate **6** via the non-symmetric β -cyano ethyl amidite route

In the course of the phosphoramidite route, the non-symmetric amidite, which contains one masking unit and one protecting group, is to be coupled to the diphosphate. Prior to this step, the non-symmetric amidite must be synthesized. In this instance, a β-cyano ethyl protecting group was selected instead of a Fm protecting group as displayed in the retrosynthetic analysis in chapter 4.1.1. This was due to the fact that this particular amidite 27 is commercially available and does not require synthesis. The synthesis of the non-symmetric amidite was carried out according to reaction conditions established by Jeschik [141] using a reduced number of equivalents of triethylamine because of the base lability of the protecting group. The detailed reaction conditions are displayed in Figure 4-12. 1.0 equivalent of the amidite 27 was dissolved in tetrahydrofuran (THF) and slowly added to a solution of the acyloxy benzyl ester 22 and 1.5 equivalents of triethylamine in THF at 0 °C. The reaction was stirred at room temperature until TLC showed full conversion of the starting material 22. The non-symmetric amidite 28 was obtained in a yield of 88 %.

The next step was the reaction of the amidite **28** with the FdU-DP **8**. Reaction conditions were employed following a protocol from Jeschik^[141] using FdU-DP as tetrabutylammonium salt and 1.5 equivalents of pyridinium-trifluoroacetate (pyTFA) as activator.

Figure 4-12: Synthesis of the non-symmetric phosphoramidite 28 with a β -cyano ethyl moiety as protecting group.^[141]

The advantage of pyTFA in comparison to the use of DCI as an activator, as described in the synthesis of the FdU-MP **9**, is the enhanced water solubility, which contributes positively to the subsequent purification of the product **26** via RP chromatography. [141] Exact reaction conditions are displayed in Figure 4-13.

For the synthesis, 1.5 equivalents of the non-symmetric amidite **28** and, in a separate flask, 1.0 equivalents of the FdU-DP **8** were co-evaporated with acetonitrile and dried *in vacuo* for three hours. Afterwards, the compounds were dissolved in acetonitrile. It was only possible to dissolve the diphosphate in acetonitrile with an excess of tetrabutylammonium counterions. Unfortunately, this excess led to the formation of a colorless precipitate when adding 1.5 equivalents of the pyTFA activator. It is conceivable that an ion pair could be formed with the tetrabutylammonium cations, which is insoluble in acetonitrile. Nevertheless, the reaction was conducted and after 30 minutes of reaction time at room temperature, *tert*-butyl hydroperoxide was added for oxidation of the phosphite to the phosphate. In the subsequent automated RP column chromatography for purification, it was not possible to identify the product **26**. This may be attributed to the excess of tetrabutylammonium salts interfering in the reaction.

Figure 4-13: Synthesis of the [β -cyano ethyl][C11AB]-FdU-TP **26** via the phosphoramidite route. [141]

4.1.6 Synthesis of the intermediate **6** via the non-symmetric Fm-phosphonate route

After unsuccessful synthesis attempts of the intermediate **6** via the phosphoramidite route and the *H*-phosphonate route employing a β-cyano ethyl moiety as protecting group, the use of a more lipophilic *H*-phosphonate should be tested to avoid a possible loss of the pyrophosphate during the aqueous work-up. A Fm moiety was chosen since this group is more lipophilic but can also be deprotected under mildly basic conditions following an E1CB mechanism. The Fm moiety is often used within our group and was also employed by Reimer in the synthesis of monomasked compounds via the phosphoramidite route^[53], which was already discussed in section 4.1.1. Due to issues with the solubility of the FdU-DP **8** in relation to the appropriate number of counterions when employing the phosphoramidite method, the decision was made to re-examine the *H*-phosphonate approach, utilizing the Fm-protecting group in the process.

The synthesis of the non-symmetric *H*-phosphonate was carried out using 1.5 equivalents of diphenyl phosphite. In comparison to the synthesis of the β-cyano ethyl-*H*-phosphonate, the number of equivalents was increased with the purpose to improve the selective monosubstitution with the AB-mask. Since DPP contains two phenol groups, which are to be substituted, the ratio of equivalents is 1:2 for the DPP to the alcohols. For the first substitution reaction, 1.0 equivalent of the C11 AB mask **22** was used, and therefore, 2.0 equivalents of the second alcohol, 9-fluorenylmethanol, were used. The exact reaction conditions are displayed in Figure 4-14. The non-symmetric *H*-phosphonate **29** was obtained in a yield of 53 %. As previously discussed, the moderate yield of 53 % can be explained by the formation of the symmetric *H*-phosphonate compounds with either two Fm groups or two AB masks.

Figure 4-14: Synthesis of the non-symmetric *H*-phosphonate bearing the C11AB mask and a Fm-protecting group **29**.

After the successful synthesis and purification of the *H*-phosphonate **29**, the compound was converted into the corresponding pyrophosphate **30** with NCS and tetra-*n*-butylammonium dihydrogen phosphate solution in a yield of 76 %.^[52] The pyrophosphate was then again activated with trifluoroacetic anhydride and 1-methylimidazole as previously discussed in chapter 4.1.3.^[52] The reaction conditions are displayed in Figure 4-15. In comparison to the Tri*PPP*ro-reaction discussed previously, the reaction conditions were modified. The Fm-protecting group can be cleaved off under mildly basic conditions. Therefore, the addition of the trifluoroacetic anhydride and triethylamine mixture was conducted at 0 °C, and no further equivalents of triethylamine in the second activation step were added.

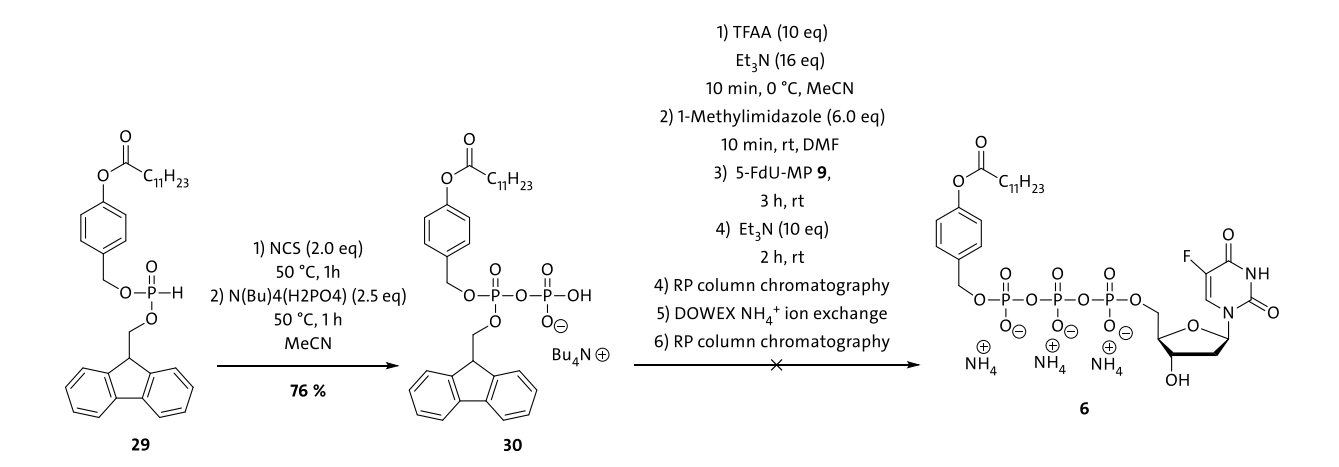


Figure 4-15: Reaction conditions of the Tri*PPP*ro synthesis and subsequent deprotection with the pyrophosphate **30** and the FdU-MP **9**.

After addition of the monophosphate, the reaction was again followed by RPIP-UV. The chromatograms are displayed in Figure 4-16. After two hours, the formation of a signal at 17.3 minutes was observed, which indicated the formation of the TriPPProcompound with one AB mask and the Fm protecting group at the γ -phosphate group. The reaction was terminated by evaporating all volatile components under reduced pressure. For the deprotection of the Fm-protecting group, the residue was dissolved in DMF, and 10 equivalents of triethylamine were added. The reaction was again followed by HPLC. After the addition of triethylamine, the signal at a retention time of 17.3 minutes showed no decrease as would have been expected since the TriPPProcompound should undergo deprotection, resulting in increased hydrophilicity. This, in turn, should result in a decrease in retention time in the chromatogram. Instead, after 1 hour of reaction time at room temperature, the formation of new signals at retention times between eight and ten minutes was observed, which were attributed to the formation of triphosphate, diphosphate and monophosphate. The reaction was terminated and after automated RP column chromatography, no product could be isolated.

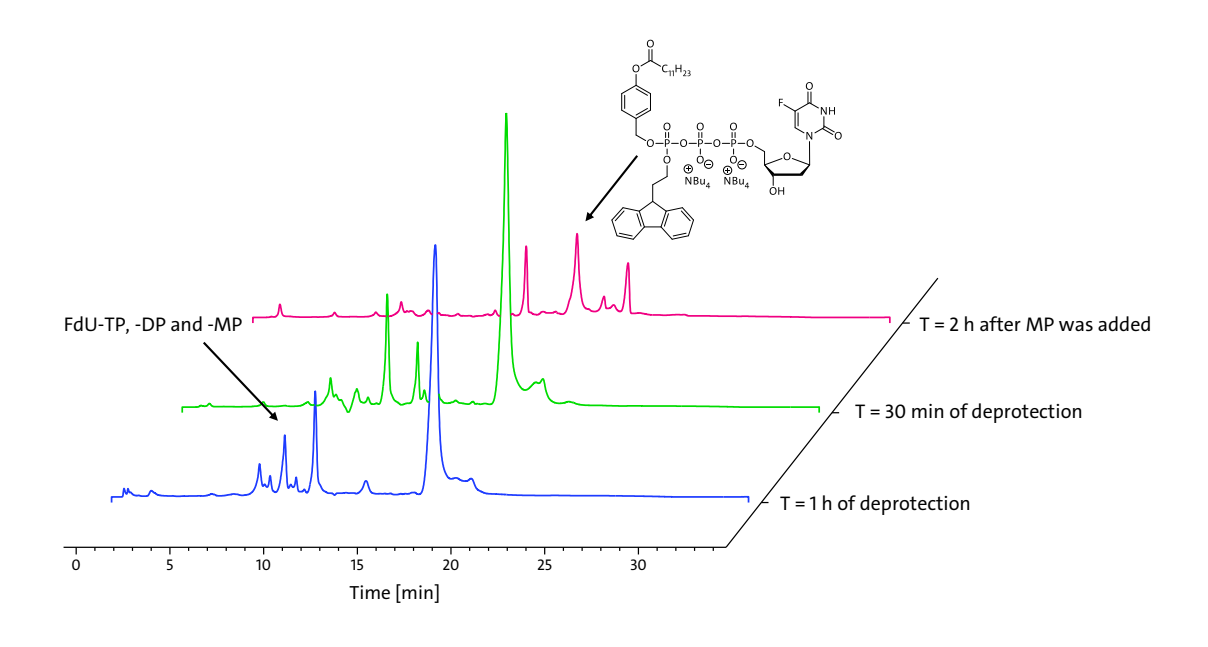


Figure 4-16: Reaction control via RPIP-UV of the coupling reaction between the activated pyrophosphate and the FdU-MP **9** with subsequent cleavage of the Fm-protecting group.

Prior to the repetition of the reaction, the HPLC signal at 17.3 minutes was investigated further regarding the suspected identity. In addressing this question, the UV spectrum of the signal was examined and found in the literature as the characteristic UV spectrum of dibenzofulvene (DBF), which is the product of the cleavage of the Fm-protecting group.[142] The deprotection mechanism with triethylamine as a base is displayed in Figure 4-17. After triethylamine abstracts the proton at the β position, DBF is eliminated. [143,144] EGELUND et al. [143] also demonstrated, that DBF can form base adducts and DBF as well as the adducts can be analyzed via HPLC as these compounds exhibit adequate retention on RP. It was therefore anticipated that the TriPPPro-compound and the DBF co-elute on the RP column, thereby preventing the distinction of the forming product. This thesis is further supported by the fact that the signal at 17.3 minutes has increased significantly after deprotection. Consequently, the reaction control of the deprotection was challenging to observe. A detailed chromatogram of the reaction control is displayed in Figure 4-18. The reaction was conducted again as displayed in Figure 4-19. To avoid undesirable early cleavage of the Fm-protecting group, it was necessary to reduce the equivalents of all reaction components once again. The equivalents of trifluoroacetic anhydride and triethylamine were reduced to 4.0 equivalents of TFAA and 5.0 equivalents of triethylamine.

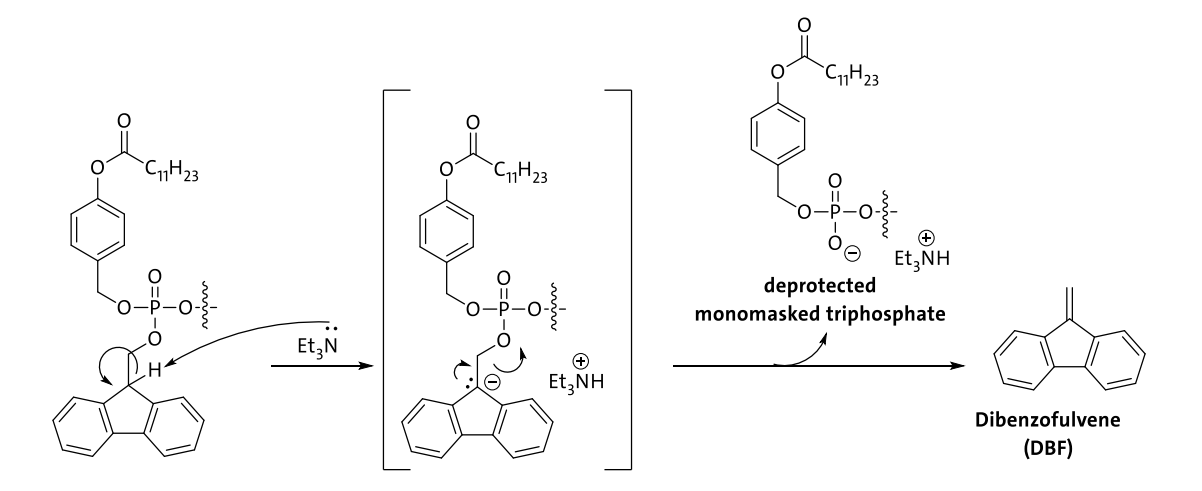


Figure 4-17: Deprotection mechanism of the Fm-protecting group with triethylamine forming the desired product and dibenzofulvene (DBF). Adapted to EGELUND *et al.*^[143]

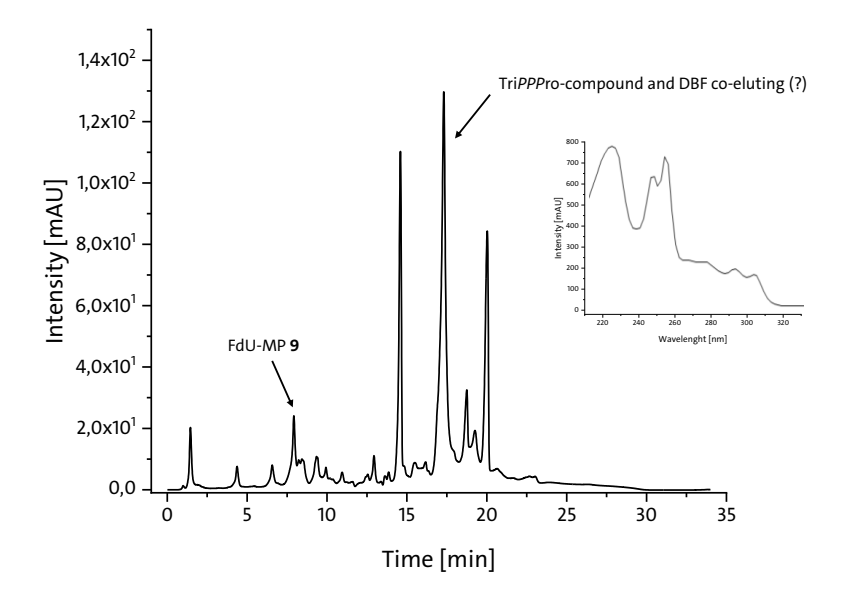


Figure 4-18: Chromatogram of the reaction control of the Tri*PPP*ro-synthesis with the Fm-protected pyrophosphate **29** and the FdU-MP **9**.

The addition to the pyrophosphate was conducted again at 0 °C and the mixture was stirred for 10 minutes as 0 °C. Only 2.0 equivalents of the nucleophilic base 1-methylimidazole were added and stirred for 15 minutes at room temperature. After addition of the FdU-MP **9**, the reaction was terminated, when the monophosphate showed almost full consumption via HPLC, and the solvent was removed under reduced pressure. Afterwards, the residue was redissolved in DMF and 10 equivalents of triethylamine were added.

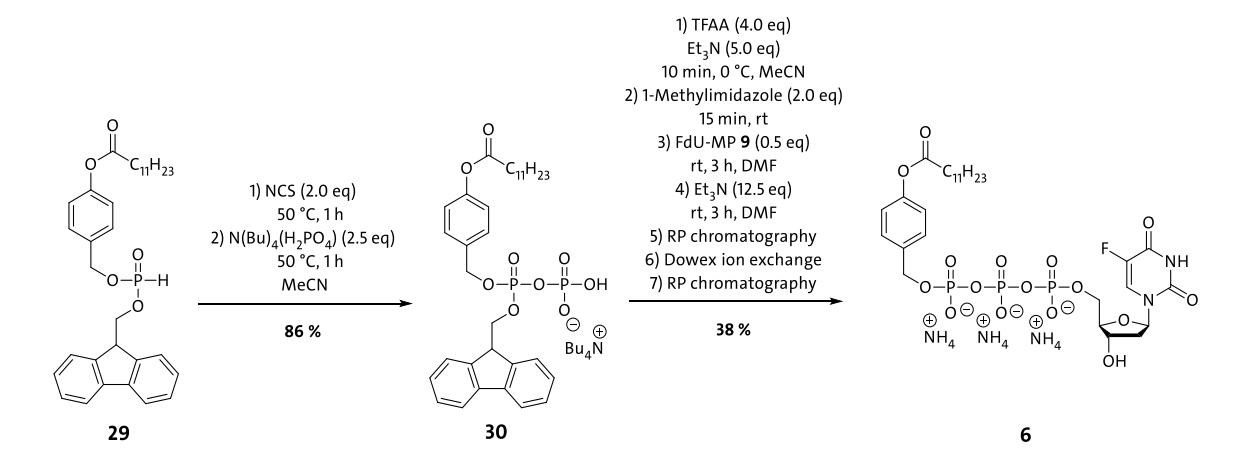


Figure 4-19: Synthesis of the monomasked [C11AB]-FdU-TP 6.

After 30 minutes of reaction time, no formation of a new signal was observed. Therefore, another 2.5 equivalents of triethylamine were added and after another 30 minutes, the formation of a new signal via HPLC with a retention time of 14.8 minutes could be observed. The crude product was purified via RP column chromatography followed by DOWEX ion exchange to ammonium counter ions. Subsequently, another RP column chromatography was conducted yielding the pure monomasked [C11AB]-FdU-TP 6 in a yield of 38 %. The proton and phosphorus NMR spectra are displayed in Figure 4-20 and Figure 4-21. In summary, previous attempts to synthesize the intermediate failed primarily due to the use of a relatively polar protecting group in combination with a comparatively short alkyl chain on the AB mask, which necessitates the selection of a more lipophilic protecting group to facilitate the work-up. Furthermore, in presence of a base-labile protecting group, the equivalents of all reagents capable of inducing cleavage should be significantly reduced.

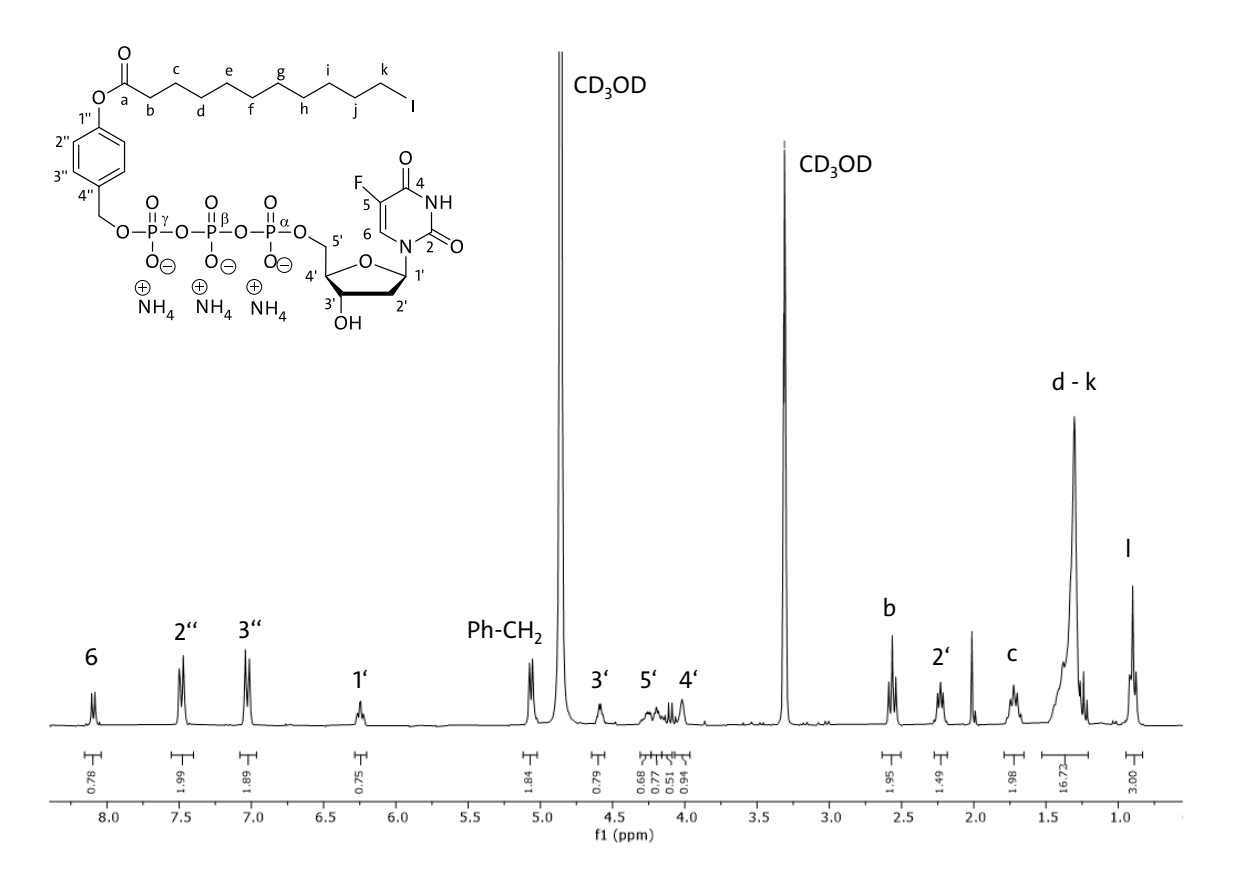


Figure 4-20: ¹H NMR spectrum of the monomasked [C11AB]-FdU-TP 6.

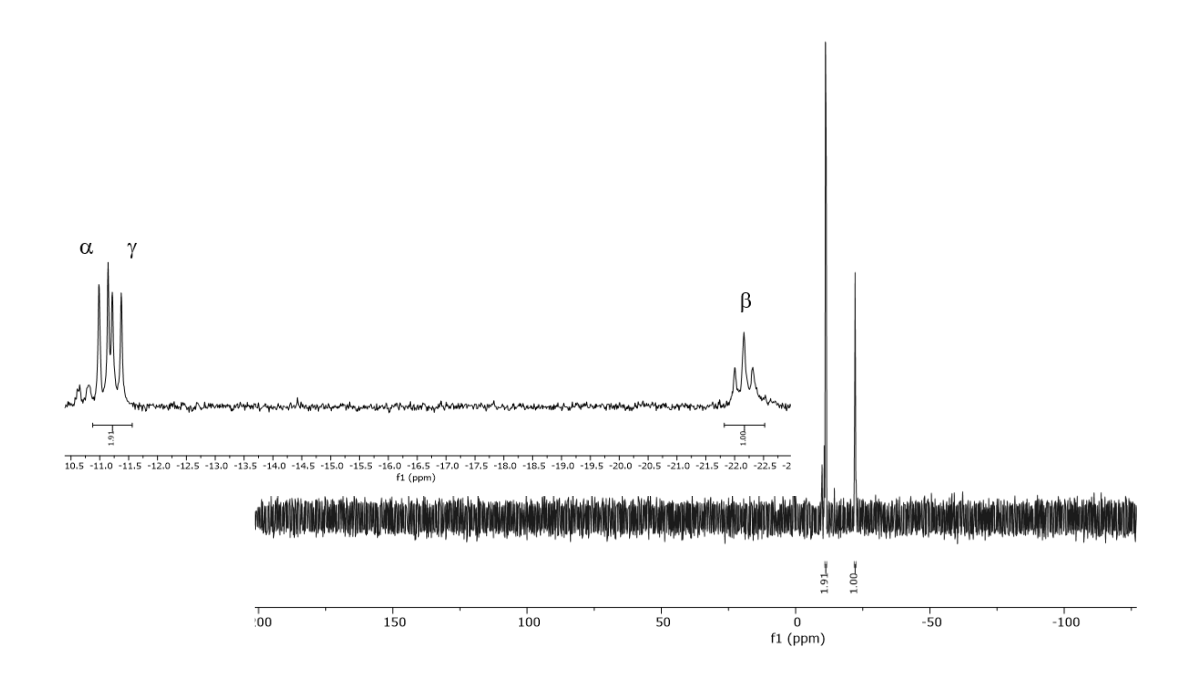


Figure 4-21: ³¹P NMR spectrum of the monomasked [C11AB]-FdU-TP 6.

4.1.7 Synthesis of the intermediate 11

To synthesize the second intermediate, the monomasked compound of the Tri*PPP*rocompound **3**, the previously tested *H*-phosphonate route employing Fm as protecting group should be applied. The Tri*PPP*ro-compound **3** is a non-symmetric prodrug bearing one ACB mask with a C16 chain length and one AB mask with a C2 chain length. In theory, two different intermediates are possible: the monomasked [C16ACB]-d4T-triphosphate and the monomasked [C2AB]-d4T-triphosphate. ACB masks are in general known to be more stable against chemical and enzymatic hydrolysis. [16,52] In stability studies regarding the hydrolysis of the Tri*PPP*rocompounds in CEM/O cell extracts, JIA observed the intermediate **11**, the [C16ACB]-d4T-TP, to be the only intermediate forming besides d4T-TP, d4T-DP and d4T-MP and concluded the fast cleavage of the short AB mask. [55] Therefore, it was decided to only synthesize the monomasked [C16ACB]-d4T-TP.

For the H-phosphonate route, d4T-MP 15 was synthesized starting from the nucleoside d4T 16, which is commercially available, employing synthesis conditions according to SOWA & OUCHI.[137] The synthesis is well established within our group and sufficiently discussed in literature. [14,15] The analytical data and yield agreed with the literature and therefore will not be discussed within this work. d4T-Monophosphate 15 was obtained as tetrabutylammonium salt. The next step was the synthesis of the non-symmetric H-phosphonate with the C16-ACB mask and Fm as protecting group. Therefore, the C16-ACB mask was synthesized via the alkyl chloroformate. The synthesis was carried out according to reaction conditions described by Dekiert^[145] with 3.0 equivalents of pyridine and 1.0 equivalent of triphosgene to generate phosgene in situ. Due to its high reactivity, the chloroformate 32 is unstable and was only purified by an aqueous work-up and used without further analysis in the subsequent reaction with the 4-hydroxybenzylalcohol 33 to obtain the C16-ACB mask in a yield of 40 % (Figure 4-22). The analytical data agreed with the literature. [55]

Figure 4-22: Synthesis of the C16-ACB mask **34** starting from 1-hexadecanol **31** via the chloroformate **32**. [55,145,146]

The next step was the synthesis of the non-symmetric *H*-phosphonate **35.** Therefore, the synthesis, employed in chapter 4.1.6 was used. 2.0 equivalents of diphenyl phosphite were dissolved in pyridine and cooled down to 0 °C. Compound **34** was dissolved in pyridine and slowly added dropwise. After complete consumption of the ACB mask as indicated by TLC, 2.0 equivalents of 9-fluorenylmethanol were added.

After 2 hours of reaction time at room temperature, the solvent was evaporated followed by co-evaporation with toluene and dichloromethane. Automated NP chromatography yielded the pure compound **35** with 45 % (Figure 4-23).

Figure 4-23: Synthesis of the non-symmetric H-phosphonate 35.

As already described, the *H*-phosphonate was converted into the pyrophosphate via *N*-chlorosuccinimide and tetra-*n*-butylammonium dihydrogen phosphate solution. The pyrophosphate **36** was obtained in a yield of 88 %. Subsequently, compound **36** was gradually activated with trifluoroacetic anhydride and 1-methylimidazole. Again, for the Tri*PPP*ro-synthesis, a reduced number of equivalents for all components (TFAA, triethylamine, 1-methylimidazole) was used to prevent the cleavage of the Fm-group. Detailed reaction conditions are displayed in Figure 4-24.

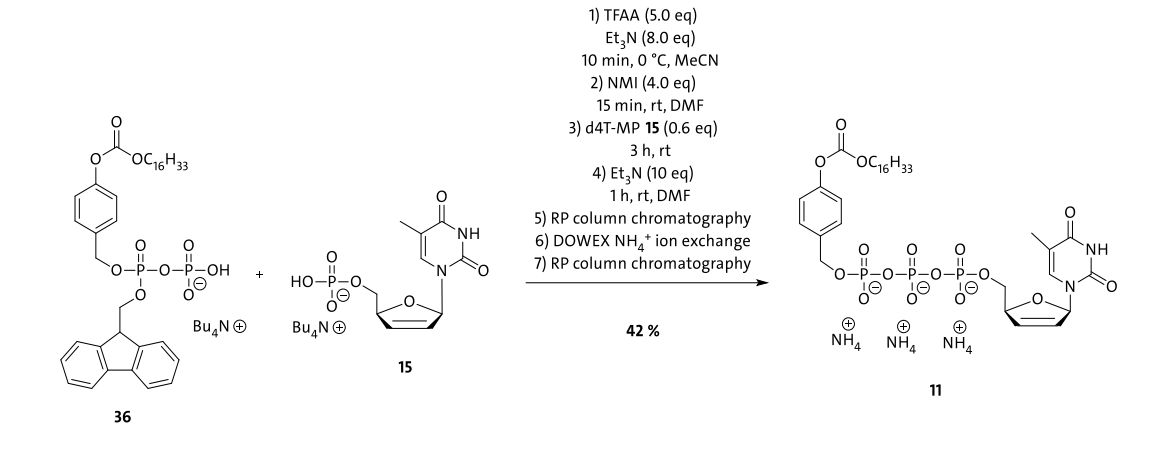


Figure 4-24: Synthesis of the monomasked [C16ACB]-d4T-TP 11.

The reaction was followed by HPLC and, due to the increased lipophilicity of the compound, originating from the C16 alkyl chain in comparison to the C11-AB mask of intermediate 6, the coupling product did not co-elute with DBF. It could therefore be assumed that the coupling product had been identified, which facilitated the reaction controls (Figure 4-25). This observation further strengthens the hypothesis of the formation of DBF or a DBF base adduct, which shows very similar retention times compared to the TriPPPro-compound. After consumption of the d4T-MP 15, the solvent was evaporated under reduced pressure and the residue was dissolved in DMF and 10 equivalents of triethylamine were added for the deprotection. The reaction was again followed by HPLC and terminated upon the observation of a minimal quantity of d4T-TP. The crude product was purified by automated RP column chromatography, followed by an ion exchange with DOWEX to ammonium counter ions. Subsequently, another automated RP column chromatography was conducted yielding the pure monomasked [C16ACB]-d4T-TP 11 in 42 %. JIA reported a yield of 10 % for the compound 11 employing the H-phosphonate route using β -cyano ethyl as a protecting group.^[136] The analytical data was in agreement with the ones reported by JIA^[136] and the proton and phosphorus NMR spectra are displayed in Figure 4-26 and Figure 4-27.

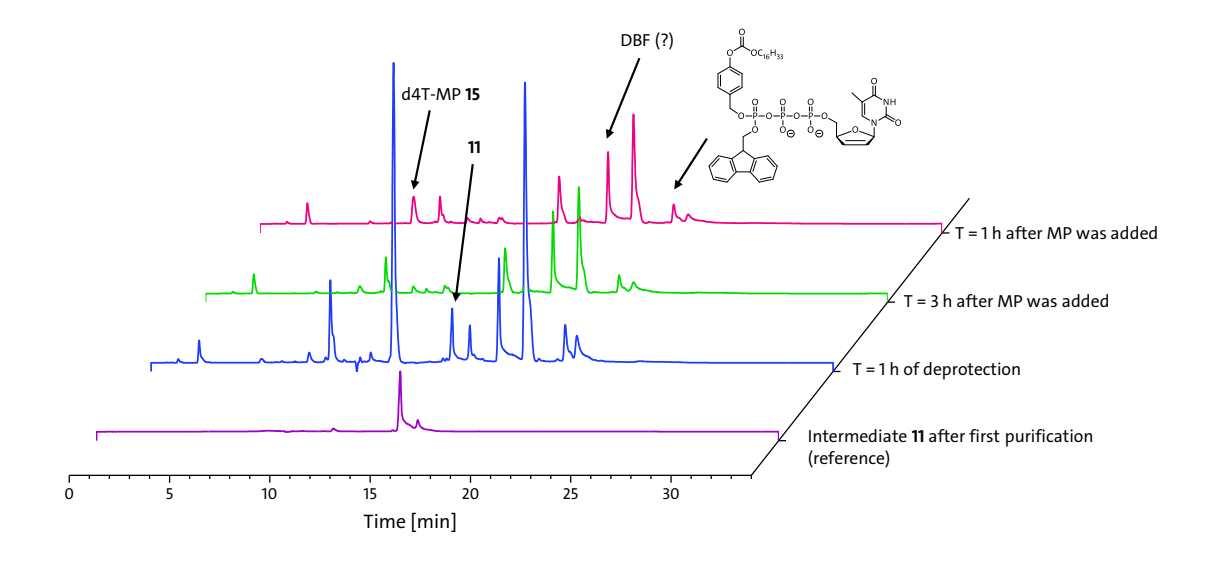


Figure 4-25: Reaction control via RPIP-UV of the coupling reaction with the activated pyrophosphate and the d4T-MP **15** with subsequent deprotection of the Fm-protecting group and compound **11** after the first purification.

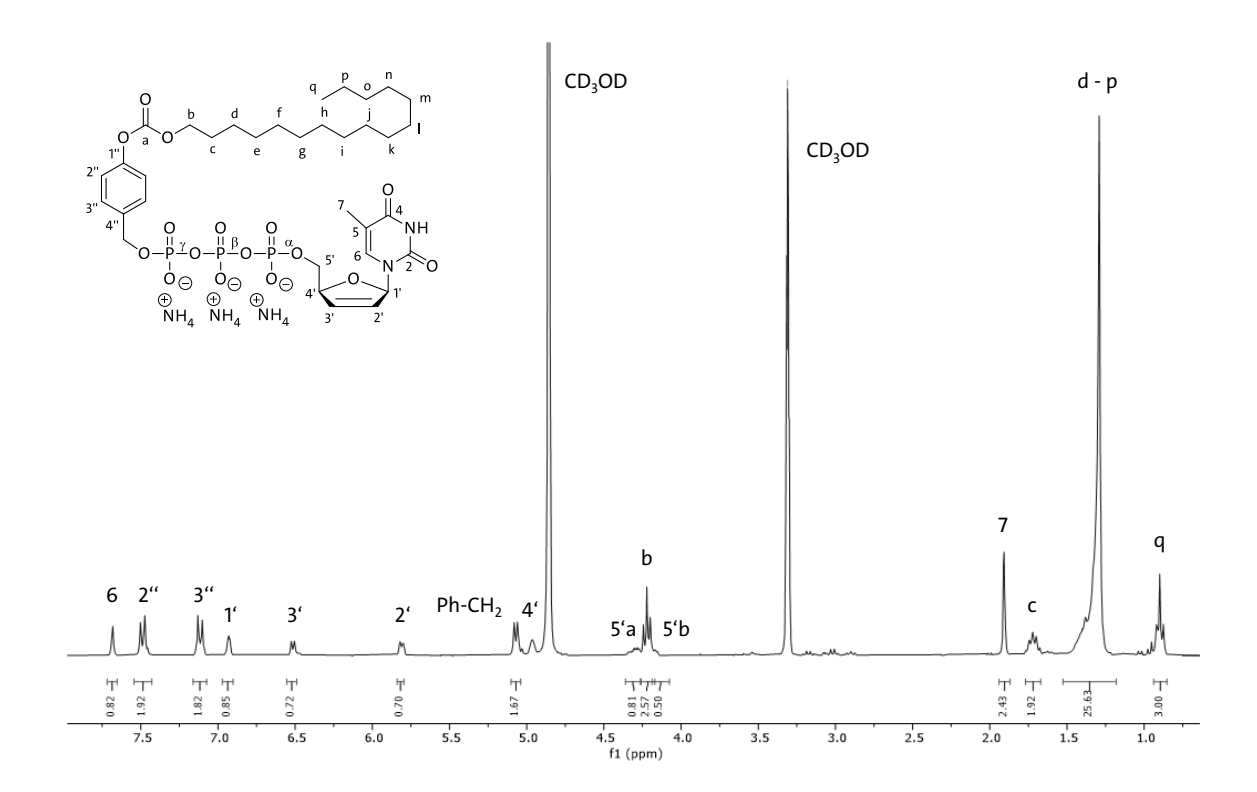


Figure 4-26: ¹H NMR spectrum of the monomasked [C16ACB]-d4T-TP 11.

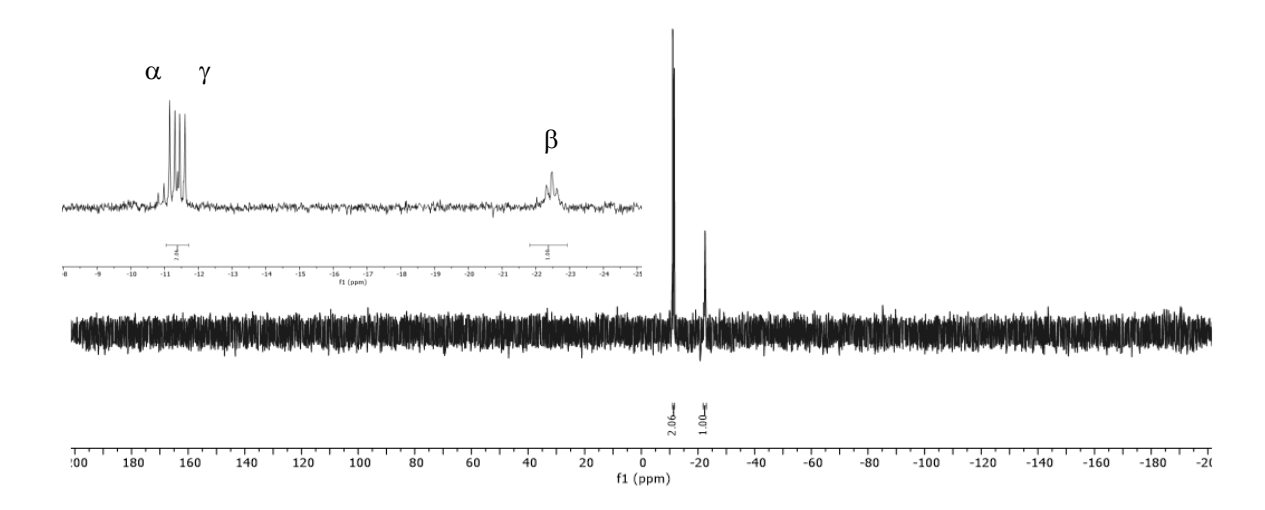


Figure 4-27: ³¹P NMR spectrum of the monomasked [C16ACB]-d4T-TP 11.

Following the successful synthesis of the missing analytes, the MS method was developed, starting with the initial tuning for each analyte to build the MRM method.

4.2 Initial MS tuning

For each analyte, a stock solution was prepared, comprising 1.0 mg of the compound dissolved in 1.0 mL of a 1:1 (% v/v) mixture of acetonitrile and water. These stock solutions were stored at -20 °C and utilized as a spike-in for the preparation of all working solutions employed in this study. The stability of the stock solutions was frequently monitored via RPIP-UV runs. The stock solutions of each analyte were then used in a ten-fold dilution for the initial MS tuning, with the solution being injected via a syringe pump directly into the mass spectrometer. Both positive and negative ionization modes were tested, since it has been investigated that nucleosides and nucleotides can exhibit an enhanced sensitivity for positive ionization due to the nitrogen atoms in the nucleobase. [147] In this context, the signal intensities were found to be consistently higher in the negative ionization mode, which can be attributed to the negatively charged phosphate groups. After the detection of the first precursor ion signal, which was always [M-H]⁻, product ion scan spectra were measured. The three most intense fragment ion signals were selected, optimized and acquired as the MRM method. The selectivity for each analyte is very high due to the three different mass transitions. As an example, Figure 4-28 displays the possible structures of the fragment ions that were detected for FdU-TP 7 as the most intense signals. The combination of the precursor and the product ion forms the characteristic mass transition, which is visible in the resulting chromatogram. Due to this selectivity, it is not necessary for the peaks in the chromatogram to be baseline separated. The high sensitivity in negative ionization mode is comprehensible since the characteristic phosphate fragment of m/z 78.9 was observed in all measurements, given that all TriPPPro-compounds and their metabolites bear negatively charged phosphate groups.

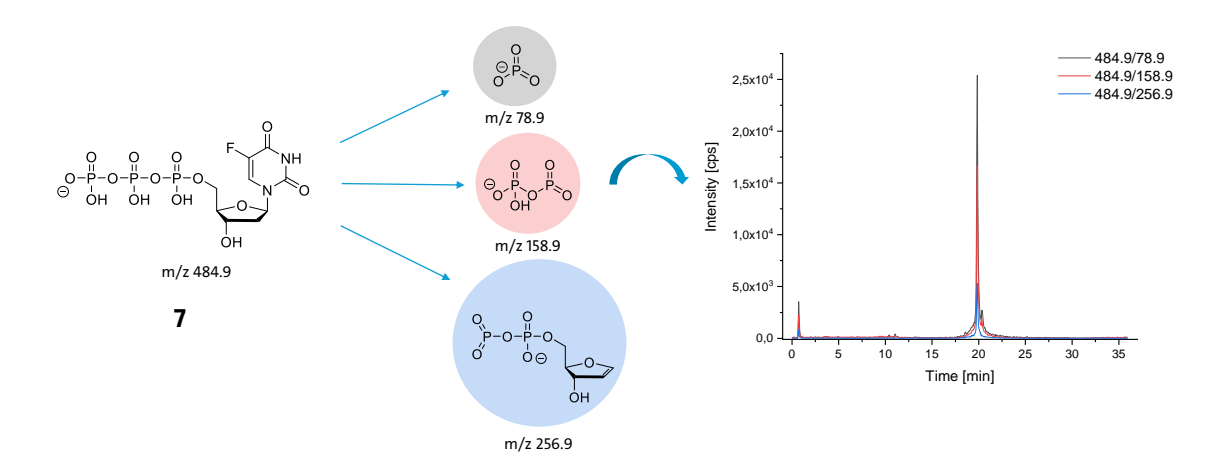


Figure 4-28: Possible fragmentation ions of FdU-TP **7** in negative ionization mode and resulting mass transitions in the final chromatogram.

As shown in Table 4-1, the precursor ion masses that were detected in the first quadrupole (Q1) and the associated product ion masses from the third quadrupole (Q3) for each analyte are listed. The combination of the Q1 and Q3 masses is representative for the mass transitions and thus forms the basis for the MRM methods for the FdU- and d4T-compounds, including internal standards (ISD). It should be noted that in the ongoing course of HPLC method development, not all compounds were available right from the beginning for inclusion in the MRM method. Therefore, many chromatograms that will be discussed in the following subsections, do not display all analytes from Table 4-1 at once.

Table 4-1: Precursor ion mass (Q1 mass) and product ion masses (Q3 masses) for each analyte after initial MS tuning. Based on these mass transitions, MRM methods for the FdU and d4T compounds, including internal standards (ISDs), were developed.

Compound	Q1 mass [Da]	Q3 mass [Da]
		155.0
FdU 10	244.9	128.8
		111.9
	324.9	128.9
FdU-MP 9		194.9
		78.9
		78.8
FdU-DP 8	404.9	274.9
		158.6
FdU-TP 7		78.9
	484.9	158.9
		256.9

Compound	Q1 mass [Da]	Q3 mass [Da]
		386.9
Tri <i>PPP</i> ro-compound 1	977.1	256.9
		78.9
		78.8
Tri <i>PPP</i> ro-compound 2	1061.1	387.0
		256.7
		78.9
Intermediate 5	731.0	404.8
		256.8
		78.9
Intermediate 6	772.9	447.0
		256.9
		193.0
d4T 16	223.0	125.0
		122.0
		79.0
d4T-MP 15	303.0	125.0
		177.0
		78.9
d4T-DP 14	382.9	256.7
		158.8
	462.9	78.9
d4T-TP 13		158.9
		238.9
		238.9
Tri <i>PPP</i> ro-compound 3	999.1	78.9
·		158.8
		365.0
Tri <i>PPP</i> ro-compound 4	889.2	238.8
·		78.9
		78.9
Intermediate 11	837.0	533.0
		364.8
		78.9
Intermediate 12	699.0	383.0
		158.8
		78.8
Uridine-¹⁵N₂ 5'-MP (ISD)	333.9	97.0
		116.9
		364.9
C14-ACB;C18-ACB-d4TTP (ISD)	1071.2	238.8
•		78.9

4.3 Development of the HPLC method

After the initial MS tuning, the next key step in method development would be the chromatographic development (s. Figure 4-1, p. 34). For the analysis of the Tri*PPPro*-compounds and their corresponding metabolites from complex mixtures, for example cell lysate, the chromatographic separation is essential. In the following subsections, two different approaches for a suitable HPLC method will be discussed in detail. In an effort to reduce the complexity, the method development was conducted only with the FdU derivatives and started with the MP **9**, the DP **8** and the Bis[C11AB]-prodrug **2**. In the course of the research project, the remaining compounds (s. Figure 4-2, p. 35) were included in the MRM method. Later on, the developed HPLC-MRM method was applied to the d4T-derivatives (s. Figure 4-3, p. 36).

The focus was to achieve simultaneous retention of the lipophilic TriPPProcompounds and their hydrophilic metabolites and therefore, four types of stationary phases were tested. The first column was the Atlantis Premier BEH C₁₈ AX, a mixed mode column. The other three columns were HILIC columns with different functionalities of the stationary phase: XBridge BEH HILIC, XBridge Premier BEH Amide and the Atlantis Premier BEH Z-HILIC column. All columns used within this work were manufactured by Waters™. The advantages of mixed-mode chromatography or HILIC were already discussed in chapter 2.3. In consideration of these factors, successful retention and separation was a conceivable outcome. The Atlantis Premier BEH C18 AX column features lipophilic C18 chains and positively charged tertiary alkylamine groups below pH 8, enabling anion exchange for polar metabolites.[148] Therefore, it seemed suitable for TriPPPro-compounds, as well as for the metabolites. Unlike the bare hybrid particles of the XBridge BEH HILIC column, the XBridge Premier BEH Amide and Atlantis Premier BEH Z-HILIC columns are modified with amide groups or sulfobetaine moieties, respectively, enabling zwitterionic interactions. The next subsections will focus on the method

development employing the forementioned mixed mode column and also HILIC as type of separation.

4.3.1 Application of a mixed-mode stationary phase

On the basis of preliminary research performed, a LC gradient elution was designed, which is shown in Table 4-2. The mixed-mode column tolerates 100% aqueous elution, which is particularly advantageous for the analysis of polar compounds. The initial conditions of the LC gradient are also very important for the sample preparation and the resulting injection solvent. It has been observed that chromatographic performance, as indicated by peak shapes or signal intensities, can be adversely affected by a mismatch between the injection solvent and the initial conditions of the gradient employed during analysis.

Table 4-2: Gradient elution for the mixed mode column.

Time [min]	Eluent A [%]	Eluent B [%]	
0	100	0	
2	100	0	
10	20	80	
12	2	98	
17	2	98	
20		0	
25	100	0	

Preliminary development tests were conducted using the Tri*PPP*ro-compound **2** as lipophilic compound and FdU-MP **9** and FdU-DP **8** as hydrophilic compounds. Besides the gradient elution, LC method development also consists of a variety of parameters, which can be modified. The different factors which have been employed are displayed in Table 4-3. These factors, which are mentioned above, include two

different kinds of salts: ammonium acetate (AAc) and ammonium formate (Af) in different concentrations, varying between 5 and 20 mM. This buffer comprises eluent A. The importance of mobile buffer composition on the electrospray ionization mass spectrometry response was investigated thoroughly in literature.[149–151] It is well known that the chemical environment of the compounds in the ESI source affects the ionization efficiency and thus the signal intensity. [106,152,153] Therefore, a stable pH value should be employed by using different salts in their buffering range. In addition, the salts function as additives, thereby exerting a further influence through the formation of ion pairs or interaction with the stationary phase of the column. Therefore, buffers are useful in controlling retention and improving peak shapes, particularly for ionizable compounds. [154] The pH value of eluent A is dependent on the buffer capacity of the salt, which is in turn dependent on the pKa values of the molecules utilized. [155] Ammonium cations exhibit a pKa value of 9.25, acetate anions of 4.76 and formate anions of 3.86. [156] Therefore, two different pH-values of 9.2 and 4.3 were selected. In this context, the pKa values of the analytes must also be considered.

Table 4-3: Different parameters (type of salt, additive concentration and composition of the mobile phase B), which were employed in the method development for the mixed-mode column.

Eluent A			Eluent B
Salt	Concentration [mM]	pH value	MeCN/IPA/H2O (50:45:5, % v/v/v) + Salt Concentration [mM]
	20	9.2	20
	10	9.2	10
Ammonium acetate	5	9.2	5
(AAc)	20	4.3	20
	10	4.3	10
	5	4.3	5
Ammonium formate (Af)	20	4.3	20
	10	4.3	10
	5	4.3	5

If the pH value of the mobile phase is in the range of the pKa value of the analyte, the molecules are partly protonated as well as deprotonated. The presence of these two different charged species leads to different behavior in chromatographic elution and can influence peak shape in terms of fronting, tailing or even peak splitting. Mixed-mode chromatography is known for secondary or even tertiary interactions.^[78,157] This is mainly attributed to the combination of interactions from the stationary phase, however, the variety of factors introduced by the eluents also contributes to a high level of complexity. In order to control some of these interactions, it was decided to maintain the salt concentration in both eluents. Therefore, eluent B is a mixture of acetonitrile, isopropanol and water. The small percentage of water is essential due to the low solubility of the salts in acetonitrile and water. Eluent B is accountable for the elution of the analytes from the column, given that organic solvents exhibit a higher elution capacity in mixed-mode chromatography in comparison to water or aqueous solutions. The first measurements employed AAc buffer in different concentrations with a pH value of 9.2 for eluent A. The chromatograms are shown in Figure 4-29.

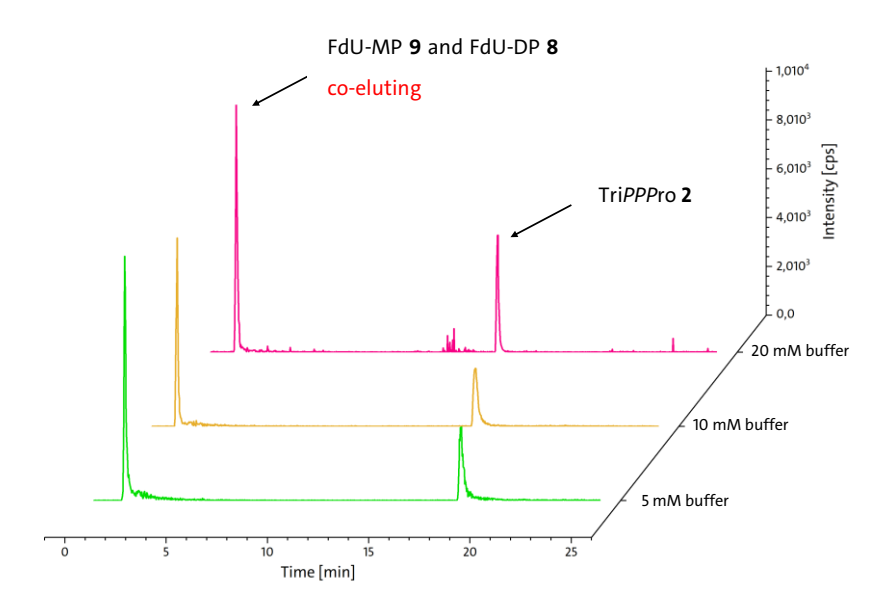


Figure 4-29: Ammonium acetate (AAc) buffer with a pH value of 9.2 in different concentrations (5 – 20 mM) as eluent A in mixed-mode measurements (analyte concentration: 500 ng/mL in 100 % water, 5 μ L injection).

Displayed is the total ion current (TIC) for every measurement. In general, all tested analytes exhibited a retention in this method. However, the polar metabolites, FdU-MP 9 and FdU-DP 8 coeluted and displayed only one signal in the TIC. A more thorough look at the EICs with the corresponding mass transitions for the MP (m/z)324.9 -> 194.9) and the DP (m/z 404.9 -> 78.8) showed that these two compounds exhibited the same retention time and were not separable. It was also demonstrated that the peak shape, especially the one of the TriPPPro-compound, improved with higher salt concentrations. Simultaneously, the retention time decreased. This may be due to a process, which can be described as "salting-out". [158] It is mainly described for biomolecules, such as proteins in association with chromatography, but this terminology could also be used as an explanation for the reduced retention time of the analytes present in this work. An increase in salt concentration results in the partitioning of analytes into the organic mobile phase due to the reduced ability of these analytes to remain solvated in the aqueous phase. [158] In other words, the higher concentration of salt may act as displacer of the analytes from the active binding sites of the stationary phase into the organic mobile phase, which then elutes the compounds.

When the pH value of the AAc buffer was changed to 4.3, it was possible to achieve simultaneous retention of all analytes tested and a separation of the FdU-MP **9** and FdU-DP **8** (Figure 4-30). In comparison to the measurement with the pH value of 9.2, the polar metabolites (MP and DP) showed increased retention time. Below a pH value of 8.5, the functionalized particles of the stationary phase are positively charged and therefore electrostatic interactions with the negatively charged phosphate groups of the MP and DP led to an increase in retention. For these measurements, the previously described "salting-out" effect was only of minor significance. No reduction in retention time was observed in the presence of elevated buffer concentrations. Conversely, a substantial enhancement in peak shape was observed. In the case of a buffer concentration of 5 mM, the peaks exhibited a broad profile, indicative of tailing.

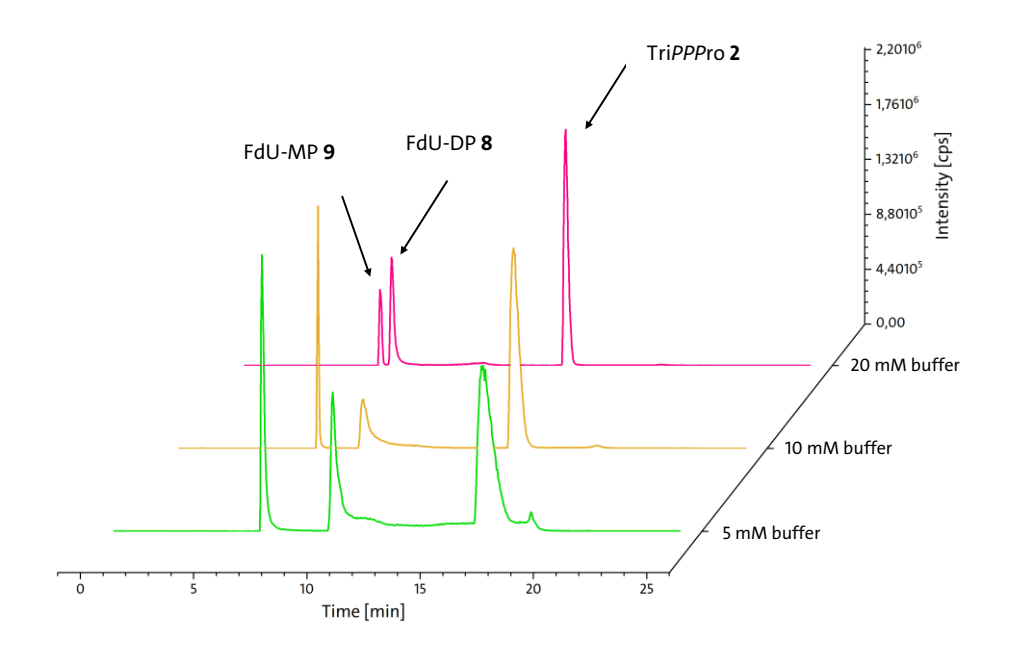


Figure 4-30: Ammonium acetate (AAc) buffer with a pH value of 4.3 in different concentrations (5 – 20 mM) as eluent A in mixed-mode measurements (analyte concentration: 500 ng/mL in 100 % water, 5 μ L injection).

However, when a buffer concentration of 20 mM was employed, the peaks became narrower and more symmetrical.

The second salt which was tested was ammonium formate. Af buffer was employed using a pH value of 4.3 to have the advantage of the anion exchanger of the stationary phase, which was demonstrated to be necessary in the previous section. Buffer concentrations were varied between 5 – 20 mM. The TICs are displayed in Figure 4-31. In general, the chromatographic performance was rated worse than in comparison to the measurements employing the AAc buffer. A possible explanation for this could be the size of the anion. Formate anions are smaller than acetate anions and may not be able to effectively displace the analytes from the active binding sites of the stationary phase. This resulted in poor peak shape such as broadening of the signals and tailing. These effects were particularly strong when using only 5 mM of Af buffer concentration. As shown in the TIC in Figure 4-31, the MP signal with a retention time of about 9.5 minutes exhibited of a peak shoulder, which can lead to peak splitting in extreme cases.

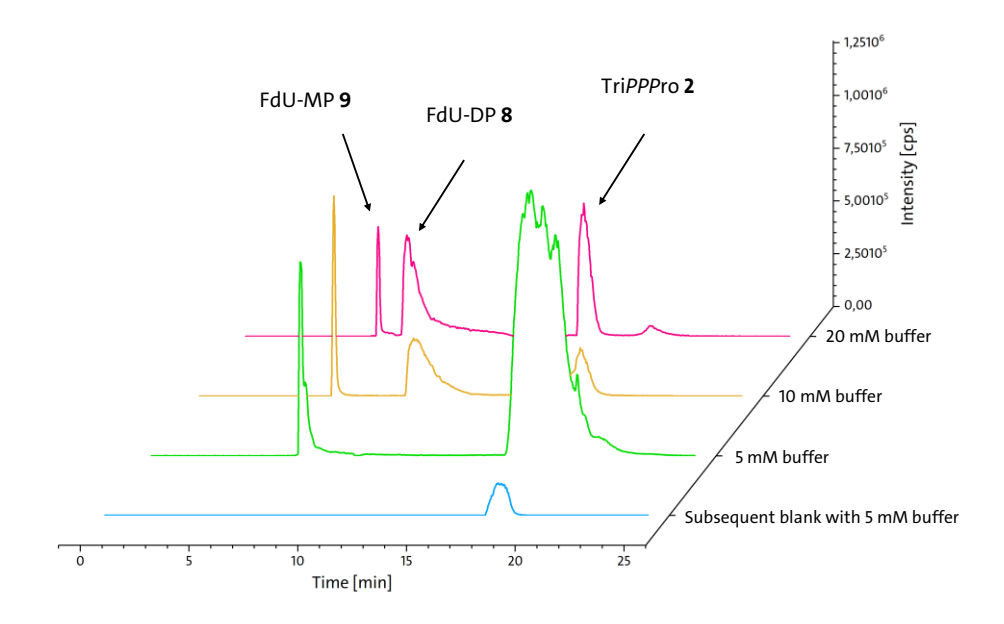


Figure 4-31: Ammonium formate (Af) buffer with a pH value of 4.3 in different concentrations (5 - 20 mM) as eluent A in mixed-mode measurements (analyte concentration: 500 ng/mL in 100 % water, 5 μ L injection).

The DP signal appeared very broad and was tailing for approximately 5 min of run time. The most lipophilic compound, the TriPPPro-compound 2, was not retained within this run, but eluted in the subsequent blank measurement. This effect is called "carry over". In general, carry over is caused by residual analyte from a sample analyzed in earlier measurements and can affect several samples within a series of runs for example in calibration curves. [159] The carry over effect is unwanted since it can affect both the precision and accuracy of the method. Its investigation and elimination should be part of method development. When carry over is occurring during measurements, the reason should be thoroughly investigated to eliminate the source of carry over. The cause could be cross-contamination during sample preparation, as well as contamination from the chromatographic system such as autosampler carry over or column carry over. [159] With regard to these measurements, the effect is clearly column carry over, which can be overcome by changing the mobile phase conditions. Nevertheless, monitoring potential carry over effects in relation to ongoing method development is essential.

The best results so far have been achieved by employing an AAc buffer with a concentration of 20 mM and a pH value of 4.3 for the three analytes. Unfortunately, the FdU-DP 8 did not show reproducible peak intensities, and the peak shape varied from measurement to measurement. Also, because of the poor peak shape, the sensitivity of the diphosphate was quite low in comparison to the other analytes.

Cellular uptake studies with quantification of the metabolites have never been done before, therefore the concentration ranges are unknown. The strategy to overcome this issue is to employ large quantification ranges from very low concentrations (between 0.1 ng/mL – 10 ng/mL) to high concentrations (500 ng/mL – 1000 ng/mL). It is important that these concentrations are in the linear range for all analytes. The concentration of the analyte has to be directly proportional to the measured analyte peak area after conduction of calibration curves. Therefore, it must be ensured that peak shape is not affected by overloading the column or detector saturation, and for very small concentrations it was desired to still produce a significant signal, which can be integrated. Inadequate peak shapes such as tailing, fronting and peak splitting have been shown to result in the inability to integrate the peaks reasonably.

Consequently, the initial method development trials focused on both sensitivity and peak shape. The results so far were not satisfactory for the FdU-DP **8** and therefore, LC parameters were varied more with a closer look to the diphosphate. The buffer concentration was kept constant, since 20 mM seem to improve peak shape. Instead, the pH value was varied within the buffering range of ammonium acetate and the column temperature was elevated up to 40 °C. It is known in literature, that an increase in column temperature can significantly improve the performance of the chromatographic separation since peak symmetry can be improved due to limitation of secondary interactions. ^[160] The EICs of the diphosphate employing different parameters for eluent A are displayed in Figure 4-32. The most satisfactory results were obtained with an AAc buffer with 20 mM, a pH value of 5.0 and 40 °C of operating column temperature.

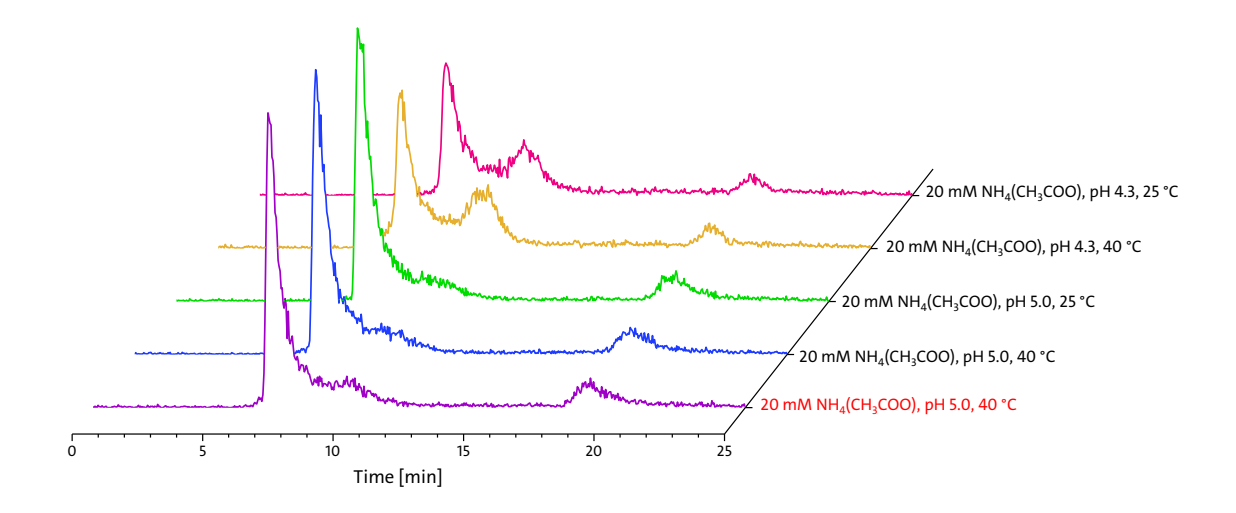


Figure 4-32: Extracted ion chromatograms (EICs) of the FdU-DP 8 with different parameters for eluent A (analyte concentration: 500 ng/mL in 100 % water, 5 μ L injection).

As Figure 4-32 demonstrates, even minor alterations in parameters such as the pH value or the column temperature can significantly impact the peak shape and, consequently, the signal intensity. Unfortunately, the next compound included in the method, the nucleoside 5-FdU **10**, could not be separated on the column. Due to the characteristic mass transitions, they can still be distinguished since they exhibit different precursor and fragment ions. The EICs are displayed in Figure 4-33.

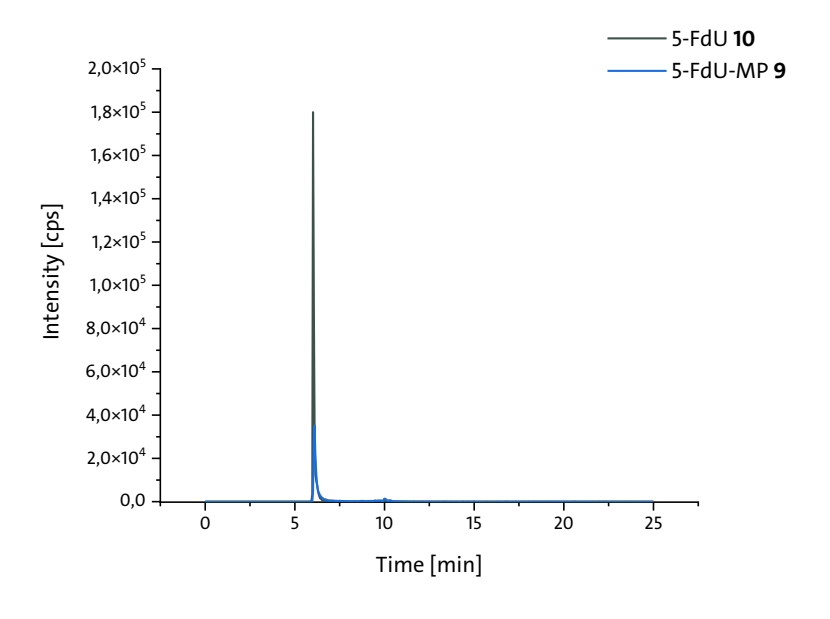


Figure 4-33: EICs of 5-FdU **10** and 5-FdU-MP **9** on the mixed-mode column (analyte concentration: 500 ng/mL in 100 % water, $5 \mu \text{L}$ injection).

Consequently, fully baseline separated peaks are not required. However, it was still advisable to avoid a complete overlay. The primary reason for this is that fully superimposed peaks can lead to matrix effects as they compete in the ESI source during ionization and can lead to signal enhancement or signal reduction. [161–163] It can be assumed that due to the complex matrix of the cell lysate, matrix components will lead to measurable matrix effects in any case. Therefore, at least a separation of the analytes can be aimed for. Although several attempts have been made, there was no possibility to achieve a separation of the nucleoside and the monophosphate with the AAc buffer in the pH value range.

Therefore, a different strategy was followed. Instead of using a pH value of around 4.5, a higher pH value should be tested. Derissen *et al.*^[130] were able to separate 5-FU nucleotides employing a pH value of 6.0. With a pH value of 6.0, the modified residues from the stationary phase of the column are still positively charged, thereby employing the anion exchanger which is essential for the separation of MP and DP, but also for a satisfactory retention of the compounds. On the other hand, negatively charged compounds such as the metabolites are more affected by the pH value than neutral compounds. The nucleoside and monophosphate are structurally very close, which mainly allows the separation to be successful with help of the free charges. This cannot be done in the buffer range of ammonium acetate between 3.5 and 4.5. For the employment of a pH value of 6.0, a different salt was used. The buffer capacity of ammonium bicarbonate (NH₄HCO₃) is between pH values of 5.4 and 7.4.^[156]

For initial testing, an NH₄HCO₃ buffer with a concentration of 10 mM in water was used as eluent A. For eluent B, the mixture of acetonitrile and isopropanol (45:50, % v/v) was used with 5 % of water for the solubility of ammonium bicarbonate with a concentration of 10 mM. The results are displayed in Figure 4-34. The EICs of the analytes 5-FdU 10, 5-FdU-MP 9, 5-FdU-DP 8 and the FdU-Tri*PPP*ro-compounds 1 and 2 are shown.

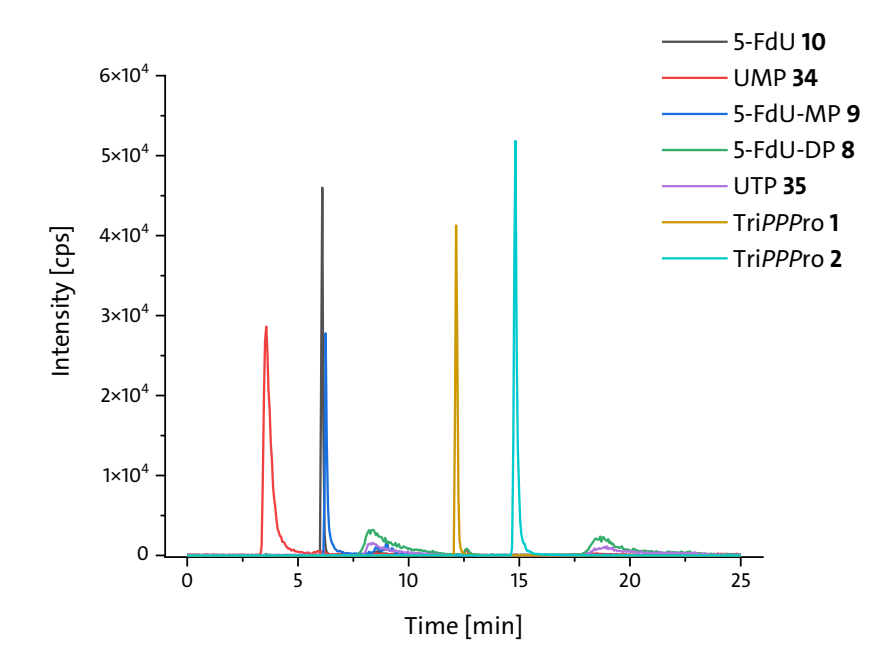


Figure 4-34: EICs of the different analytes employing an ammonium bicarbonate (NH_4HCO_3) buffer with a concentration of 10 mM and a pH value of 6.0 as eluent A on the mixed-mode column (analyte concentration: 500 ng/mL in 100 % water, 5 μ L injection).

Furthermore, the natural nucleotides UMP **34** and UTP **35** were included in the MRM method, because these compounds were tested as potential internal standards as isotopically labeled analytes.

In general, it was possible to achieve simultaneous retention for all analytes tested. For almost all of them, the peak shapes and signal intensities were satisfactory. It was possible to achieve a separation of the nucleoside 10 and the monophosphate 9. Only FdU-DP 8 coeluted with UTP 35. Both analytes also showed poor peak shapes and peak splitting. Nonetheless, the preliminary findings indicated that this would provide a good starting point for focusing on the retention and separation of the diand triphosphates. On the basis of this method, the linearity of the compounds should be evaluated. For quantification, it is necessary to find the linear range of the compound, where the analyte concentration is directly proportional to the integrated analyte peak area. Therefore, calibration curves with at least 6 non-zero calibration standard (CS) samples were constructed and measured in duplicate for the analytes 10, 9, 2 and 1. FdU-DP 8 was not considered within this test since chromatographic performance such as peak shape still needed to be optimized. It is

recommended to perform either duplicate or triplicate measurements of every sample analyzed to provide enough data for statistical validation of the results. All CS samples were prepared in 100 % water, stored in liquid nitrogen and directly thawed prior to analysis. Table 4-4 displays the CS samples for FdU-MP **9**.

Table 4-4: Calibration standard (CS) samples for FdU-MP **9**, including corresponding concentrations in ng/mL, integrated peak areas of the duplicates including the resulting mean and the coefficient of variation (CV) in %.

Concentration	Analyte Peak Area 1	Analyte Peak Area 2	Mean Analyte Peak Area	%CV
[ng/mL]	[counts]	[counts]	[counts]	
5.00	2.02E+03	7.66E+02	1.39E+03	45
10.0	4.90E+03	1.10E+03	3.00E+03	63
20.0	8.30E+03	7.19E+03	7.75E+03	7.2
40.0	1.67E+04	1.68E+04	1.68E+04	0.3
80.0	3.13E+04	3.22E+04	3.18E+04	1.4
320	1.37E+05	1.23E+05	1.30E+05	5.4
640	2.39E+05	2.63E+05	2.51E+05	4.5

The individual concentrations of the samples ranging from 5.00 ng/mL to 640 ng/mL and the integrated analyte peak areas of the duplicates are shown. The mean value μ could be calculated from the duplicates. The standard deviation σ enabled the determination of the coefficient of variation (CV) and was calculated by dividing the standard deviation σ by the mean value μ . CV can be employed to express the precision and repeatability of measurements in percentage (%CV). The FDA also recommends to use %CV determinations for validation of analytical assays. [164] The %CV of duplicates should be less than 20 %. A larger %CV indicates greater inconsistency of the measured data and possible errors. In this case, %CV of the lowest CS samples (5.00 ng/mL and 10.0 ng/mL) were above 20 % (45 % and 63 %, respectively). In validation experiments, this measurement series must be rejected due to the high %CV for the two lowest CS samples. At least 75 % of the duplicate measurements should have deviations below 20 %. In particular, CS samples at very

low concentrations can lead to possible errors and therefore higher %CV due to the decreased S/N ratio, resulting in greater integration errors.

Within these testing conditions, the data was still used for linear regression analysis since it was only used to get the first impression of linearity and was not performed in matrix but in solvent. On the basis of the data from Table 4-4, a regression analysis was performed to determine the relationship between the concentration x and the instrument response y, which is in this case the integrated peak area. The "method of least squares" was utilized in every regression analysis employed in this study. This method determines the line of best fit for a set of data. The experimental values, which are the integrated peak areas, rarely fit perfectly, but instead show differences between the observed and the predicted values, which are called residuals. The objective of the least squares method is to minimize the sum of the squared residuals, thereby providing the most accurate estimate of the model parameters. For quantification, linear regression is used, where the relationship between x and y is always a straight line and the linear regression equation (equation 1) can be described as follows:

$$y = mx + b$$

where;

y is the instrument response

m is the slope

x is the concentration of the analyte

b is the intercept.

The linearity of the determined calibration curve is expressed through the coefficient of determination R^2 . The best fit for the calibration curve is indicated with a value for R^2 close to 1.^[135] For assessment of the linearity, R^2 should be inspected for every constructed calibration curve. The calibration curve for FdU-MP **9** is shown in Figure 4-35 including the plotted integrated peak areas in duplicate (grey squares and blue

dots), the linear regression equation of the fitted line and the corresponding R^2 . In general, it can be concluded that a linear relationship is present between x and y, as demonstrated by the R^2 of 0.9997 and visual inspection of the data points around the fitted line. Initial findings for linearity of the FdU-MP **9** with this chromatography method were found to be satisfactory.

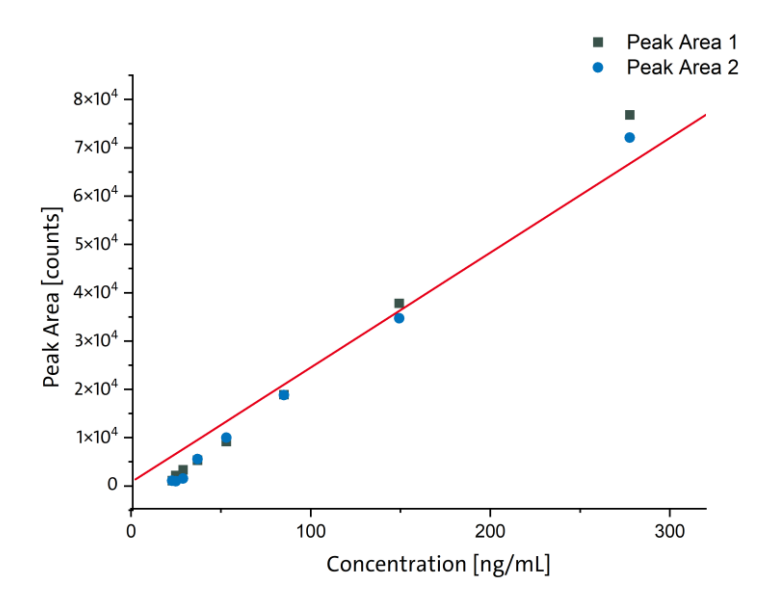


Figure 4-35: Calibration curve of FdU-MP 9 calculated from the mean values of peak area 1 and peak area 2 including linear regression equation and coefficient of determination R^2 .

The results obtained for nucleoside **10** were found to be highly comparable, and thus, they will not be addressed in this chapter. The underlying data can be found in chapter 7.2, Supplementary data, Table 7-2 and Figure 7-1).

Linearity was assessed for TriPPPro-compounds 1 and 2 using six non-zero CS samples (20.0 – 640 ng/mL). For compound 1, linearity could not be evaluated due to insufficient signal intensity. The first detectable signal occurred only above 80.0 ng/mL in the first replicate, and no signal was observed in the second. Higher concentrations also showed marked signal loss. In contrast, compound 2 exhibited sufficient signal intensity, and CS samples were analyzed in duplicate. The data is displayed in Table 4-5. Similar to the observations concerning TriPPPro-compound 1, the signal intensities and, by consequence, the integrated analyte peak areas of the second replicate exhibited significant variation.

Table 4-5: Calibration standard (CS) samples for Tri*PPP*ro-compound **2**, including corresponding concentrations in ng/mL, integrated peak areas of the duplicates including the resulting mean and the coefficient of variation (CV) in %.

Concentration [ng/mL]	Analyte Peak Area 1 [counts]	Analyte Peak Area 2 [counts]	Mean Analyte Peak Area [counts]	%CV
20.0	1.40E+04	1.92E+03	7.96E+03	76
40.0	2.72E+04	4.46E+03	1.58E+04	72
80.0	4.63E+04	6.43E+03	2.64E+04	76
160	1.22E+05	1.32E+04	6.76E+04	80
320	2.97E+05	2.09E+04	1.59E+05	87
640	6.59E+05	1.18E+05	3.89E+05	70

Although CS samples were stored in liquid nitrogen and were thawed directly prior analysis, a reduction in peak area between 82 % and 93 % was observed resulting in major variations (%CV between 72 % and 87 %). For visualization, the data from Table 4-5 was used to perform linear regression analysis, which is displayed in Figure 4-36. As already mentioned, the major deviation between the duplicates can also be seen very clearly.

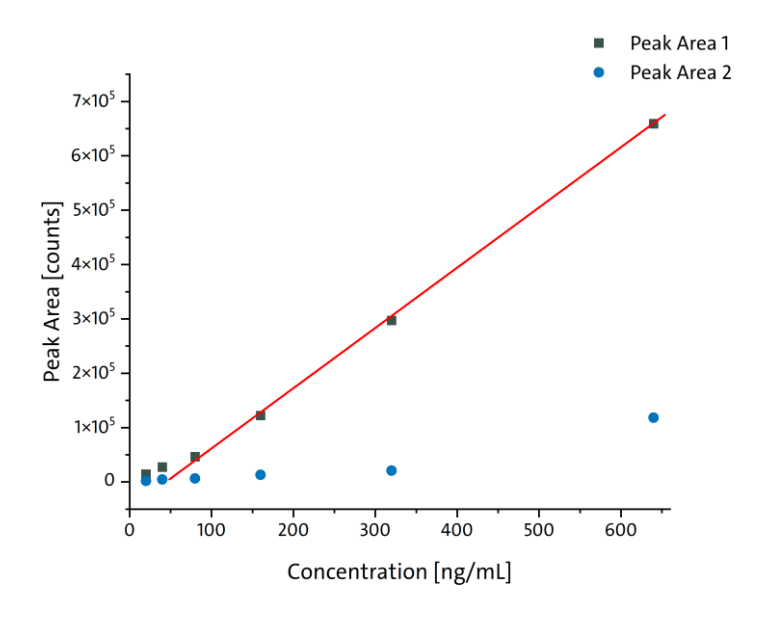


Figure 4-36: Calibration curve of Tri*PPP*ro-compound **2** calculated from the mean values of peak area 1 and peak area 2 including linear regression equation and coefficient of determination R^2 .

However, on basis of the least squared method, a linear calibration could still be determined with a value of 0.9905 for R^2 . This illustrates that the coefficient of determination, R^2 , should not be the only variable to assess the linearity. Instead, the underlying data indicates no linear relationship across the entire range of the x values, which is particularly noticeable in the low concentration range between 20.0 ng/mL and 80.0 ng/mL. In terms of linearity for the prodrug compounds, the LC method developed so far seemed not suitable.

To investigate a possible explanation for the major deviations between the CS samples, chemical stability was assessed in hydrolysis studies. It was hypothesized that the poor chemical stability of the FdU-prodrug compounds in pure water could be the reason for the decreased signal intensity and resulting peak area. WITT already determined chemical stability of the prodrugs in phosphate buffered saline (PBS) under physiological conditions (pH value of 7.3 at 37 °C) and calculated half-life values $t_{1/2}$ of 55 h and 52 h for Tri*PPP*ro-compound 1 and 2, respectively. [61] The half-life values indicate acceptable chemical stability. Nevertheless, they fail to account for the poor replicate analysis of the CS samples in water when it comes to the calibration curve measurement.

Therefore, hydrolysis studies of the Tri*PPP*ro-compound **2** were conducted in ultrapure water, suitable for LC-MS measurements. This ultrapure water exhibited a pH value of 6.9. A solution of Tri*PPP*ro-compound **2** with the concentration of 1 mg/mL was incubated at 37 °C for 24 h. At appropriate times, aliquots of this solution were subjected to analysis via RPIP-UV since the LC-MS/MS method did not include all known metabolites at that time. The chromatograms are displayed in Figure 4-37.

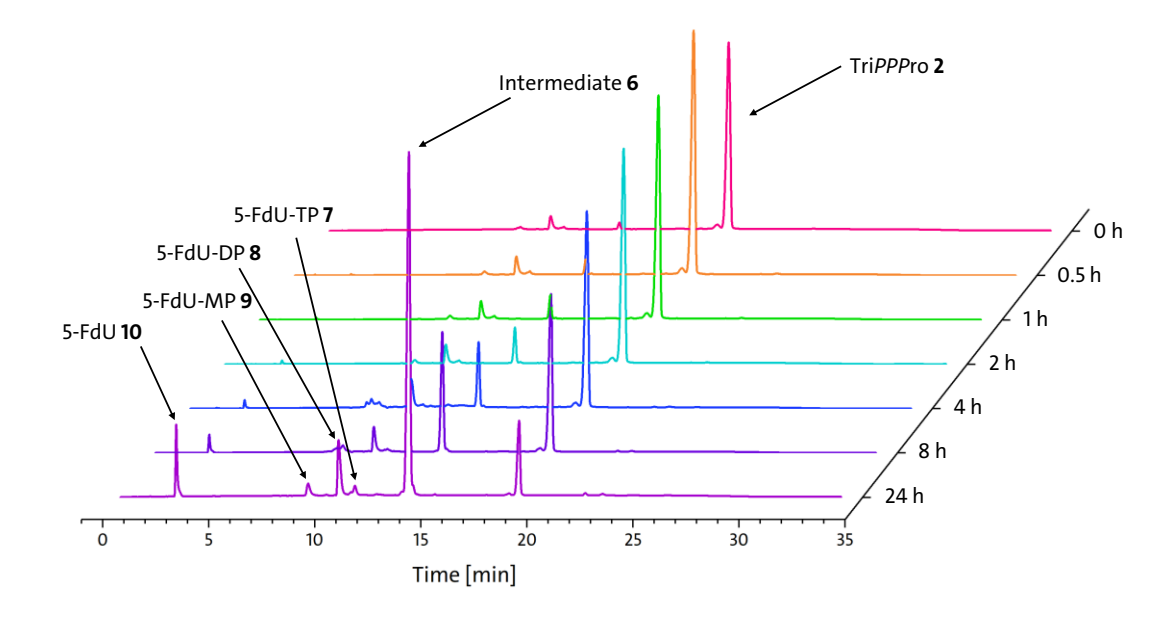


Figure 4-37: Hydrolysis study of Tri*PPP*ro-compound **2** (concentration of 1 mg/mL) in ultrapure water (pH value of 6.9 at 37 °C). Measurements followed by RPIP-UV at a wavelength of 270 nm.

The identity of the compounds was initially estimated from the UV spectra generated during the measurements but was also confirmed by co-injection of the pure compounds in ongoing studies. However, it should be noted that the volume of the incubation solution was only sufficient for seven aliquots. Nevertheless, the data obtained were sufficient to emphasize the chemical hydrolysis of Tri*PPP* rocompound **2** in ultrapure water to the corresponding metabolites.

Following a 24 h period, a signal for the prodrug was still detectable, but the amount of compound, as expressed by the peak area, was already more than reduced by half. The progression of the chemical hydrolysis is also displayed in Figure 4-38 for all detected compounds. It is evident that the predominant metabolite was the intermediate **6**, as previously mentioned, yet the formation of FdU-DP **8** was also observed. This increased formation of the diphosphate was also observed by WITT.^[61] It had already been established that prodrugs with longer alkyl chains on the AB mask (such as C11 here) showed a different hydrolysis behavior than prodrugs with shorter alkyl chains at the masking unit.^[52,136] This could be due to the fact that the negative charges of the phosphate units are more strongly shielded with longer alkyl chains, which favors a nucleophilic attack on the phosphorus anhydride bond between β - and γ -phosphate resulting in the formation of diphosphate.

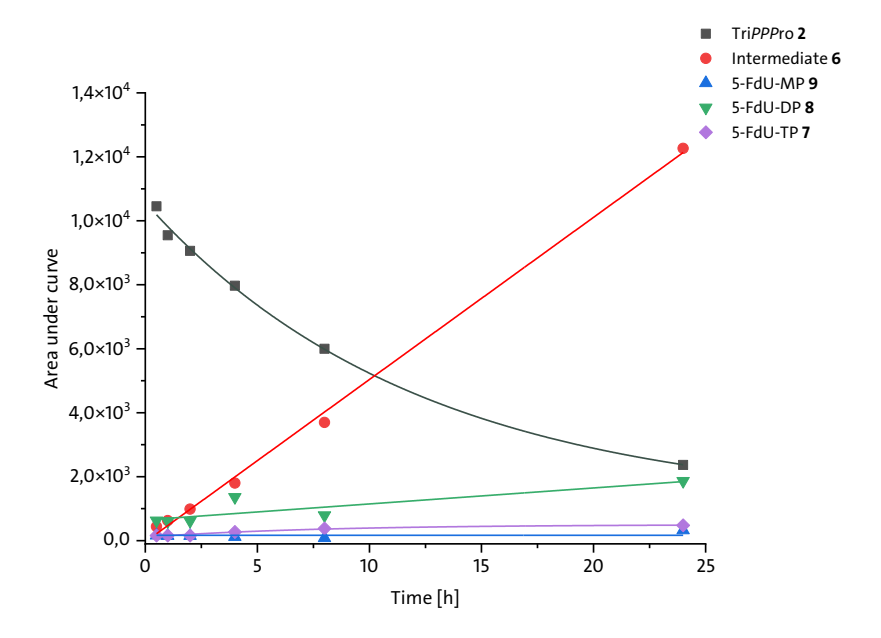


Figure 4-38: Progression of the chemical hydrolysis of Tri*PPP*ro-compound **2** in ultrapure water.

Based on an exponential fit of the decay curve for the Tri*PPP*ro-compound $\bf 2$, the half-life, $t_{1/2}$, was calculated using following equation (equation 2):

$$t_{1/2} = \frac{\ln{(2)}}{k}$$

where:

 $t_{1/2}$ is the half-life

In is the natural logarithm

k is the decay constant.

The $t_{1/2}$ value of compound ${\bf 2}$ in ultrapure water has been calculated with an estimated result of 11 h, based on the data gained over a 24 h time period. This finding significantly deviated from the $t_{1/2}$ value of 52 h that WITT had previously determined for the compound ${\bf 2}$ in PBS buffer. Nevertheless, it is only possible to hypothesize about a possible explanation, as no further experiments have been conducted on this issue. It may be reasonable to assume that the pH value difference of 0.5 and the absence of salts, in comparison to PBS buffer, can cause a significant effect on the chemical stability of the prodrug.

On the basis of this data, a sample processing workflow in highly aqueous solvents was too difficult to realize since the stability of the prodrugs in the injection solvent did not produce satisfactory results concerning calibration curves in duplicate measurements. As an alternative, it was decided to restart the HPLC method development. However, one parameter has already been defined: the injection solvent must comprise a non-nucleophilic solvent such as acetonitrile. As previously outlined, there is a correlation between the injection solvent and the initial conditions of the LC gradient. Consequently, any discrepancy between these factors may result in suboptimal chromatographic performance. [166] A suitable chromatography method to avoid this problem is HILIC, where the mobile phase is composed primarily of acetonitrile (see section 2.3.1). In the following section, a detailed discussion of the development of the HPLC method employing HILIC will be given.

4.3.2 Application of HILIC stationary phases

In order to avoid the need for chemical labelling of the compounds, Pertenbreiter wanted to establish a direct method for investigating the intracellular concentrations of therapeutically relevant nucleotide analogues from cell lysate. [95] For this purpose, different chromatography systems were tested in combination with mass spectrometric analysis in negative ESI mode. The first column tested was a HILIC column manufactured by the company Macherey-Nagel (EC 150/2 NUCLEOSHELL® HILIC) using a modified stationary phase with zwitterionic ammonium sulphonic acid to enhance selectivity for polar metabolites, such as triphosphates, diphosphates and monophosphates. The second column was an RP column, also manufactured by Macherey-Nagel (EC 50/2 NUCLEODUR® C₁₈ Gravity). The tested compounds comprised a symmetrically masked Di*PP*ro compound with

C6-AB masks and the corresponding DP and MP. As mobile phases, an Af buffer with a pH value of 8.3 and acetonitrile were used. [95] The gradient is displayed in Table 4-6.

Table 4-6: HILIC gradient according to Pertenbreiter. [95] 10 mM ammonium formate (Af) buffer, pH 8.3 as eluent A and acetonitrile as eluent B.

Time [min]	Eluent A [%]	Eluent B [%]
0	5	95
25	50	50
27	50	50
30	5	95
35	5	95

Unfortunately, Pertenbreiter observed that the lipophilic DiPPro-prodrug did not show retention on the HILIC column, whereas the polar metabolites did not exhibit retention on the RP column. Therefore, two separate methods were developed to investigate cellular uptake studies.^[95] The log P value as physiochemical property of compounds is frequently employed to express the lipophilicity these compounds, thereby serving as a metric for the suitability of them for HILIC. Of greater interest in this context is the log D value, which is strongly pH dependent. Log P and Log D values were determined for the TriPPPro-compounds 1 and 2 using the averages from two different prediction tools in the program Marvin (Consensus and ChemAxon, Budapest, Hungary). The results are listed in Table 4-7. It is acknowledged that predicted values can vary from their true values. Therefore, the purpose of prediction is simply to provide an estimate of the lipophilicity and retention behavior of the prodrugs. Evidently, the consideration of log D values is of great importance, as the trend of enhanced hydrophilicity with increasing pH value is clearly noticeable. This may be due to the fact that with increasing pH value the free phosphate groups (α and β) become deprotonated and the presence of the fully deprotonated charged species leads to increased polarity.

Table 4-7: Calculated log *P* and log *D* values for Tri*PPP*ro-compound **1** and **2** using the averages of two different prediction tools in the software program Marvin (Consensus and ChemAxon).

Compound	Log P	Log D	
compound		рН	logD
		1.5	6.51
Tri <i>PPP</i> ro-	7.20	5.0	2.93
compound 1	7.20	6.5	1.65
		7.4	0.94
		1.5	9.04
Tri <i>PPP</i> ro-	9.72	5.0	5.46
compound 2		6.5	4.17
		7.4	3.46

With regard to the method development, high pH values in the mobile phase are of great importance as a strategy to achieve retention for the lipophilic Tri*PPP*rocompounds.

The primary column to be tested was the XBridge BEH HILIC, as it was already available to the group and could be readily accessed. According to the manufacturer, the column is not suitable for operation with high pressure (above 415 bar) and high pH values (surpassing a pH value of 9). However, it is sufficient for initial testing. As first testing conditions, the gradient which was developed from Pertenbreiter was used (s. Table 4-6, p. 82) employing an Af buffer with the concentration of 10 mM and a pH value of 8.3. The EICs of the different analytes are displayed in Figure 4-39. As illustrated, almost all analytes included in the MRM method so far, exhibited retention. UTP 35 eluted in under one minute from the column, which needed improvement since very short retention times can lead to increased matrix effects. In HPLC, non-retained components elute within the first minute, known as column void elution. During gradient elution, the initial and/or final segments of the run are often diverted to waste to prevent ion source contamination, particularly when analyzing biological matrices.

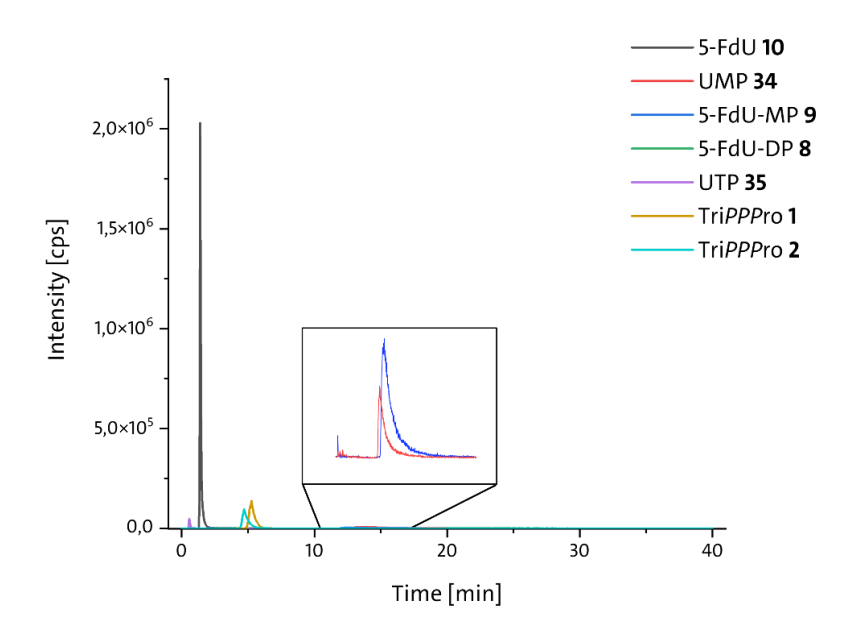


Figure 4-39: EICs of the analytes tested on the XBridge BEH HILIC column (analyte concentration: 500 ng/mL in acetonitrile/water 95:5 % v/v, 5 µL injection).

The nucleoside **10** also exhibited a low retention time from 1.3 minutes, but peak shape and peak intensity were exceptionally good. It was also possible to achieve signals for the two lipophilic Tri*PPP*ro-compounds, which was a surprising result. It was expected that it would be much more difficult to achieve good retention for the prodrugs. Unfortunately, the UMP **34** and the FdU-MP **9** were co-eluting from the column, which was an unfavorable outcome. Also, the peaks were very broad due to extensive tailing, which also resulted in very low signal intensity. Therefore, the EICs of the two compounds are shown in larger size.

Peak tailing is a prevalent issue in HILIC, and there is a substantial amount of literature on the subject. [69,166–168] Solvent mismatches, but also secondary interactions with the stationary phase can lead to wider peak widths and tailing. For compounds with free phosphate groups, it was also observed that interactions with stainless steel from the chromatographic hardware can lead to tailing. [169] No signal was observed for the FdU-DP **8**, since the peak was too broad. In summary, the preliminary test with the XBridge HILIC column was very promising. Following the optimization of both the stationary phase and the mobile phase, it was anticipated

that the HILIC retention mechanism had the potential to achieve simultaneous retention for all analytes.

Based on the results obtained so far, two other HILIC columns (s. section 4.3) were tested that were more robust than the XBridge BEH HILIC in terms of pH range and operating pressure. Furthermore, both the amide and the Z-HILIC column were equipped with the premier technique, a hardware technology developed from Waters™, which significantly reduces unwanted analyte/surface interactions. This technique appeared to give promising results regarding the free phosphate groups of all analytes.

For the elution, the same HPLC gradient was used as previously described (s. Table 4-6, p. 82). Instead of ammonium formate, ammonium bicarbonate was used since this additive showed promising results in method development with the mixed-mode column with a basic pH value of 9.4. For eluent A, NH₄HCO₃ buffer in a concentration of 10 mM and a pH value of 9.4 was used. Eluent B was a mixture of acetonitrile and water (97:3 % v/v) with 10 mM of NH₄HCO₃. The addition of salt to both mobile phases has been shown to be effective in previous measurements. This ensures that the employed conditions remain constant throughout the entire gradient elution process. The only disadvantage however is the low solubility of NH₄HCO₃ in acetonitrile. Therefore, 3 % of water was added to eluent B. It was observed that, over a certain time period, NH₄HCO₃ precipitated. In order to ensure the quality of the buffer, it had to be freshly prepared frequently and stirred for several minutes at room temperature before use.

Figure 4-40 displays the measurements on the two different column types. On the left side, the chromatogram shows all EICs of the analytes tested on the XBridge Premier BEH amide column and on the right side, the chromatogram shows the measurements on the Atlantis Premier BEH Z-HILIC. In direct comparison of the chromatograms, the results obtained with the amide column were more promising compared to the Z-HILIC column.

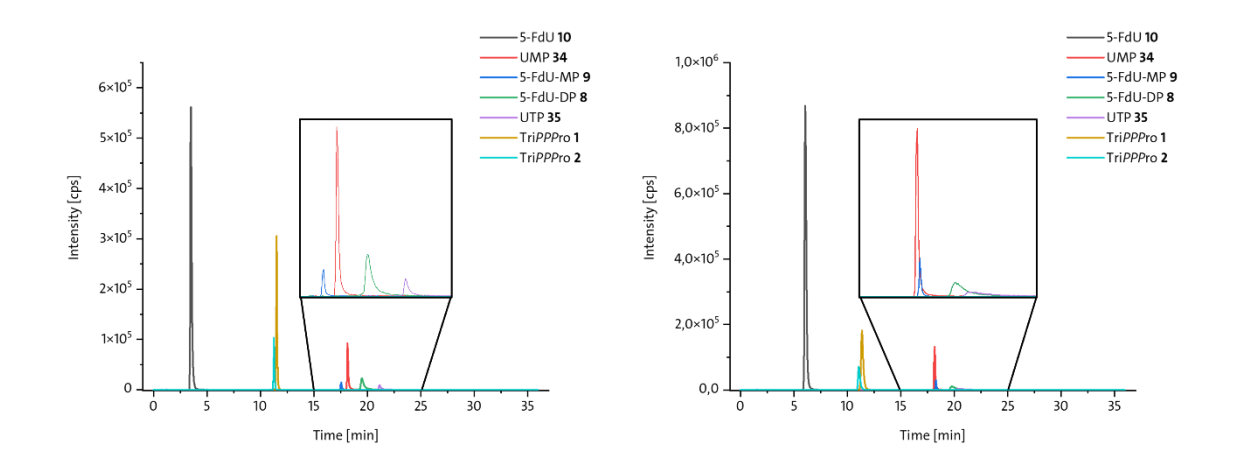


Figure 4-40: Left: EICs of the analytes tested on the XBridge Premier BEH amide column, right: EICs of the analytes tested on the Atlantis Premier BEH Z-HILIC column (ammonium bicarbonate (NH₄HCO₃) buffer, 10 mM, pH of 9.4, analyte concentration: 500 ng/mL in acetonitrile/water 95:5 % v/v, 5 μ L injection).

Due to the zwitterionic sulphobetaine residues on the stationary phase, the Z-HILIC offers an alternative separation compared to the amide column. In this case, the conditions of the mobile phase with the high pH value of 9.4 performed very well in combination with the amide column. While all analytes were separated on the amide column, 5-FdU-DP **9** and UTP **35** co-eluted as potential internal standards and showed significant peak tailing on the Z-HILIC column. Overall, it was decided to use the amide column for further method development.

Another challenge was the preparation of the mobile phases. NH₄HCO₃, as previously noted, precipitated in eluent B due to its low solubility in acetonitrile and decomposed at room temperature into water, ammonia, and carbon dioxide. The carbon dioxide formation was particularly problematic, causing air bubbles in the pump and pressure fluctuations. This prompted an evaluation of alternative salts with greater acetonitrile solubility, thermal stability, suitable buffer capacity around pH 9, and MS compatibility. Only acetate and formate buffers were considered. Three runs using the current MRM method with seven analytes were performed under identical conditions—same analyte concentration, injection solvent, and volume—on an amide column with different buffer salts. The results are displayed in Figure 4-41.

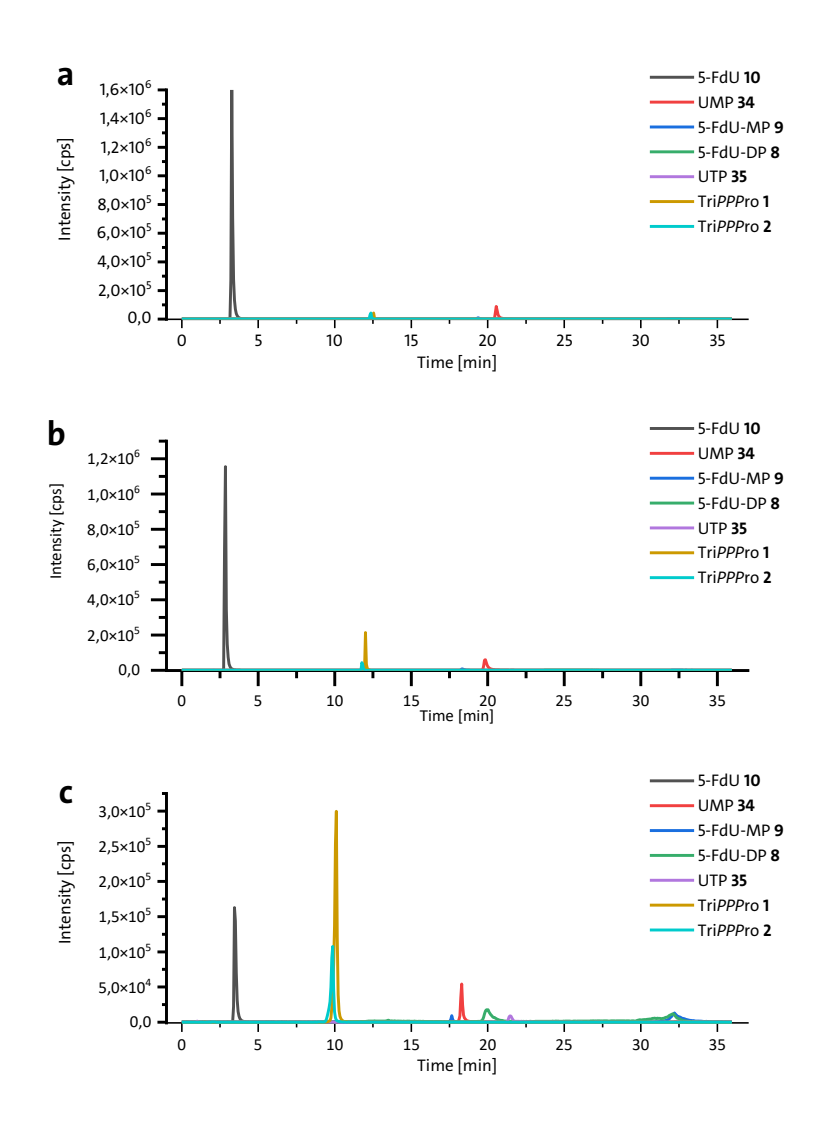


Figure 4-41: EICs for seven analytes with different chromatographic conditions.

a: AAc buffer, 10 mM, pH 9, b: Af buffer, 10 mM, pH 9, c: NH₄HCO₃ buffer, 10 mM, pH 9. Analyte concentration: 500 ng/mL in acetonitrile/water 95:5 % v/v, 5 μL injection.

For mobile phase A, the corresponding salt was dissolved in water with a concentration of 10 mM and the pH value was adjusted to 9 with ammonia solution. For mobile phase B, 10 mM of the same salt were dissolved in an acetonitrile/water mixture (97:3 % v/v).

Figure 4-41a displays the chromatographic run with AAc buffer, b with Af buffer and c with NH₄HCO₃ buffer. Overall, the results with NH₄HCO₃ buffer were by far the best in terms of simultaneous retention and peak shapes. Peak intensities of the prodrugs and the monophosphates were very low with AAc or Af buffer, while the signals detected for FdU-DP **8** and UTP **35** were very broad and despite the analyte concentration of 500 ng/mL exhibited of very low signal intensity. It was already

assumed that NH_4HCO_3 buffer resulted in the best chromatographic outcome since the salt did show good results with the mixed mode column as well. In comparison to the other two salts, the NH_4HCO_3 buffer exhibits excellent buffering capacity in the high pH value range because of its mixed buffer characteristics. The buffer not only has the ammonium – ammonia species but also the hydrogen carbonate – carbonate species as buffering system around pH of 8 – 10. This may be the reason for the good results employing NH_4HCO_3 as an additive. Signal intensities for the nucleotide **10**, the diphosphate **8** and the triphosphate **35** were still not ideal, but can be further optimized.

5-FdU-TP **7** was incorporated into the MRM method, with the EIC of the most intense mass transition (quantifier) shown in Figure 4-42. The compound had a retention time of 20.9 min and a satisfactory peak shape without tailing. However, the signal intensity was only 7000 cps, which is low for a 500 ng/mL concentration, a phenomenon also observed for FdU-DP **8** and UTP **35**.

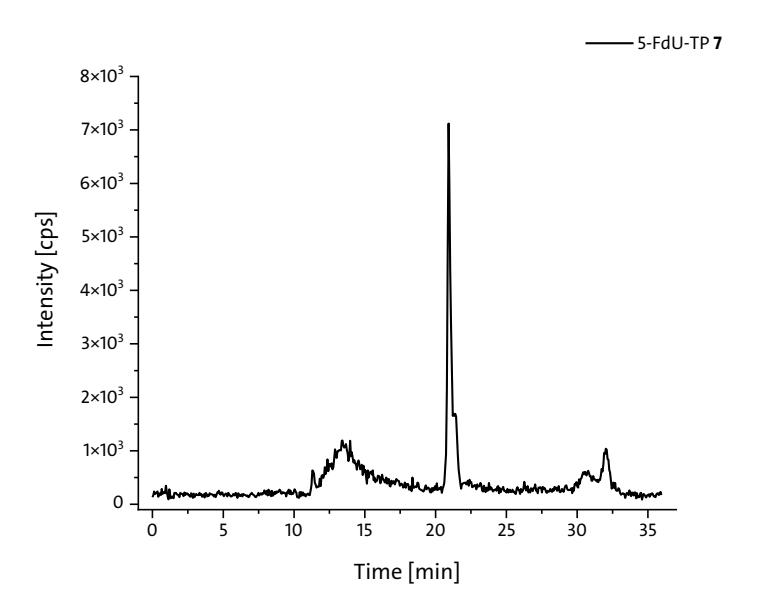


Figure 4-42: EIC of 5-FdU-TP **7** with established HILIC-MRM method. Analyte concentration: 500 ng/mL in acetonitrile/water 95:5 % v/v, 5 μL injection.

In summary, the results obtained when employing the amide column with HILIC conditions and an NH₄HCO₃ buffer of high pH value were reasonably satisfactory for all analytes and the method development was completed. However, further

improvements in the signal intensities could be achieved by optimizing the LC method. The following chapter will provide a detailed description of the optimization studies using statistical design of experiments (DoE) for the chromatographic parameters and flow injection analysis (FIA) for the MS parameters.

4.4 Optimization studies of the HPLC-MS/MS method

In order to enhance the optimization of the LC method with greater efficacy, it was determined that a statistical approach should be employed, given the method's complexity and the fact that optimizing one factor at a time (OFAT) can be ineffective and time-consuming. [170,171] The OFAT approach is disadvantageous in the case of complex systems, as it does not take into account possible interactions between the factors. [172] With the DoE approach, all factors are varied simultaneously which ensures that all relevant factors and their possible combinations result in optimal conditions to maximize peak intensities. Subsequently, the MRM method was optimized using FIA. The subsequent subsections will describe the procedure of the statistical experiment for optimization of the LC parameters and the procedure of FIA for optimization of the MS parameters.

4.4.1 Design of Experiment (DoE)

The DoE approach enables the investigation of the influence of each experimental factor in a simultaneous manner, with a predefined number of experiments.^[173] This technique is especially powerful for optimization studies of multivariate systems such as LC-MS/MS since many different factors such as mobile phase conditions, sample preparation or MS parameter influence the detection of analytes.^[174] In

literature, DoE is a common tool to optimize the LC-method^[175,176] or the MS-method^[175,177] for quantification in biological matrices. In this work, DesignExpert (version 11) was used as software to plan the experiment and analyze the data. The DoE can also be used as an initial screening to identify the factors that need to be optimized in a second experiment. In this work, however, the DoE was only used as an optimization study as the preliminary work (chapter 4.3, p 63 ff.) was used to identify possible factors for optimization.

A possible workflow for implementing a DoE optimization approach is displayed in Figure 4-43. The first step is the selection of factors and factor levels for the DoE. The factors are the independent variables of the method, whereas the factor levels describe specific values or settings of a factor. Possible factors for the optimization study of the LC method can be the type of stationary phase, the composition of the mobile phase (e.g., pH value, organic solvent, additive), the flow rate or the column temperature. In regard to the HILIC method used in this work, it has been established through previous research^[166,178] that the type and proportion of the organic solvent, the type and concentration of the additive for the buffer including the pH value have all a significant influence on the chromatographic performance in HILIC. Column temperature can also have an effect on retention in certain cases, albeit a comparatively small one.^[178]

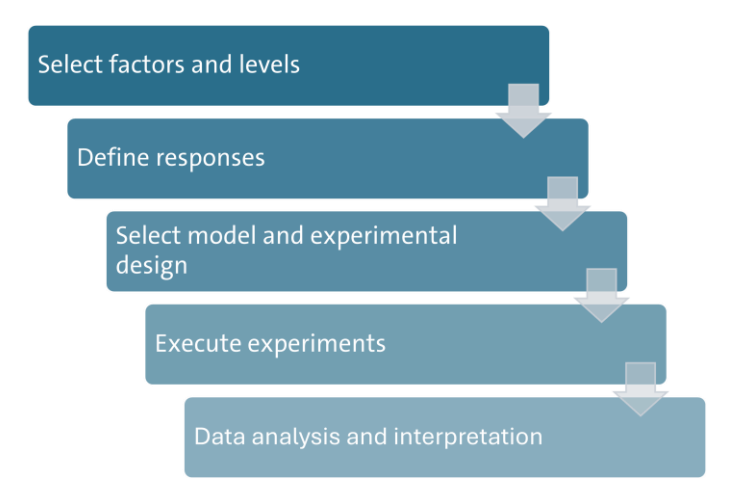


Figure 4-43: Steps for implementing a design of experiment (DoE) optimization approach. Adapted to Thorsteinsdóttir.^[179]

On basis of this literature research and preliminary method development, the column operating temperature, the pH value of the mobile phase A and the ammonium bicarbonate concentration (as additive concentration) of the mobile phase A and B were selected as factors. Table 4-8 summarizes the factors with their defined properties. For the experiment it should be distinguished between numeric and categoric factors, where numeric factors can be counted or measured, while categoric factors can only be described or represented by names or symbols.

Table 4-8: Selected factors for the optimization of the LC method.

Factor	Name	Units	Change	Туре	Minimum	Maximum
(a)	Column temperature	°C	Hard	Numeric	35.0	55.0
(B)	pH value of A	Unitless	Easy	Numeric	8.30	10.0
(C)	Additive concentration of A and B	mM	Easy	Numeric	5.00	20.0

In this case, all factors were numerical, with a continuous range for all factors defined only by minimum and maximum values. It was also possible to define so-called hard-to-change (HTC) factors. HTC factors are factors that are difficult to randomize due to time constraints, as it can take a long time to heat the column up to 55 °C and cool it down to 35 °C after only one run. It also takes time to stabilize the conditions after adjustment. The column-temperature was therefore defined as a continuous HTC factor (a), whereas pH value (B) and additive concentration (C) were easy-to-change (ETC) continuous numerical factors. The amide column was chosen as the stationary phase, and it was decided not to include all analytes in the optimization process as the prodrugs consistently showed favorable retention and peak shape characteristics. The most challenging analytes in terms of peak shape and intensity were 5-FdU 10, FdU-MP 9, FdU-DP 8 and FdU-TP 7. Therefore, the peak intensity, expressed as peak height, was defined as response. The response is the

dependent variable and should be a value which can be measured. The factors and responses form the design matrix.

An experimental design is selected based on the matrix to model the relationship between factors and responses. In this study, a split-plot optimal response surface methodology (RSM) was used, combining principles of RSM and optimal design. The optimal design identifies the most informative combinations of factor levels within the design matrix. Evaluating all combinations of three factors (e.g., temperature in 5 °C steps, pH in 0.1 steps, and additive concentration in 5 mM steps) would require 360 runs. Instead, the optimal design allows for statistical modeling with a reduced number of experiments to efficiently identify optimal conditions. [179]

The advantage of the second modeling design, RSM, is that it considers the curvature of the design matrix, which means that this design supports the estimation of quadratic terms rather than just linear terms. This makes it easier to interpret complex systems and facilitates data interpretation with the ability to generate 3D response surface plots. [179,180] The split-plot design had to be chosen because of the HTC factor (a), which represents the column temperature. Normally, before running the experiment, the order of the runs in the design matrix is randomized to avoid systematic errors. [179] This is the most reliable method of creating homogeneous treatment groups. With the HTC factor (a) in the matrix, there was a restricted randomization which presented a statistical challenge. In split-plot designs, there are two levels of randomization to reduce the number of times an HTC factor is reset. The HTC factor was grouped together to form 'sub-plots', while the complete matrix is called the 'whole-plot'. [181] It was then possible to randomize the runs within the sub-plot and to randomize the groups within the whole-plot. Table 4-9 summarizes the design matrix with the responses R1 to R4 for the analytes 10, 9, 8 and 7.

The matrix was divided into three blocks, each block representing one measurement day. A total of 14 individual runs were performed with an analyte mixture including all four analytes in acetonitrile and water (95:5 % v/v) as injection solvent with a

concentration of 500 ng/mL. The mass transition of each analyte with the highest peak intensity, the quantifier, was used to measure the response for each analyte. All chromatograms were analyzed and the peak intensities obtained by peak height were entered into the design matrix (Table 4-9). The next step was the analysis of the data including interpretation, which will be discussed in the following subsection.

Table 4-9: Design of experiment (DoE) matrix including determined responses for 5-FdU **10** (R1), 5-FdU-MP **9** (R2), 5-FdU-DP **8** (R3) and 5-FdU-TP **7** (R4).

Block	Group	Run	Factor (a)	Factor (B)	Factor (C)	R1	R2	R3	R4
Day 1	1	1	55	9.609	20	3.80E+05	3.80E+03	3.53E+03	7.00E+02
Day 1	1	2	55	8.4	10	7.00E+05	5.00E+03	7.45E+03	1.15E+03
Day1	1	3	45	8.3	20	5.90E+05	7.00E+03	4.49E+03	1.05E+03
Day 1	2	4	45	9.4815	10	5.20E+05	4.89E+03	6.07E+03	1.49E+03
Day 1	2	5	45	8.5	5	7.50E+05	6.36E+03	9.68E+03	2.85E+03
Day 2	3	6	45	9.2	10	5.50E+05	6.49E+03	1.30E+04	1.51E+03
Day 2	3	7	45	10	20	2.00E+05	2.85E+03	5.96E+03	8.00E+02
Day 2	4	8	35	9.32	20	2.20E+05	3.39E+03	5.32E+03	5.00E+02
Day 2	4	9	35	10	5	3.60E+05	3.40E+03	1.60E+04	2.01E+03
Day 2	4	10	35	8.6	10	3.80E+05	3.60E+03	1.50E+04	1.44E+03
Day 3	5	11	55	8.5	20	7.00E+05	8.00E+03	8.96E+03	8.73E+02
Day 3	5	12	55	10	5	5.80E+05	4.38E+03	1.04E+04	(7.33E+02)*
Day 3	6	13	45	9.1	5	5.00E+05	3.60E+03	1.40E+04	2.55E+03
Day 3	6	14	45	9.8	10	3.00E+05	3.57E+03	7.36E+03	1.20E+03

Factor (a): column temperature in °C

Factor (B): pH value of the mobile phase A

Factor (C): Additive concentration in mobile phases A and B

R1 – 4: Peak intensity of the analyte in cps; * run was ignored later in ongoing validation of the model

4.4.2 Evaluation of the DoE

The selected responses for the method optimization are displayed in Table 4-10. On the basis of these responses, the statistical experiment needed to be validated by analyzing the results.

Table 4-10: Selected responses for the method optimization.

Response	Name	Units	Minimum	Maximum
R1	Peak intensity (5-FdU 10)	cps	200000	750000
R2	Peak intensity (5-FdU-MP 9)	cps	2847	8000
R3	Peak intensity (5-FdU-DP 8)	cps	3527	16000
R4	Peak intensity (5-FdU-TP 7)	cps	500	2853

The first compound analyzed was 5-FdU 10, evaluated using the diagnostics tool in DesignExpert. Initially, peak intensities were analyzed without transformation. While transformations can reduce variance in cases of wide response ranges, diagnostics such as the Box-Cox plot help determine necessity. In this case, the Box-Cox plot displayed in Figure 4-44 indicated a λ value of 1, with the 95% confidence interval including 1, confirming that no transformation was required. Based on this, a design space model was selected. The software automatically proposed a quadratic model according to RSM principles, though terms could be manually adjusted based on fit statistics to optimize the model. In the case of 5-FdU 10, the term for the column temperature (a) was not significant, indicating that there was no interaction between column temperature and the other factors.

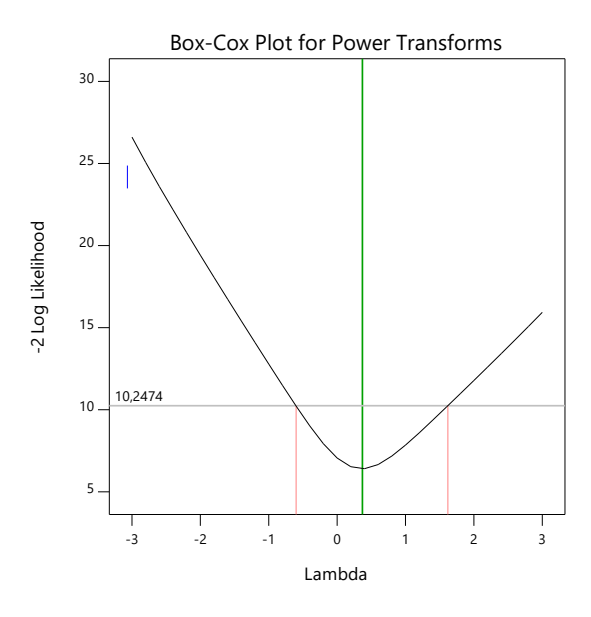


Figure 4-44: Box-cox plot for power transformations for 5-FdU 10. The blue line indicates the parameter λ , which has a value of 1. The red lines denote the 95 % confidence interval. Created with DesignExpert (version 11).

The term (a) was excluded from the model, leading to a reduced quadratic process order with the terms (B) and (C). The statistics of the chosen model were analyzed using analysis of variance (ANOVA) with restricted maximum likelihood (REML) because of the HTC factor in the design matrix. The most significant values of the ANOVA are the F-values and p-values. The values obtained are indicative of statistical significance, suggesting that the outcomes observed in the experiment are unlikely to have occurred randomly. It is desirable to have high F-values and low p-values. The results for all analytes are displayed in Table 4-11.

Table 4-11: Summary of the selected models for processing the data including the resulting equation with the coefficient of determination R^2 and the results of the ANOVA (REML).

Analyte	Model	Model Equation		ANOVA (REML)	
Analyte	Model			F-value	p-value
5-FdU 10	Reduced	4.79e+05 - 1.466e+05 - 1.042e+05 - 51447.58	0.9241	13.53	0.0218
3140 10	Quadratic	- 39080.15 + 44064.86	0.5241	13.33	(significant)
5-FdU-MP 9	Reduced	4841.69 – 1334.45	0.5894	11.12	0.0094
3-1 dO-141F 3	4641.69 – 1554.45 linear		0.5654	11.12	(significant)
5-FdU-DP 8	Reduced	0.0115 + 0.0014 + 0.0024 + 0.0001 – 0.0004 + 2.17e-	0.9095	13.55	0.0031
3140 DI 6	Quadratic 06		0.5055	13.33	(significant)
5-FdU-TP 7	Reduced	1027.42 - 161.77 - 843.33 + 79.86 - 86.33 + 652.83	0.9564	31.02	0.0028
J-1 40-1F 1	Quadratic*	1027.42 - 101.77 - 643.33 + 79.80 - 60.33 + 632.83	0.9304	31.02	(significant)

^{*} Model for 5-FdU-TP **7** after the elimination of one outlier.

This analysis was repeated for the other compounds as well. For FdU-MP **9**, the box-cox plot also indicated that no transformation of the data was required (s. Supplementary data, Figure 7-2). The model which was chosen for FdU-MP was reduced linear, since no influence of the terms (a), column temperature, and (C), additive concentration in the mobile phases, was observed. The box-cox plot for 5-FdU-DP **8** suggested a transformation of the data. The inverse square root transformation was selected where λ = -0.5. With that value, the parameter λ was within the 95% confidence interval. The box-cox plot is also included in the Supplementary data (Figure 7-6).

A reduced quadratic model was selected including the parameters (B) and (C). In the case of 5-FdU-TP 7, no transformation was required (s. box-cox plot in

Supplementary data, Figure 7-10). The chosen models and the resulting equations with their fit statistics, expressed in the coefficient of determination R^2 and the results of the ANOVA (REML) analysis expressed with F- and p-values for the other analytes are summarized in Table 4-11 as well. As mentioned above, the column temperature (a) was never a significant factor. With the exclusion of the terms, the models for every analyte were quite strong. The subsequent step in validating the model was to look for possible outliers and data patterns. This can be done by analyzing different scatter plots in the software program.

As mentioned above in chapter 4.4.1, the randomization of the data was important to avoid systematic errors. Therefore, all scatter plots should only show random patterns. The validation will be discussed in detail for the responses of 5-FdU 10. It should be noted that the other plots are not presented in detail as they are largely redundant. These plots can be found in the chapter 7.2 Supplementary data. The first plot, which was analyzed, was the normal probability plot, which is shown in Figure 4-45 on the left-hand side as the normal plot of residuals. The purpose of this plot was to determine whether the residuals are normally distributed, in which case the points will follow a straight line.

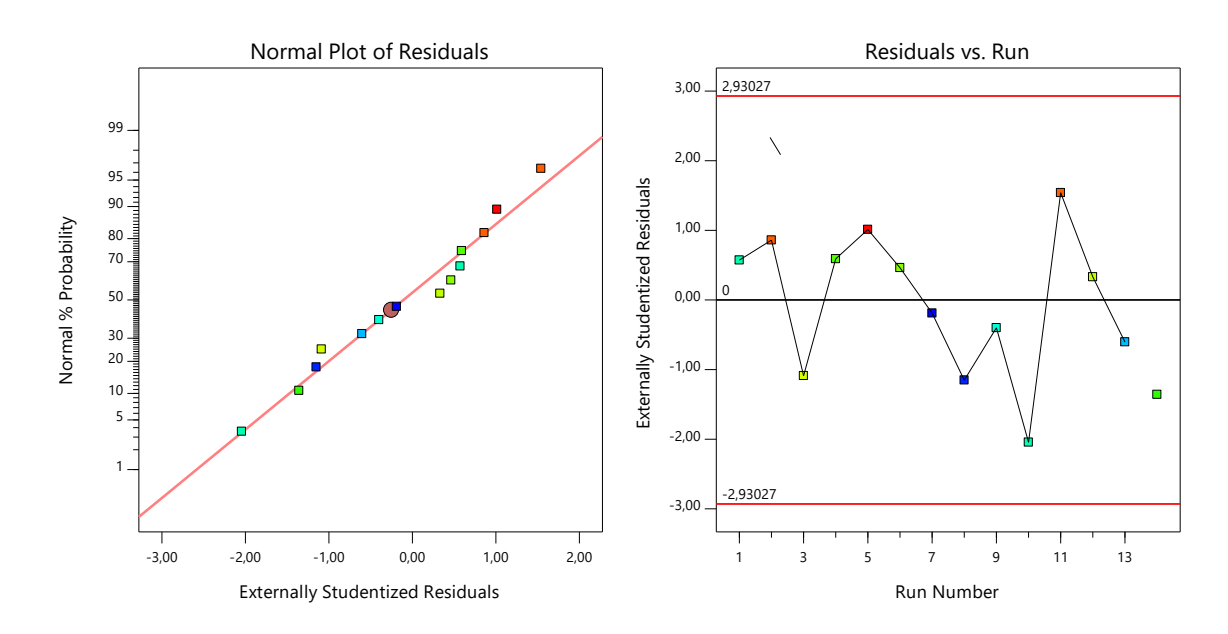


Figure 4-45: Normal Plot of Residuals (left) and Residuals vs. Run (right) for 5-FdU **10**. Created with DesignExpert (version 11).

At this point, it was possible to flag possible outliers to track them in the other diagnostic plots. For 5-FdU **10**, the data points were approximately linear, which was good. The next scatter plot was the residuals versus run plot on the right-hand side of Figure 4-45. The plot showed the residuals against the order in which the data were collected and should show a random scatter. Otherwise, the plot indicated variables that may have influenced the response during the experiment. This was not the case for this experiment.

The next plot, which was relevant, was the residuals versus predicted plot. It is illustrated in Figure 4-46 on the left-hand side. It shows the difference between observed and predicted values. A negative residual is indicative of an overestimation of the predicted value, while a positive residual suggests an underestimation. The plot should show a random pattern around the residual = 0 line, which is displayed as black line in the plot. In this case, the plot did not show any specific pattern or outliers, which was satisfactory. In Figure 4-46 on the right-hand side, the predicted versus actual plot visualizes the quality of the chosen model.

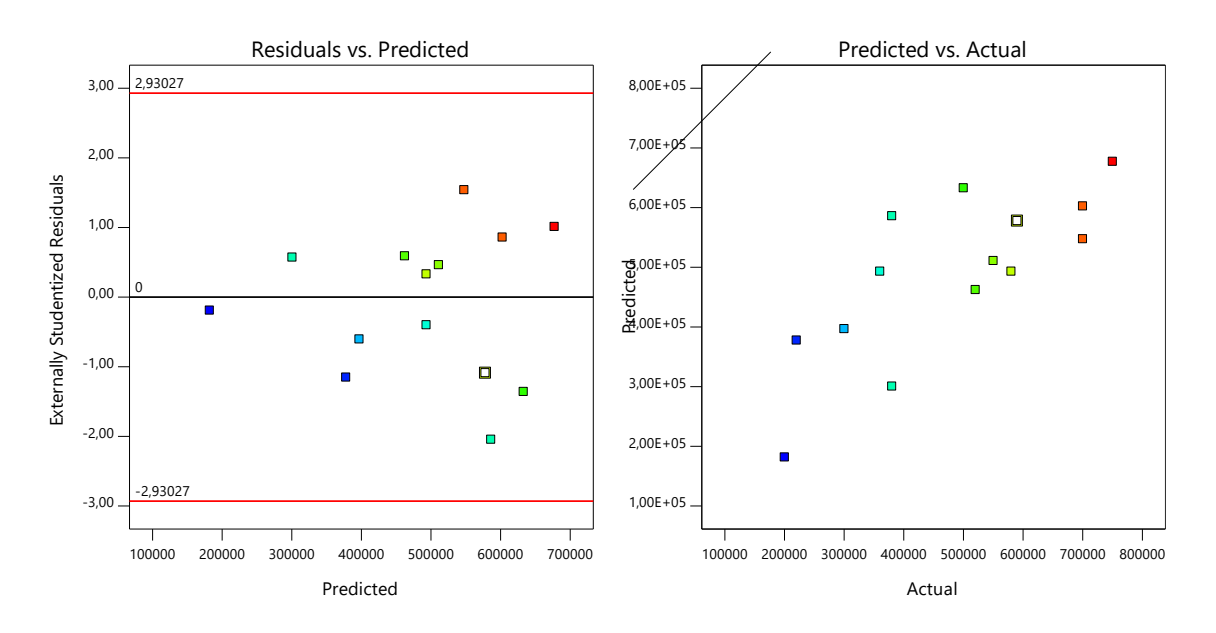


Figure 4-46: Residuals versus Predicted (left) and Predicted vs. Actual (right) for 5-FdU **10**. Created with DesignExpert (version 11).

The predictive capability of the model is evaluated by plotting the predicted values against the actual values determined during the experiment. The data points should be therefore close to the fitted line. This plot also indicated a good fit for 5-FdU **10**.

The last two scatter plots that were analyzed in this validation were the cook's distance plot and the leverage versus run plot. They are displayed in Figure 4-47.

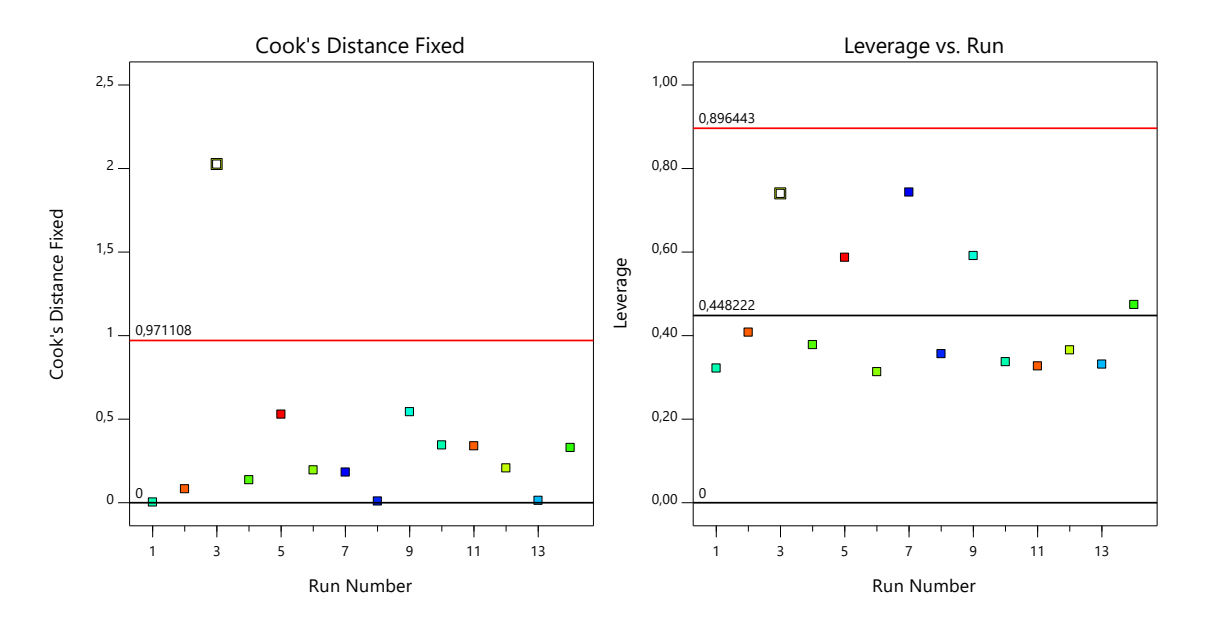


Figure 4-47: Cook's distance plot (left) and leverage versus run plot (right) for 5-FdU **10**. Created in DesignExpert (version 11).

The plot on the left-hand side illustrates the cook's distance, which is a graph showing how much influence each data point has on the chosen regression model. Data points with higher cook's distance have more influence on the coefficients of the model. The scatter plot for FdU 10 displayed a data point with a high value, which should be investigated further. Large values are associated with cases with high leverage and large studentized residuals. As discussed previously, no studentized residual was outstanding and so far, no outlier has been detected. Therefore, the leverage versus run plot was also analyzed, which is displayed on the right-hand sight in Figure 4-47. The leverage is a numerical value ranging from 0 to 1, denoting the extent to which a data point can influence the model fit. A value of 1 indicates a perfect fit between the model and the observation. As shown in the scatter plot, the data point with the high value of the cook's distance plot was not an outlier in the

leverage versus run plot indicating no data points were highly influential. Therefore, it was determined that the high value in the cook's distance did not invalidate the model.

In summary, the scatter plots indicated a strong and valid model for the model which was chosen to analyze 5-FdU 10. Moving on to the next analyte, the diagnostic scatter plots for 5-FdU-MP 9 also indicated no outliers and a valid model. The scatter plots can be found in the Supplementary data (Figure 7-3 to Figure 7-5). For 5-FdU-DP 8, the validation was similar. The results are summarized in the Supplementary data (Figure 7-7 to Figure 7-9).

In contrast, the analysis of the 5-FdU-TP **7** was different. At first, the box-cox plot suggested no transformation (Figure 4-48). A quadratic model including the column temperature (a) was chosen. The fit statistics and ANOVA (REML) indicated a significant model, and diagnostic tools were used to validate it.

The initial plots—normal plot of residuals and residuals versus run (Figure 4-49)—revealed a clear outlier, which was flagged for further analysis. This flagged data point, marked with a white and black border, also appeared as an outlier in the residuals versus predicted plot (Figure 4-50, left).

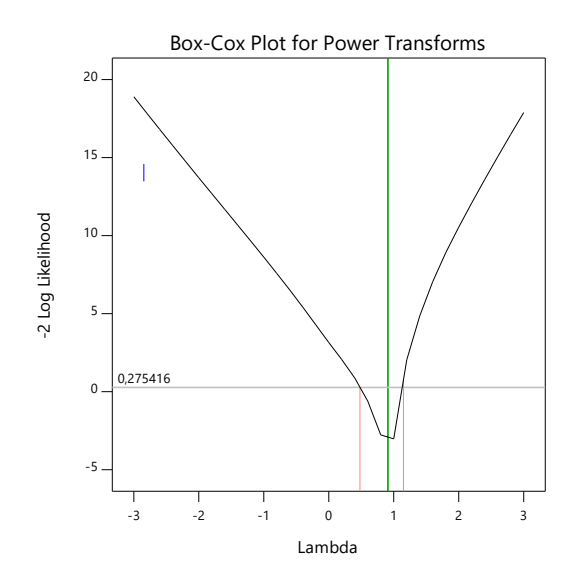


Figure 4-48: Box-cox plot for power transformations for 5-FdU 10. The blue line indicates the parameter λ , which has a value of 1. The red lines denote the 95 % confidence interval. Created with DesignExpert (version 11).

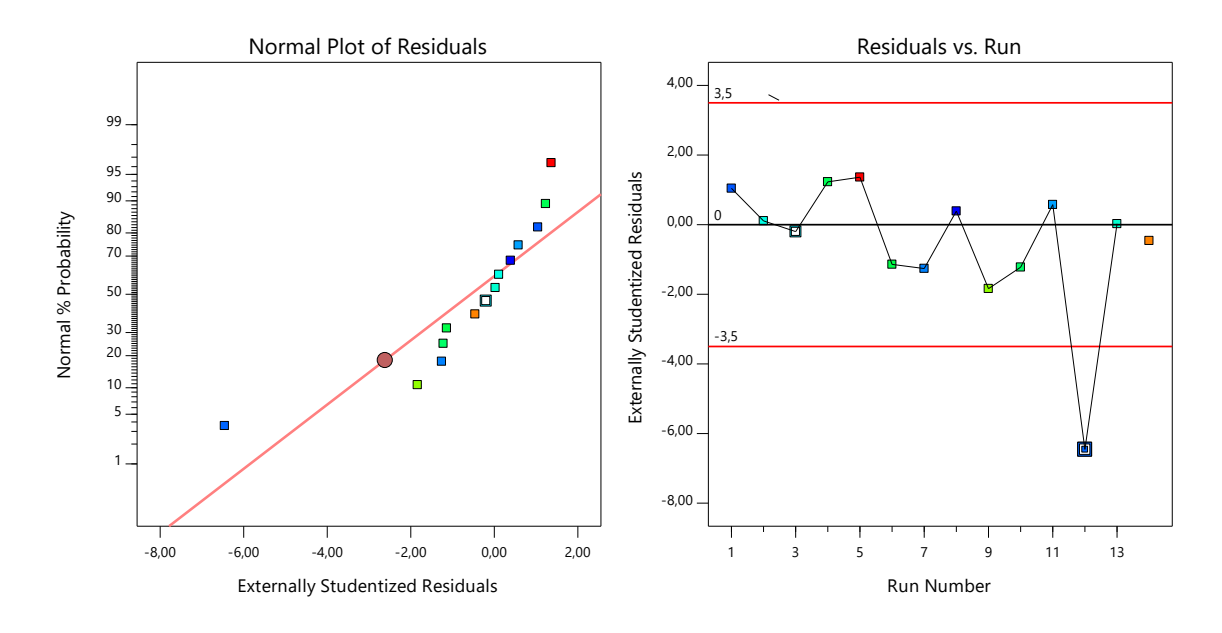


Figure 4-49: Normal Plot of Residuals (left) and Residuals vs. Run (right) for 5-Fd-TP **7**. Created with DesignExpert (version 11).

However, as illustrated in Figure 4-50 on the right-hand side, the data point was not particularly noteworthy in the predicted versus actual plot. Moving on the cook's distance plot and the leverage versus run plot, which are displayed in Figure 4-51, the flagged data point also stood out there. The data point presented an extremely high value for cook's distance (Figure 4-51, left), which indicated a highly influential point and underlined, that this data point was far from the remaining cases.

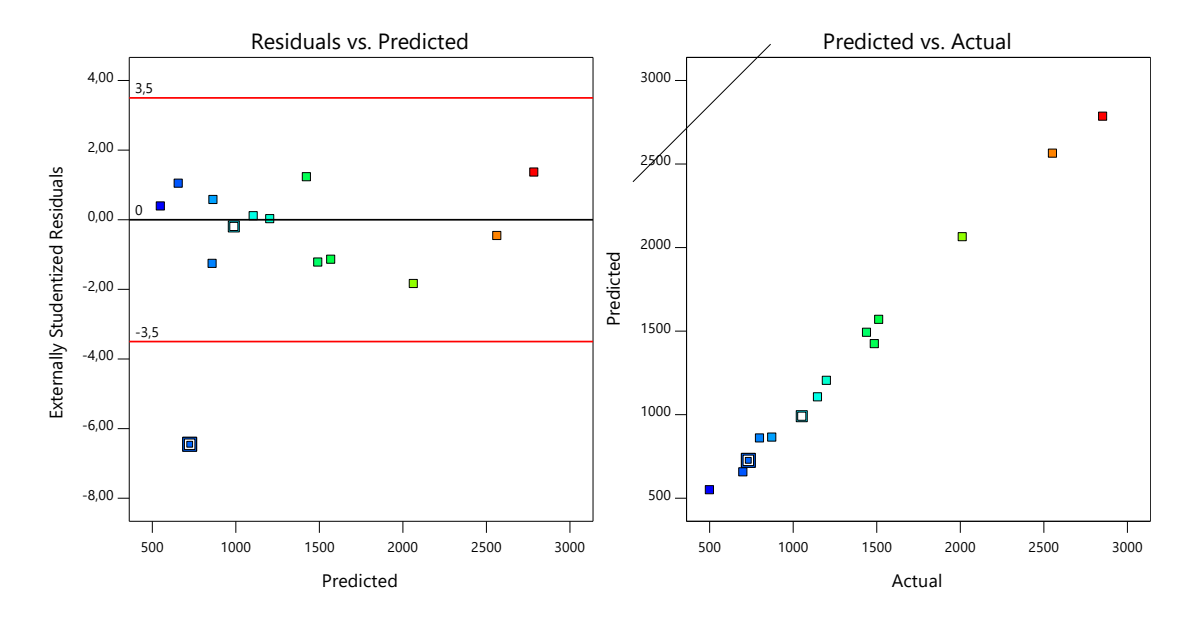


Figure 4-50: Residuals versus Predicted (left) and Predicted vs. Actual (right) for 5-FdU-TP **7**. Created with DesignExpert (version 11).

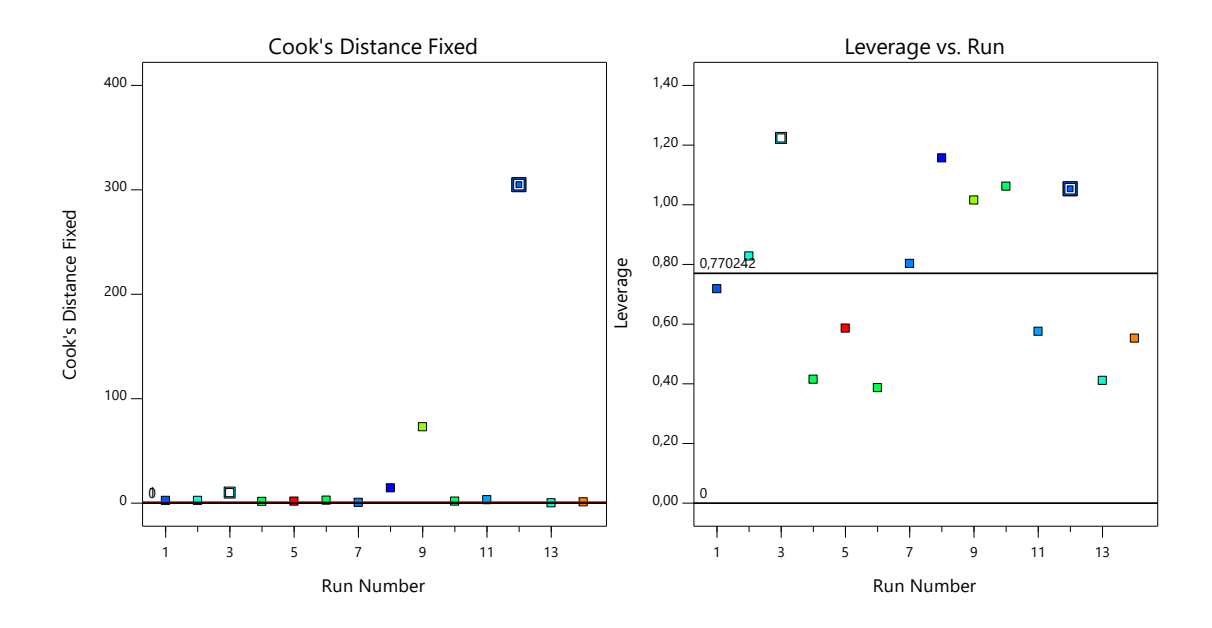


Figure 4-51: Cook's distance plot (left) and leverage versus run plot (right) for 5-FdU-TP **7**. Created in DesignExpert (version 11).

The summation of these visual inspections of all scatter plots led to the decision to exclude the data point from the analysis of 5-FdU-TP **7** as the multitude of diagnostic tools suggested that there was some sort of error, which in turn invalidated the model. Therefore, as already indicated in Table 4-9, one value of the 5-FdU-TP **7** was ignored, and the design matrix was re-analyzed. After the elimination of the outlier, the optimal model for 5-FdU-TP **7** was also reduced quadratic, excluding the terms for column temperature (a). This was already summarized in Table 4-11. The diagnostic scatter plots of the re-analysis can also be found in Supplementary data (Figure 7-11 to Figure 7-13).

After validation of every chosen model, the results of the design matrix for every analyte can be illustrated using different graphs. By plotting the response of every analyte against the combinations of numeric factors, the relationship between this response and the different factors is illustrated. These specific two-dimensional contour plots are displayed in Figure 4-52 for every analyte. The program shows the design space with graduated color shading. The response, which is the peak intensity of the analyte, is a function of the factor (B) pH value of A (x axis) and (C) the additive concentration (y axis). It is displayed as black lines in the contour plot. The factor (a), the column temperature, could not be displayed but could be varied in the software.

Given that the column temperature was not a significant term, it exerted no influence on the contour plot. As indicated by the curved lines, the model of the responses of FdU 10, FdU-DP 8 and FdU-TP 7 were quadratic and the model of the response of FdU-MP 9 was linear. The red points represent the actual points that were determined by executing the experiments from the design matrix. The design space surrounding these points is defined as the predicted response, which is determined by the program based on the selected model. Blue colors indicated low values, while red colors indicated high values for the responses. It was evident from the visual examination of the contour plots that the maximum values of the response for each analyte were predicted to occur at a low pH value of the mobile phase A and a low additive concentration in the mobile phase.

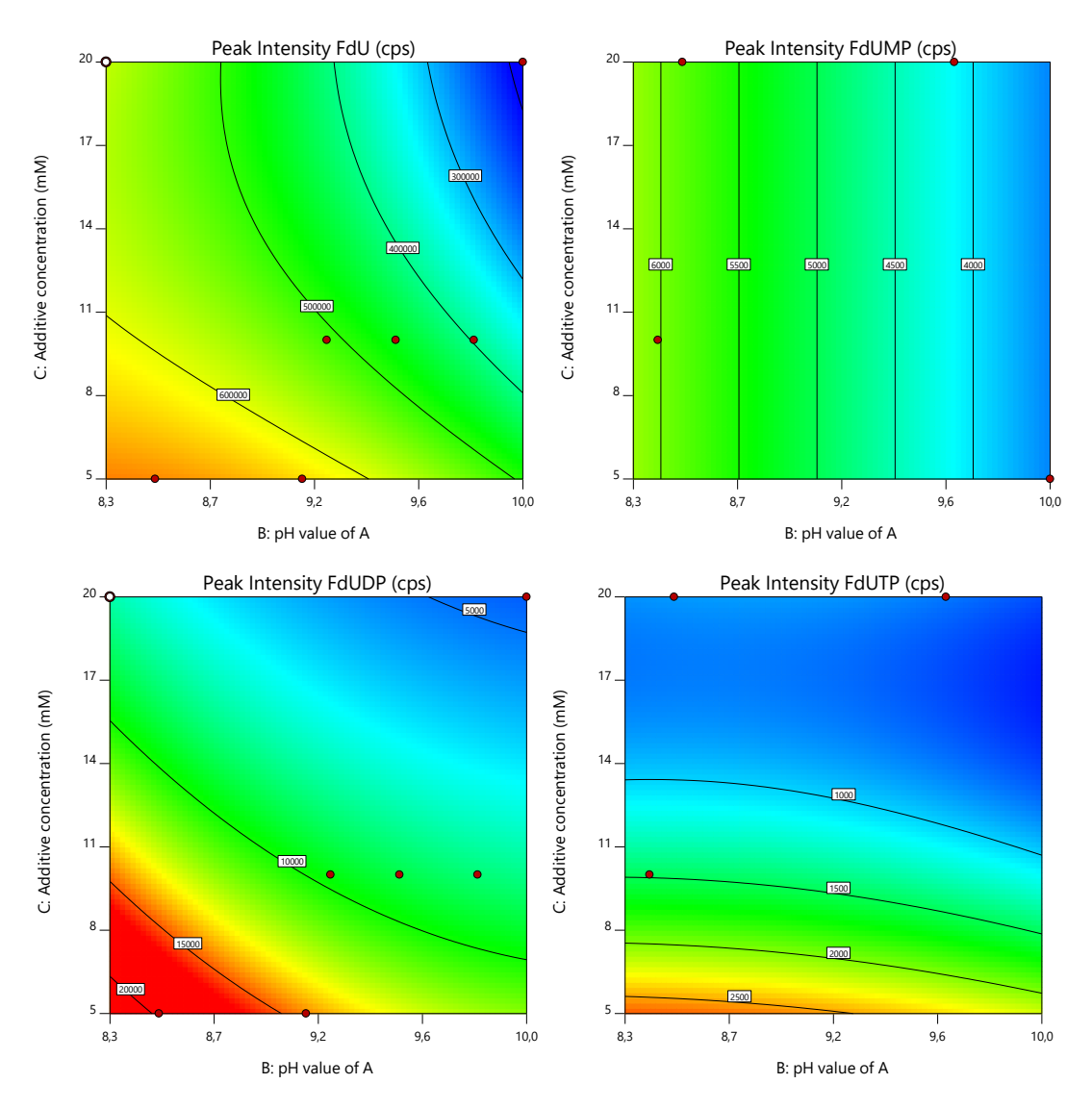


Figure 4-52: Two-dimensional contour plots for every analyte.

For a better representation of the optimal conditions, three-dimensional surface plots were generated for each analyte. The graphs are displayed in Figure 4-53. Again, the peak intensity as a response was plotted as a function of factor (B), pH value and factor (C), additive concentration. The surface is therefore one "slice" of the factor (a), column temperature. However, as already mentioned, the column temperature was not identified as a significant term and therefore did not influence the predicted design space. The three-dimensional surface plots were ideal to explore the interaction between the factors (B) and (C) and their resulting response. For these graphs, the maximum peak intensity was also indicated by a red color code. To complete the DoE, a numerical optimization was carried out with the goal of maximizing the responses of every analyte.

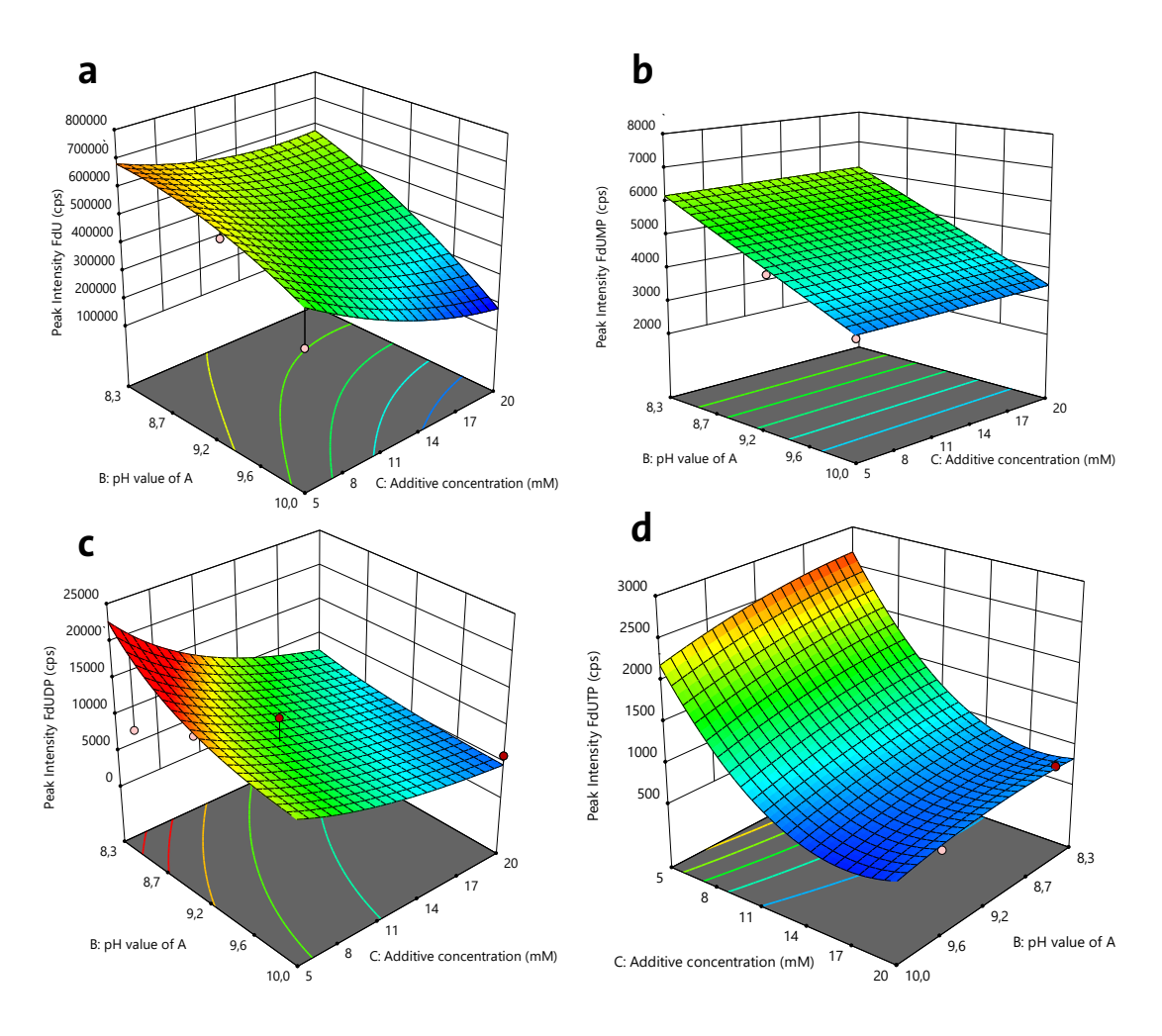


Figure 4-53: Three-dimensional surface plots for a: FdU 10, b: FdU-MP 9, c: FdU-DP 8 and d: FdU-TP 7.

For every possible solution to achieve the goal, the software program created ramps to visualize the best factor settings and also the desirability of the predicted responses. These ramps view of the best solution with the highest desirability value is displayed in Figure 4-54. The experimental design indicated that all factors should take the lowest possible values within their tested range in order to obtain the best possible response for each analyte.

Based on this optimization, it was decided to design a HPLC method with an operating column temperature of 25 °C, which was lower than the DoE determined. The choice was made based on the experience of decomposition of the NH₄HCO₃ buffer at higher temperatures. Also, the DoE indicated that the column temperature exhibited no impact on the peak intensity.

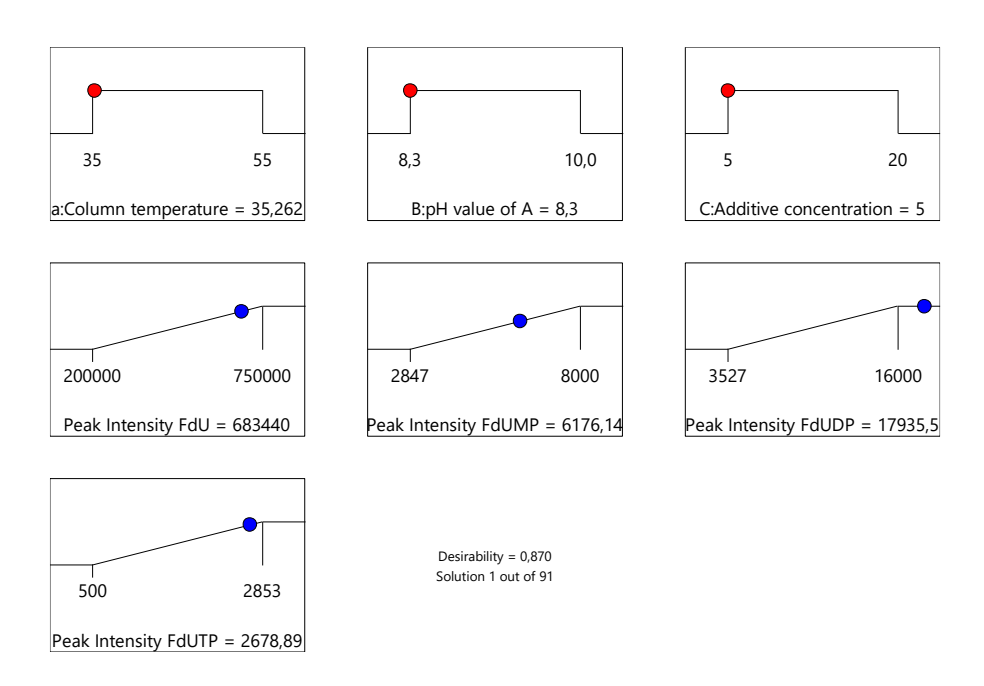


Figure 4-54: Numerical optimization ramps view for a possible solution. Created in DesignExpert (version 11).

The pH value of the NH₄HCO₃ buffer for mobile phase A was adjusted to 8.3 and the additive concentration was set to 5 mM. Furthermore, an effective solution was identified for the problem of the solubility of NH₄HCO₃ in acetonitrile. Rather than adding the buffer to both mobile phase A and B, it was decided to design a ternary gradient, where mobile phase A consisted of an NH₄HCO₃ buffer with a concentration of 100 mM, which was constantly delivered at a rate of 5 %. Eluent B

and C were acetonitrile and water, respectively, which were utilized to execute the gradient elution while maintaining a constant 5 mM concentration on the column throughout the duration of the run. The optimized HPLC gradient is displayed in Table 4-12. The optimized LC method was tested on all analytes. At this point, almost all analytes were available for MS tuning and incorporation into the MS method. Therefore, the chromatogram shows the EICs of the FdU 10, the FdU-MP 9, FdU-DP 8, FdU-TP 7, the C8-AB monomasked FdU-TP 5, and the TriPPPro-compounds 1 and 2. The MRM method also included UMP 34 and UTP 35 as potential standards. Only the monomasked [C11AB]-FdU-TP 6 was still not incorporated in the method as this time.

Table 4-12: Optimized ternary HPLC gradient. Eluent A consisted of a 100 mM NH₄HCO₃ buffer with a pH value adjusted to 8.3, eluent B and eluent C are pure acetonitrile and water, respectively.

Time [min]	Eluent A [%]	Eluent B [%]	Eluent C [%]
0	5	95	0
5	5	95	0
25	5	50	45
27	5	50	45
27.5	5	95	0
36	5	95	0

The chromatogram is displayed in Figure 4-55. All analytes included in the method showed a retention time, were baseline separated and peak shape as well as peak intensities were acceptable. Overall, the result was extremely satisfactory. The designed HPLC method was capable of simultaneously retaining both lipophilic prodrugs, their intermediates and also all resulting polar metabolites in a single HPLC run. As seen in the chromatogram in Figure 4-55, no compound did elute after 22 minutes. However, it was decided to purge the column to 45 % of acetonitrile, as the cell lysate contains a large number of naturally occurring nucleotides, which will be also extracted from the cell pellet and elute.

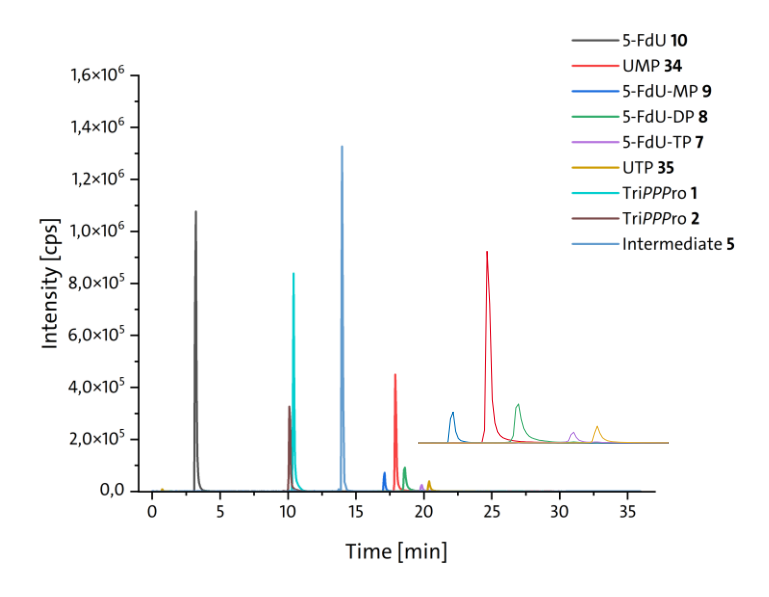


Figure 4-55: EICs of all analytes displayed with the optimized HPLC method (analyte concentration: 500 ng/mL in acetonitrile/water 95:5 % v/v, 5 μ L injection).

They were not detected due to the filtering of defined mass transitions within the MRM method, but the compounds still have to be completely eluted from the column. The last 8.5 minutes of the gradient were used to re-equilibrate the column to the starting conditions of the gradient for the next measurement. Given the column volume of 0.25 mL and the flow rate of 0.3 mL/min, the column reequilibration took approximately 10 column volumes. This is reasonable for HILIC as the water-enriched layer needs to be stabilized again for the next measurement.

4.4.3 Optimization using FIA

After the optimization of the HPLC method with establishment of the ternary gradient on the amide column, the MS parameters of the MRM method were adjusted to the LC method. The peak intensity was already optimized to a certain extent via DoE. The aim, however, is to achieve the lowest possible detection limits and to further improve the intensity of the signals, it is useful to optimize the ionization parameters. The ionization yield is influenced by the ionization parameters and thus directly affects the intensity of the detected mass transitions

of the individual analytes. The source parameters and substance specific parameters for the precursor and product ions were optimized at the beginning of the measurement. However, during the initial tuning the sample was injected directly into the mass spectrometer using a syringe pump as already described in chapter 4.2. With this initial MS tuning, the influence of the HPLC flow rate and solvent composition were not considered. Therefore, the source parameters of the spectrometer as well as the compound specific parameters were optimized using FIA. The optimized source parameters include curtain gas (CUR), temperature (TEM), ion source gas 1 and 2 (GS1 and 2) and ion spray voltage (IS). The substance-specific parameters include the declustering potential (DP), the collision energy (CE) and the collision cell exit potential (CXP). The values for these parameters were varied one factor in each chromatographic run and the settings at which the intensity of the individual mass transitions is highest were determined. The optimized parameters were then used to create an improved MRM method. Some major differences in source and substance specific parameters compared to the original values were found for all analytes. The optimized source parameters are displayed in Table 4-13.

Table 4-13: Optimized source parameters for the MRM method. CUR = curtain gas, TEM = temperature, GS = ion source gas, IS = ion spray voltage, au = arbitrary unit

Parameter	Value
CUR	20 au
TEM	700 °C
GS 1	60 au
GS 2	70 au
IS	-4000 V

The substance specific parameters for every mass transition are displayed in Table 4-14. The entrance potential (EP) and the dwell time were not optimized but default values were used due to time constraints.

Table 4-14: Optimized substance specific parameters for every mass transition. DP = declustering potential, EP = entrance potential, CE = collision energy, CXP = collision exit potential.

Compound	Mass transition	Precursor ion (Da)	Product ion (Da)	DP (V)	EP (V)	CE (V)	CXP (V)	Dwell time (msec)
5-FdU 10	Quantifier	244.9	155.0	- 80.00	- 10.0	- 20.00	- 30.0	150.0
5-Fu0 10	Qualifier	244.9	128.8	- 100.0	- 10.0	- 20.00	- 30.0	150.0
Tri <i>PPP</i> ro-	Quantifier	977.1	386.9	-200.0	- 10.0	- 40.00	- 10.0	150.0
compound 1	Qualifier	977.1	256.9	-200.0	- 10.0	- 60.00	- 10.0	150.0
Tri <i>PPP</i> ro-	Quantifier	1061.1	256.7	- 60.00	- 10.0	- 60.00	- 5.00	150.0
compound 2	Qualifier	1061.1	387.0	- 60.00	- 10.0	- 60.00	- 20.0	150.0
Inter-	Quantifier	731.0	78.9	- 80.00	- 10.0	- 100.0	- 10.0	150.0
mediate 5	Qualifier	731.0	404.8	- 80.00	- 10.0	- 40.00	- 10.0	150.0
FdU-MP 9	Quantifier	324.9	194.9	- 120.0	- 10.0	- 20.00	- 20.0	150.0
FUU-IMP 9	Qualifier	324.9	128.9	- 150.0	- 10.0	- 40.00	- 20.0	150.0
באון הה פ	Quantifier	404.9	78.8	- 120.0	- 10.0	- 100.0	- 15.0	150.0
FdU-DP 8	Qualifier	404.9	274.9	- 120.0	- 10.0	- 20.00	- 5.00	150.0
CALL TO 7	Quantifier	484.9	78.9	- 100.0	- 10.0	- 100.0	- 10.0	150.0
FdU-TP 7	Qualifier	484.9	158.9	- 180.0	- 10.0	- 60.00	- 20.0	150.0

4.4.4 Evaluation of calibration curves in solvent

After initial MS tuning, chromatographic development and MS optimization, the next key step in LC-MS/MS method development was the evaluation of the linearity and sensitivity. As already explained in subsection 4.3.1, calibration curves with at least 6 non-zero CS samples were constructed and measured in duplicate to check for the linear range of every analyte. This was performed in solvent as a model system. Starting with the development of a mixed-mode gradient, the sample preparation was in highly aqueous solutions leading to decomposition of the prodrugs and therefore to calibration curves of the duplicates with very high values for the %CV. Using the established HILIC method, sample preparation was carried out with high acetonitrile content. Calibration curves were constructed for FdU 10, FdU-MP 9, FdU-DP 8, FdU-TP 7, TriPPPro-compounds 1 and 2, as well as intermediate 5. For intermediate 6, there was still no data available since it could not be incorporated into the MRM method as this point. As an example, calibration curves are discussed in detail for FdU-MP and TriPPPro-compound 2. Table 4-15

summarizes the 6 non-zero CS samples for FdU-MP **9**, including the concentration in ng/mL, the determined analyte peak areas in duplicate, their mean value as well as the corresponding %CV. CS samples were prepared in acetonitrile/water (95:5 % v/v) to test linearity.

Table 4-15: CS samples for FdU-MP **9**, including corresponding concentrations in ng/mL, integrated peak areas of the duplicates (analyte peak area 1 and 2) including the resulting mean and the %CV.

Concentration	Analyte Peak	Analyte Peak	Mean Analyte Peak	%CV
[ng/mL]	Area 1 [counts]	Area 2 [counts]	Area [counts]	%CV
10	1.64E+04	1.56E+04	1.60E+04	2.5
90	5.68E+05	5.78E+05	5.73E+05	0.9
170	1.21E+06	1.20E+06	1.21E+06	0.4
250	1.53E+06	1.50E+06	1.52E+06	1.0
330	2.10E+06	1.92E+06	2.01E+06	4.5
500	3.11E+06	3.21E+06	3.16E+06	1.6

The use of pure solvent was serving as a model system since blank matrix exhibited limited availability. In comparison to the CS samples that were constructed for the measurements with the mixed-mode column, these samples demonstrated very low %CV values.

Based on these CS samples, regression analysis was performed by constructing a calibration curve. An important thing that should be considered when constructing calibration curves with the method of least squares is weighting. The simple least squares regression method is based on assigning equal weight to all points, which is not appropriate when some data points are much less accurate than others, for example, due to decreased S/N ratio. The solution to this issue is to employ weighted regression, which considers the variability in the y values. With a weighting of 1/x, for example, data points with lower concentration values have less influence on the calibration curve. In addition to the evaluation of the calibration curve including the coefficient of determination R^2 , the resulting residuals should also be investigated. The residue is the difference between the observed value for y, the integrated peak

area, and the y value calculated using the equation of the fitted line. This is illustrated in Figure 4-56 as an example. The values used for this plot were hypothetical to demonstrate the origin of the residual plot. The ideal residual plot is one that is randomly scattered around zero, and there should be no trend in the spread of residuals with concentration, such as curved responses or increasing standard deviations with increasing concentration. Therefore, the use of residual plots is ideal to evaluate obtained calibration curves.

The calibration curve including linear regression equation and coefficient of determination R^2 for 5-FdU-MP **9** and the corresponding residual plot for the weighted linear regression are displayed in Figure 4-57. The data from Table 4-15 was weighted with 1/x. The calibration curve demonstrated a high value for R^2 , which was considered satisfactory. However, it is important to note that a high value for the coefficient of determination and the investigation of the residual plot should not be the only criteria for assessing linearity.

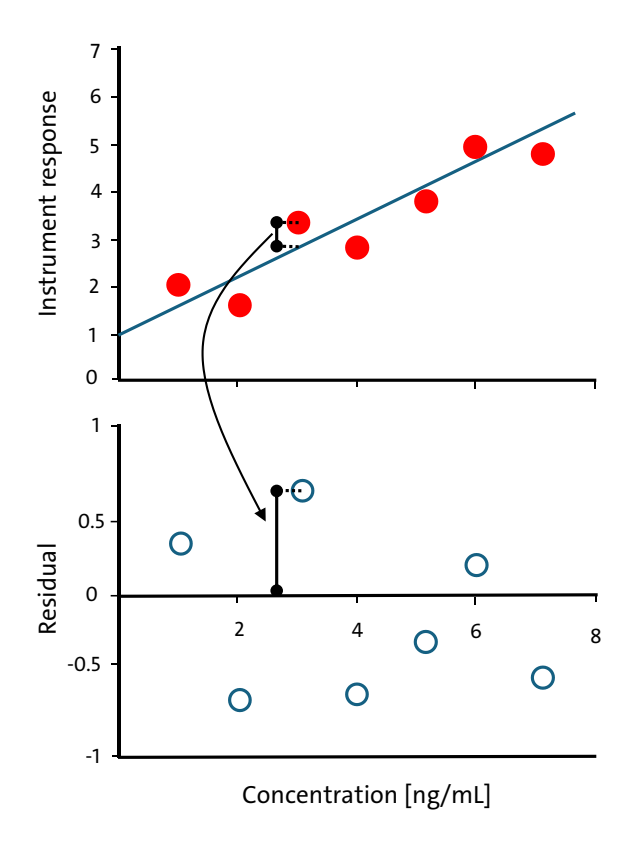


Figure 4-56: Construction of a residual plot for the investigation of calibration data. Values were hypothetical.

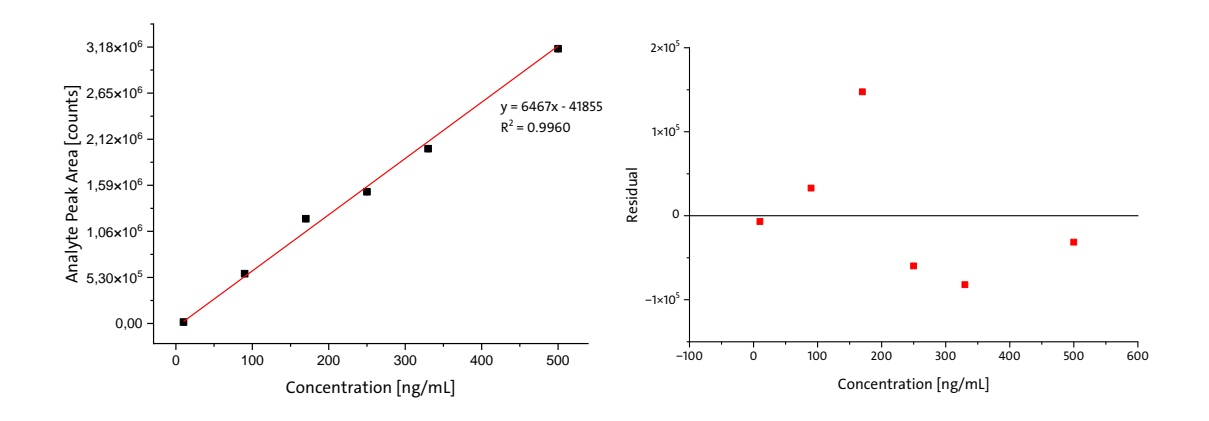


Figure 4-57: Calibration curve of 5-FdU-MP **9** using the method of least weighted squares (1/x weighting, left) and corresponding residual plot (right).

Instead, a back-calculation was performed for each CS sample and the difference between the nominal (theoretical) and calculated concentration was assessed. The back-calculation was conducted by utilizing the established linear regression of the calibration curve. Employing the analyte peak area y, the equation was solved for the concentration x. The FDA determined that the CS samples should be ±15 % of the nominal concentration, except the lowest CS sample, which should be ±20 % of the nominal concentration. In addition, at least 75 % and a minimum of 6 non-zero CS samples should meet the abovementioned criteria. [164] The results of the back-calculation for 5-FdU-MP **9** are displayed in Table 4-16. It was demonstrated that all six non-zero calibration samples met the criteria indicated by the table entry "true".

Table 4-16: Assessment of the quality of the calibration curve using back-calculation for FdU-MP **9** with 6 non-zero CS samples. Linear regression was done using the method of least weighted squares (1/x).

Concentration x [ng/mL]	Mean Analyte Peak Area y [counts]	Calculated x [ng/mL]	Accuracy [%]	Deviation [%]	Requirement fulfilled?
10	1.60E+04	8.95	89	11	True
90	5.73E+05	95.08	106	6	True
170	1.21E+06	192.81	113	13	True
250	1.52E+06	240.75	96	4	True
330	2.01E+06	317.29	96	4	True
500	3.16E+06	495.12	99	1	True

The second example to be discussed concerns the results for TriPPPro-compound 2. In particular, the prodrugs presented a challenge when assessing linearity with the mixed-mode column due to their low stability in highly aqueous solutions. In this case, the samples were also prepared in acetonitrile/water (95:5 % v/v) as model system. The 6 non-zero CS samples for TriPPPro-compound 2 are summarized in Table 4-17 including their concentrations in ng/mL, the integrated analyte peak areas in duplicate, their mean value and the value for CV in percent. As expected, the prodrug exhibited a higher stability in a non-nucleophilic solvent and the duplicate measurements only deviated between 0.4 to 7.9 %. This was a highly desirable outcome.

Table 4-17: CS samples for Tri*PPP*ro-compound **2**, including corresponding concentrations in ng/mL, integrated peak areas of the duplicates including the resulting mean and the %CV.

Concentration	Analyte Peak	Analyte Peak	Mean Analyte Peak	9/6\/
[ng/mL]	Area 1 [counts]	Area 2 [counts]	Area [counts]	%CV
10.0	6.24E+04	7.29E+04	6.77E+04	7.8
90.0	1.56E+06	1.73E+06	1.65E+06	5.2
170	3.28E+06	2.80E+06	3.04E+06	7.9
250	3.83E+06	3.86E+06	3.85E+06	0.4
330	5.11E+06	5.26E+06	5.19E+06	1.4
500	7.32E+06	6.86E+06	7.09E+06	3.2

On basis of the CS samples, a calibration curve for the prodrug was constructed using the method of least squares and the corresponding residual plot was investigated. The results are displayed in Figure 4-58. With the exception of the lowest CS sample, the calibration curve was linear with a coefficient of determination of 0.9877. The residual plot displayed a random scatter, which was satisfactory.

Back-calculations were also performed on the basis of the linear regression equation and displayed in Table 4-18. Almost all CS samples met the criteria for accuracy, except for the lowest CS concentration, which was expected based on the calibration curve.

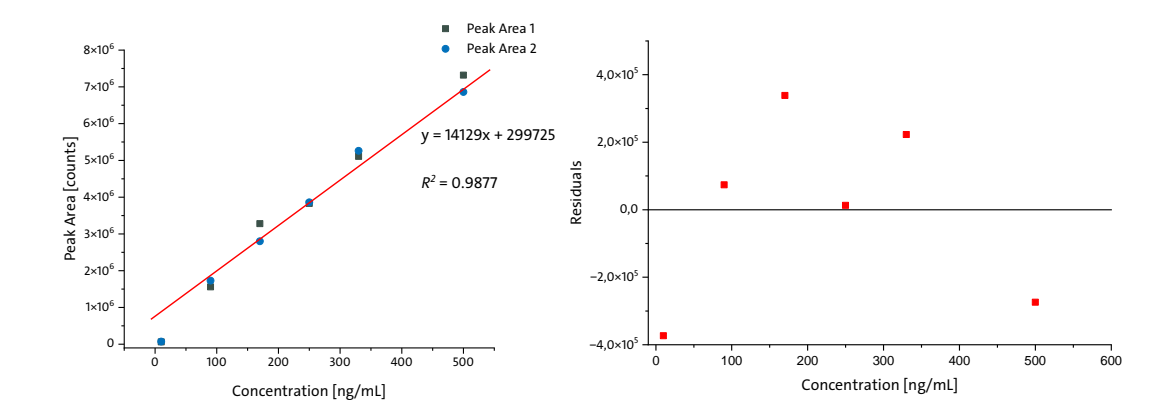


Figure 4-58: Calibration curve of Tri*PPP*ro-compound **2** using the method of least squares (left) and corresponding residual plot (right).

Table 4-18: Assessment of the quality of the calibration curve using back-calculation for Tri*PPP* rocompound **2** with 6 non-zero CS samples. Linear regression was done using the method of least squares.

Concentration x [ng/mL]	Mean Analyte Peak Area y [counts]	Calculated x [ng/mL]	Accuracy [%]	Deviation [%]	Requirement fulfilled?
10	6.77E+04	-16.4	-164	264	False
90	1.65E+06	95.2	106	6	True
170	3.04E+06	194	114	14	True
250	3.85E+06	251	100	0	True
330	5.19E+06	346	105	5	True
500	7.09E+06	481	96	4	True

Nevertheless, 83% of the CS samples fulfilled the criteria, indicating that the calibration curve was overall acceptable. It was investigated if a 1/x weighting could overcome the high deviation of the lowest CS sample, which was not the case. In this particular instance, the weighting led to a lower deviation for the lowest CS sample, which was expected using 1/x weighting. However, it also led to higher deviations for other CS samples. Consequently, the calibration data were invalid. Therefore, it should always be investigated whether weighing would be a possibility to improve the results. As demonstrated in Figure 4-58, the data for Tri*PPP*ro-compound 2, without weighting, exhibited very good results in terms of linearity. This finding

suggests the presence of a linear relationship within the specified concentration range, which was very promising.

4.5 Application to d4T derivatives and natural nucleotides

After the successful development and optimization of an HPLC-MS/MS method that was able to simultaneously elute and separate the lipophilic FdU-derived prodrugs and their corresponding polar metabolites, the method should be extended to other analytes. The second set of analytes of interest were the two different Tri*PPP*ro-compounds **3** and **4**, including all possible metabolites. The d4T-derivatives were already discussed in chapter 4.2, where all mass transitions were detected and summarized in a separated MRM method. The chemical structures of these analytes have previously been displayed in Figure 4-3 (p. 36). In addition to the d4T-derivatives as a new set of analytes for quantification, the method should also be tested for the application of natural nucleotides. The subsequent subsections will address these subjects.

4.5.1 HPLC-MRM method with d4T derivatives

Each analyte in the MRM method for the d4T derivatives was initially analyzed individually under established HILIC-MS/MS conditions. The amide column was used at 25 °C with a ternary gradient and NH₄HCO₃ buffer (pH 8.3). Analytes were prepared in acetonitrile/water (95:5 v/v) at 500 ng/mL. The EICs of the most intense transitions (quantifiers) are shown in Figure 4-59. All analytes showed acceptable retention times, though peak intensities varied significantly. Intermediate 11 and d4T-MP 15 exhibited low signal intensities, while d4T-DP 14 showed broad peak shape.

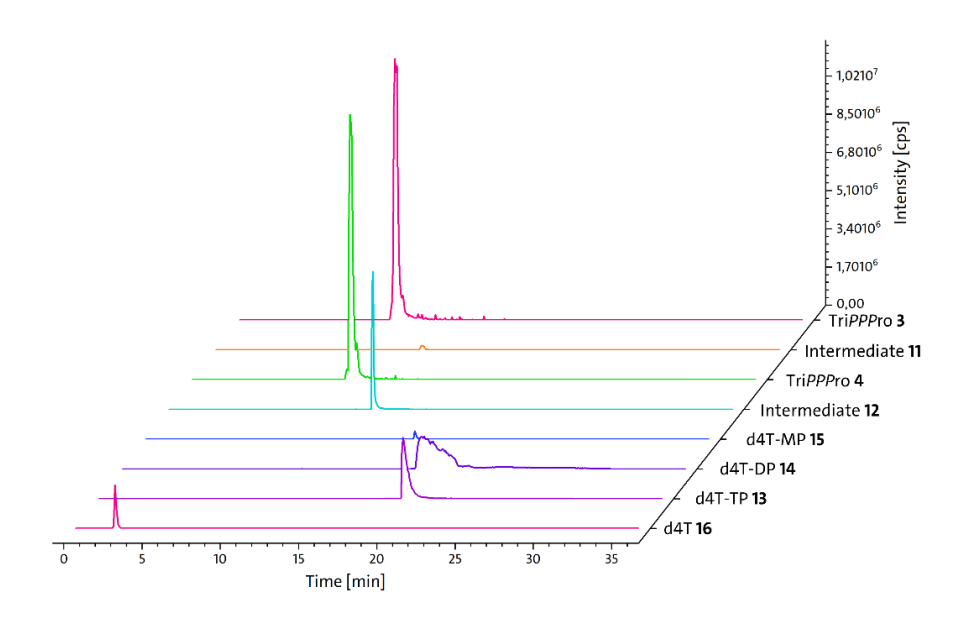


Figure 4-59: EICs of the tested d4T-derivatives including the two different Tri*PPP*ro-compounds 3 and 4 and their resulting metabolites with the established HILIC-MRM method (analyte concentration: 500 ng/mL in acetonitrile/water 95:5 % v/v, 5 μ L injection).

To further improve peak intensities, the source parameters of the MS as well as the substance specific parameters for every analyte were optimized using FIA. The results for the optimized source parameters are displayed in Table 4-19.

Table 4-19: Optimized source parameters for the MRM method. CUR = curtain gas, TEM = temperature, GS = ion source gas, IS = ion spray voltage, au = arbitrary unit

Parameter	Value
CUR	20 au
TEM	700 °C
GS 1	60 au
GS 2	60 au
IS	-4000 V

As illustrated in Table 4-20, the optimized substance-specific parameters for the quantifier and qualifier are displayed for each analyte. The default settings for the extraction process and the dwell time were utilized. After optimization, there was no need for further improvement of the method as all analytes were adequately retained and no sensitivity issues were observed.

Table 4-20: Optimized substance specific parameters for every mass transition. DP = declustering potential, EP = entrance potential, CE = collision energy, CXP = collision exit potential.

Compound	Mass transition	Precursor ion (Da)	Product ion (Da)	DP (V)	EP (V)	CE (V)	CXP (V)	Dwell time (msec)
d4T 16	Quantifier	223.0	125.0	- 60.00	- 10.0	- 20.00	- 10.0	150.0
	Qualifier	223.0	193.0	- 100.0	- 10.0	- 20.00	- 15.0	150.0
Tri <i>PPP</i> ro- compound 3	Quantifier	999.1	238.9	- 150.0	- 10.0	- 80.00	- 15.0	150.0
	Qualifier	999.1	78.9	- 180.0	- 10.0	- 100.00	- 10.0	150.0
Tri <i>PPP</i> ro- compound 4	Quantifier	889.2	365.0	- 180.00	- 10.0	- 40.00	- 20.00	150.0
	Qualifier	889.2	238.8	- 200.00	- 10.0	- 50.00	- 15.0	150.0
Inter- mediate 11	Quantifier	837.0	533.0	- 50.00	- 10.0	- 52.00	- 33.0	150.0
	Qualifier	837.0	78.9	- 50.00	- 10.0	- 134.0	- 33.0	150.0
Inter- mediate 12	Quantifier	699.0	383.0	- 200.0	- 10.0	- 38.00	- 10.0	150.0
	Qualifier	699.0	78.9	- 200.0	- 10.0	- 134.0	- 10.0	150.0
d4T-MP 15	Quantifier	303.0	79.0	- 80.0	- 10.0	- 60.00	- 5.00	150.0
	Qualifier	303.0	125.0	- 120.0	- 10.0	- 20.00	- 15.0	150.0
d4T-DP 14	Quantifier	382.9	78.9	- 100.0	- 10.0	- 80.00	- 15.0	150.0
	Qualifier	382.9	256.7	- 150.0	- 10.0	- 20.00	- 20.0	150.0
d4T-TP 13	Quantifier	462.9	78.9	- 180.0	- 10.0	- 100.0	- 10.0	150.0
	Qualifier	462.9	158.9	- 120.0	- 10.0	- 40.0	- 15.0	150.0

4.5.2 HPLC-MRM method with natural nucleotides

In addition to the second set of analytes, the method should also be tested for the application of natural nucleotides. The analysis of natural nucleotides remains a major challenge in the context of LC-MS/MS.^[69] Therefore, a few nucleotides including monophosphates, diphosphates and triphosphates were tuned as described in chapter 4.2 and incorporated into an MRM method. The mass transitions are displayed in Table 4-21. The subsequent measurements with the established method are displayed in Figure 4-60.

Table 4-21: Determined mass transitions after the initial tuning for the MRM method for the analysis of natural nucleotides including precursor ions (Q1 mass) and product ions (Q3 mass).

Compound	Q1 mass [Da]	Q3 mass [Da]
		78.9
AMP 36	345.9	96.9
		134.0
		79.0
ADP 37	425.8	134.1
		158.7
	505.9	78.9
ATP 38		158.8
		408.1
		78.9
CMP 39	322.0	96.9
		138.9
		78.9
CTP 40	481.6	158.9
		384.0
		79.0
GMP 41	361.9	66.1
		63.1
		78.9
GDP 42	441.9	158.9
		150.0
		78.9
GTP 43	521.8	158.9
		424.0
		78.9
UDP 44	402.9	158.9
		111.0

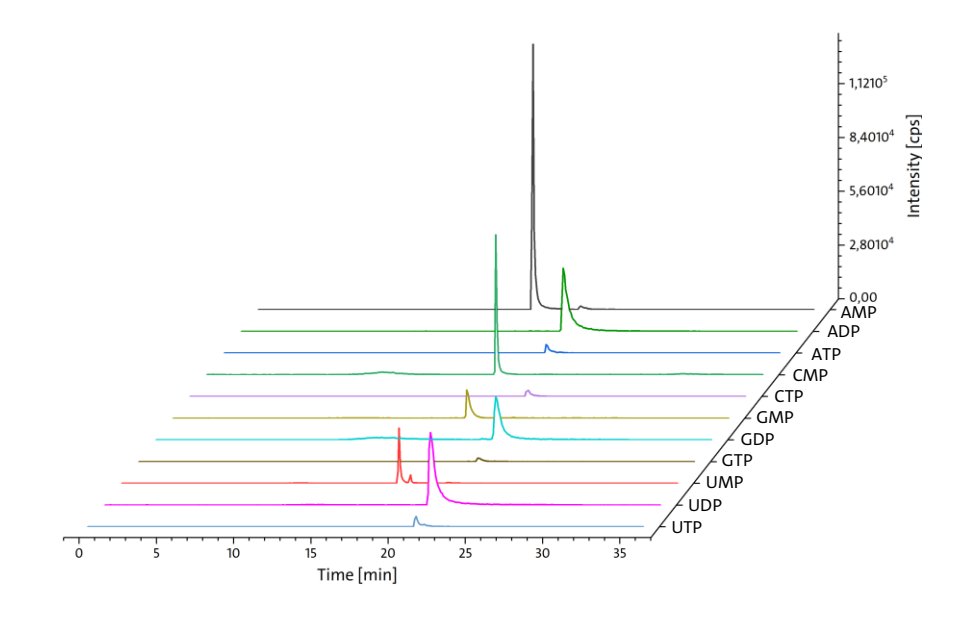


Figure 4-60: EICs of the tested natural nucleotides with the established HILIC-MRM method (analyte concentration: 500 ng/mL in acetonitrile/water 95:5 % v/v, 5 μ L injection).

Figure 4-60 shows the EICs of the mass transitions with the highest peak intensity. All monophosphates exhibited very good peak shapes and high signal intensities. All diphosphates exhibited acceptable results, although there was some peak tailing. All triphosphates showed very low peak intensities, which was already observed with 5-FdU-TP. Nevertheless, they were still detectable, and no peak was so broad that it could not be analyzed.

To summarize, the established HILIC-MS/MS method was successfully adapted for use with d4T derivatives, allowing the separation of lipophilic prodrugs and their polar metabolites. In a preliminary trial, the method was also employed for the analysis of natural nucleotides.

The next key step in the development and optimization of an HPLC-MS/MS method was the extraction procedure of the compounds from the biological matrix (s. Figure 4-1, p. 34). Following the establishment of the HILIC-MRM method, it was necessary to develop a method for sample preparation for the different samples obtained after cellular uptake studies.

4.6 Establishment of a sample preparation method

Cellular uptake studies with HT29 and SW620 cells were performed at the Center for Experimental Medicine at Institute of Anatomy and Experimental Morphology at University Medical Center Hamburg-Eppendorf by Maike Märker. Cellular uptake studies in CEM/O cells were performed at the Leibniz Institute of Virology in Hamburg by Tina Meyer. The establishment of the sample preparation method was achieved by employing blank matrices, wherein the cellular uptake study was conducted without the incubation of a compound, but with DMSO. The samples obtained comprised the incubation medium and the cells as a pellet. For both sample types, a sample preparation method was required that was appropriate for the

subsequent LC-MS/MS measurement. The preliminary tests were mainly carried out with HT29 mock-samples (incubation medium and cell pellets) and FdU-analytes.

Within our group, cellular uptake studies have been carried out on numerous occasions using the already mentioned fluorescently modified compounds, ddBCNA's (s. subsection 2.2.2). These studies aimed to detect prodrugs and metabolites in RPIP-FLD runs, confirming Tri*PPP*ro uptake and active metabolite release. Samples were prepared via protein precipitation (PPT) with methanol/water, cell pellets were sonicated and filtered.

It was tested to see if this protocol could simply be adapted as sample preparation method for the HILIC-MS/MS measurements. As a trial, an HT29 cancer cell pellet that was only incubated with DMSO as a mock-sample, was spiked with several FdU-analytes in known concentrations. Subsequently, the spiked cell pellet was suspended in a mixture of methanol and water (2:1, % v/v). The mixture was then left on ice for 10 minutes in order to allow the proteins to precipitate. Afterwards, the sample was centrifuged for 10 minutes and 100 μ L from the resulting supernatant were filtered through a syringe filter and transferred to a fresh vial. It was then subjected to the analysis. The workflow for the PPT is displayed in Figure 4-61.

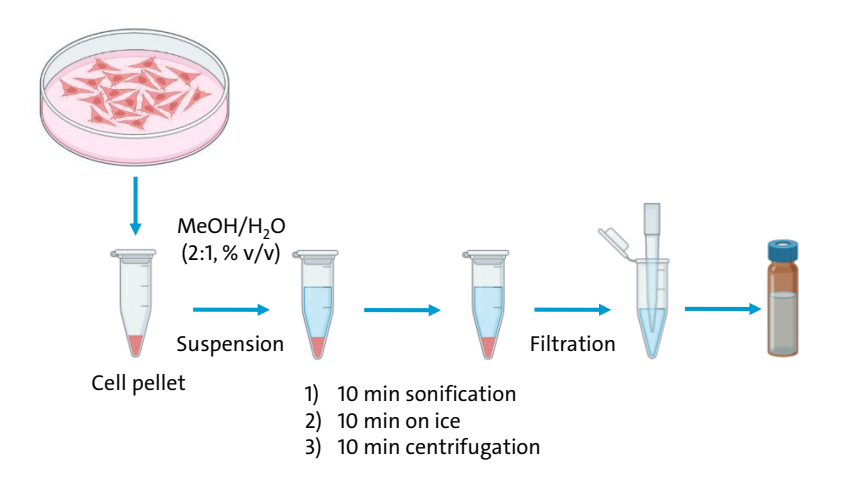


Figure 4-61: Workflow for sample preparation with a mock-sample of HT29 cells including cell lysis and subsequent protein precipitation (PPT) in a mixture of methanol and water (2:1 %v/v). Created with BioRender.

Unfortunately, the chromatogram obtained only displayed a signal for 5-FdU 10 and the TriPPPro-compound 1, all other signal intensities were greatly reduced. Also, the signal for TriPPPro-compound 1 appeared very broad. This was not the expected result since the spiked concentration of the analytes was 500 ng/mL which should lead to a good signal intensity. A reason for the low intensity could be nonspecific binding (NSB) of the analytes to the filter material (regenerated cellulose) of the syringe filter, which would lead to massive signal decrease. In order to investigate these findings, different analyte mixtures were measured in pure solvent as a model system given the limited amount of mock cell pellets available. A filtered and an unfiltered solution of all analytes were measured and compared as displayed in Figure 4-62. The upper chromatogram shows the filtered, the lower the unfiltered analyte mix. It was concluded that the use of syringe filters was suboptimal since some analytes were not detectable at all. Furthermore, the NSB proved to be nonreproducible, thus no correction factor could be used. Syringe filters can prove advantageous in the elimination of undesirable matrix components in a qualitative context; however, they do have a quantitative impact.

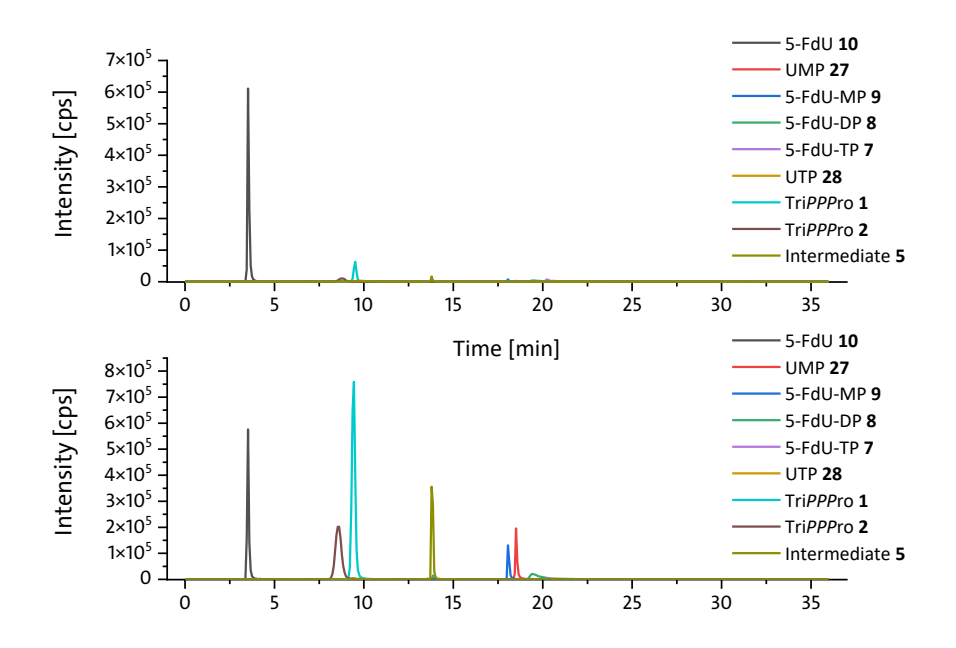


Figure 4-62: Upper chromatogram: EICs of all analytes after the use of a syringe filter, lower chromatogram: EICs of all analytes without the syringe filter (analyte concentration: 500 ng/mL in acetonitrile/water 95:5 % v/v, 5 μ L injection, triplicate measurement).

Another reason for analyte loss can be NSB as a result of adsorption of the analytes to inner surfaces of the used labware including the HPLC vials, tubings on the HPLC system or pipette tips.^[161] It is described in literature, that hydrophilic drugs can bind through electrostatic interaction to free silanol groups on glass surfaces and free phosphate groups interact with stainless steel. [161,183] To avoid NSB of all analytes, all metal capillaries on the HPLC system were exchanged for PEEK capillary tubings and instead of glass vials, polypropylene (PP) vials were used instead. In addition, the solvent composition employed for PPT was tested due to the observation of broad signals, a finding which could be indicative of a problem with the injection solvent. Therefore, an analyte mix was prepared in a mixture of methanol/water and directly measured. The resulting chromatogram is displayed in Figure 4-63. As displayed, most signals, especially in the first 10 minutes of the gradient elution showed retention time shift, peak broadening and peak splitting. This was an effect caused by the highly polar injection solvent, which was methanol and water. This does not align with the initial gradient of the HILIC method, which started with 95 % of acetonitrile. In literature, there are many examples that demonstrated the sensitivity of HILIC to parameters such as the composition of the injection solvent.

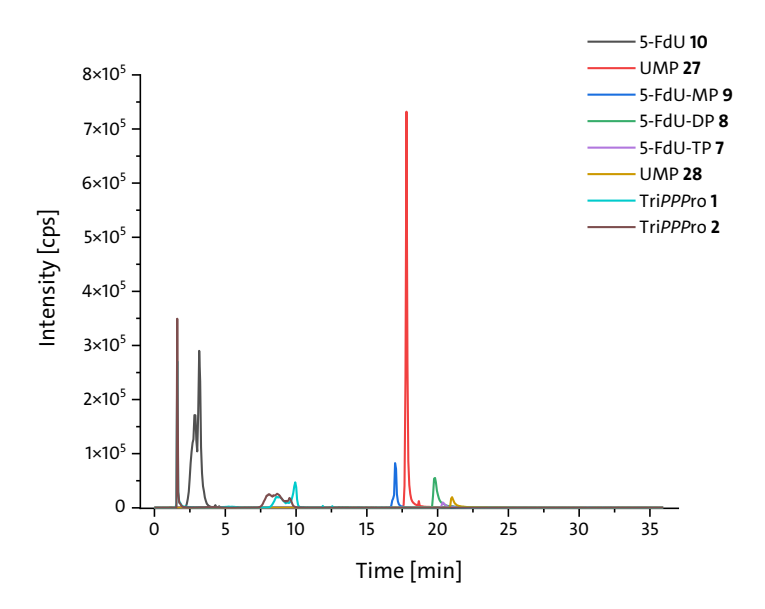


Figure 4-63: EICs of all analytes (analyte concentration 500 ng/mL in methanol/water 2:1 % v/v, 5 μ L injection).

The injection solvent exhibited elevated polarity, resulting in an initial elution force that was higher than the ideal, which caused a shift in the retention times of the analytes especially in the first minutes of the gradient. Peak splitting and tailing became prevalent, constituting undesirable outcomes. A similar distortion was also described in RP-C18 chromatography, when there are differences in solvent viscosity.

Consequently, an alternative sample preparation method compatible with the LC method and without the use of a filtration step was required. There are different strategies for sample preparation methods and purification of the biological matrix. The first method with minimum effort is to simply dilute the sample because unwanted matrix components will be diluted as well. This, however, is only possible with high concentrations of analyte present in the sample. The second method is the PPT, where a mixture of water and methanol or acetonitrile is used for precipitation. For a better clean-up, a liquid-liquid extraction (LLE) with a polar and a non-polar solvent is performed. The maximum effort is the performance of a solid phase extraction (SPE). SPE also involves method development as, in this case, the stationary phase needs to retain non-polar Tri*PPP*ro-compounds and polar nucleotides and nucleosides, while also separating potential interferences. Due to the time-consuming process, SPE was ruled out.

Instead, different modifications for PPT with cell pellets were to be tested. The first test involved the feasibility of PPT with acetonitrile instead of methanol and water (2:1, % v/v) and an additional dilution step with acetonitrile. The solvent composition in the end would be similar to the initial HILIC gradient and circumvent peak distortion.

To assess the quality of the sample preparation methods, different parameters were determined such as the absence or presence of matrix effects (ME), the recovery rate of the analytes (RE) and the overall process efficiency (PE). Therefore, the different sets were prepared, and the obtained absolute analyte peak areas were used for calculation. For set 1, the analytes were spiked onto the cell pellet before the sample

preparation process. For set 2, the analytes were spiked into the cell lysate after the sample preparation process. Set 3 were the obtained analyte peak areas in a neat solution (only solvent). According to Matuszewski *et al.*^[184], the ME, RE and PE can be calculated using following equations:

ME [%] =
$$\frac{\text{Set 2}}{\text{Set 3}} \cdot 100$$

RE [%] =
$$\frac{\text{Set 1}}{\text{Set 2}} \cdot 100$$

PE [%] =
$$\frac{(ME \cdot RE)}{100}$$

where:

ME is the matrix effect

RE is the recovery rate

PE is the process efficiency

Set 1 is the pre-spike set of analytes

Set 2 is the post-spike set of analytes

Set 3 is the neat blank set of analytes.

Set 1 and 2 were prepared using mock-samples of HT29 cancer cell pellets and performing a PPT using acetonitrile and water (2:1, % v/v) with an additional dilution step (1:10) in the end with acetonitrile. Set 3 only contained solvent and the analytes. The workflow is displayed in Figure 4-64. All samples were measured in triplicate with two different levels of concentrations (high: 312 ng/mL, low: 3.12 ng/mL). After the centrifugation step, $100~\mu L$ of the supernatant were transferred into a fresh microtube for the subsequent dilution with pure acetonitrile. A colorless precipitate was observed while the mixture was vortexed for set 1 and set 2. Therefore, it was decided to include a second centrifugation step for 60 seconds before transferring the mixture into the HPLC vial.

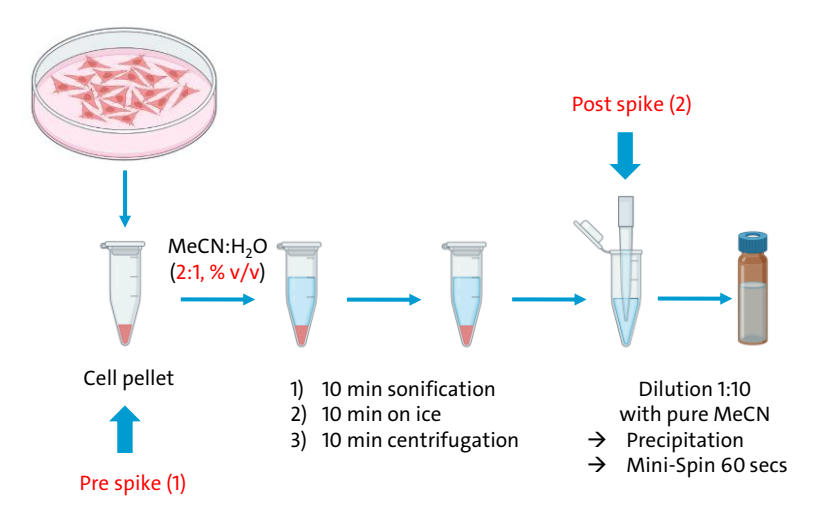


Figure 4-64: Workflow for sample preparation with a mock-sample of HT29 cells including cell lysis and subsequent PPT in a mixture of acetonitrile and water (2:1 %v/v). Created with BioRender.

The results for ME, RE and PE are displayed in Table 4-22. It should be noted that no data was available for intermediate **6** at that time. The ME, as calculated using equation 3, displays the absolute ME. A value above 100 % indicates signal enhancement, whereas a value below 100 % indicates signal suppression through matrix components.^[184] The ideal absolute ME would be 100 %. It is important to note that ME do not necessarily need to be eliminated.

Table 4-22: Tested PPT procedure with determination of matrix effects (ME, recovery rates (RE) and process efficiency (PE).

Analyte,	ME [%]	RE [%]	PE [%]
concentration level			
5-FdU 10 , high	123	112	138
5-FdU 10 , low	222	75	172
Tri <i>PPP</i> ro-compound 1 , high	90	47	43
Tri <i>PPP</i> ro-compound 1 , low	217	22	49
TriPPPro-compound 2, high	58	9.0	5.2
Tri <i>PPP</i> ro-compound 2 , low	463	2.7	13
Intermediate 5 , high	22	39	8.6
Intermediate 5 , low	64	82	52
5-FdU-MP 9 , high	9.0	457	41
5-FdU-MP 9 , low	15	248	37
5-FdU-DP 8 , high	_*	-	-
5-FdU-DP 8 , low	-	-	-
5-FdU-TP 7 , high	-	-	-
5-FdU-TP 7 , low	-	-	-

^{*} No data available.

For 5-FdU **10** a signal enhancement was found, with the lower concentration level showing a significantly higher signal enhancement. While both Tri*PPP*rocompounds displayed signal suppression at high concentrations, the signals were also enhanced significantly for low concentrations. For intermediate **5** and 5-FdU-MP **9** signal intensities were suppressed at both concentration levels. Overall, the calculated ME for 5-FdU **10** and also for Tri*PPP*ro-compound **1** with 123 % and 90 % respectively are acceptable values, while 22 % and 9 % for the intermediate and the monophosphate displayed severe ME.

For the RE, the ideal value would also be 100% indicating that all compound was extracted from the biological matrix. By comparing set 1 and set 2, the matrix effect has been taken into account as it could influence the ratio. The obtained RE for FdU 10 at both concentration levels were acceptable while especially Tri*PPP*rocompound 2 could be recovered very poorly (9.0% and 2.7%). This Tri*PPP*rocompound exhibited the longer alkyl chains and therefore higher lipophilicity compared to the other prodrug. A possible explanation for that could be that the prodrug-compounds, Tri*PPP*ro-compound 1 to a lesser extent, were also precipitated as a consequence of their long alkyl chains and lipid-like structure.

The RE values obtained for FdU-MP **9** were significantly elevated (457 % and 248 %), which can be attributed to a significant increase in the integrated peak areas of set 1 compared to set 2. As the pre-spike concentration of all analytes was increased by a factor of ten to match the concentration of the post-spike and neat-blank samples following the dilution step during the sample preparation, it was initially hypothesized that this dilution step could result in inaccurate recovery rates. However, for comparison, an analyte mix containing all compounds was spiked onto the cell pellet at the same concentration and processed simultaneously. Only FdU-MP **9** showed increased recovery rates. It is noteworthy that the effect observed at the elevated final concentration (5-FdU-MP **9**, high) was markedly stronger (457 %) compared to the effect seen with the lower concentration (5-FdU-MP **9**, low, 248 %). A similar trend was observed for the other analytes, with the exception of

intermediate $\bf 5$, although the magnitude of the effect was less pronounced. In order to exclude potential dilution errors, a concentrated FdU-MP working solution (5 μ g/mL) was subjected to a series of tenfold dilutions and evaluated against a calibration curve. The results were consistent and showed no anomalies.

PE considers both ME and RE. For example, the signal intensity of FdU **10** at a high concentration level was enhanced due to matrix effects and 112 % of the compound were recovered leading to an overall signal enhancement of 38 %.

Furthermore, it was observed that no signals were detected for FdU-TP **7** and FdU-DP **8** in set 1 and set 2. Consequently, the calculation of ME, RE and PE for these two analytes at both concentrations was not possible. While the analytes could be detected in the neat blank set, the analytes may have been degraded in the presence of cell lysate. A literature search revealed that human prostate cancer cells have elevated levels of alkaline phosphatase. The phosphatases could be responsible for the stepwise degradation of the triphosphate and also diphosphate. This effect could be even higher when the analytes were spiked onto the intact cell pellet during the sample preparation leading to increasing amounts of monophosphate in the prespike samples.

To overcome this problem, a phosphatase inhibitor (PI) cocktail was purchased with different components for the inhibition of enzymes especially in cell extracts. The cocktail contained sodium orthovanadate, sodium molybdate, sodium tartrate and imidazole. Gollnest observed the same phenomenon of degradation of the triphosphate and also used the PI to prevent the dephosphorylation process of d4T-TP in cell extracts. [52] Unfortunately, the results with the addition of 2 μ L of a mixture of two different cocktails (1:1, % v/v) were not satisfactory and the approach was not pursued further. In consideration of the microliters of inhibitor cocktail that were added, it is conceivable that the quantity was insufficient to have a significant inhibitory effect. According to the manufacturer, one mL of the cocktail inhibits phosphatase activity at a protein concentration of approximately 5 mg/mL.

Therefore, the protein concentration of the cancer cell lysates used in these studies were determined using a Bradford test (s. section 5.8) and are summarized in Table 4-23.

Table 4-23: Determined protein concentration via Bradford assay for the different cancer cell lysates with varying precipitation solvent mixtures (acetonitrile or methanol with water).

Sample (extraction solvent)	Protein concentration (μg/mL)
HT29 cell lysate (MeCN:H₂O)	415
HT29 cell lysate (MeOH:H₂O)	150
SW620 cell lysate (MeCN:H₂O)	160
SW620 cell lysate (MeOH:H₂O)	160

It was a surprising result that the solvent exchange from acetonitrile to methanol resulted in a large difference between the protein concentration of the HT29 cell lysate samples. When carrying out PPT with acetonitrile, the resulting protein concentration was 415 μ g/mL. In comparison to the precipitation with methanol, the measured protein concentration was only at 150 μ g/mL indicating that the precipitation could be more effective with methanol than with acetonitrile for HT29 cells.

For SW620 cell lysate, there was no difference between the solvents (both $160 \, \mu g/mL$). This led to the decision to use between $83 \, \mu L$ and $30 \, \mu L$ of PI depending on the cell line and solvent. Since methanol could be more effective for PPT when using HT29 cancer cells, it was decided to test the PPT with methanol and water as well as acetonitrile and water with subsequent dilution with acetonitrile. It was determined that the addition of acetonitrile at the end of sample preparation was an effective method of avoiding solvent mismatch and eliminating peak distortion. However, pure acetonitrile could not be used because it was observed that the PI cocktail precipitated. Therefore, it was decided to dilute with acetonitrile and water (95:5 % v/v) instead. No precipitation was observed anymore.

The determined values for ME RE and PE for the PPTs with either methanol and water or acetonitrile and water are summarized in Table 4-24. In general, it was possible to obtain signals for di- and triphosphate in both the pre- and post-spike sets.

Table 4-24: Tested PPT procedures with determination of ME, RE and PE with the use of phosphatase inhibitor (PI), no data available for the intermediate **6**.

Analyte	MeCN:H₂O with PI			MeOH:H₂O with PI			
	ME [%]	RE [%]	PE [%]	ME [%]	RE [%]	PE [%]	
5-FdU 10	138	68	94	111	290	323	
Tri <i>PPP</i> ro-compound 1	49	84	41	124	0.1	0.2	
Tri <i>PPP</i> ro-compound 2	50	13	6.7	111	0.0	0.0	
Intermediate 5	141	59	84	63	117	73	
5-FdU-MP 9	329	14	45	61	7.1	4.3	
5-FdU-DP 8	266	14	37	62	163	102	
5-FdU-TP 7	201	19	37	53	192	102	

ME were overall better with the use of methanol instead of acetonitrile. For the analytes within the first minutes of the HPLC gradient, a signal enhancement between 11% and 24% were determined. The analytes that eluted later from the column all exhibited signal suppression. With acetonitrile in the precipitation mixture, almost all signals exhibited of signal enhancement expect for the prodrugs. The prodrugs displayed severe ME with around 50% signal suppression. This could be due to endogenous phospholipids, which were not effectively removed. Phospholipids are structurally similar to the prodrugs and may cause suppressing problems. Also, for all unmasked analytes, FdU-MP, FdU-DP and FdU-TP, severe ME were detected either as signal enhancement (acetonitrile) or signal suppression (methanol). It could be assumed that during this specific retention time, all other intracellular compounds present with free phosphate groups will be co-eluting, thus interfering with the analyte ions present in the ESI source. Values for the RE were significantly poor for the prodrugs with methanol as precipitating solvent. It was already hypothesized that the lipophilic prodrugs might get precipitated as well due

to their lipid-like structure. Overall, PE was almost always better with acetonitrile as precipitating solvent (between 6.7 % and 94 %).

To identify if phospholipids were present in the sample and to which intensity, a mock-sample of HT29 was suspended with methanol and water for lysis and PPT. After subsequent dilution with acetonitrile, the sample was measured. To detect the phospholipids, known mass transitions published by Braun et al.[186] were used to build an MRM method in positive ionization mode. The transitions used for this method are displayed in Table 4-25. The EICs of the resulting measurement are displayed in Figure 4-65. It was evident that almost all of these phospholipids were present in the cell lysate sample. Especially the 16:0 18:2 phosphocholine (PC) with a signal intensity of about 4.3x10⁵ cps and the 16:0 PC with an intensity of about 7.0x10⁴ cps were predominant. 16:0 Lyso-PC, as well as 18:1 Lyso-PC and 18:0 Lyso-PC exhibited signal intensities between 1.1x10³ to 1.0x10⁴, which was not that severe. The signals of 18:0 PC and 20:0 PC were found to be negligible in comparison. However, all signals demonstrated retention times ranging from ten to twelve minutes, thus co-eluting with the TriPPPro-compounds. The mass transitions documented in the existing literature were exclusively in positive ionization mode. However, given the amphiphilic nature of the phospholipids, it was hypothesized that they would also ionize in negative ionization mode, thereby competing with the analyte ions from the prodrugs in the ESI source.

Table 4-25: Mass transitions for phospholipids in ESI positive ionization mode adapted from BRAUN *et al.*^[186]

Substance	Mass (Da)	Q1	Q3	DP (V)	CE (V)
16:0 Lyso-PC*	495.6	495.6	184.1	85	40
18:1 Lyso-PC	521.7	521.7	184.1	85	40
18:0 Lyso-PC	523.7	523.7	184.1	80	40
12:0 PC	621.8	621.8	184.1	90	40
16:0 PC	734.0	734.0	184.1	90	40
16:0 18:2 PC	758.1	758.1	184.1	100	40
16:0 18:1 PC	760.1	760.1	184.1	105	40
18:0 PC	790.1	790.1	184.1	100	40
20:0 PC	846.3	846.3	184.1	90	40

*PC: phosphocholine.

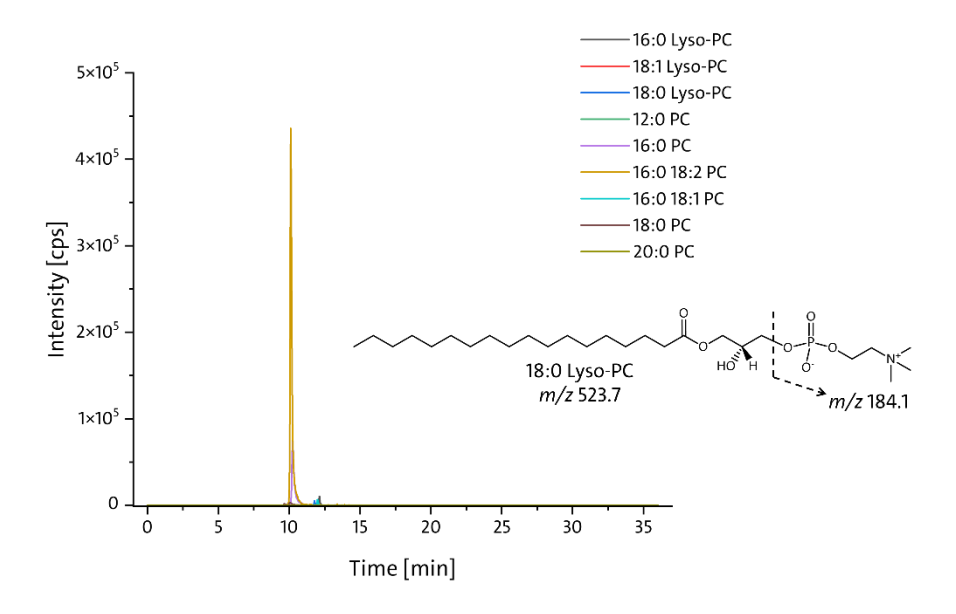


Figure 4-65: EICs of the tuned phospholipids after PPT and dilution of a mock-sample of a HT29 cell pellet. Displayed is the structure of 18:0 Lyso-PC as an example including the fragment ion with m/z 184.1

As is described in many publications, LLE is used for the removal of endogenous phospholipids from biological samples. [187–191] The conventional two-phase extraction process is the method by Folch with methanol, water and chloroform in varying proportions. [192] This method did not appear to be suitable for the Tri*PPP* rocompounds, as they tend to diffuse into the organic phase due to their lipophilicity. Nevertheless, it was tested with neat solvent before testing it with mock-samples of cell pellets. For that, a mixture of 100 μ L of chloroform with 120 μ L of water and 80 μ L of methanol was spiked with all analytes, mixed thoroughly and after phase separation via centrifugation, the aqueous as well as the organic phase were diluted (1:10) with acetonitrile. Both samples were measured and the EICs are displayed in Figure 4-66. As expected, the Tri*PPP* ro-compounds but also the nucleoside were detected in the organic chloroform phase.

For this reason, an extraction with methyl *tert*-butyl ether (MTBE) was tested, which was also reported in the literature.^[191] It was hoped that the Tri*PPP*ro-compounds did not exhibit optimal solubility in ether and will therefore diffuse into the aqueous phase.

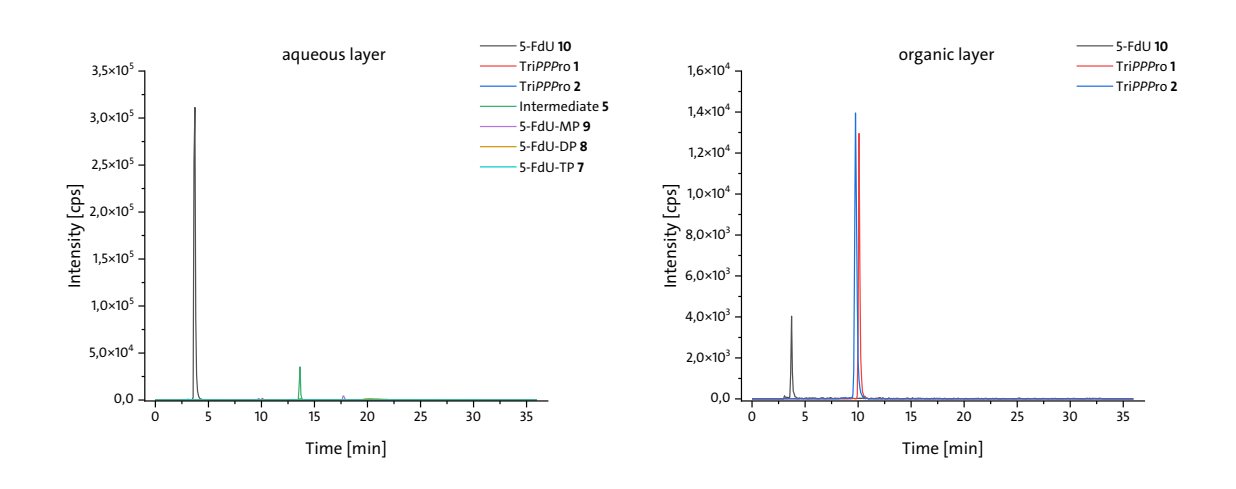


Figure 4-66: EICs of all analytes in the aqueous (left) and organic (right) layer after liquid-liquid extraction (LLE) with chloroform, water and methanol (1:1.2:0.8 %v/v/v).

The preliminary test was conducted with pure solvent in a mixture of MTBE, water and methanol (10:2.5:3.0 % v/v/v). All analytes were spiked into the mixture and mixed thoroughly. Phase separation was achieved through centrifugation. The aqueous as well as the organic phase were diluted with acetonitrile and measured. The resulting chromatograms of the aqueous and organic layer are displayed in Figure 4-67. All analytes were detected in the aqueous layer (left hand side). Unfortunately, the peak shapes of the di- and triphosphate appeared broad, and the signal intensity was reduced, but no explanation was found for this phenomenon at that time.

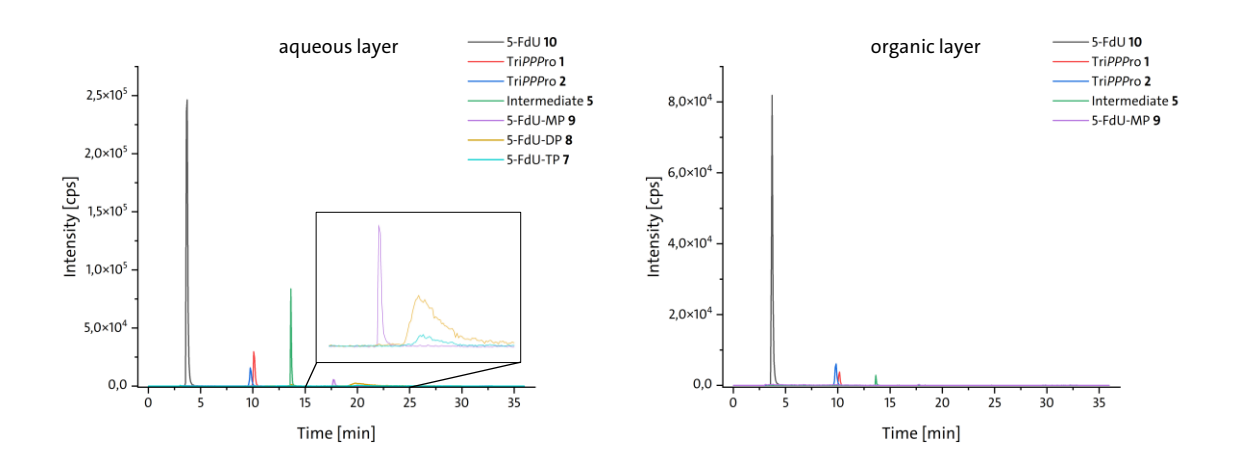


Figure 4-67: EICs of all analytes in the aqueous (left) and organic (right) layer after liquid-liquid extraction (LLE) with methyl *tert*-butyl ether (MTBE), water and methanol (10:2.5:3.0 %v/v/v).

The chromatogram of the organic layer (right hand side) showed that especially the nucleoside, but also the TriPPPro-compounds and the intermediate **5** diffused into the organic layer during the extraction. The signal intensity for the nucleoside and the TriPPPro-compound **2** in the aqueous phase was found to be three times higher, for the TriPPPro-compound **1** and the intermediate **5** the signal intensity was higher by a factor of 8 and 29, respectively. This result was promising and therefore, the LLE was tested using a mock-sample of a HT29 cell pellet.

However, the workflow has been adapted slightly by replacing the ultrasonic treatment for cell lysis with the use of a bead mill for lysis, extraction and homogenization of the sample in a single step. The extraction efficiency was evaluated by comparing the absolute peak area of intracellularly available UMP from the cancer cells after the employment of different sample preparation methods (LLE and PPT) with either a sonication treatment for 10 minutes or a bead mill treatment for 3 minutes at room temperature. In the bead milling process, ceramic beads were used instead of stainless-steel beads to prevent NSB of free phosphate groups to the metal. The results of this experiment are displayed in Figure 4-68. The absolute peak areas of the extracted UMP were always higher when using a bead mill regardless of the sample preparation method (LLE or PPT).

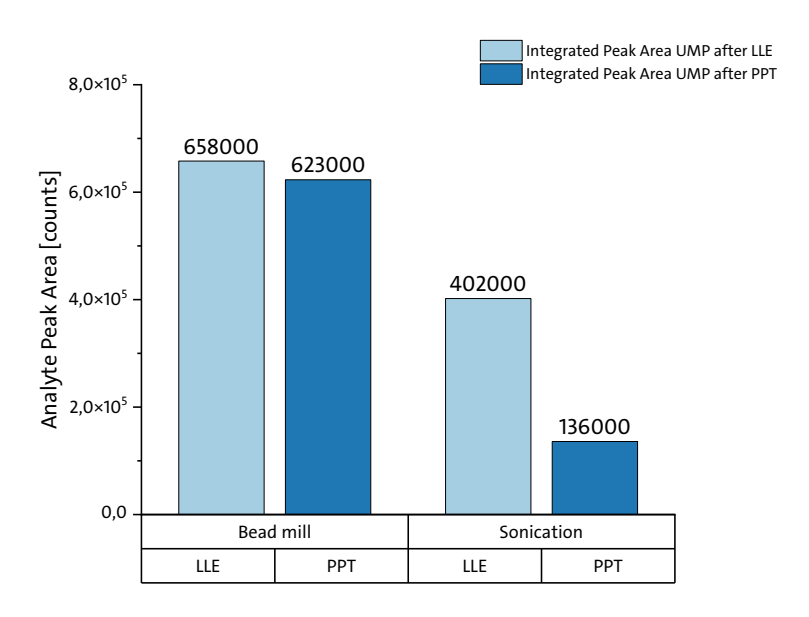


Figure 4-68: Integrated analyte peak area of endogenous UMP from HT29 cancer cell lysate after different sample preparation methods.

Since the bead mill has additional advantages over sonification, it was decided to use the bead mill in future experiments. Bead mills enable efficient and reproducible cell lysis through controlled mechanical forces (speed, time, temperature). In contrast, ultrasonic baths show uneven energy distribution and heat buildup, risking analyte degradation.

On the basis of these preliminary tests, the LLE protocol was tested on mock-samples of HT29 cancer cell pellets and evaluated by calculating ME, RE and PE using the three different sets (pre-spike, post-spike and neat blank). The workflow is schematically displayed in Figure 4-69. At this point, two different methods were tested. Either only the aqueous phase was diluted with a mixture of acetonitrile and water, or both layers (aqueous and organic) were mixed and diluted together in acetonitrile and water.

The samples of all sets were measured in triplicates and the mean integrated analyte peak area was used to determine ME, RE and PE. The results are summarized in Table 4-26. It is important to note that the cell count of each cell pellet was factored into the extraction volume calculation for better comparability. The extraction volume was always adjusted to a final cell count of 5 million cells per milliliter.

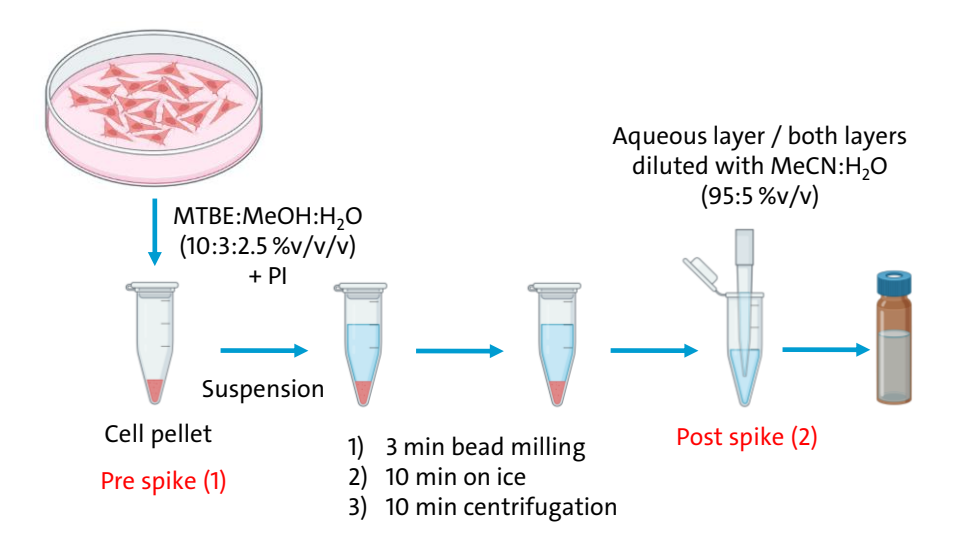


Figure 4-69: Established workflow for the LLE of cell pellets with suspension in MTBE:MEOH: H_2O (10:3:2.5 %v/v/v) + PI and subsequent cell lysis and extraction with 3 min of bead milling, protein precipitation in 10 min on ice and phase separation via centrifugation. The aqueous or both layers were diluted with a mixture of acetonitrile and water.

Table 4-26: Tested liquid-liquid extraction (LLE) procedures with determination of ME, RE and PE.

Analyte	LLE procedu	ure, aqueous	phase only	LLE procedure, both phases			
Allalyte	ME [%]	RE [%]	PE [%]	ME [%]	RE [%]	PE [%]	
5-FdU 10	42	61	25	83	76	63	
Tri <i>PPP</i> ro-compound 1	85	0	0	137	45	62	
Tri <i>PPP</i> ro-compound 2	87	0	0	176	28	49	
Intermediate 5	92	78	72	82	115	95	
Intermediate 6	110	34	37	37	321	118	
5-FdU-MP 9	85	265	225	46	609	281	
5-FdU-DP 8	121	14	17	69	87	60	
5-FdU-TP 7	226	7	15	96	44	43	

In conclusion, it is evident that significant improvements in ME and RE could be achieved with LLE using MTBE as the organic phase and a mixture of methanol, water and PI as the aqueous phase. Notably, the outcomes regarding RE for both Tri*PPP*ro-compounds (1: 45 %, 2: 28 %) were found to be good, especially considering the fact that they were very difficult to recover from cell extracts and their structural similarity to phospholipids, which were also highly abundant in cancer cell lysate (s. Figure 4-65, p. 130).

Blank matrices from mock uptake studies enable matrix-matched calibration to correct for matrix effects. This allows post-extraction spiking for evaluating linearity, sensitivity (LOD/LOQ), and precision ($n \ge 3$). While effective, this method requires large matrix volumes and can contaminate the MS.

The established sample preparation method was also adapted to the incubation medium, which was the second type of sample obtained after cellular uptake studies. Since the incubation medium did not contain any cell material, no lysis or extraction needed to be performed. Consequently, the bead milling step was omitted. The incubation medium was on an aqueous basis, primarily composed of PBS buffer. Therefore, the LLE was performed by adding only portions of MTBE and methanol to the mixture. In place of PI, an equivalent amount of water was added.

The sample was thoroughly mixed for several minutes and then placed on ice for 10 minutes. Following this, phase separation was achieved via centrifugation, subsequent to a dilution step with a mixture of acetonitrile and water. These steps were analogous to the sample preparation method for the cell pellets. In the following chapter, the determination of ME, RE and PE for all analytes in all matrices was carried out during the method validation experiments. The extracted cell pellets will be further described as cell lysate, while the prepared incubation medium will be referred to as supernatant. The two different sample types are also displayed schematically in Figure 4-70.

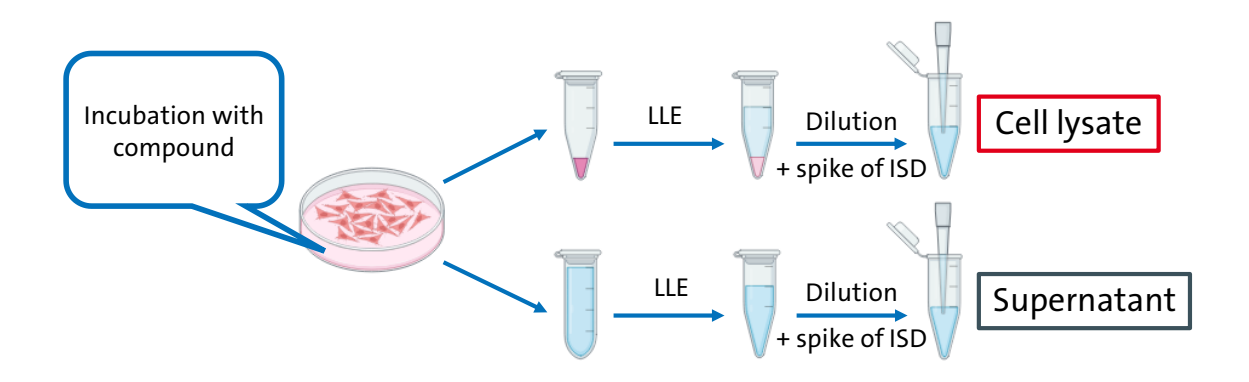


Figure 4-70: Sample preparation workflow for the two different sample types following cellular uptake studies.

4.7 Validation experiments for different matrices

After the establishment of a sample preparation workflow using LLE with MTBE, methanol and water including a dilution step, the next key step in method development would be to evaluate "matrix effect and selectivity" (s. Figure 4-1, p 34). In a broader sense, this stage involves method validation. This process consists of a series of experiments to collect parameters that confirm that the analytical method developed is suitable for its intended purpose. This validation was performed for every analyte (FdU- and d4T analytes) and every matrix, cell lysates and

supernatants, used. These parameters for the validation experiments were selected in accordance with the official EMA guidelines on bioanalytical method validation^[193], however, a reduced scope was used. Due to the exploratory nature of the study and the non-clinical application of the method, a full validation in line with regulatory guidelines was not feasible. Instead, a fit-for-purpose validation for *in vitro* systems was carried out, focusing on key parameters (specificity, selectivity, linearity, accuracy, precision, carry over, stability and matrix effect) relevant to the intended use. Furthermore, the blank matrix was not available in sufficient quantity, which limited the number of applications and samples that could be prepared. Therefore, experiments such as precision, stability or matrix effect were only determined using one concentration level.

For the validation, it was decided to include internal standards for every analyte of interest to improve the accuracy of the method. In method development, UMP 34 UTP 35 were already tested as potential internal standards. Since the results were promising, isotopically labeled uridine-¹³C₉, ¹⁵N₂ 5'-MP (UMP-ISD) **36** and uridine-¹³C₉ 5'-TP (UTP-ISD) 37 should be purchased. As no isotopically labeled UDP was commercially available, it was necessary to use UTP-ISD 37 for all diphosphates and triphosphates. However, due to a supply shortage, only UMP-ISD **36** could be utilized. While this was not the ideal solution, the structural similarity between UMP-ISD and the di- and triphosphates, as well as its elution in the retention time window, were sufficient to use it as an ISD for FdU-MP 9, FdU-DP 8, FdU-TP 7, d4T-MP 15, d4T-DP 14 and d4T-TP 13. For all other analytes, there were no commercially available isotopic labeled compounds. An ISD can also be a non-labeled analog with similar chemical and physical properties to ensure comparable response in the analysis. Therefore, d4T 15 was chosen as the ISD for FdU 10, and vice versa. The same principle was used for TriPPPro-compounds 1 and 2 as well as for intermediates 5 and 6. For TriPPProcompounds 3 and 4, a different compound was used as ISD. This compound, C4ACB;C18ACB-d4T-TP **38**, is displayed in Figure 4-71 and was also synthesized by JIA.

Figure 4-71: C4ACB;C18ACB-d4T-TP **38** as ISD for Tri*PPP*ro-compound **3** and Tri*PPP*ro-compound **4**.

The reason for choosing this compound was that TriPPPro-compound 3 and 4 were not as similar to each other (structurally and retention time window) as TriPPProcompound 1 and 2. Therefore, a compound was chosen that showed similarities for both 3 and 4 and had a retention time between these analytes. For intermediates 11 and 12, intermediate 6 was used as an ISD.

The validation experiments comprised of different samples, which are summarized in Table 4-27 for reasons of simplicity.

Table 4-27: Terms and definition of different sample types used in the validation experiments.

Term	Definition			
Double Blank	Biological matrix derived from mock-samples without			
	addition of analyte or ISD			
Blank	Biological matrix derived from mock-samples with addition			
Diank	of ISD in known concentration			
Calibration standard (CS) sample	Biological matrix derived from mock-samples with addition			
cumbration standard (es) sample	of analyte and ISD in known concentration			
Quality control (QC) sample	Biological matrix derived from mock-samples with addition			
educity control (QC) sumple	of analyte and ISD in known concentration			

4.7.1 Validation in HT29 cell lysate

In the subsequent subsections, a detailed account of the validation experiments conducted for each FdU-derived analyte within HT29 cell lysates will be presented. The data obtained herein serve to establish the robustness and applicability of the method for cellular uptake investigations involving FdU-prodrug metabolism and its intracellular metabolite products.

4.7.1.1 Specificity and selectivity

For assessment of the specificity and selectivity of the method, samples containing the analytes of interest and ISDs were compared to double blanks of HT29 cell lysate. In order to ascertain potential interferences, such as unspecific signals from mass transitions, the double blanks were examined in the corresponding retention time windows. The TIC of the double blank of HT29 cell lysate is displayed in Figure 4-72 including an overlay of all EICs of every analyte at a very low concentration level. The intensities of the unspecific signals varied between $1.0 \cdot 10^4$ and $6.0 \cdot 10^4$ cps.

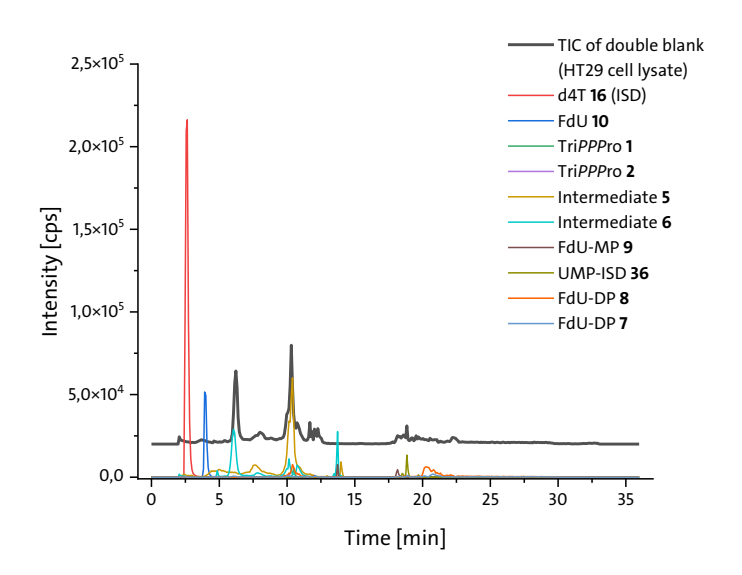


Figure 4-72: Total ion current (TIC) of a double blank sample of HT29 cell lysate in grey. EICs of all analytes as an overlay were added as comparison.

The first intense interference at 6.22 min did not co-elute with any analyte. The second one at 10.31 min was in the retention time window of the prodrugs, however retention times were not exactly the same (Tri*PPP*ro-compound **2**: rt = 10.16 min, Tri*PPP*ro-compound **1**: rt = 10.49 min) and signal intensities of the prodrugs at very low concentrations were higher (about $1.1 \cdot 10^4$ cps). Between the retention time window of 17.9 min and 22.9 min, an unspecific signal at 18.8 min was present. However, FdU-MP **9** displayed a retention time of 18.15 min, and UMP-ISD **36** of 18.23 min. As displayed, the unspecific signals were mainly mass transitions from intermediates **5** and **6**. However, these unspecific signals were always only a single mass transition, whereas the retention of an analyte could clearly be distinguished since three mass transitions were assigned to every analyte in the MRM method. The signal was only considered specific if all three mass transitions (quantifier, qualifier and a third) showed an intensity at exactly the same retention time. Therefore, the specificity and selectivity were on a very high level.

4.7.1.2 Range and linearity

The selection of the measuring range was based on two factors: the lowest and highest concentrations of compounds that would be expected. As there is no previous quantitative data on cellular uptake studies of Tri*PPP*ro-compounds, there was no benchmark for expected intracellular concentrations. However, the incubation concentration of the prodrugs was $10\,\mu\text{M}$. Assuming that all of the prodrug is taken up by the cells without being metabolized, the resultant intracellular concentration of the prodrug-compound would be approximately $10.000\,\text{ng/mL}$. Due to the dilution step, the expected concentration was approximately $1000\,\text{ng/mL}$. The objective was therefore to establish a linear range extending from the lowest detectable concentration up to $1000\,\text{ng/mL}$. However, constructing calibration curves that represented such an extensive concentration

range proved to be a difficult task and, for almost all analytes, the highest CS sample had a concentration of 500 ng/mL. The calibration curves in HT29 cell lysate for every analyte are summarized in Table 4-28 including the regression equation, standard errors for intercept and slope, determination coefficient, the linearity range, as well as the number of points used to construct the calibration curve. Every calibration curve was weighted with a factor of 1/x. The weighting of calibration curves was already discussed in detail in chapter 4.4.4. The data for the construction of every calibration curve can be found in the Supplementary data, chapter 7.2.3. All calibration curves were measured in duplicate where no duplicate displayed a CV higher than 13 %. No duplicate measurements could be performed for FdU-DP and -TP due to high values for %CV.

Table 4-28: Calibration curve statistics for every analyte in HT29 cell lysate.

Analyte	Regression equation (1/x weighted)	Standard error of intercept	Standard error of slope	Determination coefficient (<i>R</i> ²)	Linearity range [ng/mL]	Number of points
FdU 10	y = 0.00349x + 0.00326	0.0177	0.000171	0.9905	10 – 500	6
Tri <i>PPP</i> ro- compound 1	y = 0.00475x + 0.00298	0.0108	0.000267	0.9874	2 – 500	6
Tri <i>PPP</i> ro- compound 2	y = 0.00101x + 0.00831	0.00236	0.0000343	0.9954	10 – 500	6
Intermediate 5	y = 0.00216x + -0.00462	0.00733	0.0000708	0.9956	10 – 500	6
Intermediate 6	y = 0.00166x + -0.00544	0.00531	0.0000544	0.9957	15.5 – 500	6
FdU-MP 9	y = 0.0431x -1.53	0.375	0.00187	0.9924	35 – 500	6
FdU-DP 8	y = 0.0144x - 0.0555	0.0383	0.000266	0.9980	8.5 – 500	8
FdU-TP 7	y = 0.00272x - 0.258	0.0834	0.000198	0.9792	100 – 1000	6

Also, for every calibration curve, back calculations were performed with at least 75 % of the samples with a deviation below 15 % (or 20 % for the lowest CS sample). Every residual plot was checked for a random scatter. The data will be shown and discussed exemplary for the analyte FdU 10 in HT29 cell lysate, but all data for each analyte in every matrix can be found in the Supplementary data, section 7.2.4. The calibration curve and the residual plot are displayed in Figure 4-73. The linear range of the nucleoside was between 10 ng/mL and 500 ng/mL with a determination coefficient of 0.9905. The residual plot on the right-hand side of Figure 4-73 displayed a random scatter. Overall, all parameters in terms of linearity correspond to the EMA guidelines.

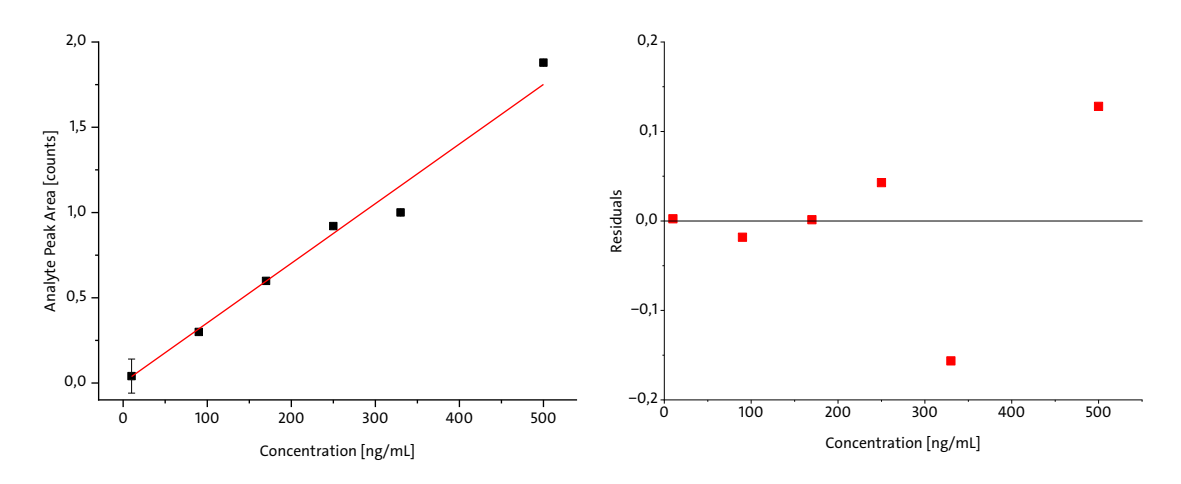


Figure 4-73: Calibration curve of FdU 10 (left) and residual analysis (right).

4.7.1.3 Limits of detection and quantification

On the basis of the calibration curve, the limit of detection (LOD) and the limit of quantification (LOQ) can be calculated. The LOD is the smallest detectable concentration, whereas the LOQ defines the concentration, which can still be quantified with sufficient accuracy.^[194] LOD can be calculated as follows (equation 6):

$$LOD = \frac{3 \cdot \sigma}{m}$$

where:

LOD limit of detection

 σ standard deviation

m slope of calibration curve.

LOQ can be calculated using equation 7:

$$LOQ = \frac{10 \cdot \sigma}{m}$$

where:

LOQ limit of quantification.

For the determination of the standard deviation σ , a solution of every analyte was prepared with a very low concentration (10 ng/mL for FdU 10, Tri*PPP*ro-compound 1 and 2, intermediate 5 and 6, and FdU-MP 9; 50 ng/mL for FdU-DP 8 and FdU-TP 7) in HT29 cell lysate. This analyte mix was measured at least three times. The resulting standard deviation of the peak areas and the slope of the corresponding calibration curve were used to calculate LOD and LOQ according to equation 6 and 7. Raw data can be found in the Supplementary data, chapter 7.2.3. The results for LOD and LOQ for every analyte are summarized in Table 4-29.

Table 4-29: Limit of detection (LOD) and limit of quantification (LOQ) for all analytes in HT29 cell lysate.

Analyte	Limit of detection (LOD) [ng/mL]	Limit of quantification (LOQ) [ng/mL]		
FdU 10	2.66	8.88		
Tri <i>PPP</i> ro-compound 1	0.40	1.35		
Tri <i>PPP</i> ro-compound 2	2.30	7.68		
Intermediate 5	2.99	9.96		
Intermediate 6	4.63	15.4		
FdU-MP 9	5.10	15.3		
FdU-DP 8	2.75	8.32		
FdU-TP 7	4.08	13.6		

4.7.1.4 Accuracy and precision

The accuracy of the method was determined by using quality control (QC) samples, where the analyte was spiked in HT29 cell lysate. Three different concentration levels were prepared for every analyte (low, mid, high) and analyzed with the calibration curve in duplicate. The results are summarized in Table 4-30. The corresponding integrated peak areas can be found in the Supplementary data, chapter 7.2.3.

Table 4-30: Determined accuracy of QC levels (low, mid, high) for every analyte in HT29 cell lysate.

QC				Accuracy [%]				
level	FdU 10	Tri <i>PPP</i> ro-	Tri <i>PPP</i> ro-	Inter-	Inter-	FdU-	FdU-	FdU-
icvei	140 10	compound 1	compound 2	mediate 5	mediate 6	MP 9	DP 8	TP 7
Low	120	100	114	88	114	101	92	89
Mid	99	97	101	99	91	115	94	94
High	90	90	107	109	97	114	103	91

The concentration of the mean value of the integrated peak area was then calculated with use of the calibration curve and the deviation between the calculated and the true value was assessed. The deviation should not be higher than ±15 % for mid and high QC (±20 % for low QC). [193] As displayed, all QC samples were within the defined ranges.

In order to assess precision, each analyte was spiked into HT29 cell lysate at low-concentration level and measured in triplicate for intra-day precision and in triplicate on three different days for inter-day precision. The mean value of the integrated analyte peak area and the standard deviation were used to calculate %CV for each analyte to express both intra- and inter-day precision. The deviation should not be higher than ±20 %.^[193] The results are summarized in Table 4-31. The corresponding raw data can be found in the Supplementary data, chapter 7.2.3. Intra-day precision exhibited a range between 3.9 and 18 % for all analytes, while inter-day precision demonstrated a greater variation, ranging from 9.3 to 52 %.

Table 4-31: Intra- and inter-day precision expressed as %CV for every analyte in HT29 cell lysate.

Analyte	Intra-day precision (%CV)	Inter-day precision (%CV)
FdU 10	8.2	13
Tri <i>PPP</i> ro-compound 1	9.8	52
Tri <i>PPP</i> ro-compound 2	18	10
Intermediate 5	12	12
Intermediate 6	6.6	9.3
FdU-MP 9	16	32
FdU-DP 8	9.2	22
FdU-TP 7	3.9	19

TriPPPro-compound 1 displayed an unusually high value for CV of 59 %. The observed variation was attributed to the elevated mean value of the analyte peak area of the prodrug on the second day of the measurement series. Each day the sample was freshly prepared with HT29 cell lysate in exactly the same way. On the first day, the average integrated peak area was approximately $5.4 \cdot 10^4$, and on the third day it was 9.0 · 10⁴. Unlike on days 1 and 3, signal intensities were elevated on day 2, with an average integrated peak area of approximately 2.0 · 105. It is conceivable that discrepancies in the extraction efficiency of the mock samples may result in varying matrix effects and result in specific signal enhancement on that day for this analyte. An attempt was made to eliminate the variance by using ISD corrected values. However, the results obtained with TriPPPro-compound 2 as ISD for TriPPProcompound 1 were not satisfactory. Different possibilities were tested to eliminate high deviations in the inter-day precision. Because of the enhanced signal, it was secured that mobile phases were always prepared freshly so that buffer strength and pH value were constant and did not influence the ionization efficiency of the analytes in the source. The column was always equilibrated for an adequate period of time (35 minutes, 20 column volume).

4.7.1.5 Carry over

To evaluate carry-over, the double blank measurement after the injection of the highest QC sample was examined and if analyte was detected, the integrated peak area was compared to the one from the lowest CS sample. The peak area in the blank measurement should not be 20 % higher than the peak area of the lowest CS sample.[193] Therefore, every double blank was compared to the lowest CS sample and integrated analyte peak areas were compared. The results are summarized in Table 4-32. With the exception of FdU-DP 8, no analyte demonstrated a significant (> 20 %) carry-over. In order to address the problem of carry-over for the diphosphate, a number of different strategies were pursued. Initially, the needle wash solution was substituted to prevent analyte carry-over from the autosampler needle. Re-injection from the same autosampler vial was not performed. The measurement sequence for samples containing FdU-DP 8 was modified, with all measurements initiated from the lowest CS sample. Subsequent to each highconcentration sample, a double blank measurement was conducted to ensure that no carry-over of the analyte occurred into subsequent CS or QC samples. Carry-over is particularly noticeable at the lower end of a calibration curve.

Table 4-32: Carry over of the analytes from the highest QC sample into the subsequent double blank (DB) measurement compared to the analyte peak area of the lowest CS sample.

	Carry over in comparison to the lowest CS sample								
	FdU 10	Tri <i>PPP</i> ro- cmpd. 1	Tri <i>PPP</i> ro- cmpd. 2	Inter- mediate 5	Inter- mediate 6	FdU- MP 9	FdU- DP 8	FdU- TP 7	
Peak Area DB	6.50E+2	0.00	1.09E+2	3.04E+3	4.06E+3	2.95E+3	2.48E+4	0.00	
Peak Area lowest CS	1.52E+5	2.17E+4	3.25E+4	1.50E+5	1.17E+5	1.10E+5	5.94E+4	5.72E+3	
Carry over [%]	0.4	0.0	0.3	2.0	3.5	2.7	42	0.0	

cmpd. = compound

The values obtained from the CS samples are frequently elevated beyond the expected values, or the calibration curve shows a curvature. This phenomenon was not observed in the case of FdU-DP **8** (s. Supplementary data, chapter 7.2.4). Consequently, carry-over was managed by the aforementioned strategies.

4.7.1.6 Stability

The analyte stability in the used matrix was tested in three different experiments. Analytes were spiked into blank HT29 cell lysate at a known concentration and subsequently aliquoted. One aliquot was measured directly, one was stored for 24 hours in the autosampler at 10°C, one was stored on the benchtop at room temperature for 24 hours, and one was frozen at -20°C and thawed again after 24 hours. All measurements were performed in triplicate. The mean integrated analyte peak area of each stability sample was then compared to the mean value of the freshly prepared sample, and the deviation was determined as a percentage. The results of these experiments are summarized in Table 4-33. The underlying raw data can be found in Supplementary data, chapter 7.2.3. In almost all cases, a decrease in integrated analyte peak area was observed.

Table 4-33: Stability expressed as deviation of the samples compared to the fresh sample for every analyte in HT29 cell lysate.

	Stability [%]								
	FdU 10	Tri <i>PPP</i> ro-	Tri <i>PPP</i> ro-	Inter-	Inter-	FdU-	FdU-	FdU-	
	140 10	cmpd. 1	cmpd. 2	mediate 5	mediate 6	MP 9	DP 8	TP 7	
Benchtop	-22	-51	-38	-26	-33	-20	-39	19	
(22 °C)	22	31	30	20	33	20	33	15	
Auto-									
sampler	-5.8	-33	-43	25	27	-18	-28	19	
(10 °C)									
Freezer	-23	-43	-49	-24	-44	-27	-24	-3	
(-20 °C)	23	- -7-3	43	24	74	21	24	ر.	

cmpd. = compound

It is important to note that stability is expressed as the deviation of the corresponding sample from the freshly prepared sample. Hence, it was concluded that an increase in the presented value corresponds to a decrease in stability. In general, the compounds presented moderate stability at room temperature (deviations between 19 % and -51 %). Especially the prodrug compounds were most unstable on the benchtop. The process of freezing the samples at -20 °C and subsequently thawing them resulted in reduced stabilities for FdU 10, TriPPProcompound **2**, intermediate **6**, and FdU-MP **9**. This observation may be explained by the potential introduction of water and the formation of inhomogeneities during the thawing process, both of which can promote degradation. The stability of the samples was the highest for almost all samples when stored in the autosampler at 10 °C. For intermediates **5** and **6**, as well as for FdU-TP **7**, the integrated analyte peak area after 24 hours at 10 °C was higher than that of the freshly spiked sample. Instrumental or measurement variations may have led to enhanced signal intensity and thus higher peak areas; otherwise, no explanation for this phenomenon was found. The results of the stability study suggested that analyte containing cell lysate samples should not be frozen and thawed repeatedly. All spiked-in samples were prepared freshly and measurement series, e.g. calibration curves in duplicate, did not exceed 16 hours of sample storage in the autosampler. The samples obtained after cellular uptake studies were stored at -80 °C and, following thawing, were not refrozen. Stock solutions of every analyte were stored at -20 °C in aliquots to avoid frequent thawing and refreezing. These stock solutions were repeatedly analyzed by RPIP-UV to detect any possible degradation of the compound. Consequently, if any degradation was observed, the sample was disposed of.

4.7.1.7 Matrix effect, recovery and process efficiency

For HT29 cell lysate, the values for ME, RE and PE were already determined during the establishment of the sample preparation method and summarized in Table 4-26 (s. chapter 4.6, p. 134).

4.7.1.8 Dilution integrity

During the present validation process, no assessment of dilution integrity was conducted, as matrix-matched calibrators and internal standards were used for all CS and QC samples. All dilution steps were carried out in a blank matrix. The only dilution performed with pure solvent was in the sample preparation method, but was already assessed in the matrix effect studies and recovery tests. The possibility of potential errors caused by the dilution step during the sample preparation have been already discussed in section 4.6. This also applies to the other validation processes for the other matrices within this work.

4.7.2 Validation in HT29 supernatant

In the following subsections, the validation experiments for every FdU-derived analyte in HT29 supernatant will be discussed. The supernatant is the incubation medium after sample preparation.

4.7.2.1 Specificity and selectivity

To evaluate potential interferences, including non-specific signals arising from mass transitions, double blank samples were analyzed within the respective retention time windows. The TIC of the double blank of HT29 supernatant is displayed in Figure 4-74 including an overlay of all EICs of every analyte at a very low concentration level.

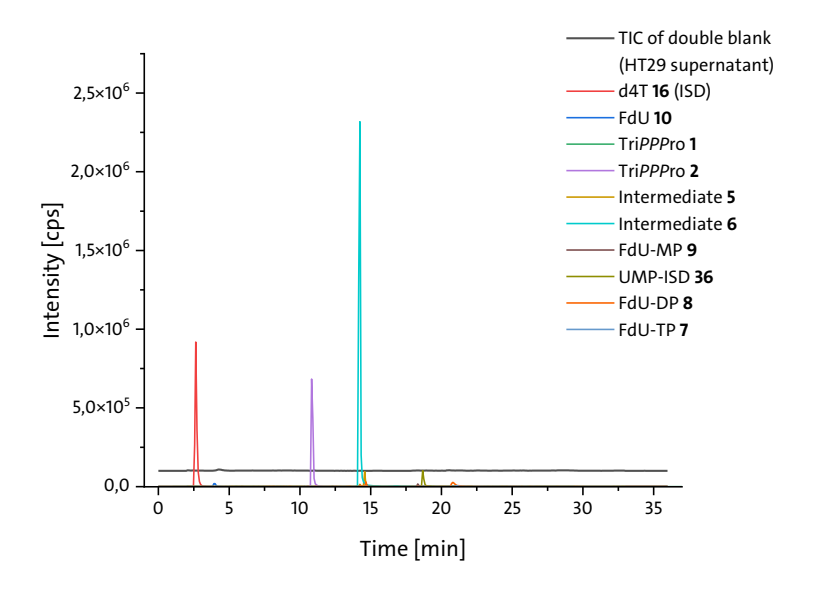


Figure 4-74: Total ion current (TIC) of a double blank sample of HT29 supernatant in grey. EICs of all analytes as an overlay were added as comparison.

4.7.2.2 Range and linearity

For all analytes except for FdU-TP **7**, calibration curves in blank HT29 supernatant were constructed, measured in duplicate and evaluated. The data underlying the regression analysis can be found in Supplementary data, chapter 7.2.4. The calibration curves statistics, such as equation, standard errors of intercept and slope, as well as the determination coefficient, the linear range and the number of points used to construct the calibration curve are summarized in Table 4-34.

Table 4-34: Calibration curve statistics for every analyte in HT29 supernatant.

Analyte	Regression equation (1/x	Standard error of	Standard error of	Determination	Linearity range	Number of
	weighted)	intercept	slope	coefficient (R²)	[ng/mL]	points
FdU 10	y = 0.00166x - 0.0489	0.0232	0.000124	0.9782	75 – 500	6
Tri <i>PPP</i> ro- compound 1	y = 0.0153x - 0.0587	0.0209	0.000290	0.9986	9 – 500	6
Tri <i>PPP</i> ro- compound 2	y = 0.000903 + 0.00133	0.000400	8.83E-6	0.9996	2-500	6
Intermediate 5	y = 0.000676 - 0.00133	0.00444	2.53E-5	0.9944	50 – 620	6
Intermediate 6	y = 0.00172x + 0.00657	0.00751	7.50E-5	0.9925	10 – 500	6
FdU-MP 9	y = 0.00354x + 0.106	0.00960	9.02E-5	0.9974	15 – 750	6
FdU-DP 8	y = 0.00222x + 0.0150	0.0212	0.000112	0.9900	75– 500	6
FdU-TP 7		No data available				

All calibration curves were weighed with a factor of 1/x. Unfortunately, the results for FdU-TP **7** failed repeatedly the validation requirements, and therefore this analyte was excluded.

4.7.2.3 Limits of detection and quantification

LOD and LOQ were calculated for every analyte using equation 6 and equation 7. All analytes were spiked in blank HT29 supernatant and measured repeatedly (n = 5). The mean value for the integrated analyte peak area was used to calculate LOD and LOQ. The results are summarized in Table 4-35. The underlying raw data can be found in the Supplementary data, chapter 7.2.3.

Table 4-35: Limit of detection (LOD) and limit of quantification (LOQ) for all analytes except FdU-TP **7** in HT29 supernatant.

Analyte	Limit of detection (LOD) [ng/mL]	Limit of quantification (LOQ) [ng/mL]
FdU 10	16.0	55.0
Tri <i>PPP</i> ro-compound 1	2.90	8.79
Tri <i>PPP</i> ro-compound 2	0.440	1.47
Intermediate 5	12.2	40.6
Intermediate 6	2.87	9.57
FdU-MP 9	4.09	12.4
FdU-DP 8	89.3	270

4.7.2.4 Accuracy and precision

As already described in section 4.7.1.4, accuracy of the method was determined using QC samples, where the analyte was spiked in HT29 supernatant. Three different concentration levels were prepared for every analyte (low, mid, high) and analyzed with the calibration curve in duplicate. The concentration of the mean value of the integrated peak area was then calculated with use of the calibration curve and the deviation between the calculated and the true value was assessed. The deviation should not be higher than ± 15 % for mid and high QC (± 20 % for low QC). The results are summarized in Table 4-36.

Table 4-36: Determined accuracy of QC levels (low, mid, high) for every analyte in HT29 supernatant.

	Accuracy [%]						
QC level	FdU 10	Tri <i>PPP</i> ro-	Tri <i>PPP</i> ro-	Inter-	Inter-	FdU-MP 9	FdU-DP 8
	140 10	cmpd. 1	cmpd. 2	mediate 5	mediate 6	ruo Mii 3	140 DI 3
Low	114	93	81	109	120	84	80
Mid	115	104	102	114	108	104	96
High	110	102	90	104	115	98	115

cmpd. = compound

For all analytes, all QC samples met the predefined acceptance criteria. Low QC samples were also used to evaluate precision. For that, every analyte was spiked into HT29 supernatant and measured five times for intra-day precision and for five times on three different days for inter-day precision. The mean value of the integrated analyte peak area and the standard deviation were used to calculate %CV for each analyte to express both intra- and inter-day precision. The results are summarized in Table 4-37. As displayed, the intra- and inter-day precision was acceptable (%CV < 20 %) for every analyte and the results were overall reproducible. In combination with the results for accuracy, it is important to implement suitable control mechanisms to monitor the method. It was established that unknown samples, i.e. samples after cellular uptake studies, were only measured in combination with a calibration curve and QC samples.

Table 4-37: Intra- and inter-day precision expressed as %CV for every analyte in HT29 supernatant.

Analyte	Intra-day precision (%CV)	Inter-day precision (%CV)		
FdU 10	6.3	15		
Tri <i>PPP</i> ro-compound 1	4.9	11		
Tri <i>PPP</i> ro-compound 2	9.2	17		
Intermediate 5	9.2	9.0		
Intermediate 6	12	12		
FdU-MP 9	15	15		
FdU-DP 8	18	8.4		

The underlying raw data for accuracy and precision can be found in the Supplementary data, chapter 7.2.3.

4.7.2.5 Carry over

As already discussed, carry-over was evaluated by examining the double blank measurement after the injection of the highest QC sample and if some analyte was detected, the integrated peak area was compared to the one from the lowest CS sample. The peak area in the blank measurement should not be 20 % higher than the peak area of the lowest CS sample. Therefore, every double blank was compared to the lowest CS sample and integrated analyte peak areas were compared. The results are summarized in Table 4-38. No significant carry-over was determined for any analyte in the HT29 supernatant matrix.

Table 4-38: Carry over of the analytes from the highest QC sample into the subsequent double blank (DB) measurement compared to the analyte peak area of the lowest CS sample.

	Carry over in comparison to the lowest CS sample						
	FdU 10	Tri <i>PPP</i> ro-	Tri <i>PPP</i> ro-	Inter-	Inter-	FdU-MP 9	FdU-DP 8
	Fu0 10	cmpd. 1	cmpd. 2	mediate 5	mediate 6	TUO-MIF 3	140-DF 6
Peak Area	7.52E+0	8.63F+03	1.02F+02	1.33E+02	5.7E+03	5.75E+03	1.00E+04
DB	2	6.03E+U3	3 1.02L+02	1.551 102	J.7 L 103	J.1 JL+03	1.001+04
Peak Area	4.34E+0	8.33E+05	5.66E+03	6.70E+05	1.28E+05	1.64E+05	1.69E+05
lowest CS	5	6.552105	3.002103	0.701103	1.201103	1.042103	1.052103
Carry over [%]	0.2	1.0	1.8	0.0	4.5	3.5	5.9

cmpd. = compound

4.7.2.6 Stability

The analyte stability in the used matrix was tested in three different experiments. Analytes were spiked into blank HT29 supernatant at a known concentration and subsequently aliquoted. One aliquot was measured directly, one was stored for 24 hours in the autosampler at 10°C, one was stored on the benchtop at room temperature for 24 hours, and one was frozen at -20°C and thawed again after 24 hours. All measurements were performed in triplicate. The mean integrated

analyte peak area of each stability sample was then compared to the mean value of the freshly prepared sample, and the deviation was determined as a percentage. The results of these experiments are summarized in Table 4-39. The underlying raw data can be found in the Supplementary data, chapter 7.2.3. For some analytes, signal enhancement was detected resulting in significant positive deviations (37% and 39% for the Tri*PPP*ro-compounds 1 and 2, respectively). This phenomenon was previously observed in stability studies using HT29 cell lysate, albeit with different analytes. Besides that, most analytes displayed very high stabilities after 24-hour storage in the autosampler and in the freezer including one freeze-thaw cycle. Tridi- and monophosphate exhibited low stabilities under all tested conditions. Especially for FdU-DP, no signal could be detected anymore after 24-hour storage at the benchtop at 22 °C or in the freezer at -22 °C.

Table 4-39: Stability expressed as deviation of the samples compared to the fresh sample for every analyte in HT29 supernatant.

	Stability [%]						
	FdU 10	Tri <i>PPP</i> ro-	Tri <i>PPP</i> ro-	Inter-	Inter-	FdU-	FdU-
	ruo 10	cmpd. 1	cmpd. 2	mediate 5	mediate 6	MP 9	DP8
Benchtop	0.5	11	-5.9	-22	-21	-91	_
(22 °C)	0.5	11	-5.9	-22	-21	-91	
Auto-							
sampler	13	37	39	-1.2	4.2	-15	-79
(10 °C)							
Freezer	2.9	35	22	-10	-5.5	-76	_
(-20 °C)	2.9	,,	22	10	ر.ر	70	

cmpd. = compound

4.7.2.7 Matrix effect, recovery and process efficiency

The values for ME, RE and PE were determined using three distinct sample sets: prespike, post-spike and neat-blank samples prepared in HT29 supernatant. ME, RE and PE were calculated according to equations 3, 4 and 5 (p. 123) respectively, and the

corresponding results are summarized in Table 4-40. A distinct signal suppression was observed for intermediate **5** and FdU-MP **9**, reflected by ME values significantly below 100 %. All remaining analytes exhibited ME values with acceptable ranges, indicating no substantial ion suppression or enhancement affecting quantification. Nevertheless, matrix-matched calibration was applied for all analytes to minimize the impact of ME and ensure accurate quantification. In most cases, the recovery values for the analytes were significantly higher than expected due to elevated integrated peak areas observed in all pre-spiked samples. A definitive explanation for this phenomenon could not be determined, as the results were consistent across replicates, ruling out potential sources of error such as pipetting or calculation mistakes. The signal enhancement observed for all analytes may be attributed to differing matrix effects in pre-spiked samples compared to post-spiked samples.

Table 4-40: Determined ME, RE and PE for every analyte in HT29 supernatant.

Analyte	ME [%]	RE [%]	PE [%]
5-FdU 10	78	220	171
Tri <i>PPP</i> ro-compound 1	97	167	163
Tri <i>PPP</i> ro-compound 2	91	105	96
Intermediate 5	52	452	237
Intermediate 6	90	332	298
5-FdU-MP 9	47	511	240
5-FdU-DP 8	77	461	353

4.7.3 Validation in SW620 cell lysate

The subsequent subsections provide a detailed discussion of the validation experiments performed for each FdU-derived analyte in lysates of the SW620 cell line.

4.7.3.1 Specificity and selectivity

Specificity was assessed by examination of the double blank for potential interferences. The TIC of the double blank of SW620 cell lysate is displayed in Figure 4-75 including an overlay of all EICs of every analyte at a very low concentration level. Within the specified retention time windows of all analytes, no evidence of interfering peaks or unspecific signals was observed.

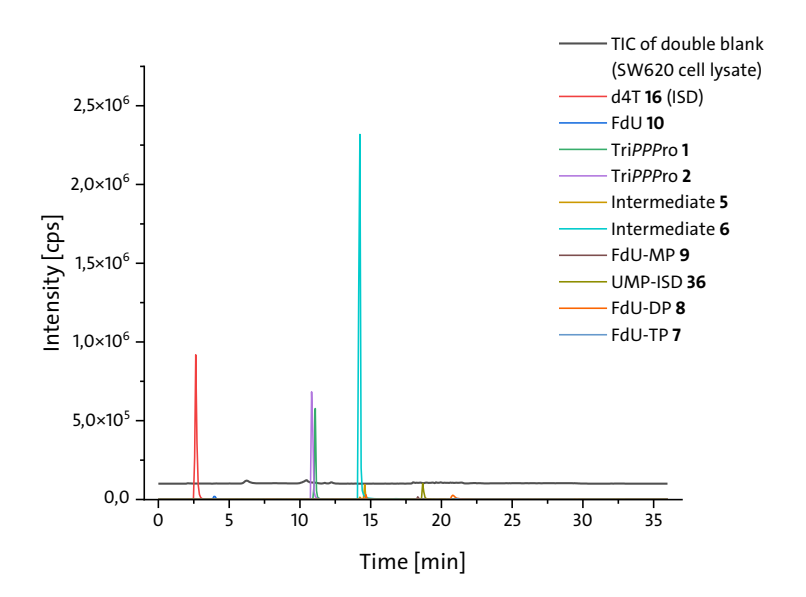


Figure 4-75: Total ion current (TIC) of a double blank sample of SW620 cell lysate in grey. EICs of all analytes as an overlay were added as comparison.

4.7.3.2 Range and linearity

For all analytes, calibration curves in blank SW620 cell lysate were constructed, measured in duplicate and evaluated. The raw data underlying the regression analysis can be found in Supplementary data, chapter 7.2.4. The calibration curves statistics, such as equation, standard errors of intercept and slope, as well as the determination coefficient, the linear range and the number of points used to construct the calibration curve are summarized in Table 4-41. All calibration curves were weighed with a factor of 1/x.

Table 4-41: Calibration curve statistics for every analyte in SW620 cell lysate.

Analyte	Regression equation (1/x weighted)	Standard error of intercept	Standard error of slope	Determination coefficient (<i>R</i> ²)	Linearity range [ng/mL]	Number of points
FdU 10	y = 1.07x + 1.47	1.03	5.20E-03	0.9907	0.5 - 500	6
Tri <i>PPP</i> ro- compound 1	y = 0.00274x + 0.0444	0.00973	1.41E-04	0.9895	10 - 500	6
Tri <i>PPP</i> ro- compound 2	y = 0.00280x + 0.000450	0.00152	5.41E-05	0.9985	1.0 - 500	6
Intermediate 5	y = 6.77E-4x - 0.00469	0.00240	1.52E-05	0.9954	50 - 500	6
Intermediate 6	0.00135x - 0.00442	0.00288	4.17E-05	0.9962	11 - 500	6
FdU-MP 9	y = 0.00107x + 0.0155	0.00232	3.04E-05	0.9960	15 - 500	6
FdU-DP 8	y = 0.0706x - 4.12	1.43	5.09E-03	0.9796	60 - 850	6
FdU-TP 7	y = 0.0208x -1.03	0.500	1.35E-03	0.9837	100 - 850	6

4.7.3.3 Limits of detection and quantification

LOD and LOQ were calculated for every analyte using equation 6 and equation 7. All analytes were spiked in blank SW620 cell lysate and measured repeatedly (n = 5). The mean value for the integrated analyte peak area was used to calculate LOD and LOQ. The results are summarized in Table 4-42. The raw data supporting these findings are available in Supplementary data, chapter 7.2.3.

Table 4-42: Limit of detection (LOD) and limit of quantification (LOQ) for all analytes in SW620 cell lysate.

	Limit of detection	Limit of quantification (LOQ)
Analyte	Limit of detection	Limit of quantification (LOQ)
	(LOD) [ng/mL]	[ng/mL]
FdU 10	0.000251	0.000836
Tri <i>PPP</i> ro-compound 1	0.0205	0.0683
Tri <i>PPP</i> ro-compound 2	0.000717	0.00239
Intermediate 5	14.7	48.9
Intermediate 6	3.21	10.7
FdU-MP 9	4.19	14.0
FdU-DP 8	0.809	2.70
FdU-TP 7	1.08	3.59

4.7.3.4 Accuracy and precision

The accuracy of the method was determined using QC samples, where the analyte was spiked in SW620 cell lysate. The results are summarized in Table 4-43. Based on the data, the accuracy of the method was deemed acceptable, meeting the predefined acceptance criteria. In order to assess precision, each analyte was spiked into SW620 cell lysate and measured five times for intra-day precision and for five times on three different days for inter-day precision. The results are summarized in Table 4-44.

The underlying raw data for accuracy and precision can be found in the Supplementary data, chapter 7.2.3.

Table 4-43: Determined accuracy of QC levels (low, mid, high) for every analyte in SW620 cell lysate.

QC		Accuracy [%]										
level	FdU 10	Tri <i>PPP</i> ro-	Tri <i>PPP</i> ro-	Inter-	Inter-	FdU-	FdU-	FdU-				
ievei	ruo 1 0	cmpd. 1	cmpd. 2	mediate 5	mediate 6	MP 9	DP 8	TP 7				
Low	105	N/A	134	68	85	83	84	103				
Mid	112	99	107	93	93	106	65	75				
High	98	106	85	91	106	108	84	95				

cmpd. = compound

Table 4-44: Intra- and inter-day precision expressed as %CV for every analyte in SW620 cell lysate.

Analyte	Intra-day precision (%CV)	Inter-day precision (%CV)
FdU 10	8.8	24
Tri <i>PPP</i> ro-compound 1	15	15
Tri <i>PPP</i> ro-compound 2	5.9	14
Intermediate 5	7.4	19
Intermediate 6	6.3	10
FdU-MP 9	4.1	2.6
FdU-DP 8	10	11
FdU-DP 7	29	10

The data obtained for intra- and inter-day precision were considered acceptable, as nearly all analytes showed variations within ±20%, which are regarded as normal measurement fluctuations in mass spectrometry. Higher values for inter-day precision were already observed in HT29 cell lysate and may be attributed to matrix effects and varying mock-samples used for the samples. Unfortunately, it is not entirely possible to avoid the use of different cell lysate samples, as a single cell pellet permits only a limited number of sample preparations.

4.7.3.5 Carry over

As already discussed, carry-over was evaluated by examining the double blank measurement after the injection of the highest QC sample and if some analyte was detected, the integrated peak area was compared to the one from the lowest CS sample. The results are summarized in Table 4-45.

Table 4-45: Carry over of the analytes from the highest QC sample into the subsequent double blank (DB) measurement compared to the analyte peak area of the lowest CS sample.

	Carry over in comparison to the lowest CS sample [%]								
	FdU 10	Tri <i>PPP</i> ro-	Tri <i>PPP</i> ro-	Inter-	Inter-	FdU-	FdU-	FdU-	
		cmpd. 1	cmpd. 2	mediate 5	mediate 6	MP 9	DP 8	TP 7	
Peak Area	3.23E+2	2.02E+2	1.09E+2	4.58E+3	2.10E+4	1.57E+3	5.84E+3	4.36E+2	
DB									
Peak Area	3.21E+4	3.83E+5	1.90E+4	4.82E+5	1.47E+5	1.89E+4	2.85E+4	3.18E+4	
lowest CS									
1 DB ⋅CS	1.0	0.1	0.6	1.0	14	8.3	20	1.4	

cmpd. = compound

Strategies to overcome higher carry over effects for FdU-DP **8** were already described in relation to the samples in HT29 cell lysate (s. chapter 4.7.1.5, p 145) and were adapted to the measurements in SW620 cell lysate. It was demonstrated that the carry-over effect did not affect the linear relationship between concentration and signal response for any analyte (s. chapter 7.2.4).

4.7.3.6 Stability

For assessing sample stability in SW620 cell lysate, the analytes were spiked into SW620 cell lysate and stored for 24 hours at different conditions as previously described in section 4.7.1.6. The results are summarized in Table 4-46. The stability tests clearly demonstrate that all compounds exhibit low stability under all three

tested conditions. A signal loss of up to 88% relative to the freshly spiked sample was already evident during storage in the autosampler at 10 °C. Even at -20 °C, significant degradation occurred, with signal losses reaching -66 %. This instability is likely due to enzymatic or chemical hydrolysis in the cell lysate and highlights the importance of rapid and cooled sample processing. Consequently, as previously mentioned in the context of HT29 cell lysate, all cell lysate samples were freshly prepared, and measurement sequences were kept as short as possible to ensure reliable duplicate measurements with low %CV values.

Table 4-46: Stability expressed as deviation of the samples compared to the fresh sample for every analyte in SW620 cell lysate.

	Stability [%]							
	FdU 10	Tri <i>PPP</i> ro-	Tri <i>PPP</i> ro-	Inter-	Inter-	FdU-	FdU-	FdU-
	140 10	cmpd. 1	cmpd. 2	mediate 5	mediate 6	MP 9	DP 8	TP 7
Benchtop	-46	-50	-63	11	-27	-46	-85	-58
(22 °C)	.0	30	03		_,	.0	03	30
Auto-								
sampler	-54	-48	-54	-3.2	-22	-17	-83	-88
(10 °C)								
Freezer	-46	-51	-66	-6.0	-33	-65	-52	-70
(-20 °C)	.0	3.	30	2.0	33	33	32	. •

cmpd. = compound

4.7.3.7 Matrix effect, recovery and process efficiency

The values for ME, RE and PE were determined using three distinct sample sets: prespike, post-spike and neat-blank samples prepared in SW620 cell lysate. ME, RE and PE were calculated according to equations 3, 4 and 5 (p. 123), respectively, and the corresponding results are summarized in Table 4-47. 5-FdU 10 and intermediate 6 displayed acceptable ME, while intermediate 5 had strong signal enhancement and the remaining analytes strong signal suppression.

Table 4-47: Determined ME, RE and PE in [%] in SW620 cell lysate.

Analyte	ME [%]	RE [%]	PE [%]
5-FdU 10	87	155	135
Tri <i>PPP</i> ro-compound 1	56	7	4
Tri <i>PPP</i> ro-compound 2	24	6	1
Intermediate 5	169	174	294
Intermediate 6	84	106	89
5-FdU-MP 9	8	261	22
5-FdU-DP 8	8	149	12
5-FdU-TP 7	15	221	34

This underlines the importance of the matrix-matched calibration to overcome these effects. The recovery rates for prodrugs 1 and 2 were very low at 7% and 6%, respectively. This issue has already been addressed in the context of recovery from HT29 cell lysate. However, all attempts to improve the recovery were unsuccessful. The ME and RE for each analyte resulted in process efficiencies ranging between 1% and 294%.

4.7.4 Validation in SW620 supernatant

In the following subsections, the validation experiments for each FdU-derived analyte in SW620 cell supernatant will be presented and discussed.

4.7.4.1 Specificity and selectivity

To identify potential interferences, such as non-specific signals from mass transitions, double blank samples were analyzed within the corresponding retention time windows.

The TIC of the double blank from SW620 cell lysate is shown in Figure 4-76 along with an overlay of the EICs for each analyte at a very low concentration level. No potential interferences could have been identified.

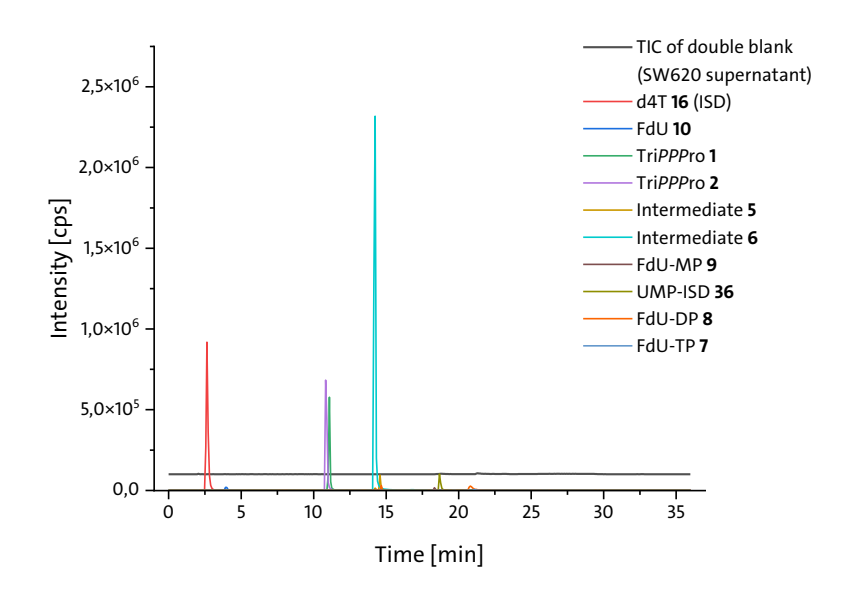


Figure 4-76: Total ion current (TIC) of a double blank sample of SW620 supernatant in grey. EICs of all analytes as an overlay were added as comparison.

4.7.4.2 Range and linearity

For all analytes, calibration curves in blank SW620 supernatant were constructed, measured in duplicate and evaluated. The raw data underlying the regression analysis as well as the calibration curves and residual plots can be found in Supplementary data, subsection 7.2.4.2. The calibration curves statistics, such as equation, standard errors of intercept and slope, as well as the determination coefficient, the linear range and the number of points used to construct the calibration curve are summarized in Table 4-48. All calibration curves were weighed with a factor of 1/x.

Table 4-48: Calibration curve statistics for every analyte in SW620 supernatant.

Analyte	Regression equation (1/x weighted)	Standard error of intercept	Standard error of slope	Determination coefficient (R ²)	Linearity range [ng/mL]	Number of points
FdU 10	y = 0.0087x - 0.0078	2.39E-02	3.85E-04	0.9922	5 - 500	6
Tri <i>PPP</i> ro- compound 1	y = 0.016x + 0.0053	2.33E-02	3.21E-04	0.9984	8 - 500	6
Tri <i>PPP</i> ro- compound 2	y = 0.00028x - 0.00035	1.12E-05	6.95E-04	0.9938	5 - 500	6
Intermediate 5	y = 0.0010x + 0.0047	1.72E-03	2.46E-05	0.9978	7 - 500	6
Intermediate 6	y = 0.0051x - 0.0015	1.44E-02	2.32E04	0.9918	5 - 500	6
FdU-MP 9	y = 0.046x - 0.24	3.71E-01	1.26E-03	0.9970	50 - 900	6
FdU-DP 8	y = 0.031x - 0.11	2.46E-01	1.07E-03	0.9954	50 - 900	6
FdU-TP 7	y = 0.0054x - 0.80	4.07E-02	1.66E-04	0.9962	50 - 900	6

4.7.4.3 Limits of detection and quantification

LOD and LOQ were calculated for every analyte using equation 6 and equation 7. All analytes were spiked in blank SW620 supernatant and measured repeatedly (n = 5). The mean value for the integrated analyte peak area was used to calculate LOD and LOQ. The results are summarized in Table 4-49. The corresponding raw data can be found in the Supplementary data, subsection 7.2.3.

Table 4-49: Limit of detection (LOD) and limit of quantification (LOQ) for all analytes except FdU-TP 7 in HT29 supernatant.

Analyte	Limit of detection (LOD) [ng/mL]	Limit of quantification (LOQ)	
FdU 10	0.193	0.645	
Tri <i>PPP</i> ro-compound 1	2.41	8.02	
Tri <i>PPP</i> ro-compound 2	0.886	2.95	
Intermediate 5	8.07	26.9	
Intermediate 6	0.735	2.45	
FdU-MP 9	0.437	1.46	
FdU-DP 8	3.21	10.7	
FdU-TP 7	3.77	12.6	

4.7.4.4 Accuracy and precision

The accuracy of the method was determined using QC samples, in which the analyte was spiked in SW620 supernatant. The results are summarized in Table 4-50. Based on the data obtained, the accuracy was found to be within acceptable limits. Due to a measurement error, mid-level QC samples could not be obtained for FdU-MP **9**, FdU-DP **8**, and FdU-TP **7**. This is indicated as 'N/A' in the table below.

Table 4-50: Determined accuracy of QC levels (low, mid, high) for every analyte in SW620 supernatant.

QC			Accuracy [%]					
level	FdU 10	Tri <i>PPP</i> ro-	Tri <i>PPP</i> ro-	Inter-	Inter-	FdU-	FdU-	FdU-
ievei	FaU 10	cmpd. 1	cmpd. 2	mediate 5	mediate 6	MP 9	DP 8	TP 7
Low	83	90	116	91	91	51	67	60.0
Mid	112	95	107	113	102	N/A	N/A	N/A
High	85	107	107	114	80	63	86	85

cmpd. = compound

In order to assess precision, each analyte was spiked into SW620 supernatant and measured five times for intra-day precision and for five times on three different days for inter-day precision. The mean value of the integrated analyte peak area and the standard deviation were used to calculate %CV for each analyte to express both intra- and inter-day precision. The results are summarized in Table 4-51. While all values obtained for the intra-day precision were in the accepted criteria, inter-day precision showed higher values for %CV for some analytes. Nevertheless, when considered alongside the results for accuracy and intra-day precision, the method was still deemed acceptable, as variations in inter-day precision may be attributed to the use of different matrix lots. The associated raw data for accuracy and precision can be found in the Supplementary data, subsection 7.2.3.

Table 4-51: Intra- and inter-day precision expressed as %CV for every analyte in SW620 supernatant.

Analyte	Intra-day precision (%CV)	Inter-day precision (%CV)
FdU 10	7.0	15
Tri <i>PPP</i> ro-compound 1	8.8	49
Tri <i>PPP</i> ro-compound 2	3.5	57
Intermediate 5	4.3	59
Intermediate 6	4.2	47
FdU-MP 9	5.4	36
FdU-DP 8	11	4.7
FdU-TP 7	12	5.1

4.7.4.5 Carry over

As previously discussed, carry-over was evaluated by analyzing the double blank measurement following the injection of the highest QC sample. If any analyte was detected, the integrated peak area was compared to that of the lowest CS sample. The results are summarized in Table 4-52. Except for FdU-TP 7, no significant carry-

over effect was determined. As previously mentioned, strategies to address carryover effects have been discussed, and no significant impact on the linearity of the method was observed.

Table 4-52: Carry over of the analytes from the highest QC sample into the subsequent double blank (DB) measurement compared to the analyte peak area of the lowest CS sample.

	Carry over in comparison to the lowest CS sample								
	FdU 10	Tri <i>PPP</i> ro-	Tri <i>PPP</i> ro-	Inter-	Inter-	FdU-	FdU-	FdU-	
		cmpd. 1	cmpd. 2	mediate 5	mediate 6	MP 9	DP 8	TP 7	
Peak Area	1.16E+4	1.81E+3	1.02E+2	1.69E+3	1.37E+4	1.02E+4	5.84E+3	2.59E+4	
DB									
Peak Area	8.59E+4	1.84E+5	8.88E+3	8.35E+4	7.08E+4	8.31E+4	2.85E+4	5.84E+4	
lowest CS									
Carry	14	1.0	1.2	2.0	19	12	20	44	
over [%]									

cmpd. = compound

4.7.4.6 Stability

For assessing sample stability in SW620 supernatant, the analytes were spiked into SW620 supernatant and stored for 24 hours at different conditions as previously described in section 4.7.1.6. The results are summarized in Table 4-53. Most compounds showed significant degradation at room temperature, with Tri*PPP* rocompound 1 and 2, as well as FdU-MP 9 and FdU-TP 7, being the least stable. Autosampler storage at 10 °C improved stability, particularly for FdU-DP 8 and FdU-TP 7. However, at -20 °C, several compounds, including Tri*PPP* ro-derivatives and FdU-MP, exhibited notable degradation, with only FdU 10 remaining consistently stable.

Table 4-53: Stability expressed as deviation of the samples compared to the fresh sample for every analyte in SW620 supernatant.

	Stability [%]							
	FdU 10	Tri <i>PPP</i> ro-	Tri <i>PPP</i> ro-	Inter-	Inter-	FdU-	FdU-	FdU-
	140 10	cmpd. 1	cmpd. 2	mediate 5	mediate 6	MP 9	DP 8	TP 7
Benchtop (22 °C)	22	-39	-50	-16	-17	-38	-11	-38
Auto- sampler (10 °C)	20	13	-30	-11	-6.5	-44	-1.2	-2.5
Freezer (-20 °C)	-0.5	-43	-48	-35	-31	-51	-29	-27

cmpd. = compound

4.7.4.7 Matrix effect, recovery and process efficiency

The values for ME, RE and PE were determined using three distinct sample sets: prespike, post-spike and neat-blank samples prepared in SW620 supernatant. ME, RE and PE were calculated according to equations 3, 4 and 5, respectively, and the corresponding results are summarized in Table 4-54.

Table 4-54: Determined ME, RE and PE in [%] in SW620 supernatant.

Analyte	ME [%]	RE [%]	PE [%]
5-FdU 10	35	128	45
Tri <i>PPP</i> ro-compound 1	156	65	101
Tri <i>PPP</i> ro-compound 2	104	113	117
Intermediate 5	120	197	237
Intermediate 6	127	166	211
5-FdU-MP 9	101	185	186
5-FdU-DP 8	90	165	148
5-FdU-TP 7	55	251	139

Most of the analytes displayed acceptable ME, while FdU **10** as well as FdU-TP **7** exhibited significant signal suppression. The recovery rates were unusually high as already described for HT29 supernatant. A reason for this could be an unspecific signal enhancement in pre spiked samples resulting in elevated integrated peak areas for the analytes. The ME and RE led to values for the PE between 45 % and 237 %.

4.7.5 Validation in CEM/O cell lysate

In the subsequent subsections, the validation experiments for each d4T-derived analyte in CEM/O cell lysate will be systematically presented and analyzed.

4.7.5.1 Specificity and selectivity

In order to ascertain potential interferences, such as unspecific signals from mass transitions, the double blanks were examined in the corresponding retention time windows. The TIC of the double blank of CEM/O cell lysate is displayed in Figure 4-77 including an overlay of all EICs of every analyte at a very low concentration level. No potential interferences were detected.

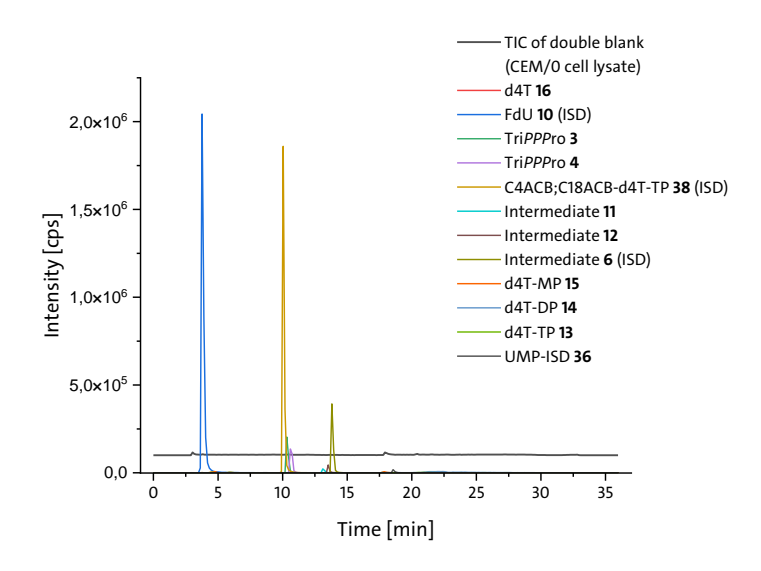


Figure 4-77: Total ion current (TIC) of a double blank sample of CEM/0 cell lysate in grey. EICs of all analytes as an overlay were added as comparison.

4.7.5.2 Range and linearity

For all analytes, calibration curves in blank CEM/O cell lysate were constructed, measured in duplicate and evaluated. The raw data underlying the regression analysis can be found in Supplementary data, subsection 7.2.4.3 The calibration curves statistics, such as equation, standard errors of intercept and slope, as well as the determination coefficient, the linear range and the number of points used to construct the calibration curve (1/x weighted) are summarized in Table 4-55.

Table 4-55: Calibration curve statistics for every analyte in CEM/0 cell lysate.

Analyte	Regression equation (1/x weighted)	Standard error of intercept	Standard error of slope	Determination coefficient (R ²)	Linearity range [ng/mL]	Number of points
d4T 16	y = 4.3E-05x + 6.10E-04	1.32E-04	9.86E-07	0.9979	10 - 1000	6
Tri <i>PPP</i> ro-compound 3	y = 0.020x + 0.0092	0.00920	0.000365	0.9980	0.5 - 500	7
Tri <i>PPP</i> ro- compound 4	y = 0.0018x - 0.087	0.0334	0.000127	0.9741	105 - 500	6

Analyte	Regression equation (1/x weighted)	Standard error of intercept	Standard error of slope	Determination coefficient (R ²)	Linearity range [ng/mL]	Number of points
Intermediate 11	y = 0.0025x - 0.00043	0.00939	6.63E-05	0.9965	20 - 500	6
Intermediate 12	y = 0.00147x - 0.01406	0.0162	9.96E-05	0.9775	27 - 700	6
d4T-MP 15	y = 6.10E-4x + 0.00102	0.00282	2.10E-05	0.9941	10 - 1000	6
d4T-DP 14	y = 0.00153x - 0.06266	0.0572	0.000115	0.9723	175 - 1000	6
d4T-TP 13	y = 2.49E-04 + 0.053	0.00414	8.34E-06	0.9944	175 - 1000	6

4.7.5.3 Limits of detection and quantification

LOD and LOQ were calculated for every analyte using equation 6 and equation 7. All analytes were spiked in blank CEM/O cell lysate and measured repeatedly (n = 5). The mean value for the integrated analyte peak area was used to calculate LOD and LOQ. The results are summarized in Table 4-56. The associated data can be found in the Supplementary data, subsection 7.2.3.

Table 4-56: Limit of detection (LOD) and limit of quantification (LOQ) for all analytes in CEM/0 cell lysate.

Analyte	Limit of detection (LOD) [ng/mL]	Limit of quantification (LOQ) [ng/mL]
d4T 16	0.00916	0.0278
Tri <i>PPP</i> ro-compound 3	0.0114	0.0346
Tri <i>PPP</i> ro-compound 4	34.8	105
Intermediate 11	5.69	17.2
Intermediate 12	8.65	26.2
d4T-MP 15	1.85	5.59

Analyte	Limit of detection (LOD) [ng/mL]	Limit of quantification (LOQ) [ng/mL]
d4T-DP 14	0.953	2.89
d4T-TP 13	24.1	73.0

4.7.5.4 Accuracy and precision

As previously described, the accuracy of the method was determined using QC samples, where the analyte was spiked in CEM/O cell lysate. The results are summarized in Table 4-57. All QC samples, except for the low QC sample of TriPPProcompound 4, were within the acceptable criteria and the method was found to be overall accurate. An unexplained enhancement of the ISD signal was observed in the low QC sample of TriPPProcompound 4, leading to an unusually high calculated concentration.

Table 4-57: Determined accuracy of QC levels (low, mid, high) for every analyte in CEM/O cell lysate.

QC	Accuracy [%]								
level	d4T 16	Tri <i>PPP</i> ro-	Tri <i>PPP</i> ro-	Inter-	Inter-	d4T-	d4T-	d4T-	
icvei	u41 10	cmpd. 3	cmpd. 4	mediate 11	mediate 12	MP 15	DP 14	TP 13	
Low	123	92	277	100	105	107	113	96	
Mid	90	95	100	109	88	87	102	101	
High	101	92	109	81	68	92	106	109	

cmpd. = compound

In order to assess precision, each analyte was spiked into CEM/O cell lysate and measured five times for intra-day precision and for five times on three different days for inter-day precision. The results are summarized in Table 4-58. Overall, intra- and inter-day precision for the analytes in CEM/O cell lysate was found to be satisfactory, with only the inter-day precision of intermediate 11 exhibiting a slightly elevated %CV value. The underlying raw data can be found in the Supplementary data, subsection 7.2.3. Higher values for inter-day precision were already observed in HT29

cell lysate and may be attributed to matrix effects and varying mock-samples used for the samples. Unfortunately, it is not entirely possible to avoid the use of different cell lysate samples, as a single cell pellet permits only a limited number of sample preparations.

Table 4-58: Intra- and inter-day precision expressed as %CV for every analyte in CEM/0 cell lysate.

Analyte	Intra-day precision (%CV)	Inter-day precision (%CV)
d4T 16	13	16
Tri <i>PPP</i> ro-compound 3	19	13
Tri <i>PPP</i> ro-compound 4	17	15
Intermediate 11	7.3	24
Intermediate 12	3.1	14
d4T-MP 15	4.8	10
d4T-DP 14	9.2	16
d4T-TP 13	10	13

4.7.5.5 Carry over

As already discussed, carry-over was evaluated by examining the double blank measurement after the injection of the highest QC sample and if some analyte was detected, the integrated peak area was compared to the one from the lowest CS sample. The results are summarized in Table 4-59. Significant carry-over effects for d4T 16 and d4T-MP 15 were observed, with values of 47% and 31%, respectively. Strategies were implemented to prevent carry-over from negatively impacting linear regression or other replicate measurements. No significant influence was observed when evaluating the calibration curves or the corresponding residual plots for these analytes.

Table 4-59: Carry over of the analytes from the highest QC sample into the subsequent double blank (DB) measurement compared to the analyte peak area of the lowest CS sample.

	Carry over in comparison to the lowest CS sample [%]							
	d4T 16	Tri <i>PPP</i> ro-	Tri <i>PPP</i> ro-	Inter-	Inter-	d4T-	d4T-	d4T-
	u41 16	cmpd. 3	cmpd. 4	mediate 11	mediate 12	MP 15	DP 14	TP 13
Peak Area	1.56E+3	1.19E+3	1.97E+3	0.0	9.97E+3	4.91E+3	0.0	0.0
DB	1.305+3	1.136+3	1.976+3	0.0	9.976+3	4.51673	0.0	0.0
Peak Area	3.33E+3	2.55E+4	3.54E+6	1.51E+5	1.24E+5	1.58E+4	8.4E+4	4.56E+4
lowest CS	3.33213	2.550 14	3.34210	1.51215	1.24613	1.30114	0.4614	4.501.4
1 DB ⋅CS	47	4.7	0.1	0.0	8.0	31	0.0	0.0

cmpd. = compound

4.7.5.6 Stability

To evaluate sample stability in CEM/O cell lysate, the analytes were spiked into the lysate and stored under various conditions for 24 hours, as detailed in subsection 4.7.1.6. The results are summarized in Table 4-60. Most compounds showed degradation at room temperature, with d4T-TP 13, d4T-DP 14, and d4T-MP 15 being the least stable. Storage at 10 °C moderately improved stability, though degradation of d4T metabolites remained substantial. Even at -20 °C, d4T-TP 13 and d4T-DP 14 showed marked instability. In contrast, Tri*PPP*ro-compound 4 and intermediates 11 and 12 remained stable across all conditions.

Table 4-60: Stability expressed as deviation of the samples compared to the fresh sample for every analyte in CEM/0 cell lysate.

		Stability [%]						
	d4T 16	Tri <i>PPP</i> ro-	Tri <i>PPP</i> ro-	Inter-	Inter-	d4T-	d4T-	d4T-
	u41 10	cmpd. 3	cmpd. 4	mediate 11	mediate 12	MP 15	DP 14	TP 13
Benchtop (22 °C)	-40	-11	2.0	11	32	-56	-61	-81
Auto- sampler (10 °C)	-16	-13	2.6	13	1.9	-50	-43	-41

	Stability [%]							
	d4T 16	Tri <i>PPP</i> ro-	Tri <i>PPP</i> ro-	Inter-	Inter-	d4T-	d4T-	d4T-
	41110	cmpd. 3	cmpd. 4	mediate 11	mediate 12	MP 15	DP 14	TP 13
Freezer (-20 °C)	-35	-11	3.4	6.5	2.8	-52	-70	-91

cmpd. = compound

4.7.5.7 Matrix effect, recovery and process efficiency

For CEM/O cell lysate, only the ME could be determined due to a shortage of intact CEM/O mock cell pellets, which prevented the preparation of pre-spike sets. Post-spike and neat-blank samples were prepared, and the ME for all analytes in cell lysate was calculated using equation 3. The results are summarized in Table 4-61. For the nucleoside d4T 16, significant signal suppression was observed. This may be attributed to a co-eluting interference from the PI cocktail, which was used to inhibit phosphatase activities. The cocktail contained imidazole, which could have co-eluted with the nucleoside during the initial minutes of the LC gradient.

Table 4-61: Determined ME [%] in CEM/O cell lysate.

Analyte	ME [%]
d4T 16	10
Tri <i>PPP</i> ro-compound 3	81
Tri <i>PPP</i> ro-compound 4	213
Intermediate 11	56
Intermediate 12	64
d4T-MP 15	100
d4T-DP 14	76
d4T-TP 13	33

The intermediates, as well as the triphosphate 13, also exhibited signal suppression, while TriPPPro-compound 4 displayed signal enhancement. All other ME were within acceptable limits. For the d4T-derivatives, a matrix-matched calibration in CEM/O cell lysate was applied to compensate for these effects.

4.7.6 Validation in CEM/O supernatant

In the following subsections, the validation experiments for every d4T-derived analyte in CEM/O supernatant will be discussed.

4.7.6.1 Specificity and selectivity

To assess potential interferences, including non-specific signals from mass transitions, double blank samples were examined within the relevant retention time windows. The TIC for the CEM/O supernatant double blank is presented in Figure 4-78, accompanied by an overlay of the EICs of each analyte at a low concentration level. Some unspecific interferences were observed within the retention time window of the mono-, di-, and triphosphates; however, due to the three characteristic mass transitions for each analyte, high specificity and selectivity were ensured.

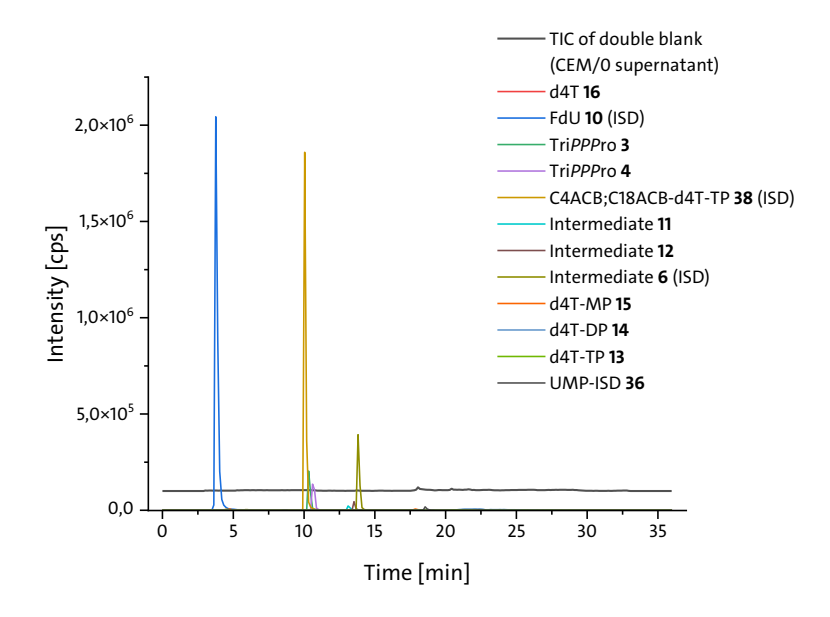


Figure 4-78: Total ion current (TIC) of a double blank sample of CEM/0 supernatant in grey. EICs of all analytes as an overlay were added as comparison.

4.7.6.2 Range and linearity

For all analytes, calibration curves in blank CEM/O supernatant were constructed, measured in duplicate and evaluated. The raw data underlying the regression analysis as well as the calibration curves and residual plots can be found in Supplementary data, subsection 7.2.4. The calibration curves statistics, such as equation, standard errors of intercept and slope, as well as the determination coefficient, the linear range and the number of points used to construct the calibration curve are summarized in Table 4-62. All calibration curves were weighed with a factor of 1/x.

Table 4-62: Calibration curve statistics for every analyte in CEM/O supernatant.

Analyte	Regression equation (1/x weighted)	Standard error of intercept	Standard error of slope	Determination coefficient (R ²)	Linearity range [ng/mL]	Number of points
d4T 16	y = 3.55E-05x + 5.02E-04	1.29E-04	8.37E-07	0.9967	20 – 500	7
Tri <i>PPP</i> ro- compound 3	y = 0.00158x + 0.0496	0.0178	0.00158	0.9907	100 – 500	6
Tri <i>PPP</i> ro- compound 4	y = 0.00109x + 7.99E-4	0.0160	0.00109	0.9843	100 – 500	6
Intermediate 11	y = 0.00193x - 0.00226	0.0313	0.00193	0.9809	100 – 500	6
Intermediate 12	y = 0.0103x - 0.0909	0.0294	0.0103	0.9982	25 – 500	7
d4T-MP 15	y = 0.00959x - 0.0462	0.0357	0.00959	0.9965	20 – 500	7
d4T-DP 14	y = 9.96E-4 - 0.0494	0.0156	0.000996	0.9897	90 – 1000	7
d4T-TP 13	y = 6.67E-4x - 0.0250	0.00892	0.000667	0.9925	90 – 1000	7

4.7.6.3 Limits of detection and quantification

LOD and LOQ were calculated for every analyte using equation 6 and equation 7. All analytes were spiked in blank CEM/O supernatant and measured repeatedly (n = 5). The mean value for the integrated analyte peak area was used to calculate LOD and LOQ. The results are summarized in Table 4-63. The corresponding raw data can be found in the Supplementary data, subsection 7.2.3.

Table 4-63: Limit of detection (LOD) and limit of quantification (LOQ) for all analytes in CEM/0 supernatant.

Limit of detection (LOD) [ng/mL]	Limit of quantification (LOQ) [ng/mL]		
2.85	8.64		
16.7	50.5		
16.6	50.3		
31.2	94.50		
8.22	24.9		
2.23	6.75		
18.7	56.7		
16.6	50.5		
	[ng/mL] 2.85 16.7 16.6 31.2 8.22 2.23 18.7		

4.7.6.4 Accuracy and precision

The accuracy of the method was determined using QC samples, where the analyte was spiked in CEM/O supernatant. The results are summarized in Table 4-64. The method was found to be accurate, as nearly all QC samples across different concentration levels were determined with high accuracy deviating between -21% and 26%.

Table 4-64: Determined accuracy of QC levels (low, mid, high) for every analyte in CEM/0 supernatant.

QC	Accuracy [%]								
level		Tri <i>PPP</i> ro-	Tri <i>PPP</i> ro-	Inter-	Inter-	d4T-	d4T-	d4T-	
ievei		cmpd. 3	cmpd. 4	mediate 11	mediate 12	MP 15	DP 14	TP 13	
Low	109	29	97	40	126	115	93	102	
Mid	105	117	91	53	103	88	79	87	
High	106	116	93	28	111	90	93	91	

cmpd. = compound

In order to assess precision, each analyte was spiked into CEM/O supernatant and measured five times for intra-day precision and for five times on three different days for inter-day precision. The mean value of the integrated analyte peak area and the standard deviation were used to calculate %CV for each analyte to express both intra- and inter-day precision. The results are summarized in Table 4-65. Intra-day precision varied between 3.0 % and 23 % for each analyte and inter-day precision ranged between 5.9 % and 30 %.

Table 4-65: Intra- and inter-day precision expressed as %CV for every analyte in CEM/O supernatant.

Analyte	Intra-day precision (%CV)	Inter-day precision (%CV)
d4T 16	16	30
Tri <i>PPP</i> ro-compound 3	9.2	25
Tri <i>PPP</i> ro-compound 4	12	8.7
Intermediate 11	17	5.9
Intermediate 12	10	9.4
d4T-MP 15	3.0	17
d4T-DP 14	23	18
d4T-TP 13	21	14

4.7.6.5 Carry over

As already discussed, carry-over was evaluated by examining the double blank measurement after the injection of the highest QC sample and if some analyte was detected, the integrated peak area was compared to the one from the lowest CS sample. The results are summarized in Table 4-66. As previously discussed, the higher carry-over effect of 33 % for d4T **16** was reduced by injecting a sequence of low to high concentration samples, followed by double blanks after the high concentration levels. No negative impact on linearity was observed for d4T.

Table 4-66: Carry over of the analytes from the highest QC sample into the subsequent double blank (DB) measurement compared to the analyte peak area of the lowest CS sample.

	Carry over in comparison to the lowest CS sample [%]							
	d4T 16	Tri <i>PPP</i> ro-	Tri <i>PPP</i> ro-	Inter-	Inter-	d4T-	d4T-	d4T-
	u41 10	cmpd. 3	cmpd. 4	mediate 11	mediate 12	MP 15	DP 14	TP 13
Peak Area	2.21E+3	3.05E+03	2.57E+03	4.83E+03	2.24E+04	3.28E+4	4.64E+3	7.09E+3
DB	2.216+3	3.032103	2.372103	4.032103	2.246104	J.20L14	4.04613	7.03213
Peak Area	6.6E+3	1.46E+07	7.21E+06	7.31E+05	1.56E+05	1.43E+5	2.89E+4	3.66E+4
lowest CS	0.0113	1.401107	7.212100	7.512105	1.502 105	1.43613	2.031.14	J.00L14
1 DB ⋅CS	33	0.0	0.0	0.7	14	23	16	19

Cmpd. = compound

4.7.6.6 Stability

To evaluate sample stability in CEM/O supernatant, the analytes were spiked into the lysate and stored under various conditions for 24 hours, as detailed in subsection 4.7.1.6. The results are summarized in Table 4-67. Tri*PPP*ro-compounds **3** and **4**, as well as intermediates **11** and **12**, showed good stability at all temperatures, although unusual signal increase was observed for all measurements with Tri*PPP*rocompound **3**.

Table 4-67: Stability expressed as deviation of the samples compared to the fresh sample for every analyte in CEM/0 supernatant.

	Stability [%]							
	d4T 16	Tri <i>PPP</i> ro-	Tri <i>PPP</i> ro-	Inter-	Inter-	d4T-	d4T-	d4T-
	u41 10	cmpd. 3	cmpd. 4	mediate 11	mediate 12	MP 15	DP 14	TP 13
Benchtop	-22	32	38	22	6.4	-15	0.5	-2.7
(22 °C)	22	32	50	LL	0.4	15	0.5	2.1
Auto-								
sampler	-77	52	27	-23	-23	-22	-1.0	25
(10 °C)								
Freezer	-36	30	34	13	13	-13	-2.3	15
(-20 °C)	50	30	54	15	15	i.J	2.3	כו

cmpd. = compound

The nucleoside as well as the MP, DP and TP exhibited variable stability, with significant degradation at 10 °C, especially d4T **16** (-77 %). Stability improved at -20 °C but remained moderate for some metabolites (d4T **16** and d4T-MP **15**).

4.7.6.7 Matrix effect, recovery and process efficiency

The values for ME, RE, and PE were determined using three separate sample sets: pre-spike, post-spike, and neat-blank samples, all prepared in CEM/O supernatant. ME, RE, and PE were calculated using equations 3, 4, and 5, respectively, with the resulting data summarized in Table 4-68.

Table 4-68: Determined ME, RE and PE in [%] in CEM/O supernatant.

Analyte	ME [%]	RE [%]	PE [%]
d4T 16	12	178	21
Tri <i>PPP</i> ro-compound 3	78	150	117
Tri <i>PPP</i> ro-compound 4	133	79	105
Intermediate 11	83	137	113
Intermediate 12	121	90	109
d4T-MP 15	86	224	193
d4T-DP 14	104	240	251
d4T-TP 13	110	176	193

Except for d4T **16**, where significant signal suppression was observed, all other ME were found to be acceptable. Tri*PPP*ro-compound **4** showed a slight signal enhancement. Matrix-matched calibration was used to compensate for signal enhancement or suppression caused by matrix interferences. As already observed, some analytes displayed unusually high values for RE resulting in overall PE values between 21 % and 251 %.

4.8 Quantification of prodrugs and metabolites in cell extracts

After the development, optimization, and validation of the HILIC-MRM method, various cellular uptake studies were conducted. TriPPPro-compounds 1 and 2 were incubated with two different cancer cell lines, while TriPPPro-compounds 3 and 4 were incubated with a human T4-lymphoblastoid cell line. The intra- and extracellular concentrations of these prodrugs and their resulting metabolites were subsequently determined. The quantification results will be discussed in the following subsections.

4.8.1 Cellular uptake studies with HT29 cancer cells

Cellular uptake studies were conducted by incubating HT29 colorectal cancer cells with either 10 μM of Tri*PPP*ro-compound **1** or **2** for varying durations of 1 h, 2 h, 6 h or 24 h. Following incubation, the samples underwent the established sample preparation procedure and spiking of the ISDs, after which both the cancer cell lysate and the corresponding supernatant were analyzed using the developed and optimized HILIC-MS/MS method. All analyses were performed in triplicate to ensure reproducibility and statistical validity. The cell lysate reflects the intracellular accumulation of analytes, representing TriPPPro-compound that successfully permeated the cell membrane. In contrast, the supernatant corresponds to the extracellular incubation medium, containing compounds that remained outside the cells and were not taken up by. Based on the ratio of the mean integrated peak area of each analyte to that of the ISD, the analyte concentrations were determined using the corresponding calibration curve. The calculated concentrations were initially obtained in ng/mL, including measurement uncertainty. For clarity and comparability, these values were converted to μM , as the incubations were performed using 10 μM of the respective compound. The determined concentrations for cellular uptake studies with the TriPPPro-compound 1 are summarized in Table 4-69. In the context of the cellular uptake studies performed with TriPPPro-compound 1, a particularly noteworthy observation is the significant intracellular accumulation of metabolites after just 1 hour of incubation. Quantitative analysis revealed that approximately 70 % of the total analyte concentration was located within the cells, while only about 30 % remained in the extracellular supernatant. This distribution strongly indicates an efficient and rapid cellular uptake of the prodrug with the first hour of incubation. Furthermore, the intracellular metabolite profile suggests that the TriPPPro-compound 1 undergoes enzymatic conversion upon cellular entry involving the stepwise cleavage of the masking units. This metabolic transformation appears to be very efficient and results in the release of active metabolites.

Table 4-69: Determined concentration Tri*PPP*ro-compound **1** and all resulting metabolites in cell lysate and supernatant samples after cellular uptake studies with HT29 cancer cells and different incubation times (1 h, 2 h, 6 h, 24 h).

Type of sample,	Determined concentration corrected by dilution factor of 10 [μM]							
incubation time	FdU 10	Tri <i>PPP</i> ro- compound 1	Intermediate 5	FdU-MP 9	FdU-DP 8	FdU-TP 7		
Cell lysate,	_*		0.82	1.13	0.44	2.18		
1h	-	-	± 0.013	± 0.00359	± 0.0019	± 0.00560		
Supernatant,		0.09	1.99					
1h	-	± 0.0004	± 0.00120	-	-			
Cell lysate,			0.21	0.99	0.28	1.99		
2h	-	-	± 0.014	± 0.0036	± 0.0019	± 0.00560		
Supernatant,			1.92					
2h	-	-	± 0.0012					
Cell lysate,			0.30	0.99	0.28	2.02		
6h	-	-	± 0.014	± 0.0036	± 0.0019	± 0.00563		
Supernatant,			0.89					
6h	-	-	± 0.0013	-	-	-		
Cell lysate,			0.15	1.03	0.27	1.99		
24h	-	-	± 0.0014	± 0.00361	± 0.0019	± 0.00564		
Supernatant,					3.68			
24h	-	<u>-</u>	•	-	± 0.00182	_		

Among these detected metabolites, FdU-TP 7 was found to be the predominant species after 1 hour of incubation, reaching a concentration of 2.18 μM. Due to its high polarity, the triphosphate is not able to passively diffuse back across the cellular membrane, thereby effectively "trapped" within the cells. This phenomenon is commonly referred to as the *lock-in* effect. In addition, a significant concentration of FdU-MP **9** was detected, with a measured level of 1.13 μM. This observation points to the occurrence of intracellular dephosphorylation of FdU-TP via the diphosphate to the monophosphate. This confirms the metabolic activity within the cells and provides information upon the measured antitumor activity of the prodrug. As outlined in section 2.1.3, FdU-TP and FdU-MP are the responsible metabolites for antitumor activity. This can be attributed to the incorporation of FdU-TP into the DNA during replication, resulting in the formation of abnormal DNA structures that interfere with essential cellular processes. This incorporation ultimately triggers DNA damage responses and leads to apoptosis. FdU-MP exerts its cytotoxic effect by inhibiting TS, the key enzyme responsible for catalyzing the methylation of dUMP to form thymidine monophosphate TMP. The inhibition of TS leads to an accumulation of dUTP and a concomitant depletion of TTP. This imbalance in nucleotide levels contributes to misincorporation events during DNA synthesis and further impairs DNA integrity, ultimately resulting in cell death.

However, the intracellular concentration of the intermediate, characterized by the cleavage of only one masking group, was found to be 0.82 μ M, suggesting the potential for continued intracellular metabolism leading to the release of more active metabolites. Figure 4-79 displays the EICs of the analytes detected in the cell lysate following the uptake study of Tri*PPP*ro-compound 1 in HT29 cancer cells.

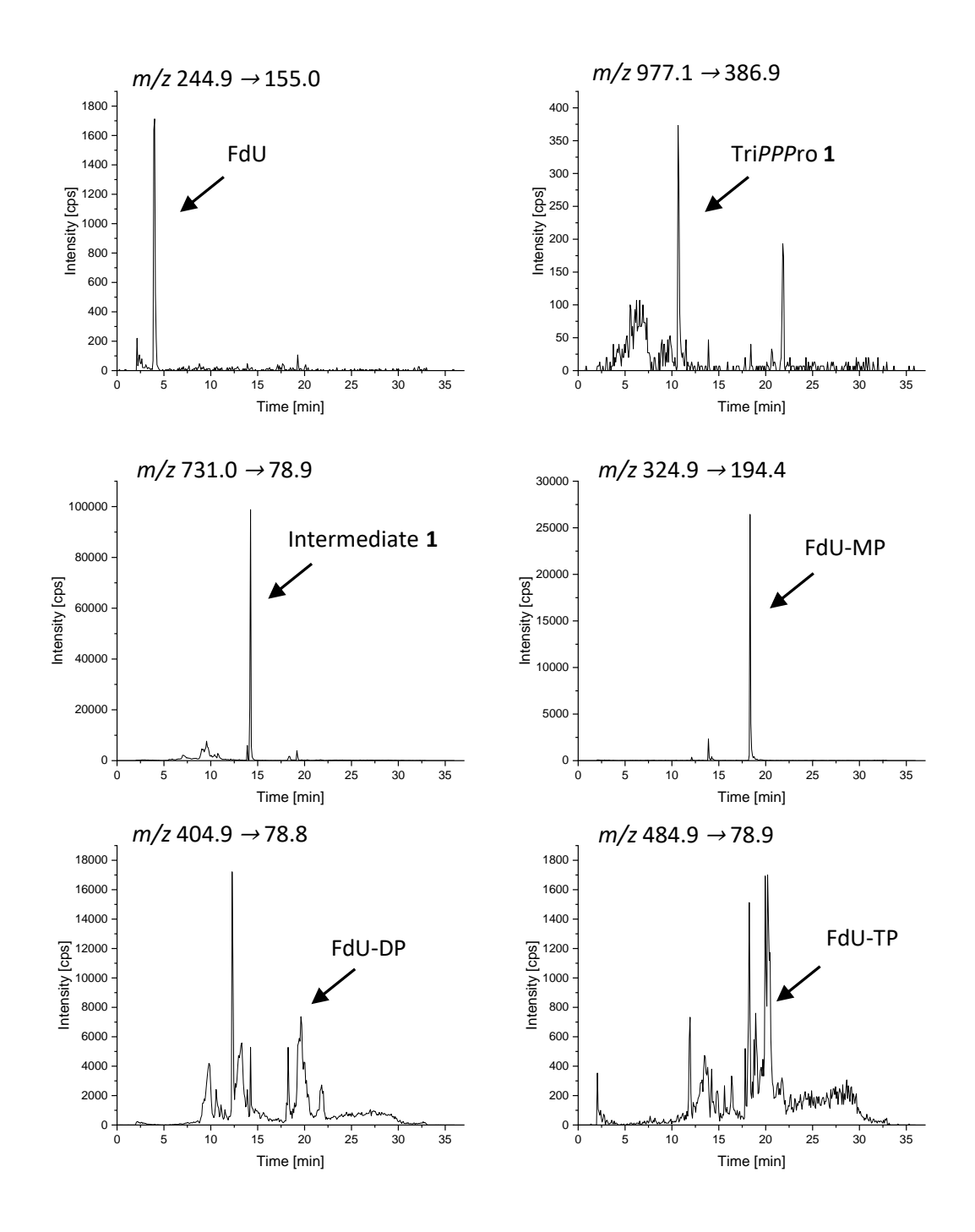


Figure 4-79: EICs of the quantifier of every analyte detected in HT29 cell lysate samples after cellular uptake study of Tri*PPP*ro-compound **1** after an incubation time of 1 h.

With regard to the supernatant, the quantification results suggest that the prodrug undergoes metabolic conversion via chemical hydrolysis within the incubation medium, which primarily consists of PBS buffer. This conclusion is supported by the detection of the mono-masked intermediate $\bf 5$ at a concentration of 1.99 μM in the supernatant sample. Due to its negatively charged functional groups and reduced

lipophilicity, this intermediate exhibit limited membrane permeability and is therefore unable to efficiently diffuse into the cells resulting in high extracellular concentration levels. These findings raised the question of whether extended incubation times would lead to higher intracellular concentrations of the pharmacologically active metabolites, particularly FdU-TP7 and FdU-MP9. However, cellular uptake studies conducted at incubation intervals of 2 hours, 6 hours, and 24 hours did not indicate any increase in the intracellular levels of the triphosphate. The concentrations remained relatively stable at approximately 2.0 μM, suggesting that maximum intracellular conversion occurs rapidly and does not further increase with longer incubation times. In contrast, the profile of extracellular metabolites evolved over time. While the monomasked intermediate was the predominant compound detected in the supernatant after 1, 2, and 6 hours, only FdU-DP 8 was observed after 24 hours. FdU-DP was detected with a concentration of 3.68 μ M. This metabolization from the intermediate directly to the diphosphate is likely due to a nucleophilic attack at the γ -phosphate group of the triphosphate moiety, a well described mechanism of chemical hydrolysis under physiological buffer conditions such as PBS.[195]

The determined concentrations for cellular uptake studies with TriPPProcompound 2 are summarized in Table 4-70. For comparison, cellular uptake studies were also conducted using a second prodrug, TriPPPro-compound 2, which features longer alkyl chains on the acyloxybenzyl masking groups. After 1 hour of incubation, approximately 78 % of the total quantified analyte concentration was detected intracellularly. This degree of cellular accumulation of all analytes is comparable to the uptake observed for TriPPPro-compound 1, indicating that the elongation of the alkyl chains does not significantly impair the cellular permeability of the prodrug under the tested conditions. These findings once again highlight the efficient cellular uptake of the TriPPPro-compound.

Table 4-70: Determined concentration Tri*PPP*ro-compound **2** and all resulting metabolites in cell lysate and supernatant samples after cellular uptake studies with HT29 cancer cells and different incubation times (1 h, 2 h, 6 h, 24 h).

Type of sample,	Determined concentration corrected by dilution factor of 10 [μM]							
incubation time	FdU 10	Tri <i>PPP</i> ro- compound 2	Intermediate 6	FdU-MP 9	FdU-DP 8	FdU-TP 7		
Cell lysate,	_*	0.09	3.60	1.45	0.22	1.99		
1h	-	± 0.0006	± 0.000834	± 0.0038	± 0.0019	± 0.00564		
Supernatant,		1.85	0.18					
1h	-	± 0.000225	± 0.0015	-	-	-		
Cell lysate,				1.67	0.34	2.14		
2h	-	-	-	± 0.0037	± 0.0019	± 0.00562		
Supernatant,		0.18						
2h	-	± 0.00027	-	-	-			
Cell lysate,			0.50	1.16	0.33	2.02		
6h	-	-	± 0.00092	± 0.0038	± 0.0019	± 0.00563		
Supernatant,	3.19 ±	0.30						
6h	0.00610	± 0.00026	-	-	-	-		
Cell lysate,			0.61	1.42	1.31	4.46		
24h	-	-	± 0.00091	± 0.00377	±0.0018	± 0.00508		
Supernatant,	_	0.05	_	_	_	_		
24h	-	± 0.0003						

The quantitative detection of various metabolites, including the monomasked intermediate **6**, FdU-TP **7**, FdU-DP **8** and FdU-MP **9**, provides further evidence for the intracellular cleavage of the masking units and the subsequent release of the active compound. In the case of Tri*PPP*ro-compound **2**, the predominant intracellular species was the intermediate **6**, detected at a concentration of 3.60 μ M. The concentration of the active metabolite FdU-TP **7** was measured at 1.99 μ M, which is consistent with the values reported in Table 4-69. Compared to Tri*PPP*rocompound **1**, the intracellular metabolic conversion of the Tri*PPP*ro-compound **2** appears to proceed more slowly, as evidenced by the higher amount of intermediate and lower accumulation of the metabolites FdU-TP, - DP and -MP. This suggests that the longer alkyl chains on the masking units influence the rate of enzymatic cleavage within the cells.

Moreover, extended incubation periods ranging from 6 hours to 24 hours with TriPPPro-compound 2 resulted in a partial increase in intracellular analyte concentration. A substantial amount of the total quantified metabolites was located within the cells, with 96 % detected intracellularly after 2 hours and as much as 99 % after 24 hours. These findings suggest that TriPPPro-compound 2 may possess greater chemical stability in the incubation medium compared to TriPPProcompound 1, thereby enabling a more sustained cellular uptake over time. The hypothesis is further supported by the comparison of analyte concentrations in the corresponding supernatants. In the case of TriPPPro-compound 1, only metabolites that are unlikely to penetrate the cell membrane, such as the intermediate or the diphosphate, were detected in the supernatant. By contrast, for TriPPProcompound 2, intact prodrug was still present extracellularly after incubation, indicating slower hydrolytic degradation in the puffer and an extended window for cellular uptake. As an example, after a 24-hour incubation period, a total of 7.19 μM of the metabolites FdU-MP, -DP, and -TP were found to be present within the cells, whereas only 3.29 μM of FdU-TP and FdU-MP were detected following a 24-hour incubation with TriPPPro-compound 1.

These findings are summarized in Figure 4-80. Black bars indicate all analytes detected following cellular uptake studies with Tri*PPP*ro-compound **1**, whereas grey bars correspond to those identified in studies using Tri*PPP*ro-compound **2**. Cell lysate samples are shown on the left side of the figure, while the corresponding supernatant samples are presented on the right. The different incubation times are denoted by labels a through d.

In summary, the release of active metabolites from prodrug compounds 1 and 2 is comparable. Only the stability against chemical and/or enzymatic hydrolysis is higher with TriPPPro-compound 2, which was also expected due to the longer alkyl chains. The quantification results demonstrate the highly efficient uptake of the prodrugs and the concentrations of the active metabolites responsible for the antitumor activity of the compounds.

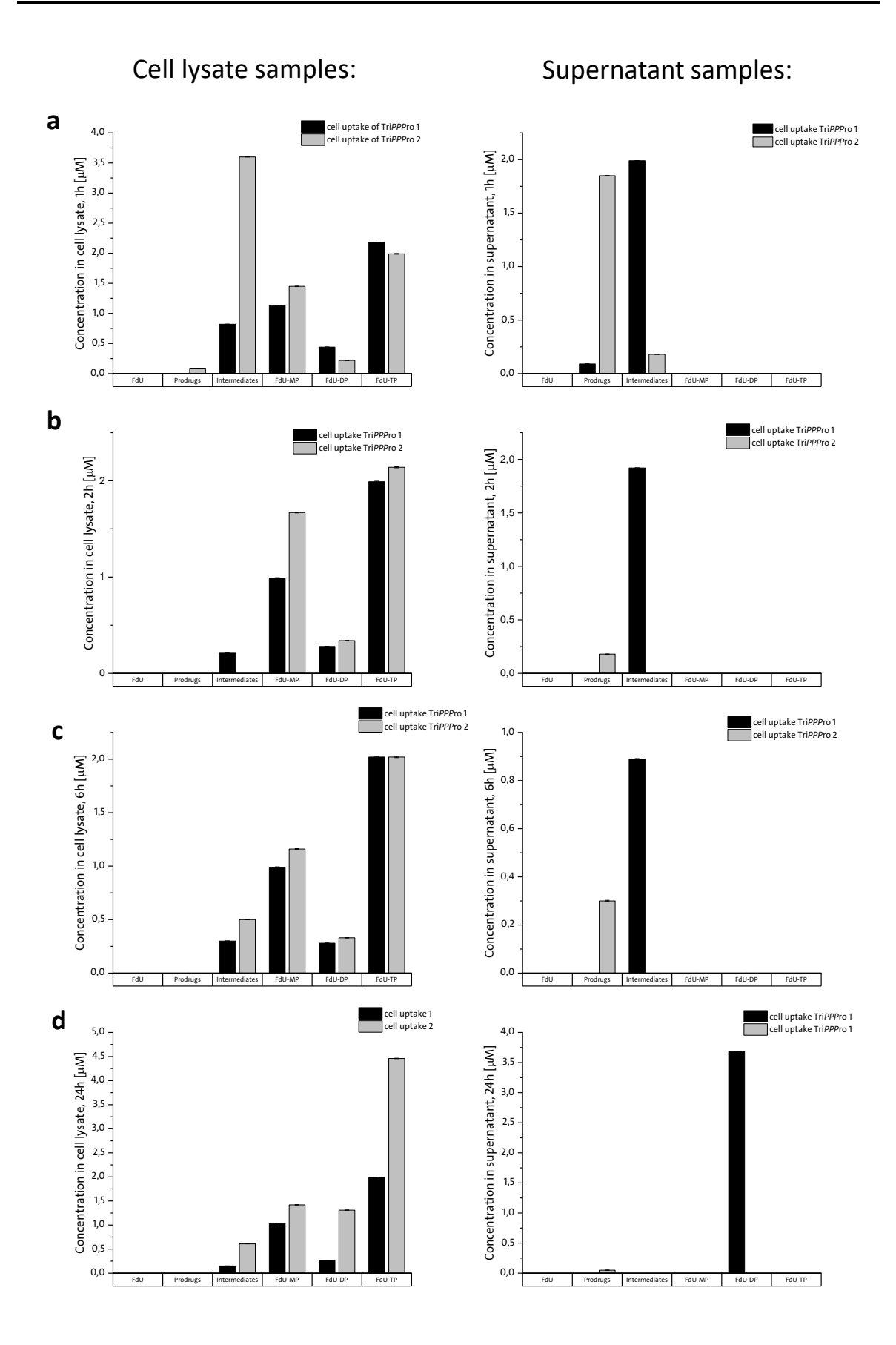


Figure 4-80: Determined concentrations of all analytes following cellular uptake studies with Tri*PPP*ro-compound **1** (black bars) and Tri*PPP*ro-compound **2** (grey bars). Cell lysate samples are displayed on the left and supernatant samples on the right after 1 h (a), 2 h (b), 6 h (c) and 24 h (d).

This antitumor activity was initially investigated by WITT^[61] with proliferation assays in different cancer cell lines. He found EC₅₀ values for Tri*PPP*ro-compound **1** of 2.9 μ M and for Tri*PPP*ro-compound **2** of 5.4 μ M in HT29 cells. With that, these compounds were significantly more active than the reference compound 5-FU.^[61] The summation of all metabolites identified and quantified from the respective Tri*PPP*ro-compounds enabled the determination of the overall recovery rate for each cell uptake study. Each cell uptake study was performed with a concentration of 10 μ M of the prodrug in the incubation solution. The results for Tri*PPP*ro-compound **1** are summarized in Table 4-71 and those for Tri*PPP*ro-compound **2** in Table 4-72. The overall recovery of the prodrug compounds **1** and **2**, along with their corresponding metabolites, was found to be moderate to very good, with recovery rates ranging between 43 to 94 %. As previously described in the sample preparation workflow (s. chapter 4.6, p. 134ff.), notably lower recoveries were observed for the intact prodrugs following cell lysis and subsequent LLE, in contrast to recovery rates of the metabolites.

Table 4-71: Overall recovery of TriPPPro-compound 1 after cellular uptake studies with HT29 cells.

Sample		Recovery [%]		
Zup.c	cell lysate	supernatant	overall	1,01
Cellular uptake, 1h	4.58	2.08	6.66	67
Cellular uptake, 2h	3.48	1.92	5.39	54
Cellular uptake, 6h	3.59	0.89	4.47	45
Cellular uptake, 24h	3.44	3.68	7.11	71

Table 4-72: Overall recovery of Tri*PPP*ro-compound **2** after cellular uptake studies with HT29 cells.

Sample		Recovery [%]		
Jap.c	cell lysate	supernatant	overall	necovery [/0]
Cellular uptake, 1h	7.34	2.03	9.36	94
Cellular uptake, 2h	4.15	0.18	4.33	43
Cellular uptake, 6h	4.01	3.49	7.50	75
Cellular uptake, 24h	7.79	0.05	7.84	78

One plausible explanation for this observation is the tendency of the prodrugs to precipitate due to their lipophilic character and amphiphilic structure, which may reduce their solubility during extraction. Additionally, another factor, though only indirectly related to the sample preparation, may be the dynamic behavior of the prodrugs during the incubation period. It is conceivable that the prodrug compound is capable of diffusing through the cell membrane in both directions until an equilibrium is reached. This raises the possibility that an amount of compound may be embedded within the lipid bilayer of the cellular membrane, rendering it inaccessible for detection in either intracellular (lysate) or extracellular (supernatant) samples. Such behavior appears to be unspecific and not easily reproducible, as indicated by variable recovery rates across different cellular uptake experiments. This variability may result from subtle differences in incubation conditions, membrane interactions, or compound stability, all of which influence the distribution and detection of the prodrugs.

4.8.2 Cellular uptake studies with SW620 cancer cells

Cellular uptake studies were also performed by incubating SW620 colorectal cancer cells with either 10 μ M of Tri*PPP*ro-compound **1** or **2** for varying durations of 1 h, 2 h, 6 h or 24 h. As previously described, following incubation, the samples underwent the established sample preparation procedure and spiking of the ISDs, after which both the cancer cell lysate and the corresponding supernatant were analyzed using the developed and optimized HILIC-MS/MS method. All analyses were performed in triplicate to ensure reproducibility and statistical validity. The obtained concentrations were converted into μ M and the results for the cell uptakes with Tri*PPP*ro-compound **1** are summarized in Table 4-73. After an incubation time of 1 hour, 86 % of the accumulated metabolites can be found inside the cells, which underlines the successful uptake for the compound in SW620 cells. All intracellularly

detected analytes exhibit relatively evenly distributed concentration levels of 1.39, 1.24, 1.46, and 1.05 μ M for the intermediate **5**, FdU-MP **9**, FdU-DP **8**, and FdU-TP **7**, respectively. The presence of these metabolites proves the successful uptake of the Tri*PPP*ro-compound **2** as well as the enzymatic cleavage of the masking units. The main metabolite detected in the supernatant after 1 hour is the intermediate with a concentration of 0.658 μ M. The intermediate was also metabolized in the PBS containing incubation medium, leading to the detection of 0.179 μ M of the monophosphate. Still, there was also a low concentration of 0.0338 μ M detected for the prodrug compound. In comparison to HT29 cells, the metabolization seemed to proceed faster in this cellular uptake studies, as evidenced by the detection of monophosphate in the supernatant after only 1 hour.

Table 4-73: Determined concentration Tri*PPP*ro-compound **1** and all resulting metabolites in cell lysate and supernatant samples after cellular uptake studies with SW620 cancer cells and different incubation times (1 h, 2 h, 6 h, 24 h).

Type of sample,		Determined concer	tration corrected b	y dilution fact	tor of 10 [μM]	
incubation time	FdU 10	Tri <i>PPP</i> ro- compound 1	Intermediate 5	FdU-MP 9	FdU-DP 8	FdU-TP 7
Cell lysate,			1.39 ±	1.24 ±	1.46 ±	1.05 ±
1h	-	-	0.000588	0.00164	0.00629	0.00441
Supernatant,		0.0228 ± 0.0004E4	0.658 ±	0.179 ±		
1h	-	0.0338 ± 0.000454	0.000725	0.00325	-	-
Cell lysate,		0.232 ± 0.000997	0.260 ±	9.69 ±	1.48 ±	1.08 ±
2h	-	0.232 ± 0.000997	0.000670	0.00179	0.00629	0.00439
Supernatant,		0.0667 ± 0.000454	0.0384 ±	0.235 ±		
2h	-	0.0667 ± 0.000454	0.000766	0.00325	-	-
Cell lysate,	_	_	0.175 ±	7.65 ±	1.48 ±	1.07 ±
6h			0.000670	0.00164	0.00629	0.00441
Supernatant,				0.274 ±	_	
6h				0.00325		
Cell lysate,		_	0.172 ±	6.67 ±	1.47 ±	1.08 ±
24h	-	-	0.000670	0.00158	0.00629	0.00439
Supernatant,				0.273 ±	_	
24h	•	•	•	0.00325		

To investigate further the metabolic conversion after prolonged incubation times, the incubation was also carried out for 2 hours, 6 hours and 24 hours. After all cellular uptake studies, the majority (97 %) of the analytes were found intracellular. The concentration of intermediate 5 slowly decreased after 2 hours, 6 hours and also 24 hours, leading to higher amounts of active metabolites. While FdU-DP and FdU-TP exhibited relatively constant concentration levels of approximately 1.50 μM and 1.08 µM, the main metabolite was the monophosphate with 9.69, 7.65 and 6.67 μM. This finding indicates the progressing metabolization of the intermediate, to the triphosphate, diphosphate and finally the monophosphate. As the concentration level of the MP was also slowly decreasing with prolonged incubation times, the formation of the nucleoside, FdU 10, would be expected. Nevertheless, no FdU was detected in the cell lysate samples. Metabolization of the prodrugcompound as well as the intermediate also occurred in the supernatant. While a small amount of prodrug was still detectable after 2 hours, FdU-MP emerged as the predominant metabolite after 6 hours and 24 hours. Since the metabolite is no longer able to diffuse into the cells due to its free charges, this aligns with the observation that the cellular uptake of the prodrug remained unchanged over time, despite extended incubation periods.

To summarize the results presented in Table 4-73, it can generally be concluded that the prodrug compound is rapidly taken up and metabolized, with FdU-MP emerging as the predominant intracellular metabolite after 2 and 6 hours. Additionally, FdU-DP and FdU-TP were also detectable within the cells. Among these, FdU-MP and FdU-TP are known to contribute to the antitumoral activity of the Tri*PPP*rocompound 1.

In comparison, the cellular uptake studies were also conducted with the second prodrug, Tri*PPP*ro-compound **2**, bearing longer alkyl chains. The results of the quantification are summarized in Table 4-74. After 1 hour of incubation, the majority of the analytes were found to be intracellular with 94 %. The predominant metabolite was FdU-MP **9** at a concentration of $4.34 \,\mu\text{M}$. Besides, Tri*PPP*ro-

compound **2**, intermediate **6** as well as FdU-DP **8** and FdU-TP **7** have also been detected. This proofs the highly successful take up of the prodrug-compound with SW620 cells, which is even better in comparison to the Tri*PPP*ro-compound **1**. The prodrug was metabolized within the cells to release the active metabolites FdU-TP and FdU-MP in relatively high concentrations. After 1 hour, the prodrug compound as well as the monomasked intermediate have been quantified in the supernatant with $0.456~\mu M$ and $0.0374~\mu M$, respectively. The prodrug gets metabolized by chemical hydrolysis in the incubation medium. With prolonged incubation times, the accumulation of metabolites inside the cells shows that 82 % to 97 % of the compound was taken up. Longer incubation times resulted in the intracellular metabolization of the intermediate **6**. After 24 hours, only $0.0843~\mu M$ was detected.

Table 4-74: Determined concentration Tri*PPP*ro-compound **2** and all resulting metabolites in cell lysate and supernatant samples after cellular uptake studies with HT29 cancer cells and different incubation times (1 h, 2 h, 6 h, 24 h).

Type of sample,	Determined concentration corrected by dilution factor of 10 [μM]						
incubation time	FdU 10	Tri <i>PPP</i> ro- compound 2	Intermediate 6	FdU-MP 9	FdU-DP 8	FdU-TP 7	
Cell lysate,		0.124 ±	1.36 ± 0.000711	4.34 ±	1.49 ±	1.05 ±	
1h	-	0.000392	1.30 ± 0.000711	0.00155	0.00629	0.00441	
Supernatant,		0.456 ±	0.0374 ±				
1h	-	0.00169	0.00142	-	-	-	
Cell lysate,			0.275 ±	15.5 ±	1.49 ±	1.06 ±	
2h	-	-	0.00997	0.00622	0.00629	0.00441	
Supernatant,		2.69 ±	1.21 ± 0.00128			-	
2h	-	0.000820	1.21±0.00128	-	-		
Cell lysate,	_	_	0.202 ±	15.5 ±	1.50 ±	1.06 ±	
6h	_	_	0.000776	0.00418	0.00629	0.00441	
Supernatant,		0.500 ±	0.0154 ±				
6h	-	0.000811	0.00142	-	-	-	
Cell lysate,			0.0843 ±	3.74 ±	1.49 ±	1.06 ±	
24h	-	-	0.000776	0.00155	0.00629	0.00441	
Supernatant,		0.0323 ±	0.0137 ±	0.249 ±			
24h	_	0.000866	0.00142	0.00325	•	•	

While the concentration levels of FdU-DP **8** and FdU-TP **7** remained relatively constant and comparable to the cellular uptake of Tri*PPP*ro-compound **1**, very high concentration levels of the MP were detected after 2 hours and after 6 hours. These elevated concentration levels need to be considered carefully, as the recovery rates for the MP were unusually high in spike-in experiments during validation experiments for SW620 cell lysate. Nevertheless, it is likely that the monophosphate is present at higher concentration levels than the other detected metabolites, as the effect with elevated recovery rates was directly related to the amount of analyte spiked onto the cell pellet.

It was previously hypothesized that prodrug 2 exhibited higher chemical stability due to the longer alkyl chains, which was further confirmed by the detection of the prodrug in the supernatant of the cellular uptake even after 24 hours. The prodrug compound is also metabolized resulting in the detection of intermediate concentrations ranging from 1.21 μ M and 0.0137 μ M. The intermediate is further metabolized and dephosphorylated, leading to the detection of 0.249 μ M of monophosphate after 24 hours.

These findings are summarized in Figure 4-81. Black bars display all analytes detected following cellular uptake studies with TriPPPro-compound 1, whereas grey bars correspond to those identified in studies using TriPPPro-compound 2. Cell lysate samples are shown on the left side of the figure, while the corresponding supernatant samples are presented on the right. The different incubation times are denoted by labels a through d. The direct comparison between the cellular uptake and the metabolism of TriPPPro-compound 1 and 2 reveals differences in their pharmacokinetic behavior. While prodrug 1 was rapidly metabolized and barely detectable in the cell lysate and supernatant samples, the prodrug 2 was quantified even after 24 hours of incubation time in the medium. This indicates slower uptake or delayed conversion. Furthermore, TriPPPro-compound 2 led to increased intracellular levels of FdU-MP at 2 hours and 6 hours (15.5 μ M), compared to a maximum of 9.69 μ M observed with TriPPPro-compound 1.

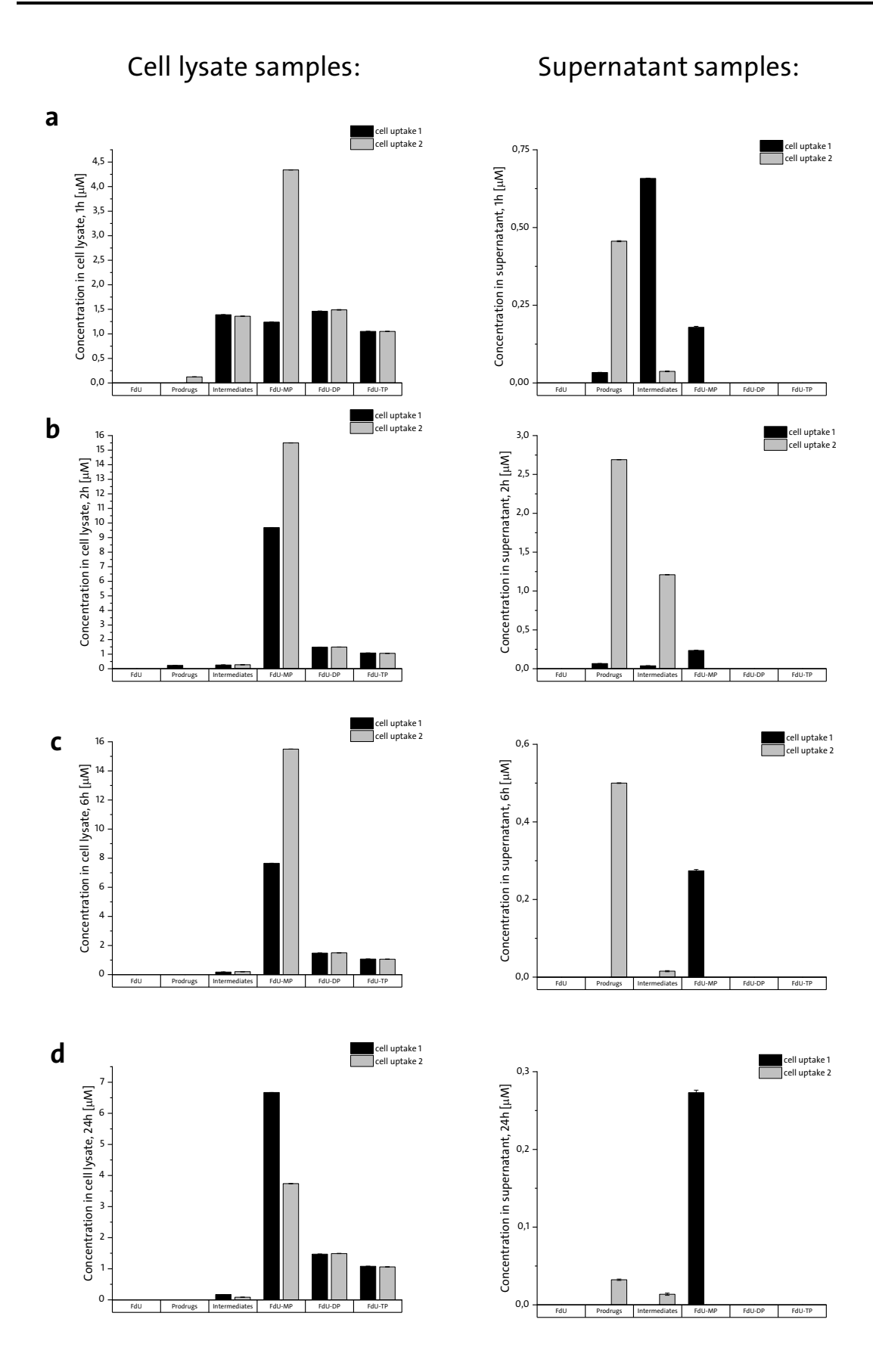


Figure 4-81: Determined concentrations of all analytes following cellular uptake studies with Tri*PPP*ro-compound **1** (black bars) and Tri*PPP*ro-compound **2** (grey bars). Cell lysate samples are displayed on the left and supernatant samples on the right after 1 h (a), 2 h (b), 6 h (c) and 24 h (d).

These findings suggest that Tri*PPP*ro-compound **2** may exhibit higher antitumoral activity in SW620 cells through prolonged systemic availability and more efficient release of the active metabolite. This hypothesis is supported by the EC₅₀ values after proliferation assays of these compounds reported by WITT. [61] For Tri*PPP*rocompound **1**, a EC₅₀ values of 2.8 μ M was determined, while Tri*PPP*ro-compound **2** displayed a EC₅₀ value of 0.07 μ M, which is more than 150-fold higher than the reference substance 5-FU. [61] By summing all metabolites identified and quantified from the respective Tri*PPP*ro-compounds, the overall recovery rate for each cell uptake study was determined again. The results for Tri*PPP*ro-compound **1** are summarized in Table 4-75 and for Tri*PPP*ro-compound **2** in Table 4-76. While the overall recovery after cellular uptake studies with Tri*PPP*ro-compound **1** are moderate to very good ranging from 60 % to 131 %, the overall recovery after cellular uptake studies with Tri*PPP*ro-compound **1** higher than anticipated.

Table 4-75: Overall recovery of TriPPPro-compound 1 after cellular uptake studies with SW620 cells.

Sample		Recovery [%]		
Sample	cell lysate	supernatant	overall	Recovery [70]
Cellular uptake, 1h			6.01	60
Cellular uptake, 2h	12.7	0.34	13.1	131
Cellular uptake, 6h	10.4	0.27	10.6	106
Cellular uptake, 24h	9.39	0.27	9.66	97

Table 4-76: Overall recovery of TriPPPro-compound 2 after cellular uptake studies with SW620 cells.

Sample		Recovery [%]		
Jup.c	cell lysate	supernatant	overall	,,,,
Cellular uptake, 1h			8.85	89
Cellular uptake, 2h	18.3	3.9	22.2	222
Cellular uptake, 6h	18.3	0.52	18.8	188
Cellular uptake, 24h	6.38	0.29	6.68	67

Recovery rates of 222 % and 188 % suggest that some analyte signals were enhanced due to composition of the matrix or other effects that were already discussed during validation experiments (section 4.7.3.7, p. 154 ff). Unfortunately, there was no explanation found for this phenomenon and therefore it was not possible to compensate for the high recovery rates.

4.8.3 Cellular uptake studies with CEM/O virus cells

With the adaptation of the HILIC-MRM method to the d4T derivatives, the quantification of TriPPPro-compounds 3 and 4 should also be performed after cellular uptake studies with CEM/O cells. TriPPPro-compounds 3 and 4 were incubated at a concentration of 10 µM for 1 hour. After incubation, the cell pellet and the incubation medium were processed using the established LLE protocol, ISDs were spiked in, and both the cell lysate and the supernatant samples were analyzed in triplicate. All detected compounds were quantified using the constructed calibration curves, and the results were converted from ng/mL to μM for comparability. The results for the cellular uptake with TriPPPro-compound 3 are summarized in Table 4-77. After accumulation of all analytes, 79 % were found to be intracellular, which underlines again the successful cellular uptake of the prodrug and the highly efficient TriPPPro-concept. The main metabolite in the cell lysate was the monomasked intermediate 11 with 4.76 μM, where the AB mask bearing a C2 alkyl chain, is cleaved off. Besides, d4T-DP 14, d4T-MP 15 and also the nucleoside d4T 16 have been detected. This also confirms the metabolization of the prodrug compound after the successful uptake. Nevertheless, a relatively high concentration of TriPPProcompound 3 was still observed at 2.00 µM, leading to the conclusion that the prodrug compound is taken up rapidly, but intracellular conversion proceeds slowly. This may be attributed to enhanced stability due to the long alkyl chain (C16) on one of the asymmetric masking units.

Table 4-77: Determined concentration Tri*PPP*ro-compounds **3** and all resulting metabolites in cell lysate and supernatant samples after cellular uptake studies with CEM/O virus cells after incubation time of 1 h.

Type of sample,	Determined concentration corrected by dilution factor of 10 [μM]							
incubation time	d4T 16	Tri <i>PPP</i> ro- compound 3	Intermediate 11	d4T-MP 15	d4T-DP 14	d4T-TP 13		
Cell lysate	0.711 ±	2.00 ±	4.76 ±	0.632 ±	1.79 ±			
	0.00370	0.000461	0.000801	0.00408	0.00640	-		
Supernatant	1.47 ±	1.20 ±						
	0.000821	0.00317	-	-	-	-		

In the supernatant, the predominant metabolite detected was the nucleoside, d4T **16** at a concentration of 1.47 μ M. The second analyte detected was the prodrug at a concentration of 1.20 μ M. It is gradually metabolized to the nucleoside through chemical hydrolysis.

Cellular uptake studies were also conducted for the second prodrug, Tri*PPP*rocompound **4**. The quantification results after 1 hour of incubation with 10 μ M of the compound are summarized in Table 4-78. As previously described, the prodrug **4** carries asymmetric protecting groups consisting of one AB masking unit and one enzyme-stable alkyl chain. As a result, only a single metabolite is formed upon enzymatic conversion. First of all, significantly higher concentrations were found to be intracellular, suggesting a highly efficient uptake of the prodrug with 81 %. The main metabolite detected was the Tri*PPP*ro-compound **4** with over 5.61 μ M. Unfortunately, the ratio of analyte peak area to ISD peak area was above the upper limit of quantification for that compound. Nevertheless, the intermediate **12** was also detected at a concentration of 0.0316 μ M. This suggests that the compound is taken up rapidly by the cells, whereas its metabolic conversion proceeds more slowly. This hypothesis is further supported by the enhanced stability of the compound in the incubation medium. The prodrug was not metabolized and remained detectable at a concentration of 1.32 μ M, while no intermediate was observed. The enhanced

stability was already described in hydrolysis studies in CEM cell extracts performed by JIA, where the prodrug proved to be highly stable.^[134]

Table 4-78: Determined concentration Tri*PPP*ro-compound **4** and all resulting metabolites in cell lysate and supernatant samples after cellular uptake studies with CEM/O virus cells after incubation time of 1 h.

Type of sample,	Determined concentration corrected by dilution factor of 10 [μM]				
incubation time	Tri <i>PPP</i> ro-compound 4	Intermediate 12			
Cell lysate	> 5.61 ± 0.00508	0.0316 ± 0.00260			
Supernatant	1.32 ± 0.00121	-			

The results for both prodrugs are also summarized in Figure 4-82. Black bars represent the cell uptake with Tri*PPP*ro-compound **3** and grey bars show the results after cell uptake with Tri*PPP*ro-compound **4**.

In general, in both cellular uptake studies confirmed efficient uptake and intracellular metabolization of the Tri*PPP*ro-compounds into their active metabolites, as evidenced by the quantification results. Tri*PPP*ro-compound **3** was metabolized more rapidly than Tri*PPP*ro-compound **4**. Nevertheless, in both cases, the intermediate was detected. For prodrug **3**, further conversion into the dephosphorylated metabolites d4T-DP **14** and d4T-MP **15** was also observed.

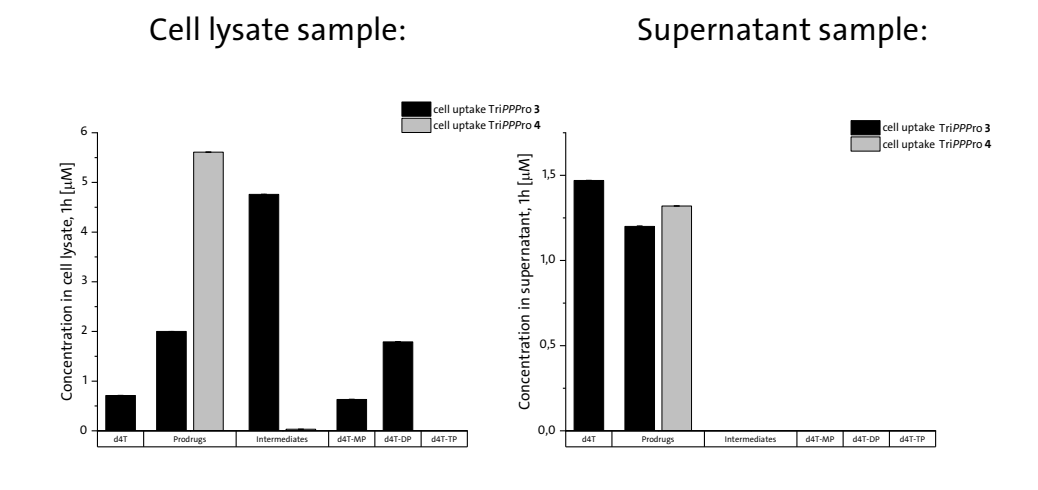


Figure 4-82: Determined concentrations of all analytes following cellular uptake studies with Tri*PPP*ro-compound **3** (black bars) and Tri*PPP*ro-compound **4** (grey bars). Cell lysate samples are displayed on the left and supernatant samples on the right.

Both Tri*PPP*ro-compounds have previously been evaluated in prior research for their antiviral activity to inhibit HIV replication in HIV-1 and HIV-2 infected wild-type CEM/0 cell cultures, as reported by JIA. [55,134] The resulting EC50 values for prodrug **3** were 0.027 μ M and 0.0048 μ M for HIV-1 and HIV-2, respectively. [55] For the prodrug compound **4**, EC50 values of 0.031 μ M and 0.035 μ M were determined, respectively. [134] Thus, both compounds demonstrated approximately 100-fold higher antiviral activity compared to the reference compound d4T.

As previously described for the FdU derivatives, the overall recovery rates for each cellular uptake study involving the d4T derivatives were likewise determined by summing all metabolites identified and quantified from the respective TriPPProcompounds. The results for the determined recoveries are displayed in Table 4-79 for TriPPProcompound 3 and in Table 4-80 for TriPPProcompound 4. While the overall recovery rate of the TriPPProcompound 3 appears slightly elevated at 126 %, the recovery rate for TriPPProcompound 4 is approximately 70 %. However, the actual recovery for compound 4 is likely underestimated, as the detected amount of prodrug compound exceeded the upper limit of quantification.

Table 4-79: Overall recovery of TriPPPro-compound 3 after cellular uptake studies with CEM/0 cells.

Sample		Recovery [%]		
	cell lysate	supernatant	overall	necestery [/0]
Cellular uptake, 1h	9.89	2.67	12.6	126

Table 4-80: Overall recovery of Tri*PPP*ro-compound **4** after cellular uptake studies with CEM/0 cells.

Sample		Recovery [%]		
	cell lysate	supernatant	overall	
Cellular uptake, 1h	> 6.93	0.03	> 6.96	> 70

4.8.4 Conclusion

The cellular uptake studies of the investigated TriPPPro-compounds clearly demonstrated the successful uptake and intracellular conversion of the prodrugs into their pharmacologically active metabolites. For the FdU-based derivatives (TriPPPro-compounds 1 and 2), rapid uptake and efficient metabolization were observed, particularly for compound 2, which yielded probably high intracellular levels of the FdU-MP 9. The presence of the longer alkyl chain at the AB mask contributed to its enhanced chemical stability, as indicated by the determined concentration level in the supernatant even after 24 hours. In contrast, TriPPProcompound 1 showed lower intracellular concentration of the MP and a faster hydrolysis in the supernatant, indicating a less chemically stable prodrug structure. Nevertheless, both compounds led to the formation of the TP and MP, which are considered active species responsible for the antitumor activity. To visualize the overall distribution and metabolic conversion of TriPPPro-compounds 1 and 2 in HT29 and SW620 cells, a schematic representation was used (Figure 4-83 and Figure 4-84), in which the size of each circle indicates the concentration of individual metabolites.

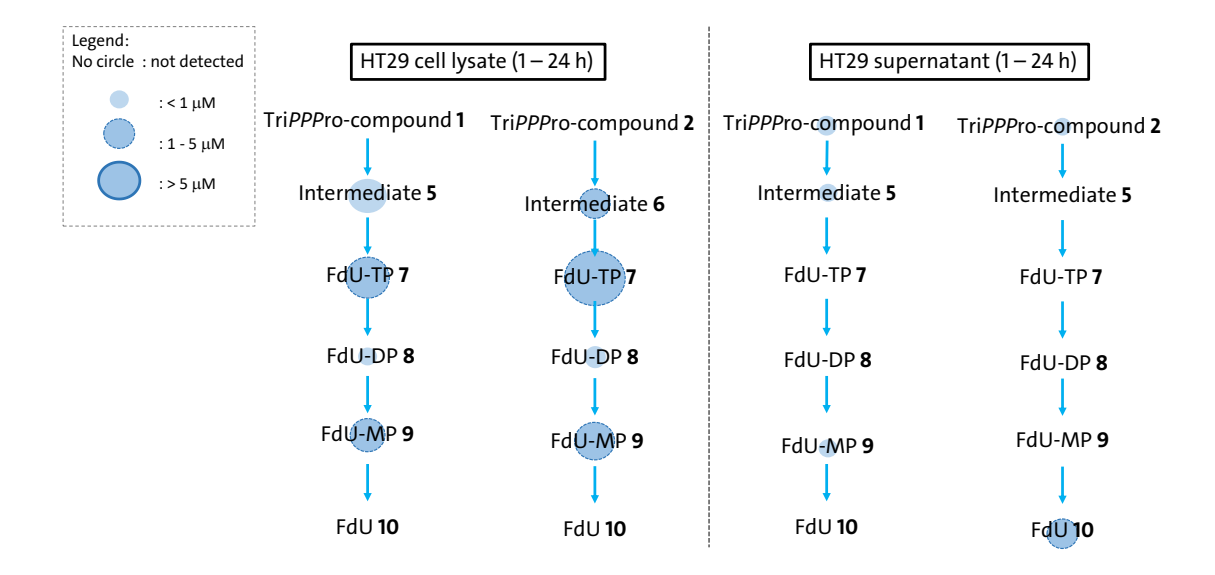


Figure 4-83: Schematic representation of the distribution of TriPPPro-compound 1 and 2 in HT29 cell lysate and supernatant quantified after cellular uptake studies. Circle size indicates metabolite concentration: absent (no circle), $< 1 \mu M$ (small), $1 - 5 \mu M$ (medium), $> 5 \mu M$ (large).

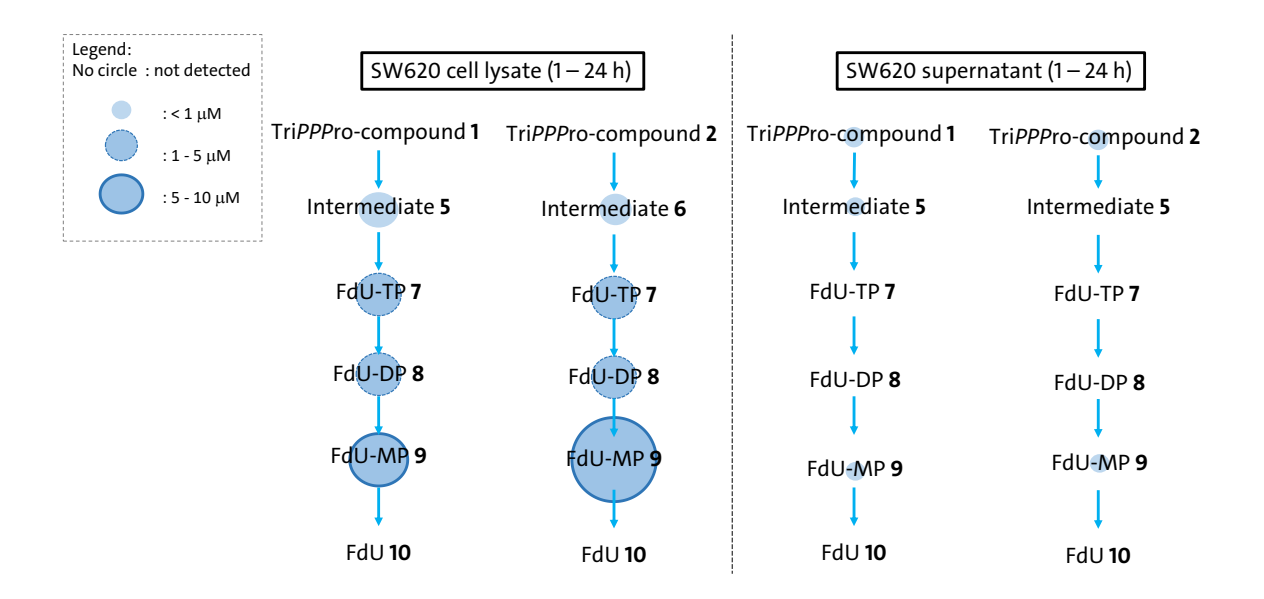


Figure 4-84: Schematic representation of the distribution of Tri*PPP*ro-compound **1** and **2** in SW620 cell lysate and supernatant quantified after cellular uptake studies. Circle size indicates metabolite concentration: absent (no circle), $< 1 \,\mu\text{M}$ (small), $1 - 5 \,\mu\text{M}$ (medium), $> 5 \,\mu\text{M}$ (large).

Since concentration trends were comparable across all incubation times (1, 2, 6, and 24 h), mean values were used.

The d4T-based derivatives (Tri*PPP*ro-compound **3** and **4**) also confirmed effective cellular uptake. Compound **3**, bearing symmetric masking groups, exhibited rapid metabolism with the formation of the intermediate **11** as well as the d4T-MP **15** and d4T-TP **14**. In contrast, compound **4**, carrying asymmetric protecting groups, demonstrated slower metabolic conversion. Overall, the intracellular formation of the mono- and dephosphorylated metabolites, combined with antiviral activity data, underscores the pharmacological potential.

For these two additional cellular uptake experiments in CEM/O cells with TriPPProcompound **3** and **4**, the same graphical representation was chosen to summarize the results (Figure 4-85). This schematic approach, using circle sizes to indicate metabolite concentrations, facilitates a clear and concise comparison of metabolic profiles across different cell models.

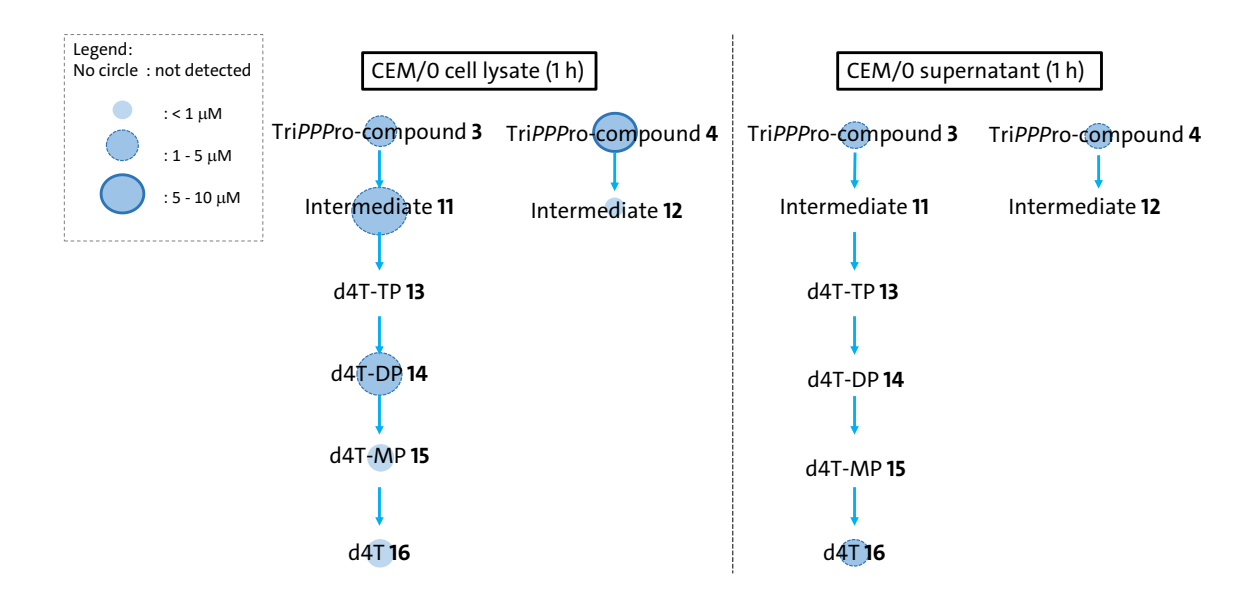


Figure 4-85: Schematic representation of the distribution of Tri*PPP*ro-compound **3** and **4** in CEM/0 cell lysate and supernatant quantified after cellular uptake studies. Circle size indicates metabolite concentration: absent (no circle), $< 1 \,\mu\text{M}$ (small), $1 - 5 \,\mu\text{M}$ (medium), $> 5 \,\mu\text{M}$ (large).

The development of a quantification method enabling the simultaneous analysis of both lipophilic Tri*PPP*ro-compounds and all hydrophilic metabolites made it possible, for the first time, to obtain comprehensive data on both the cellular uptake and metabolic conversion of the prodrugs.

Across all cellular uptake studies, the Tri*PPP*ro-approach proved highly successful and robust, regardless of the structural diversity of the Tri*PPP*ro-compounds. The prodrugs varied significantly in their masking units, alkyl chain lengths, and chemical stabilities, yet efficient uptake into tested cells was consistently observed. Even with different incubation times ranging from 1 to 24 hours, a substantial amount of prodrug or its associated metabolites were found intracellularly. Notably, in every study, at least 70 % of the initially incubated compound (10 μ M) was taken up by the cells, confirming the efficiency of the Tri*PPP*ro-strategy across multiple antiviral or antitumoral nucleoside analogues and chemical modifications.

5 Experimental section

5.1 General

5.1.1 Experimental workflow

The following workflow was established for the quantitative analysis of prodrugs and their metabolites in cell-based assays:

1) Cell incubation with prodrugs

Cells were incubated with the respective prodrugs under defined experimental conditions, as described in section 5.9.

2) Sample storage post-incubation

Following incubation, both the cell pellets and the corresponding supernatants were collected and stored at $-80\,^{\circ}\text{C}$ until the day of analysis to preserve compound stability.

3) Preparation of the LC-MS/MS system

On the day of analysis, the LC-MS/MS system was prepared according to the procedures detailed in section 5.7.

4) Sample preparation

Sample preparation included the processing of CS samples, QC samples, and unknown samples, as outlined in sections 5.1.3 and 5.1.4.

5) Sample sequence design

A standardized injection sequence was used for all analytical runs. This included two double blanks (solvent only), one blank matrix sample (cell lysate or supernatant), calibration standards (in duplicate), QC samples (in duplicate), followed by the unknown samples.

6) Data analysis

Data analysis was performed using the Analyst software (Sciex). Peak areas of the respective quantifier ions were integrated, and QC samples were evaluated to ensure method validity. The concentrations of the unknown samples were then calculated based on the external calibration curve.

5.1.2 Graphical workflow

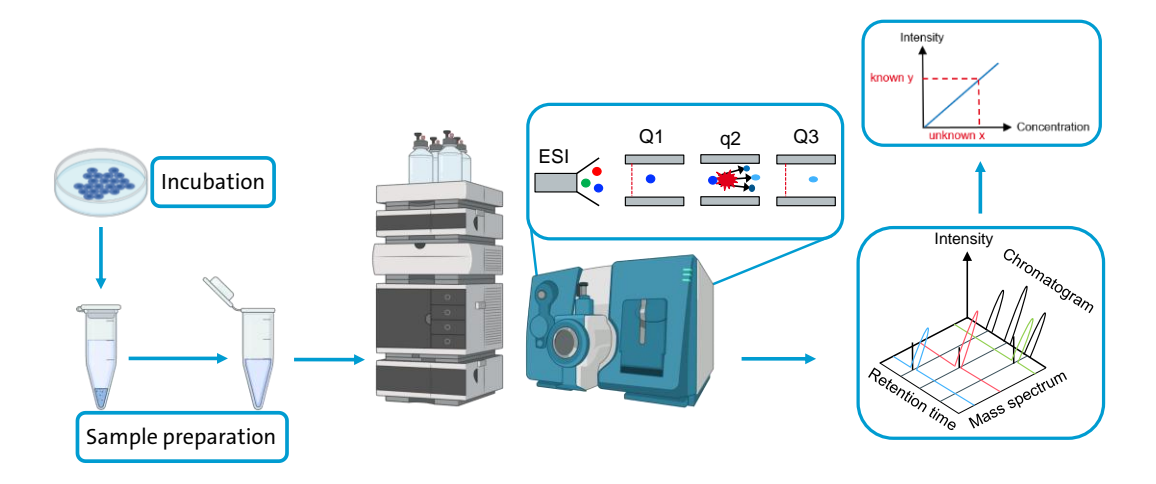


Figure 5-1: Graphical workflow for the quantitative analysis of prodrugs and their metabolites after cellular uptake studies.

5.1.3 Starting materials, reagents and solvents

The analytes 5-FdU-TP **7**, intermediate **5**, Tri*PPP*ro-compound **1** and **2** were gratefully provided by WITT.^[61]

The analytes d4T-DP **14**, d4T-TP **13**, intermediate **12**, Tri*PPP*ro-compound **3** and **4** were gratefully provided by JIA.^[136]

All starting materials and reagents for syntheses were purchased from commercial suppliers in synthesis quality and were used without further purification. All additives for LC-MS/MS measurements were purchased for LC-MS LiChropur™ from Merck.

Solvents for extraction and column chromatography (dichloromethane, ethyl acetate, methanol, and petroleum ether) were purchased in technical quality and distilled under atmospheric pressure. All other solvents were used as purchased from commercial suppliers in analytical quality (Fisher Scientific, Merck, VWR).

The anhydrous solvents were purchased from commercial suppliers (Acros Organics, Fisher Scientific, Merck, VWR).

The deuterated solvents chloroform (CDCl₃), dimethyl sulfoxide (DMSO- d_6), methanol (MeOH- d_4) and water (D₂O) were purchased from commercial suppliers (Deutero, Eurisotop).

Ultrapure water was generated under UV irradiation by a Sartorius Arum pro unit (Sartopore $0.2~\mu M$).

Solvents for LC-MS/MS measurements were purchased from VWR in LC-MS grade.

The buffer for RPIP-UV measurements was prepared in ultrapure water and the pH value was set using acetic acid (1 M).

All buffers for LC-MS/MS measurements were prepared in LC-MS grade water and acetonitrile with LC-MS grade additives.

5.1.4 Sample preparation for LC-MS/MS measurements

Cancer cells were incubated with 10 μ M TriPPPro-compound for different time periods (1 h, 2 h, 6 h, 24 h). CEM/O cells were incubated for 1 h (detailed description in section 5.9). Two samples were generated: supernatant and cell pellet. Both were stored at -80 °C until analysis. In order to ensure comparability of the quantification results for every analyte, it was necessary to conduct a cell count on the pellet. The aim was to obtain 5 million cells per mL for each sample.

The cells were lysed by suspending the pellet in a mixture of MTBE, methanol and water with a phosphatase inhibitor, followed by homogenization for three minutes. After 10 minutes on ice and centrifugation at 4 °C for 10 minutes at 14000 rpm, 50 μ L were collected from each layer and diluted with 400 μ L of an acetonitrile:water mixture (95:5, % v/v). After vortexing, 0.5 μ L of internal standard was added and samples transferred to autosampler vials.

50 μ L of supernatant were transferred to a fresh tube with 200 μ L MTBE, 60 μ L methanol and 15.5 μ L water. The sample was vortexed, placed on ice for 10 minutes and then centrifuged at 4 °C for 10 minutes at 14.000 rpm. 50 μ L of the supernatant from each layer was diluted with 400 μ L of an acetonitrile:water mixture (95:5, % v/v), vortexed, and transferred to autosampler vials.

5.1.5 Preparation of calibration standards and quality controls

Cancer and CEM/0 cells were incubated in a medium containing 100 μ L of PBS buffer or DMSO (mock samples). Cell pellets and the supernatant were processed as outlined in the sample preparation section. Double blanks had no internal standards. Cell lysate and supernatant samples were stored at -80 °C.

Stock solutions of the analytes were prepared at 1 mg/mL in acetonitrile/water (1:1, % v/v) and stored at -20 °C.

Prior to LC-MS/MS measurements, a working solution was prepared from the stock solution. It was spiked into a blank cell lysate or supernatant to obtain six non-zero CS samples. Similarly, QC samples were prepared at varying concentration levels.

5.2 Chromatography

5.2.1 Thin layer chromatography

For TLC, aluminum foils coated with silica gel and fluorescent indicator (Macherey-Nagel ALUGRAM® Xtra SIL G/UV254 No. 818333; layer thickness 0.2 mm) were utilized. All R_F -values were determined at chamber saturation, with a running distance of 8 cm. UV active compounds were detected using a UV lamp at a wavelength of 254 nm. A mixture of 5 g ammonium molybdate, 1 g cerium (IV) sulfate, 10 mL concentrated H_2SO_4 and 90 mL distilled water was used as staining reagent.

5.2.2 Column chromatography

For purification with column chromatography, silica gel was purchased from Macherey-Nagel (silica gel 60 M, 0.04-0.063 mm, 230-400 mesh).

5.2.3 Ion exchange chromatography

For ion exchange of the counter ions, DOWEX 50 W I8 ion exchange resin was purchased from Merck. The resin was stored in a 10 % ammonia solution and protected from sunlight.

5.2.4 Automated NP / RP chromatography

Automated chromatography was carried out using the PuriFlash® 430 from interchim for NP and RP chromatography. For NP chromatography, empty cartridges were packed with silica gel from Macherey Nagel (described in Column chromatography) For RP chromatography, CHROMABOND Flash RS 120 or 40 C18 ec from Macherey Nagel were used.

5.2.5 RPIP-UV chromatography

RPIP-UV measurements were carried out on a 1260 Infinity II from Agilent Technologies. The HPLC is equipped with a 1260 Quat Pump VL, 1260 vial sampler, 1260 Dide Array Detector (DAD) and the software used for analysis was Agilent Open Lab CDS. Measurements were performed with an analytical column from Macherey Nagel (EC 125/3 NUCLEODUR 100-5 C18 ec), preceded by a guard column from Macherey Nagel (EC 4/3 NUCLEODUR 100-5 C18 ec). The column compartment was operated at 25 °C.

Gradient elution was carried out using TBAA buffer (2 mM) as IP reagent and acetonitrile as mobile phases. The mobile phases were delivered at 1.0 mL/min as stepwise gradient: 0-20 min: TBAA buffer with 5-80 % of acetonitrile, 20-30 min:

isocratic (20 % TBAA buffer, 80 % acetonitrile), 30-33 min: TBAA buffer with 80-5 % of acetonitrile, 33-34 min: isocratic (95 % TBAA buffer, 5 % acetonitrile). UV detection was performed using the following wavelengths: 250 nm, 260 nm, 265 nm and 270 nm.

TBAA buffer (2 mM) was prepared using 2000 mL ultrapure water and 10.1 mL of tetra-*n*-butylammonium hydroxide in water (~40 %). The pH value was adjusted using acetic acid solution (1 M) to 6.0.

5.3 Infrared spectroscopy

Infrared spectroscopy (IR) was carried out using a Bruker Alpha P FT-IR (software: OPUS) employing the attenuated total reflection (ATR) mode at 25 °C.

5.4 Mass spectrometry

Direct injection mass spectra were measured in the Mass Spectrometry department at the Department of Chemistry at the University of Hamburg under the direction of Dr. Jennifer Menzel. Mass spectra were generated at 25 °C using ESI on a 6224 ESI-ToF coupled to a HPLC 1200 series (both Agilent Technologies). The spectra were analyzed using MestReNova software.

5.5 NMR spectroscopy

NMR spectra were measured at 25 °C in the Spectroscopy department at the Department of Chemistry at the University of Hamburg under the direction of Dr. Thomas Hackl on following devices:

Bruker Fourier 300: ¹H spectra: 300 MHz, ¹³C spectra: 75 MHz,

³¹P spectra: 122 MHz

Bruker Avance I 400: ¹H spectra: 400 MHz, ¹³C spectra: 101 MHz,

³¹P spectra: 162 MHz

Bruker Avance I 500: ¹H spectra: 500 MHz, ¹³C spectra: 126 MHz,

³¹P spectra: 202 MHz

Bruker Avance III HD 600: ¹H spectra: 600 MHz, ¹³C spectra: 151 MHz, ¹⁹F spectra:

565 MHz

NMR spectra were analyzed using MestReNova software. The standardization for 1 H spectra and 13 C spectra was carried out using the solvent resonance of DMSO- d_6 (2.50 ppm or 39.52 ppm), MeOH- d_4 (4.87 ppm or 49.00 ppm) or CDCl₃ (7.26 ppm or 77.16 ppm). For 31 P spectra, the standardization was carried out using 85 % phosphoric acid as external standard. For 19 F spectra, the standardization was carried out using TFA as external standard. The signals were assigned using two-dimensional experiments (COSY, HSQC, HMBC).

5.6 Further devices

Freeze drying system: Aqueous solutions were lyophilized using an Alpha 2-4

LDplus with a vertical dry rake from Christ.

Centrifuge:

For solutions up to 50 mL, a Heraeus Primo R centrifuge from Thermo Scientific was used at 4 °C and 8000 rpm. For centrifuging volumes <1.5 mL in Eppendorf tubes, a 5418 R centrifuge from Eppendorf was used at 14000 rpm

Thermomixer:

A Thermomixer TS basic from CellMedia was used to incubate the hydrolysis solutions.

NanoDrop:

For employing the Bradford Protein Assay for protein quantification, a NanoDrop 2000c spectrophotometer from Thermo Fisher Scientific was used.

Bead Mill:

Cell lysis, homogenization and extraction of cellular samples were performed using the Bead Mill 24 from Fisherbrand™ with ceramic beads.

5.7 LC-MS/MS system

LC-MS/MS analyses were conducted on a 1290 Infinity II HPLC system from Agilent Technologies coupled to a Sciex QTRAP 5500 mass spectrometer. Samples were maintained at 5 °C and a volume of 5 μ L was loaded onto a XBridge Premier Amide column (150 mm x 2.1 mm, particle size 2.5 μ m), preceded by a guard column (both Waters). The column oven was maintained at 25 °C. Mobile phase A was a 100 mM ammonium hydrogen carbonate buffer in water, adjusted with ammonia to a pH value of 8.3. Mobile phase B was acetonitrile, while mobile phase C was water.

The total concentration of the additive was 5 mM, requiring a ternary gradient with mobile phases A, B and C. Mobile phases delivered at 0.3 mL/min with a stepwise gradient of B and C, while A was kept constant (5 %): 95 % B, 5.1 – 25 min; 50 % B, 25.1 – 27 min; 95 % B. Total run time: 36 min. A valve was used to direct the flow to the waste compartment for two minutes at the start and three minutes at the end.

Ammonium hydrogen carbonate buffer (100 mM) was prepared using 100 mL of LC-MS grade water and 1.0 mL of ammonium hydroxide in water (~25 %).

The QTRAP 5500 mass spectrometer was operated in negative ionization mode with an ESI probe. Source and compound-dependent parameters were optimized through FIA. Source parameters: 20.0 au for the curtain gas, -4000 V for the ion spray voltage, 700 °C for the temperature, 60 au for the ion source gas 1 and 70 au for the ion source gas 2.

After optimization, three mass transitions were compared for each analyte, and the highest signal intensity was selected as the quantifier. A second transition was then selected as the qualifier. The data were acquired and processed using Analyst software (version 1.7., Sciex).

5.8 Bradford assay

A Bradford assay was performed using the Pierce™ Bradford Protein Assay Kit from Thermo Scientific™.

The standard curve was prepared using bovine serum albumin (BSA) standards diluted in the same solvent as the samples and measured in three replicates. The concentration in $\mu g/mL$ for each BSA standard was plotted against the obtained average blank-corrected 595 nm measurement.

HT29 and SW620 cell pellets were suspended in acetonitrile or methanol and water (2:1, % v/v) for cell lysis and PPT and measured at 595 nm.

5.9 Cellular uptake studies

5.9.1 Cancer cells

Cellular uptake studies with HT29 and SW620 cells were performed at the Center for Experimental Medicine at Institute of Anatomy and Experimental Morphology at University Medical Center Hamburg-Eppendorf by MAIKE MÄRKER.

For cellular uptake studies, cancer cells were cultivated in T175 flasks until reaching a confluence of 80 %, whereupon they were treated with the substances Tri*PPP* rocompound **1** and Tri*PPP* rocompound **2** with a control group using PBS. The substances were each dissolved in sterile PBS at a final concentration of 10 mM. These solutions were then frozen in aliquots (100 μ L) at -20 °C. For the experiments, one aliquot of each substance was diluted 1:10 in PBS to obtain a 1 mM solution.

Three T175 bottles were seeded for each cell line. When 80 % confluence was reached, the experiment was initiated by first aspirating the culture medium and washing the cells with PBS. Subsequently, 10 mL FCS-free medium was added containing either 100 μ L of the 1 mM solutions Tri*PPP*ro-compound **1** or **2** or 100 μ L of PBS, which corresponded to a final concentration of 10 μ M in the bottles. Incubation was carried out for 1h, 2h, 6h or 24h at 37 °C.

Subsequently, 2 mL of the incubation medium were removed and frozen, followed by another aspiration of the remaining medium. The cells were washed twice with PBS and then treated with trypsin for five minutes before the reaction was stopped by adding medium. After centrifugation for five minutes at 1500 rpm, the supernatant was removed, and the cell pellet was resuspended in 6 mL of PBS. The

cell count was determined using the Cell Counter Countess 3 from Invitrogen. After a further centrifugation, the pellet was resuspended in 1 mL PBS and transferred to a fresh tube. A final centrifugation of one minute was performed, after which the supernatant was removed, and the cell pellets were first stored at -20 °C and then at -80 °C.

5.9.2 Virus cells

Cellular uptake studies in CEM/O cells were performed at the Leibniz Institute of Virology in Hamburg by TINA MEYER.

For cellular uptake studies, virus cells were cultivated in T175 flasks until reaching a cell number of 10⁹ cells whereupon they were treated with the substances Tri*PPP* rocompound **3** and Tri*PPP* rocompound **4** with a control group using DMSO. The substances were each dissolved in water at a final concentration of 10 mM.

CEM/0 cells were expanded in cell culture medium (RPMI-1640 medium, pH 7.5, 10 % fetal calf serum, 1% penicillin/streptomycin, 200 mM L-glutamine) in T175 cell culture flasks until approximately 10^9 cells were present. Cells were added to 20 mL of cell culture medium and incubated for 1 h with a concentration of 10 μ M of the corresponding analyte (Tri*PPP*ro-compound **3** or **4**) in the cell culture medium (37 °C, 5% CO₂, 90 % RH). The cells were then washed twice thoroughly with PBS, centrifuged and stored at -80 °C.

5.10 Syntheses

5.10.1 General procedures

General procedure 1: Synthesis of non-symmetric H-phosphonates

Under nitrogen atmosphere, 1.3-1.5 eq of diphenyl phosphite was dissolved in abs. pyridine and cooled down to 0 °C. To this, 1.0 eq of the corresponding 4-(hydroxymethyl)phenylalkanoate or 4-(hydroxymethyl)phenylalkylcarbonate was added slowly for 1 h at 0°C. The reaction mixture was stirred for another hour at room temperature. After this, 1.6 eq of 3-hydroxypropionnitrile or 2.0 eq of 9-fluorenemethanol were added and the reaction mixture was stirred for another 1-2 h at room temperature. After evaporation of the solvent under reduced pressure and co-evaporation once each with toluene and dichloromethane, the crude product was purified by automated NP chromatography.

General procedure 2: Synthesis of pyrophosphates

Under nitrogen atmosphere, 1.0 eq of the corresponding *H*-phosphonate was suspended in abs. acetonitrile and heated up to 50 °C until the *H*-phosphonate is fully dissolved. After that, 2.0 eq of *N*-chlorosuccinimide were added and the reaction mixture was stirred for 1 h at 50 °C. Subsequently, 2.5 eq of tetra-*n*-butyl ammonium phosphate solution was added and the mixture was stirred for another hour at 50 °C. After evaporation of the solvent under reduced pressure, the residue was taken up in dichloromethane and washed once each with ammonium acetate solution (1 M) and water. Centrifugation was used for superior phase separation. After evaporation of the solvent under reduced pressure, the residue was coevaporated with abs. acetonitrile.

General procedure 3: Synthesis of Fm protected TriPPPro-compounds

Under nitrogen atmosphere, the corresponding pyrophosphate was dissolved in abs. acetonitrile and cooled down to 0 °C. To this, a mixture of 5.0 eq of trifluoroacetic anhydride and 8.0 eq of triethylamine in abs. acetonitrile were added dropwise. After stirring the mixture for 10 min at 0 °C, all volatile components were removed under reduced pressure. The residue was taken up in abs. *N,N*-dimethylformamide Subsequently, 4.0 eq of 1-methylimidazole were added and the reaction mixture was stirred for 15 min at room temperature. Afterwards, 0.5 eq of the corresponding monophosphate dissolved in abs. *N,N*-dimethylformamide was added. The reaction was stirred at room temperature for 3 h and the conversion was checked via HPLC. At the end of the reaction time, the solvent was evaporated under reduced pressure.

General procedure 4: Deprotection of monomasked TriPPPro-compounds

The crude product was dissolved in abs. N,N-dimethylformamide and 10.0 eq of triethylamine were added. The reaction mixture was stirred at room temperature for 1-3 h. Afterwards, all volatile compounds were removed under reduced pressure. The crude product was purified by automated RP column chromatography followed by ion exchange using DOWEX (NH_4^+). The product was then purified a second time using automated RP column chromatography.

5.10.2 Synthesis of 5-FdU monophosphate 9

5-Fluoro-3'-O-acetyl-5'-tert-butyldimethylsilyl-2'-deoxyuridine 19

The reaction was carried out under nitrogen atmosphere. 3.01 g (12.2 mmol, 1.0 eq)

of 5-fluoro-2'-deoxyuridine **10** was dissolved in 40.0 mL abs. pyridine and 2.22 g (14.7 mmol, 1.2 eq) of *tert*-butyldimethylsilyl chloride was added. After 24 h, 3.50 mL (36.7 mmol, 3.0 eq) of acetic anhydride was added. After 24 h, the solvent was removed under reduced pressure. The residue was taken up in dichloromethane and the organic phase was

washed with water and saturated sodium hydrogen carbonate solution. After the organic phase was dried over sodium sulfate, the solvent was removed under reduced pressure. The crude product was purified by column chromatography (PE/EtOAc 1:1 % v/v).

Yield: 3.42 g (8.49 mmol, 70 %) of a colorless powder.

DC: R_f value (PE/EtOAc 2:1 % v/v): 0.36.

¹H NMR: δ [ppm] (400 MHz, CDCl₃): 8.85 (d, ${}^{3}J_{H,F} = 4.8$ Hz, 1H, -NH), 8.04 (d, ${}^{3}J_{H,F} = 6.2$ Hz, 1H, H-6), 6.37 (ddd, ${}^{3}J_{H,H} = 7.9$ Hz, ${}^{3}J_{H,H} = 5.4$ Hz, ${}^{4}J_{H,H} = 1.9$ Hz, 1H, H-1'), 5.24 (d, ${}^{3}J_{H,H} = 5.9$ Hz, 1H, H-3'), 4.16 – 4.11 (m, 1H, H4'), 3.97 – 3.87 (m, 2H, H-5'a, H-5'b), 2.47 (ddd, ${}^{2}J_{H,H} = 14.0$ Hz, ${}^{3}J_{H,H} = 5.5$ Hz, ${}^{3}J_{H,H} = 1.3$ Hz, 1H, H-2'a), 2.19 – 2.12 (m, 1H, H-2'b), 2.10 (s, 3H, -OAc), 0.93 (s, 9H, -SiC(CH₃)₃), 0.14 (s, 3H, -Si(CH₃)₂), 0.14 (s, 3H, -Si(CH₃)₂).

¹³C NMR: δ [ppm] (101 MHz, CDCl₃): 170.6 (C_q -OAc), 156.7 (d, ${}^2J_{C,F}$ = 27.1 Hz, C-4), 148.8 (C-2), 139.5 (d, ${}^1J_{C,F}$ = 240 MHz, C-5), 124.0 (d, ${}^2J_{C,F}$ = 34.2 Hz, C-6), 85.9 (C-4'), 85.5 (C-1'), 75.5 (C-3'), 63.8 (C-5'), 38.3 (C-2'), 25.7 (SiC(CH₃)₃), 21.0 (OAc), 18.3 (SiC(CH₃)₃), -5.6 (Si(CH₃)₂).

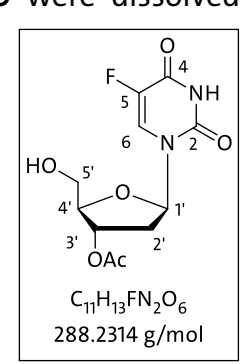
¹⁹**F NMR** δ [ppm] (565 MHz, CDCl₃): -163.05 (d, ³ $J_{F,H}$ = 6.8 Hz).

 $IR: \tilde{\nu}$ [cm⁻¹]: 3213, 3065, 2954, 2929, 2884, 2857, 1719, 1702, 1665, 1463, 1436, 1402, 1381, 1362, 1317, 1299, 1248, 1203, 1123, 1077, 1047, 1021, 1005, 972, 953, 937, 921, 886, 829, 812, 780, 753, 709, 689, 672, 625, 614, 553, 488, 474, 411.

HRMS: (ESI+, *m/z*): calc.: 425.1515, found: 425.1440 [M+Na]+.

5-Fluoro-3'-O-acetyl-2'-deoxyuridine 20

The reaction was carried out under nitrogen atmosphere. 3.41 g (8.47 mmol, 1.0 eq) of 5-fluoro-3'-O-acetyl-5'-tert-butyldimethylsilyl-2'deoxy-uridine 19 were dissolved in 100 mL of abs. dichloromethane. To this, 8.25 mL (50.8 mmol, 6.0 eq) of triethylamine trihydrofluoride were added. The reaction mixture was stirred over night at room temperature and subsequently quenched by adding silica gel. Ater the evaporation of the solvent, the crude product was purified by column chromatography using a dry load (CH₂Cl₂/MeOH 30:1 % v/v).



Yield: 2.41 g (8.38 mmol, 99 %) of a colorless powder.

DC: R_f value ($CH_2Cl_2/MeOH 30:1 \% v/v$): 0.30.

¹**H NMR**: δ [ppm] (600 MHz, DMSO- d_6): 8.21 (d, $^3J_{H,F}$ = 7.2 Hz, 1H, **H-6**), 6.15 (ddd, $^{3}J_{H,H} = 7.1 \text{ Hz}, ^{3}J_{H,H} = 5.7 \text{ Hz}, ^{4}J_{H,H} = 2.0 \text{ Hz}, 1H, H-1'), 5.21 (dt, ^{3}J_{H,H} = 4.3 \text{ Hz}, ^{4}J_{H,H} = 2.2 \text{ Hz},$ 1H, **H-3'**), 4.01 (td, ${}^{3}J_{H,H} = 3.2$, ${}^{3}J_{H,H} = 1.8$ Hz, 1H, **H-4'**), 3.63 (d, ${}^{3}J_{H,H} = 3.6$ Hz, 2H, **H-5'**), 2.31 – 2.22 (m, 2H, **H-2'**), 2.06 (s, 3H, **-OAc**).

¹³C NMR: δ [ppm] (151 MHz, DMSO- d_6): 170.0 (C_a-OAc), 157.0 (d, ${}^2J_{C.F}$ = 26.1 Hz, C-4), 149.1 (**C-2**), 140.1 (d, ${}^{1}J_{C.F}$ = 230.5 Hz, **C-5**), 124.4 (d, ${}^{2}J_{C.F}$ = 34.6 Hz, **C-6**), 84.9 (**C-4'**), 84.4 (C-1'), 74.7 (C-3'), 61.3 (C-5'), 36.9 (C-2'), 20.9 (-OAc).

¹⁹**F NMR** δ [ppm] (565 MHz, DMSO- d_6): -166.60 (d, $^3J_{EH}$ = 8.1 Hz).

IR: $\tilde{\nu}$ [cm⁻¹]: 3566, 3159, 3057, 2936, 2824, 1731, 1705, 1662, 1478, 1462, 1443, 1411, 1380, 1361, 1313, 1269, 1239, 1192, 1132, 1108, 1072, 1063, 1018, 997, 986, 972, 956, 913, 899, 885, 830, 791, 773, 742, 694, 652, 621, 605, 565, 477, 455, 432, 409.

HRMS: (ESI+, *m/z*): calc.: 311.0650, found: 311.0640 [M+Na]+.

Synthesis of 5-2'-deoxyuridine monophosphate 9

The synthesis was carried out under nitrogen atmosphere. 0.301 g (1.04 mmol, 1.0 eq)

of 5-fluoro-2'-deoxyuridine **20** was dissolved in 20 mL of tetrahydrofuran and 0.817 g (1.57 mmol, 1.5 eq) of the Fmamidite **21** was added. After this, 5.01 mL (1.25 mmol, 1.2 eq) of 4,5-dicyanoimidazole (0.25 M in acetonitrile) was added dropwise in 5 min intervals of 0.2 eq. The reaction mixture was stirred at room temperature for

2 h. For the subsequent oxidation, 0.266 mL (1.57 mmol, 1.5 eq) of *tert*-butyl hydroperoxide (5.5 M in n-decane) was added. The mixture was stirred for another 30 min at room temperature. After evaporation of the solvent under reduced pressure, the crude product was purified by automated NP chromatography (CH₂Cl₂ 100 % \rightarrow CH₂Cl₂/MeOH 9:1 % v/v). After this, the deprotection was carried out using a mixture of MeOH/H₂O/Et₃N (1:1:1 % v/v/v). The reaction mixture was stirred for 72 h at room temperature. After evaporation of the solvent under reduced pressure, the crude product was purified by automated RP chromatography.

Yield: 0.319 g (0.643 mmol, 62 %) of a colorless resin.

¹**H NMR**: δ [ppm] (400 MHz, MeOH- d_4): 8.12 (d, ${}^3J_{H,F}$ = 6.6 Hz, 1H, **H-6**), 6.30 (ddd, ${}^3J_{H,H}$ = 7.8 Hz, ${}^3J_{H,H}$ = 6.2 Hz, ${}^4J_{H,H}$ = 1.9 Hz, 1H, **H-1'**), 4.53 – 4.47 (m, 1H, **H-3'**), 4.10 – 3.98 (m, 3H, **H-4'**, **H-5'**), 3.07 (q, ${}^3J_{H,H}$ = 7.3 Hz, 10H, **H-A**), 2.31 – 2.19 (m, 2H, **H-2'**), 1.26 (t, ${}^3J_{H,H}$ = 7.3 Hz, 15H, **H-B**).

Experimental section

¹³C NMR: δ [ppm] (151 MHz, MeOH- d_4): 151.0 (C-4), 142.7 (C-2), 126.3 (d, ${}^2J_{C,F}$ = 35.0 Hz, C-6), 124.9 (d, ${}^1J_{C,F}$ = 182.5 Hz, C-5), 88.0 (d, ${}^2J_{C,P}$ = 8.7 Hz, C-5'), 86.8 (C-1'), 72.8 (C-3'), 66.0 (d, ${}^2J_{C,P}$ = 5.0 Hz, C-4'), 47.6 (C-A), 40.9 (C-2'), 9.3 (C-B).

³¹**P NMR**: δ [ppm] (162 MHz, MeOH- d_4): 1.17.

¹⁹**F NMR** δ [ppm] (565 MHz, MeOH- d_4): -167.57 (d, ${}^3J_{\text{F,H}}$ = 6.7 Hz).

IR: $\tilde{\nu}$ [cm⁻¹]: 2984, 2945, 2677, 2478, 1701, 1565, 1465, 1398, 1355, 1317, 1263, 1241, 1161, 1042, 1000, 966, 936, 916, 837, 808, 784, 752, 728, 691, 650, 609, 556, 508, 415.

HRMS: (ESI⁻, *m/z*): calc.: 325.0243, found: 325.1750 [M-H⁺]⁻.

5.10.3 Synthesis of d4T monophosphate 15

The synthesis procedure and analytical data agree with the literature.^[15]

5.10.4 Synthesis of the non-symmetric *H*-phosphonates

4-(Hydroxymethyl)phenyldodecanoate 22

The synthesis procedure and analytical data agree with the literature.^[15]

(4-(Hydroxymethyl)phenylhexadecylcarbonate 29

The synthesis procedure and analytical data agree with the literature.^[55]

[β-cyano ethyl][C11-AB]-H-phosphonate 18

The synthesis was carried out according to general procedure 1. 0.53 mL (2.1 mmol,

1.3 eq) of diphenyl phosphite was dissolved in 15.0 mL of abs. pyridine and cooled down to 0 °C. To this mixture, 0.50 g (1.6 mmol, 1.0 eq) of the 4-(hydroxymethyl)phenyldodecanoate **21**, dissolved in 5.0 mL of abs. pyridine, was slowly added. After this, 0.18 mL (2.6 mmol, 1.6 eq) of 3-hydroxypropion nitrile was added. The crude product was purified by

automated NP chromatography (PE/EtOAc/AcOH 4:6:0.05 % v/v/ v).

Yield: 0.33 g (0.77 mmol, 47 %) of a colorless oil.

DC: R_f value (PE/EtOAc/AcOH, 4:6:0.05 % v/v/v): 0.35.

¹H NMR: δ [ppm] (500 MHz,CDCl₃): 7.54 – 7.36 (m, 2H, H-2), 7.17 – 7.03 (m, 2H, H-3), 6.94 (d, ${}^{1}J_{H,P}$ = 719 Hz, 1H, P-H), 5.33 – 4.96 (m, 2H, Ph-CH₂), 4.40 – 3.97 (m, 2H, H-m), 2.72 – 2.63 (m, 2H, H-n), 2.56 (t, ${}^{3}J_{H,H}$ = 7.5 Hz, 2H, H-b), 1.75 (p, ${}^{3}J_{H,H}$ = 7.4 Hz, 2H, H-c), 1.41 – 0.99 (m, 16H, H-d, H-e, H-f, H-g, H-h, H-i, H-j, H-k) 0.88 (t, ${}^{3}J_{H,H}$ = 6.5 Hz, 3H, H-l).

¹³C NMR: δ [ppm] (101 MHz, CDCl₃): 172.2 (C-a), 151.2 (C-1), 132.7 (d, ${}^{3}J_{C,P} = 5.5$ Hz, C-4), 129.6 (C-2), 122.2 (C-3), 116.3 (C≡N), 67.3 (d, ${}^{2}J_{C,P} = 5.9$ Hz, Ph-CH₂), 59.8 (d, ${}^{2}J_{C,P} = 5.6$ Hz. C-m), 34.4 (C-b), 31.9 (C-j), 29.6, 29.6, 29.5, 29.3, 29.3, 29.1 (C-d, C-e, C-f, C-g, C-h, C-i), 24.9 (C-c), 22.7 (C-k), 19.9 (d, ${}^{3}J_{C,P} = 6.7$ Hz, C-n), 14.1 (C-l).

³¹**P NMR**: δ [ppm] (122 MHz, CDCl₃): 7.67.

IR: $\tilde{\nu}$ [cm⁻¹]: 2923, 2852, 2435, 2254, 1754, 1703, 1509, 1466, 1399, 1357, 1236, 1198, 1166, 1138, 1043, 996, 966, 813, 753, 727, 693, 520, 416.

HRMS: (ESI⁺, *m/z*): calc.: 446.2067, found: 446.2080 [M+Na]⁺.

[Fm][C11-AB]-H-phosphonate 27

The synthesis was carried out according to general procedure 1. 0.604 mL

(2.48 mmol, 1.0 eq) of diphenyl phosphite were dissolved in 15.0 mL of abs. pyridine and cooled down to 0°C. To this mixture, 0.500 g (1.63 mmol, 1.0 eq) of the 4-(hydroxymethyl)phenyldodecanoate 22, dissolved in 5.0 mL of abs. pyridine, was slowly added. After this, 0.64 g (3.3 mmol, 2.0 eq) of 9-fluorene-methanol were added. The crude product was purified by automated NP chromatography (PE/EtOAc/AcOH 4:6:0.05 % v/v/ v).

Yield: 0.47 g (0.86 mmol, 53 %) of a colorless oil.

DC: R_f value (PE/EtOAc/AcOH, 4:6:0.05 % v/v/v): 0.35.

¹**H NMR**: δ [ppm] (400 MHz, CDCl₃): 7.83 – 7.71 (m, 2H, **H-7**, **H-14**), 7.62 – 7.54 (m, 2H, H-10, H-11), 7.49 – 7.37 (m, 2H, H-8, H-13), 7.35 – 7.31 (m, 2H, H-9, H-12), 7.31 – 7.27 (m, 2H, **H-2**), 7.12 – 7.00 (m, 2H, **H-3**), 6.80 (d, ${}^{1}J_{H,P}$ = 709.9 Hz, 1H, **P-H**), 5.04 – 4.83 (m, 2H, **Ph-CH₂**), 4.47 – 4.35 (m, 2H, **H-5**), 4.20 (t, ${}^{3}J_{H,H}$ = 6.3 Hz, 1H, **H-6**), 2.55 (t, ${}^{3}J_{H,H}$ = 7.5 Hz, 2H, H-b), 1.75 (p, ${}^{3}J_{H,H}$ = 7.5 Hz, 2H, H-c), 1.46 – 1.19 (m, 16H, H-d, H-e, H-f, H-g, H-h, H-i, **H-j**, **H-k**), 0.88 (t, ${}^{3}J_{H,H}$ = 6.7 Hz, 3H, **H-l**).

¹³C NMR: δ [ppm] (101 MHz, CDCl₃): 172.2 (C-a), 151.0 (C-1), 143.0 (C-6a, C-7a), 141.5, 141.4 (C-11a, C-11b), 133.0 (d, ${}^{3}J_{C,P}$ = 6.0 Hz, C-4), 129.2 (C-2), 128.0, 128.0 (C-8, C-13), 127.3 (C-9, **C-12**), 125.0, 125.0 (**C-10**, **C-11**), 122.0 (**C-3**), 120.1, 120.1 (**C-7**, **C-14**), 67.3 (d, ${}^{2}J_{C,P} = 6.1 \text{ Hz}$, **C-5**), 66.5 (d, ${}^{2}J_{C,P}$ = 5.8 Hz, **Ph-CH₂**), 48.1 (d, ${}^{3}J_{C,P}$ = 6.6 Hz, **C-6**), 34.4 (**C-b**), 31.9 (**C-j**), 29.6, 29.5, 29.3, 29.3, 29.1 (C-d, C-e, C-f, C-g, C-h, C-i), 24.9 (C-c), 22.7 (C-k), 14.1 (C-l).

³¹**P NMR**: δ [ppm] (162 MHz, CDCl₃): 7.72.

IR: $\tilde{\nu}$ [cm⁻¹]: 3042, 2920, 2849, 2471, 2052, 1755, 1607, 1595, 1509, 1465, 1450, 1419, 1378, 1324, 1294, 1246, 1198, 1168, 1138, 1089, 1077, 1036, 1017, 971, 923, 906, 868, 848, 836, 817, 784, 763, 738, 721, 643, 620, 591, 566, 551, 527, 506, 457, 427.

HRMS: (ESI⁺, *m/z*): calc.: 549.2764, found: 549.2979 [M+H]⁺.

[Fm][C16-ACB]-H-phosphonate 30

The synthesis was carried out according to general procedure 1. 0.094 mL (0.38 mmol, 1.5 eq) of diphenyl phosphite were dissolved in 10.0 mL of abs. pyridine and cooled down to 0°C. To this mixture, 0.10 g (0.36 mmol, 1.0 eq) of the (4-(hydroxymethyl)phenylhexadecylcarbonate 29, dissolved in 5.0 mL of abs. pyridine, was slowly added. After this, 0.10 g (0.51 mmol, 2.0 eq) of 9-fluorene-methanol were added. The crude product was purified by

 $C_{38}H_{51}O_{6}P$ 634.7938 g/mol

automated NP chromatography (PE/EtOAc/AcOH 4:6:0.05 % v/v/ v).

Yield: 0.073 g (0.12 mmol, 45 %) of a colorless oil.

DC: R_f value (PE/EtOAc/AcOH, 6:4:0.05 % v/v/v): 0.35.

¹**H NMR**: δ [ppm] (400 MHz, CDCl₃): 7.80 – 7.70 (m, 2H, **H-7**, **H-14**), 7.61 – 7.53 (m, 2H, H-10, H-11), 7.46 – 7.34 (m, 2H, H-8, H-13), 7.33 – 7.29 (m, 2H, H-9, H-12), 7.29 – 7.27 (m, 2H, **H-2**), 7.20 – 7.11 (m, 2H, **H-3**), 6.78 (d, ${}^{1}J_{H,P}$ = 709.3 Hz, 1H, **P-H**), 5.00 – 4.81 (m, 2H, **Ph-CH₂**), 4.44 - 4.36 (m, 2H, H-5), 4.27 - 4.16 (m, 3H, H-6, H-b), 1.72 (p, $^{3}J = 7.8$ Hz, 2H, H-c), 1.34 – 1.20 (m, 26H, H-d, H-e, H-f, H-g, H-h, H-i, H-j, H-k, H-l, H-m, H-n, H-o, H-p), 0.86 (t, ${}^{3}J_{H,H}$ = 6.5 Hz, 3H, **H-q**).

¹³C NMR: δ [ppm] (101 MHz, CDCl₃): 164.2 (C-a), 153.5 (C-1), 143.0 (C-6a, C-7a), 141.5, 141.4 (**C-11a**, **C-11b**), 133.2 (d, ${}^{3}J_{C,P}$ = 6.0 Hz, **C-4**), 129.2 (**C-2**), 128.0, 128.0 (**C-8**, **C-13**), 127.3 (C-9, C-12), 125.0, 125.0 (C-10, C-11), 121.4 (C-3), 120.1, 120.1 (C-7, C-14), 69.1 (C-b), 67.2 (d, ${}^2J_{C,P} = 6.0 \text{ Hz}$, C-5), 66.3 (d, ${}^2J_{C,P} = 5.6 \text{ Hz}$, Ph-CH₂), 48.1 (d, ${}^3J_{C,P} = 6.5 \text{ Hz}$, C-6), 32.0 (C-p), 29.7, 29.6, 29.6, 29.5, 29.5, 29.3, 29.2 (C-e, C-f, C-g, C-h, C-i, C-j, C-k, C-l, C-m, C-n), 28.6 (C-c), 25.7 (C-d), 22.7 (C-o), 14.1 (C-q).

³¹**P NMR**: δ [ppm] (162 MHz, CDCl₃): 7.69.

IR: $\tilde{\nu}$ [cm⁻¹]: 3423.0, 3067, 2923, 2853, 2254, 2127, 1759, 1710, 1664, 1509, 1465, 1450, 1378, 1253, 1220, 1167, 1139, 1105, 1051, 1025, 1002, 963, 823, 759, 741, 621, 590, 534, 427.

HRMS: (ESI+, *m/z*): calc.: 657.3315, found: 657.3506 [M+Na]+.

5.10.5 Synthesis of the monomasked triphosphates

γ-[C11AB]5-FdU-triphosphate 6

The synthesis was carried out according to general procedure 2. 0.250 g (0.456 mmol,

1.0 eq) of the (Fm;C11-AB)-*H*-phosphonate **27** were dissolved in 20 mL of abs. acetonitrile. To this, 0.121 g (0.911 mmol, 2.0 eq) of *N*-chlorosuccinimide and 2.85 mL (1.14 mmol, 2.5 eq) of tetra-*n*-butylammonium phosphate solution (0.4 M in acetonitrile) were added. The crude product obtained was used without

further work-up or analysis due to its high reactivity (yield: 345 mg, 390 mmol, 86 % of an orange-colored resin).

The synthesis of the Tri*PPP*ro-compound was carried out according to **general procedure 3.** For the activation of the pyrophosphate **28**, the previously obtained compound was dissolved in 5 mL of abs. acetonitrile and a mixture of 0.22 mL (1.6 mmol, 4.0 eq) of trifluoroacetic anhydride and 0.27 mL (1.9 mmol, 5.0 eq) of

triethylamine dissolved in 5.0 mL of abs. acetonitrile was added to this. Afterwards, $61.5 \,\mu$ L (0.779 mmol, 2.0 eq) of 1-methylimidazole was added followed by the subsequent addition of 76.2 mg (0.156 mmol, 0.4 eq) of the FdU-MP **9** dissolved in 5.0 mL of abs. *N,N*-dimethylformamide. The reaction was stirred for 3 h at room temperature.

The deprotection was carried out according to **general procedure 4**. The residue was dissolved in 5.0 mL of abs. *N*,*N*-dimethyl-formamide and 0.54 mL (3.9 mmol, 10 eq) of triethylamine was added to this. The reaction mixture was stirred for 3 h at room temperature.

Yield: 49.3 mg (0.0597 mmol, 38 %) of a colorless wadded solid.

¹H NMR: δ [ppm] (300 MHz, MeOH- d_4): 8.09 (d, ${}^3J_{H,F}$ = 6.6 Hz, 1H, H-6), 7.59 – 7.30 (m, 2H, H-2"), 7.22 – 6.80 (m, 2H, H-3"), 6.53 – 6.15 (m, 1H, H-1"), 5.06 (d, ${}^3J_{H,P}$ = 6.2 Hz, 2H, Ph-CH₂), 4.59 (dt, ${}^3J_{H,H}$ = 4.8 Hz, ${}^3J_{H,H}$ = 3.9 Hz, 1H, H-3"), 4.33 – 4.22 (m, 1H, H-5"a), 4.23 – 4.15 (m, 1H, H-5"b), 4.07 – 3.95 (m, 1H, H-4"), 2.56 (t, ${}^3J_{H,H}$ = 7.4 Hz, 2H, H-b), 2.23 (dd, ${}^3J_{H,H}$ = 6.7 Hz, ${}^3J_{H,H}$ = 4.9 Hz, 2H, H-2"), 1.71 (q, ${}^3J_{H,H}$ = 7.4 Hz, 2H, H-c), 1.52 – 1.21 (m, 16H, H-d, H-e, H-f, H-g, H-h, H-i, H-j, H-k), 0.90 (t, ${}^3J_{H,H}$ = 6.8 Hz, 3H, H-I).

¹³C NMR: δ [ppm] (101 MHz, MeOH- d_4): 174.0 (C-a), 170.6 (C-4), 166.8 (C-4"), 151.6 (C-2), 144.2 (d, ${}^{1}J_{C,F}$ = 230.6 Hz, C-5), 139.6 (C-1"), 129.4 (C-3"), 126.4 (d, ${}^{2}J_{C,F}$ = 35.0 Hz, C-6), 122.4 (C-2"), 87.6 (d, ${}^{3}J_{C,P}$ = 8.7 Hz, C-4"), 86.6 (C-1"), 72.0 (C-3"), 68.3 (d, ${}^{2}J_{C,P}$ = 5.6 Hz, Ph-CH₂), 66.5 (d, ${}^{2}J_{C,P}$ = 5.0 Hz, C-5"), 40.6 (C-2"), 35.0 (C-b), 33.1 (C-j), 30.3, 30.6, 30.8, 30.4, 30.2, 26.0 (C-c, C-d, C-e, C-f, C-g, C-h, C-i), 23.7 (C-k), 14.4 (C-l).

³¹**P NMR**: δ [ppm] (122 MHz MeOH- d_4): -11.06 (d, ${}^2J_{P,P}$ = 19.3 Hz, **P-**α), -11.29 (d, ${}^2J_{P,P}$ = 18.8 Hz, **P-**γ), -22.16 (t, ${}^2J_{P,P}$ = 19.1 Hz, **P-**β).

HRMS: (ESI⁻, m/z): calc.: 773.1658, found: 773.1650 [M-H]⁻.

γ-[C16ACB]-d4T-triphosphate 11

The synthesis was carried out according to general procedure 2. 0.215 g (0.339 mmol,

1.0 eq) of the (Fm;C16-ACB)-*H*-phosphonate **30** were dissolved in 20 mL of abs. acetonitrile. To this, 90.5 mg (0.677mmol, 2.0 eq) of *N*-chlorosuccinimide and 2.12 mL (0.847 mmol, 2.5 eq) of tetra-*n*-butylammonium phosphate solution (0.4 M in acetonitrile) were added. The crude product obtained was used without further work-up or analysis due to its high

reactivity (yield: 290 mg, 298 mmol, 88 % of an orange-colored resin).

The synthesis of the Tri*PPP*ro-compound was carried out according to **general procedure 3.** For the activation of the pyrophosphate **31**, the previously obtained compound was dissolved in 5 mL of abs. acetonitrile and a mixture of 0.21 mL (1.8 mmol, 5.0 eq) of trifluoroacetic anhydride and 0.33 mL (2.4 mmol, 8.0 eq) of triethylamine dissolved in 5.0 mL of abs. acetonitrile was added to this. Afterwards, 94.1 μ L (1.19 mmol, 4.0 eq) of 1-methylimidazole was added followed by the subsequent addition of 119 mg (0.179 mmol, 0.6 eq) of the d4T-MP **15** dissolved in 5.0 mL of abs. *N,N*-dimethylformamide. The reaction was stirred for 3 h at room temperature.

The deprotection was carried out according to **general procedure 4**. The residue was dissolved in 5.0 mL of abs. *N*,*N*-dimethyl-formamide and 0.41 mL (3.0 mmol, 10 eq) of triethylamine was added to this. The reaction mixture was stirred for 1 h at room temperature.

Yield: 66.7 mg (0.0748 mmol, 42 %) of a colorless wadded solid.

¹**H NMR**: δ [ppm] (300 MHz, MeOH- d_4): 7.72 – 7.65 (m, 1H, **H-6**), 7.54 – 7.43 (m, 2H, **H-3''**), 7.16 – 7.07 (m, 2H, **H-2''**), 6.97 – 6.90 (m, 1H, **H-1'**), 6.55 – 6.49 (m, 1H, **H-3'**),

5.84 – 5.80 (m, 1H, H-2'), 5.07 (d, ${}^{3}J_{H,P}$ = 6.4 Hz, 2H, Ph-CH₂), 5.00 – 4.93 (m, 1H, H-4'), 4.32 – 4.26 (m, 1H, H-5'a), 4.22 (t, ${}^{3}J_{H,H}$ = 6.6 Hz, 2H, H-b),4.49 – 4.14 (m, 1H, H-5'b), 1.94 – 1.87 (m, 3H, H-7), 1.71 (q, ${}^{3}J_{H,H}$ = 6.9 Hz, 2H, H-c), 1.49 – 1.23 (m, 26H, H-d, H-e, H-f, H-g, H-h, H-i, H-j, H-k, H-l, H-m, H-n, H-o, H-p), 0.90 (t, ${}^{3}J_{H,H}$ = 7.0 Hz, 3H, H-q).

¹³C NMR: δ [ppm] (101 MHz, MeOH- d_4): 165.8 (C-4), 158.1 (C-a), 155.7 (C-2), 149.0 (C-1"), 138.8 (C-6), 136.3 (C-4"), 136.0 (C-3"), 129.8 (C-3"), 127.0 (C-2"), 122.0 (C-2"), 117.6 (C-5), 90.9 (d, ${}^3J_{C,P} = 8.7$ Hz, C-4"), 86.5 (C-1"), 70.0 (C-b), 70.0 (d, ${}^2J_{C,P} = 5.6$ Hz, Ph-CH₂), 69.9 (d, ${}^2J_{C,P} = 5.0$ Hz, C-5"), 33.1 (C-o), 30.8, 30.8, 30.7, 30.6, 30.5, 30.3, 29.7 (C-c, C-e, C-f, C-g, C-h, C-i, C-j, C-k, C-l, C-m, C-n), 26.8 (C-d), 23.7 (C-p), 14.5 (C-q), 12.5 (C-7)

³¹**P NMR**: δ [ppm] (122 MHz MeOH- d_4): -11.23 (d, ${}^2J_{P,P} = 18.9$ Hz, **P-**α), -11.53 (d, ${}^2J_{P,P} = 19.1$ Hz, **P-**γ), -22.39 (t, ${}^2J_{P,P} = 19.5$ Hz, **P-**β).

HRMS: (ESI⁻, *m/z*): calc.: 837.2535, found: 837.3000 [M-H]⁻.

5.10.6 Synthesis of the non-symmetric amidite 25

The synthesis was carried out under nitrogen atmosphere. 0.140 mL (0.649 mmol,

1.0 eq) of the 2-cyanoethyl *N*,*N*-diisopropylchlorophosphoamidite **24** was dissolved in 5.0 mL of abs. tetrahydrofuran and added to a solution of 0.199 g (0.649 mmol, 1.0 eq) of the 4-(hydroxymethyl)phenyldo-decanoate **22**

dissolved in 5.0 mL of tetrahydrofuran and

0.14 mL (0.974 mmol, 1.5 eq) of triethylamine at 0 °C. The mixture was stirred at room temperature for one hour. After this, the reaction mixture was filtered, and the residue was washed with ethyl acetate. The solvent was evaporated under reduced pressure and the crude product was purified by column chromatography (PE/EtOAc $5:1\% \text{ v/v} + 5\% \text{ Et}_3\text{N}$).

Yield: 0.291 g (0.574 mmol, 88 %) of a colorless oil.

DC: R_f value (PE/EtOAc/Et₃N 5:1 % v/v + 5 % Et₃N) 0.90.

¹H NMR: δ [ppm] (400 MHz, CDCl₃): 7.42 – 7.32 (m, 2H, H-2), 7.09 – 7.00 (m, 2H, H-3), 4.81 – 4.59 (m, 2H, Ph-CH₂), 3.94 – 3.76 (m, 2H, H-m), 3.75 – 3.56 (m, 2H, H-n), 2.62 (t, ${}^{3}J_{H,H}$ = 6.6 Hz, 2H, H-o), 2.54 (t, ${}^{3}J_{H,H}$ = 7.5 Hz, 2H, H-b), 1.75 (p, ${}^{3}J_{H,H}$ = 7.4 Hz, 2H, H-c), 1.38 – 1.24 (m, 16H, H-d, H-e, H-f, H-g, H-h, H-i, H-j, H-k), 1.19 (t, ${}^{3}J$ = 6.6 Hz, 12H, H-p), 0.88 (t, ${}^{3}J_{H,H}$ = 6.5 Hz, 3H, H-l).

¹³C NMR: δ [ppm] (101 MHz, CDCl₃): 172.6 (C-a), 150.1 (C-1), 136.9 (d, ${}^{3}J_{C,P} = 5.5$ Hz, C-4), 130.0 (C=N), 128.3 (C-2), 121.6 (C-3), 65.1 (d, ${}^{2}J_{C,P} = 18.3$ Hz, Ph-CH₂), 58.6 (d, ${}^{2}J_{C,P} = 19.0$ Hz, C-5), 43.3 (d, ${}^{2}J_{C,P} = 12.3$ Hz, C-m), 34.6 (C-b), 32.1 (C-j), 29.7, 29.6, 29.5, 29.4, 29.3 (C-d, C-e, C-f, C-g, C-h, C-i), 25.0 (C-c), 24.9, 24.8, 24.8, 24.7 (C-n), 22.8 (C-k), 20.5 (d, ${}^{3}J_{C,P} = 6.8$ Hz, C-6),14.3 (C-l).

³¹**P NMR**: δ [ppm] (122 MHz, CDCl₃): 148.6.

HRMS: (ESI⁺, m/z): calc.: 529.3166, found: 529.3270 [M+Na]⁺

5.10.7 Synthesis of 5-FdU diphosphate 8

The synthesis was carried out under nitrogen atmosphere. 0.169 g (0.353 mmol,

1.0 eq) of the 5-FdU monophosphate **9** were suspended in abs. acetonitrile and 0.784 mL (5.66 mmol, 16 eq) of triethylamine was added. To this, 0.492 mL (3.53 mmol, 10 eq) of trifluoroacetic anhydride was added dropwise. The reaction mixture was stirred for 10 min at room temperature

and after this, all volatile components were removed under reduced pressure. The residue was suspended in abs. acetonitrile and 0.490 mL (3.53 mmol, 10 eq) of

triethylamine and 0.167 mL (2.12 mmol, 6.0 eq) of 1-methylimidazole were added dropwise. The mixture was stirred for 10 min at room temperature. Meanwhile, in a separate flask, 2.65 mL (1.06 mmol, 3.0 eq) of tetra-*n*-butylammonium phosphate solution (0.4 M in acetonitrile) were dissolved in 2.5 mL of abs. acetonitrile. To this solution, the activated monophosphate was added dropwise via syringe pump (0.2 mL/min). After stirring the reaction mixture for 1 h at room temperature, water was added, and the mixture was washed twice with chloroform. The aqueous phase was concentrated under reduced pressure, followed by purification via automated RP chromatography. After ion exchange via DOWEX, the product was purified again via RP chromatography to yield the 5-FdU diphosphate **8** with triethyl ammonium as counter ions.

Yield: 35.8 mg (0.0447 mmol, 44 %) of a colorless resin.

¹**H NMR**: δ [ppm] (400 MHz, MeOH- d_4): 8.11 (d, ${}^3J_{H,F} = 6.6$ Hz, 1H, **H-6**), 6.27 (ddd, ${}^3J_{H,H} = 7.4$ Hz, ${}^3J_{H,H} = 6.7$ Hz, ${}^4J_{H,H} = 1.4$ Hz, 1H, **H-1'**), 4.61 (dt, ${}^3J_{H,H} = 5.8$ Hz, ${}^3J_{H,H} = 3.1$ Hz, 1H, **H-3'**), 4.30 – 4.20 (m, 1H, **H-5'a**), 4.19 – 4.11 (m, 1H, **H-5'b**), 4.05 – 4.00 (m, 1H, **H-4'**), 3.19 (q, ${}^3J_{H,H} = 7.3$ Hz, 2.7H, **H-A**), 2.29 – 2.23 (m, 2H, **H-2'**), 1.31 (t, ${}^3J_{H,H} = 7.3$ Hz, 4H, **H-B**).

¹³C NMR: δ [ppm] (101 MHz, MeOH- d_4): 156.8 (C-4), 148.8 (C-2), 124.6 ($^2J_{C,F}$ = 35.0 Hz, C-6), 124.2 (d, $^1J_{C,F}$ = 182.5 Hz, C-5), 85.9 (C-1'), 85.6 (d, $^2J_{C,P}$ = 8.7 Hz, C-5'), 71.6 (C-3'), 63.8 (d, $^3J_{C,P}$ = 5.0 Hz, C-4'), 47.6 (C-A), 40.9 (C-2'), 9.3 (C-B).

³¹P NMR: δ [ppm] (162 MHz, MeOH- d_4): -9.62 (d, ${}^2J_{P,P}$ = 19.8 Hz, P- α), -10.83 (d, ${}^2J_{P,P}$ = 19.8 Hz, P- β).

HRMS: (ESI⁻, *m/z*): calc.: 404.9906, found: 404.9880 [M-H]⁻.

6 Bibliography

- [1] T. Gollnest, T. Dinis de Oliveira, A. Rath, I. Hauber, D. Schols, J. Balzarini and C. Meier, Membrane-permeable Triphosphate Prodrugs of Nucleoside Analogues, Angew. Chem. Int. Ed. **2016**, *55*, 5255–5258.
- [2] M.-J. Camarasa, Prodrugs of Nucleoside Triphosphates as a Sound and Challenging Approach: A Pioneering Work That Opens a New Era in the Direct Intracellular Delivery of Nucleoside Triphosphates, ChemMedChem **2018**, *13*, 1885–1889.
- [3] T. Cihlar and A. S. Ray, Nucleoside and nucleotide HIV reverse transcriptase inhibitors: 25 years after zidovudine, Antiviral Res. **2010**, *85*, 39–58.
- [4] C. M. Galmarini, J. R. Mackey and C. Dumontet, Nucleoside analogues and nucleobases in cancer treatment, The Lancet. Oncol. **2002**, *3*, 415–424.
- [5] D. Carli, M. Honorat, S. Cohen, M. Megherbi, B. Vignal, C. Dumontet, L. Payen and J. Guitton, Simultaneous quantification of 5-FU, 5-FUrd, 5-FdUrd, 5-FdUMP, dUMP and TMP in cultured cell models by LC-MS/MS, J. Chromatogr. B Analyt. Technol. Biomed. Life Sci. **2009**, *877*, 2937–2944.
- [6] N. Zhang, Y. Yin, S.-J. Xu and W.-S. Chen, 5-Fluorouracil: mechanisms of resistance and reversal strategies, Molecules **2008**, *13*, 1551.
- [7] J. Balzarini, R. Pauwels, M. Baba, P. Herdewijn, E. de Clercq, S. Broder and D. G. Johns, The in vitro and in vivo anti-retrovirus activity, and intracellular metabolism of 3'-azido-2',3'-dideoxythymidine and 2',3'-dideoxycytidine are highly dependent on the cell species, Biochem. Pharmacol. **1988**, *37*, 897.

- [8] J. Balzarini, P. Herdewijn and E. de Clercq, Differential Patterns of Intracellular Metabolism of 2',3'-Didehydro-2',3'-dideoxythymidine and 3'-Azido-2',3'-dideoxythymidine, Two Potent Anti-human Immunodeficiency Virus Compounds, JBC **1989**, *264*, 6127.
- [9] D. Jochmans, Novel HIV-1 reverse transcriptase inhibitors, Virus Res. **2008**, *134*, 171.
- [10] C. R. Wagner, V. V. Iyer and E. J. McIntee, Pronucleotides: Toward thein vivo delivery of antiviral and anticancer nucleotides, Med. Res. Rev. **2000**, *20*, 417.
- [11] H. T. Ho and M. J. Hitchcock, Cellular pharmacology of 2',3'-dideoxy-2',3'-didehydrothymidine, a nucleoside analog active against human immunodeficiency virus, AAC **1989**, *33*, 844.
- [12] F. Pertenbreiter, J. Balzarini and C. Meier, Nucleoside Mono- and Diphosphate Prodrugs of 2',3'-Dideoxyuridine and 2',3'-Dideoxy-2',3'-didehydrouridine, ChemMedChem **2015**, *10*, 94.
- [13] H. J. Jessen, T. Schulz, J. Balzarini and C. Meier, Bioreversible Maskierung von Nucleosiddiphosphaten, Angew. Chem. Int. Ed. **2008**, *120*, 8847.
- [14] T. Schulz, J. Balzarini and C. Meier, The DiPPro approach: synthesis, hydrolysis, and antiviral activity of lipophilic d4T diphosphate prodrugs, ChemMedChem **2014**, *9*, 762.
- [15] L. Weinschenk, D. Schols, J. Balzarini and C. Meier, Nucleoside Diphosphate Prodrugs: Nonsymmetric DiPPro-Nucleotides, J. Med. Chem. **2015**, *58*, 6114.
- [16] T. Gollnest, T. D. de Oliveira, D. Schols, J. Balzarini and C. Meier, Lipophilic prodrugs of nucleoside triphosphates as biochemical probes and potential antivirals, Nat. Commun. **2015**, *6*, 8716.
- [17] L. P. Jordheim, D. Durantel, F. Zoulim and C. Dumontet, Advances in the development of nucleoside and nucleotide analogues for cancer and viral diseases, Nat. Rev. Drug Discov. **2013**, *12*, 447.

- [18] L. He, X. Wei, X. Ma, X. Yin, M. Song, H. Donninger, K. Yaddanapudi, C. J. McClain and X. Zhang, Simultaneous Quantification of Nucleosides and Nucleotides from Biological Samples, JASMS **2019**, *30*, 987.
- [19] M. Jauker, H. Griesser and C. Richert, Spontane Bildung von RNA-Strängen, Peptidyl-RNA und Cofaktoren, Angew. Chem. **2015**, *127*, 14772.
- [20] M. Idzko, D. Ferrari, A.-K. Riegel and H. K. Eltzschig, Extracellular nucleotide and nucleoside signaling in vascular and blood disease, BLOOD **2014**, *124*, 1029.
- [21] F. B. Chekeni and K. S. Ravichandran, The role of nucleotides in apoptotic cell clearance: implications for disease pathogenesis, J. Mol. Med. **2011**, *89*, 13.
- [22] K. Mujoo, J. S. Krumenacker and F. Murad, Nitric oxide-cyclic GMP signaling in stem cell differentiation, Free Radic. Biol. Med. **2011**, *51*, 2150.
- [23] S. Fortin and G. Bérubé, Advances in the development of hybrid anticancer drugs, Expert Opin. Drug Discov. **2013**, *8*, 1029.
- [24] L. F. Povirk and I. H. Goldberg, A role for oxidative DNA sugar damage in mutagenesis by neocarzinostatin and bleomycin, Biochimie **1987**, *69*, 815.
- [25] T. Chen, Y. Sun, P. Ji, S. Kopetz and W. Zhang, Topoisomerase IIα in chromosome instability and personalized cancer therapy, Oncogene **2015**, *34*, 4019.
- [26] F. Casaluce, A. Sgambato, P. Maione, F. Ciardiello and C. Gridelli, Emerging mitotic inhibitors for non-small cell carcinoma, Expert Opin. Emerg. Drugs **2013**, *18*, 97.
- [27] G. Deep and R. Agarwal, New combination therapies with cell-cycle agents, Curr. Opin. Investig. Drugs **2008**, *9*, 591.
- [28] Ø. Paulsen, N. Aass, S. Kaasa and O. Dale, Do corticosteroids provide analgesic effects in cancer patients? A systematic literature review, J. Pain Symptom Manage. 2013, 46, 96.

- [29] J. Shelton, X. Lu, J. A. Hollenbaugh, J. H. Cho, F. Amblard and R. F. Schinazi, Metabolism, Biochemical Actions, and Chemical Synthesis of Anticancer Nucleosides, Nucleotides, and Base Analogs, Chem. Rev. **2016**, *116*, 14379.
- [30] Y. Benhamou, R. Tubiana and V. Thibault, Tenofovir disoproxil fumarate in patients with HIV and lamivudine-resistant hepatitis B virus, NEJM **2003**, *348*, 177.
- [31] A. S. Ray, M. W. Fordyce and M. J. M. Hitchcock, Tenofovir alafenamide: A novel prodrug of tenofovir for the treatment of Human Immunodeficiency Virus, Antiviral Res. **2016**, *125*, 63.
- [32] E. de Clercq and A. Holý, Acyclic nucleoside phosphonates: a key class of antiviral drugs, Nat. Rev. Drug Discov. **2005**, *4*, 928.
- Y.-S. Huang, S.-Y. Chang, W.-H. Sheng, H.-Y. Sun, K.-Y. Lee, Y.-C. Chuang, Y.-C. Su, W.-C. Liu, C.-C. Hung and S.-C. Chang, Virological Response to Tenofovir Disoproxil Fumarate in HIV-Positive Patients with Lamivudine-Resistant Hepatitis B Virus Coinfection in an Area Hyperendemic for Hepatitis B Virus Infection, PloS one 2016, 11, e0169228.
- [34] C. Stedman, Sofosbuvir, a NS5B polymerase inhibitor in the treatment of hepatitis C: a review of its clinical potential, Therap. Adv. Gastroenterol. **2014**, *7*, 131.
- [35] J. Deval, Antimicrobial Strategies, Drugs **2009**, *69*, 151.
- [36] W. B. Parker, Enzymology of purine and pyrimidine antimetabolites used in the treatment of cancer, Chem. Rev. **2009**, *109*, 2880.
- [37] P. Cano-Soldado and M. Pastor-Anglada, Transporters that translocate nucleosides and structural similar drugs: structural requirements for substrate recognition, Med. Res. Rev. **2012**, *32*, 428.
- [38] G. Minuesa, I. Huber-Ruano, M. Pastor-Anglada, H. Koepsell, B. Clotet and J. Martinez-Picado, Drug uptake transporters in antiretroviral therapy, Pharmacol. Ther. **2011**, *132*, 268.

- [39] L. Eyer, R. Nencka, E. de Clercq, K. Seley-Radtke and D. Růžek, Nucleoside analogs as a rich source of antiviral agents active against arthropodborne flaviviruses, Antiviral Chem. & Chemother. **2018**, *26*, 2040206618761299.
- [40] D. S. Stein and K. H. P. Moore, Phosphorylation of Nucleoside Analog Antiretrovirals: A Review for Clinicians, Pharmacotherapy **2001**, *21*, 11.
- [41] Y. Peng, Y. Zong, D. Wang, J. Chen, Z.-S. Chen, F. Peng and Z. Liu, Current drugs for HIV-1: from challenges to potential in HIV/AIDS, Pharmacol. **2023**, *14*, 1294966.
- [42] M. H. St Clair, C. A. Richards, T. Spector, K. J. Weinhold, W. H. Miller, A. J. Langlois and P. A. Furman, 3'-Azido-3'-deoxythymidine triphosphate as an inhibitor and substrate of purified human immunodeficiency virus reverse transcriptase, AAC **1987**, *31*, 1972.
- [43] A. Yoshioka, S. Tanaka, O. Hiraoka, Y. Koyama, Y. Hirota, D. Ayusawa, T. Seno, C. Garrett and Y. Wataya, Deoxyribonucleoside triphosphate imbalance. 5-Fluorodeoxyuridine-induced DNA double strand breaks in mouse FM3A cells and the mechanism of cell death, JBC **1987**, *262*, 8235.
- [44] D. B. Longley, D. P. Harkin and P. G. Johnston, 5-fluorouracil: mechanisms of action and clinical strategies, Nat. Rev. Cancer **2003**, *3*, 330.
- [45] D. B. Olsen, A. B. Eldrup, L. Bartholomew, B. Bhat, M. R. Bosserman, A. Ceccacci, L. F. Colwell, J. F. Fay, O. A. Flores, K. L. Getty, J. A. Grobler, R. L. LaFemina, E. J. Markel, G. Migliaccio, M. Prhavc, M. W. Stahlhut, J. E. Tomassini, M. MacCoss, D. J. Hazuda and S. S. Carroll, A 7-Deaza-Adenosine Analog Is a Potent and Selective Inhibitor of Hepatitis C Virus Replication with Excellent Pharmacokinetic Properties, AAC **2004**, *48*, 3944.
- [46] L. Hruba, V. Das, M. Hajduch and P. Dzubak, Nucleoside-based anticancer drugs: Mechanism of action and drug resistance, Biochem. Pharmacol. **2023**, *215*, 115741.

- [47] N. L. Golitsina, F. T. Danehy, R. Fellows, E. Cretton-Scott and D. N. Standring, Evaluation of the role of three candidate human kinases in the conversion of the hepatitis C virus inhibitor 2'-C-methyl-cytidine to its 5'-monophosphate metabolite, Antiviral Res. **2010**, *85*, 470.
- [48] E. Mukherji, J. L. Au and L. E. Mathes, Differential antiviral activities and intracellular metabolism of 3'-azido-3'-deoxythymidine and 2',3'-dideoxyinosine in human cells, AAC **1994**, *38*, 1573.
- [49] A. Lavie, I. Schlichting, I. R. Vetter, M. Konrad, J. Reinstein and R. S. Goody, The bottleneck in AZT activation, Nat. Med. **1997**, *3*, 922.
- [50] C. de Schutter, M. Ehteshami, E. T. Hammond, F. Amblard and R. F. Schinazi, Metabolism of Nucleosides and Nucleotides Prodrugs, Curr. Pharm. Des. **2017**, *23*, 45.
- [51] W. Thomson, D. Nicholls, W. J. Irwin, J. S. Al-Mushadani, S. Freeman, A. Karpas, J. Petrik, N. Mahmood and A. J. Hay, Synthesis, bioactivation and anti-HIV activity of the bis(4-acyloxybenzyl) and mono(4-acyloxybenzyl) esters of the 5'-monophosphate of AZT, J. Chem. Soc., Perkin Trans. 1 1993, 1239-1245.
- [52] Gollnest, Tristan. *Das TriPPPro-Konzept: Entwicklung und Charakterisierung von antiviralen Nukleosidtriphosphat-Prodrugs*. PhD diss., Universität Hamburg, **2015**.
- [53] Reimer, Inga Susanne. 3'-S-Phosphorthiolatverbrückte Oligonucleotide und Fluoreszierende Nucleotid-Prodrugs für Zellaufnahmestudien. PhD diss., Universität Hamburg, **2017.**
- [54] C. Zhao, S. Weber, D. Schols, J. Balzarini and C. Meier, Prodrugs of γ-Alkyl-Modified Nucleoside Triphosphates: Improved Inhibition of HIV Reverse Transcriptase, Angew Chem. Int. Ed. **2020**, *59*, 22063.
- [55] X. Jia, D. Schols and C. Meier, Anti-HIV-Active Nucleoside Triphosphate Prodrugs, J. Med. Chem. **2020**, *63*, 6003.

- [56] C. Zhao, X. Jia, D. Schols, J. Balzarini and C. Meier, γ-Non-Symmetrically Dimasked Tri*PPP*ro Prodrugs as Potential Antiviral Agents against HIV, ChemMedChem **2021**, *16*, 499.
- [57] X. Jia, D. Schols and C. Meier, Lipophilic Nucleoside Triphosphate Prodrugs of Anti-HIV Active Nucleoside Analogs as Potential Antiviral Compounds, Adv. Sci. **2023**, *10*, 36.
- [58] C. Zhao, S. Weber, D. Schols, J. Balzarini and C. Meier, Prodrugs of γ-Alkyl-Modified Nucleoside Triphosphates: Improved Inhibition of HIV Reverse Transcriptase, Angew. Chem. Int. Ed. **2020**, *59*, 22063.
- [59] Zhao, Chenglong. Non-Symmetrically-Masked TriPPPro Prodrugs and γ-Modified Nucleoside Triphosphate Compounds as Potential Antivirals against HIV. PhD diss., Universität Hamburg, **2019**.
- [60] X. Jia, S. Weber, D. Schols and C. Meier, Membrane Permeable, Bioreversibly Modified Prodrugs of Nucleoside Diphosphate-γ-Phosphonates, J. Med. Chem. **2020**, *63*, 11990.
- [61] Witt, Julian. Synthese fluoreszenzmarkierter TriPPPro-Verbindungen für Zellaufnahmestudien und Synthese antitumoraler TriPPPro-Prodrugs. PhD diss., Universität Hamburg, **2022**.
- [62] Willard, H. H., L. L. Merritt, J. A. Dean, and F. A. Settle. *Instrumental Methods of Analysis*. CBS Publishers & Distributors, **1986**.
- [63] Ahuja, S. "Overview of Analytical Instrumentation." *Wilson & Wilson's Comprehensive Analytical Chemistry*, edited by D. Barceló, vol. 47, Elsevier, 2006, pp. 485–559.
- [64] W. Naidong, Bioanalytical liquid chromatography tandem mass spectrometry methods on underivatized silica columns with aqueous/organic mobile phases, J. Chromatogr. B Analyt Technol. Biomed. Life Sci. **2003**, *796*, 209.

- [65] N. Gautam, J. A. Alamoudi, S. Kumar and Y. Alnouti, Direct and indirect quantification of phosphate metabolites of nucleoside analogs in biological samples, JPBA **2020**, *178*, 112902.
- [66] Harry P. Gregor, F. C. Collins, Martin Pope, STUDIES ON ION-EXCHANGE RESINS: III: DIFFUSION OF NEUTRAL MOLECULES IN A SULFONIC ACID CATION-EXCHANGE RESIN, J. Collid Sci. **1951**, *6*, 304.
- [67] A. J. Alpert, HYDROPHILIC-INTERACTION CHROMATOGRAPHY FOR THE SEPARATION OF PEPTIDES, NUCLEIC ACIDS AND OTHER POLAR COMPOUNDS, J. Chromatogr. **1990**, *499*, 177.
- [68] T. Ikegami, K. Tomomatsu, H. Takubo, K. Horie and N. Tanaka, Separation efficiencies in hydrophilic interaction chromatography, J. Chromatogr. A. **2008**, *1184*, 474.
- [69] I. Kohler, M. Verhoeven, R. Haselberg and A. F. Gargano, Hydrophilic interaction chromatography mass spectrometry for metabolomics and proteomics: state-of-the-art and current trends, Microchem. J. **2022**, *175*, 106986.
- [70] D. V. McCalley, Understanding and manipulating the separation in hydrophilic interaction liquid chromatography, J. Chromatogr. A **2017**, *1523*, 49.
- [71] J. Heaton, N. Gray, D. A. Cowan, R. S. Plumb, C. Legido-Quigley and N. W. Smith, Comparison of reversed-phase and hydrophilic interaction liquid chromatography for the separation of ephedrines, J. Chromatogr. A **2012**, *1228*, 329.
- [72] A. I. Piteni and M. G. Kouskoura, HILIC Chromatography An Insight on the Retention Mechanism, J. Chromatogr. Sep. Tech. **2016**, *7*, 3.
- [73] L. W. McLaughlin, Mixed-mode chromatography of nucleic acids, Chem. Rev. **1989**, *89*, 309-319.
- [74] T. H. Walter, B. A. Alden, J. A. Field, N. L. Lawrence, D. L. Osterman, A. V. Patel, M. A. DeLoffi, Characterization of a highly stable mixed-mode

- reversed-phase/weak anion-exchange stationary phase based on hybrid organic/inorganic particles, J. Sep. Sci. **2021**, *44*, 1005.
- [75] G. Zhao, X.-Y. Dong, Y. Sun, Ligands for mixed-mode protein chromatography: Principles, characteristics and design, J. Biotech. **2009**, *144*, 3.
- [76] Y. Yang and X. Geng, Mixed-mode chromatography and its applications to biopolymers, J. Chromatogr. A **2011**, *1218*, 8813.
- [77] W. Bicker, M. Lämmerhofer and W. Lindner, Mixed-mode stationary phases as a complementary selectivity concept in liquid chromatography-tandem mass spectrometry-based bioanalytical assays, ABC **2008**, *390*, 263.
- [78] K. Zhang and X. Liu, Mixed-mode chromatography in pharmaceutical and biopharmaceutical applications, JPBA **2016**, *128*, 73.
- [79] Y. Hsieh, C. J. G. Duncan and M. Liu, A mixed-mode liquid chromatography-tandem mass spectrometric method for the determination of cytarabine in mouse plasma, J. Chromatogr. B **2007**, *854*, 8.
- [80] P. Yeung, L. Ding and W. L. Casley, HPLC assay with UV detection for determination of RBC purine nucleotide concentrations and application for biomarker study in vivo, JPBA **2008**, *47*, 377.
- [81] M. Cichna, M. Raab, H. Daxecker, A. Griesmacher, M. M. Müller and P. Markl, Determination of fifteen nucleotides in cultured human mononuclear blood and umbilical vein endothelial cells by solvent generated ion-pair chromatography, J. Chromatogr. B **2003**, *787*, 381.
- [82] S. Cohen, L. P. Jordheim, M. Megherbi, C. Dumontet and J. Guitton, Liquid chromatographic methods for the determination of endogenous nucleotides and nucleotide analogs used in cancer therapy: a review, J. Chromatogr. B Analyt. Technol. Biomed. Life Sci. **2010**, *878*, 1912.

- [83] D. Huang, Y. Zhang and X. Chen, Analysis of intracellular nucleoside triphosphate levels in normal and tumor cell lines by high-performance liquid chromatography, J. Chromatogr. B **2003**, *784*, 101.
- [84] R. Nishi, T. Yamauchi and T. Ueda, A new, simple method for quantifying gemcitabine triphosphate in cancer cells using isocratic high-performance liquid chromatography, Cancer Sci. **2006**, *97*, 1274.
- [85] E. J. Coolen, I. C. Arts, E. L. Swennen, A. Bast, M. A. C. Stuart and P. C. Dagnelie, Simultaneous determination of adenosine triphosphate and its metabolites in human whole blood by RP-HPLC and UV-detection, J. Chromatogr. B **2008**, *864*, 43.
- [86] S. L. Blanco López, J. Moal and F. San Juan Serrano, Development of a method for the analysis of nucleotides from the mantle tissue of the mussel Mytilus galloprovincialis, J. Chromatogr. A **2000**, *891*, 99.
- [87] G. Haink and A. Deussen, Liquid chromatography method for the analysis of adenosine compounds, J. Chromatogr. B **2003**, *784*, 189.
- [88] L. Zhang, H. Zhang, J. Wang and C. Pan, Determination of Trace Level of cAMP in Locusta Migratoria Manilensis Meyen by HPLC with Fluorescence Derivation, IJMS **2006**, *7*, 266.
- [89] M. Katayama, Y. Matsuda, K. Shimokawa, S. Tanabe, S. Kaneko, I. Hara and H. Sato, Simultaneous determination of six adenyl purines in human plasma by high-performance liquid chromatography with fluorescence derivatization, J. Chromatogr. B, Biomed. Appl. **2001**, *760*, 159.
- [90] R. W. Sinkeldam, N. J. Greco and Y. Tor, Fluorescent Analogs of Biomolecular Building Blocks: Design, Properties, and Applications, Chem. Rev. 2010, 110, 2579.
- [91] M. S. T. Gonçalves, Fluorescent labeling of biomolecules with organic probes, Chem. Rev. **2009**, *109*, 190.
- [92] D. P. Bhatt, X. Chen, J. D. Geiger and T. A. Rosenberger, A sensitive HPLC-based method to quantify adenine nucleotides in primary astrocyte cell

- cultures, J. Chromatogr. B Analyt. Technol. Biomed. Life Sci. **2012**, *889-890*, 110.
- [93] A. Ramos-Salazar and A. D. Baines, Fluorometric determination of adenine nucleotides and adenosine by ion-paired, reverse-phase, high-performance liquid chromatography, Anal. Biochem. **1985**, *145*, 9.
- [94] Y. Li, P. B. Soni, L. Liu, X. Zhang, D. C. Liotta and S. Lutz, Synthesis of fluorescent nucleoside analogs as probes for 2'-deoxyribonucleoside kinases, BMCL **2010**, *20*, 841.
- [95] Pertenbreiter, Florian. *Fluoreszenzmarkierte cycloSal- und DiPPro-Nucleotide*. PhD diss., Universität Hamburg, **2013**.
- [96] C. Meier, Nucleoside diphosphate and triphosphate prodrugs An unsolvable task?, Antiviral Chem. & Chemother. **2017**, *25*, 69.
- [97] A. El-Aneed, A. Cohen and J. Banoub, Mass Spectrometry, Review of the Basics: Electrospray, MALDI, and Commonly Used Mass Analyzers, Appl. Spectrosc. Rev. **2009**, *44*, 210.
- [98] L. Nováková, J. Pavlík, L. Chrenková, O. Martinec and L. Červený, Current antiviral drugs and their analysis in biological materials-Part I: Antivirals against respiratory and herpes viruses, JPBA **2018**, *147*, 400.
- [99] Gruber, L., and A. Gruner. "Grundlagen und Verfahren der Massenspektrometrie." *Springer Reference Technik*, edited by R. Kramme, Springer Berlin Heidelberg, **2019**, pp. 1–10.
- [100] Dass, Chhabil. *Fundamentals of Contemporary Mass Spectrometry*. Wiley-Interscience, Hoboken, N.J., **2007**.
- [101] O. D. Sparkman, Z. Penton, F. G. Kitson, *Gas chromatography and mass spectrometry*. *A practical quide*, Academic Press, Burlington, MA, **2011**.
- [102] P. Önnerfjord, S. Ekström, J. Bergquist, J. Nilsson, T. Laurell and G. Marko-Varga, Homogeneous sample preparation for automated high throughput analysis with matrix-assisted laser desorption/ionisation

- time-of-flight mass spectrometry, Rapid Commun. Mass Spectrom. **1999**, *13*, 315.
- [103] J. Albrethsen, Reproducibility in protein profiling by MALDI-TOF mass spectrometry, Clin. Chem. **2007**, *53*, 852.
- [104] J. Griffiths, A Brief History of Mass Spectrometry, Anal. Chem. **2008**, *80*, 5678.
- [105] J. Fenn, Electrospray ionization mass spectrometry: How it all began, JBT **2002**, *13*, 101.
- [106] N. B. Cech and C. G. Enke, Practical implications of some recent studies in electrospray ionization fundamentals, Mass Spectrom. Rev. **2001**, *20*, 362.
- [107] C. G. Huber and H. Oberacher, Analysis of nucleic acids by on-line liquid chromatography-mass spectrometry, Mass Spectrom. Rev. **2001**, *20*, 310.
- [108] R. B. Cole, Some tenets pertaining to electrospray ionization mass spectrometry, JMS **2000**, *35*, 763.
- [109] P. Kebarle, A brief overview of the present status of the mechanisms involved in electrospray mass spectrometry, JMS **2000**, *35*, 804.
- [110] P. Hommerson, A. M. Khan, G. J. de Jong and G. W. Somsen, Ionization techniques in capillary electrophoresis-mass spectrometry: principles, design, and application, Mass Spectrom. Rev. **2011**, *30*, 1096.
- [111] R. Kostiainen and T. J. Kauppila, Effect of eluent on the ionization process in liquid chromatography-mass spectrometry, J. Chromatogr. A **2009**, *1216*, 685.
- [112] P. Liigand, K. Kaupmees, K. Haav, J. Liigand, I. Leito, M. Girod, R. Antoine and A. Kruve, Think Negative: Finding the Best Electrospray Ionization/MS Mode for Your Analyte, Anal. Chem. **2017**, *89*, 5665.
- [113] Cole, R. B., editor. *Electrospray and MALDI Mass Spectrometry:*Fundamentals, Instrumentation, Practicalities, and Biological Applications. Wiley; John Wiley & Sons, Hoboken, **2012**.

- [114] C. S. Ho, C. W. K. Lam, M. H. M. Chan, R. C. K. Cheung, L. K. Law, L. C. W. Lit, K. F. Ng, M. W. M. Suen and H. L. Tai, Electrospray ionisation mass spectrometry: principles and clinical applications, Clin. Biochem. Rev. **2003**, *24*, 3.
- [115] Ardrey, R. E. *Liquid Chromatography-Mass Spectrometry: An Introduction*.

 J. Wiley, New York, **2003**.
- [116] Barner-Kowollik, C., editor. *Mass Spectrometry in Polymer Chemistry*. WILEY-VCH, Weinheim, **2012**.
- [117] Downard, Kevin. *Mass Spectrometry: A Foundation Course*. Royal Society of Chemistry; RSC Distribution Services, Cambridge, **2004**.
- [118] W. J. Griffiths, A. P. Jonsson, S. Liu, D. K. Rai and Y. Wang, Electrospray and tandem mass spectrometry in biochemistry, Biochem. J. **2001**, *355*, 545.
- [119] G. L. Glish and R. W. Vachet, The basics of mass spectrometry in the twenty-first century, Nat. Rev. Drug Discov **2003**, *2*, 140.
- [120] S. A. McLuckey, Principles of collisional activation in analytical mass spectrometry, JASMS **1992**, *3*, 599.
- [121] K. R. Jennings, Collision-induced decompositions of aromatic molecular ions, Int. J. Mass Spectrom. **1968**, *1*, 227.
- [122] F. W. McLafferty, P. F. Bente, R. Kornfeld, S.-C. Tsai and I. Howe, Metastable ion characteristics. XXII. Collisional activation spectra of organic ions, J. Am. Chem. Soc. **1973**, *95*, 2120.
- [123] R. A. Yost and C. G. Enke, Selected ion fragmentation with a tandem quadrupole mass spectrometer, J. Am. Chem. Soc. **1978**, *100*, 2274.
- [124] B. Domon and R. Aebersold, Mass Spectrometry and Protein Analysis, Science **2006**, *312*, 212.
- [125] L. Yang, M. Amad, W. M. Winnik, A. E. Schoen, H. Schweingruber, I. Mylchreest and P. J. Rudewicz, Investigation of an enhanced resolution triple quadrupole mass spectrometer for high-throughput liquid

- chromatography/tandem mass spectrometry assays, RCM **2002**, *16*, 2060.
- [126] T. Uehara, A. Yokoi, K. Aoshima, S. Tanaka, T. Kadowaki, M. Tanaka and Y. Oda, Quantitative Phosphorus Metabolomics Using Nanoflow Liquid Chromatography-Tandem Mass Spectrometry and Culture-Derived Comprehensive Global Internal Standards, Anal. Chem. **2009**, *81*, 3836.
- [127] R. M. Seifar, C. Ras, J. C. van Dam, W. M. van Gulik, J. J. Heijnen and W. A. van Winden, Simultaneous quantification of free nucleotides in complex biological samples using ion pair reversed phase liquid chromatography isotope dilution tandem mass spectrometry, Anal. Biochem. **2009**, *388*, 213.
- [128] B. Luo, K. Groenke, R. Takors, C. Wandrey and M. Oldiges, Simultaneous determination of multiple intracellular metabolites in glycolysis, pentose phosphate pathway and tricarboxylic acid cycle by liquid chromatography-mass spectrometry, J. Chromatogr. A **2007**, *1147*, 153.
- [129] C. Crauste, I. Lefebvre, M. Hovaneissian, J. Y. Puy, B. Roy, S. Peyrottes, S. Cohen, J. Guitton, C. Dumontet and C. Perigaud, Development of a sensitive and selective LC/MS/MS method for the simultaneous determination of intracellular 1-beta-D-arabinofuranosylcytosine triphosphate (araCTP), cytidine triphosphate (CTP) and deoxycytidine triphosphate (dCTP) in a human follicular lymphoma cell line, J. Chromatogr. B Analyt. Technol. Biomed. Life Sci. 2009, 877, 1417.
- [130] E. J. B. Derissen, M. J. X. Hillebrand, H. Rosing, J. H. M. Schellens and J. H. Beijnen, Development of an LC-MS/MS assay for the quantitative determination of the intracellular 5-fluorouracil nucleotides responsible for the anticancer effect of 5-fluorouracil, JPBA **2015**, *110*, 58.
- [131] B. Maralikova and W. Weinmann, Confirmatory analysis for drugs of abuse in plasma and urine by high-performance liquid chromatographytandem mass spectrometry with respect to criteria for compound

- identification, J. Chromatogr. B Analyt. Technol. Biomed. Life Sci. **2004**, *811*, 21.
- [132] A. K. Yocum and A. M. Chinnaiyan, Current affairs in quantitative targeted proteomics: multiple reaction monitoring-mass spectrometry, Brief. Funct. Genom. Proteomic **2009**, *8*, 145.
- [133] N. R. Kitteringham, R. E. Jenkins, C. S. Lane, V. L. Elliott and B. K. Park, Multiple reaction monitoring for quantitative biomarker analysis in proteomics and metabolomics, J. Chromatogr. B Analyt. Technol. Biomed. Life Sci. **2009**, *877*, 1229.
- [134] X. Jia, D. Schols and C. Meier, Pronucleotides of 2',3'-Dideoxy-2',3'-Didehydrothymidine as Potent Anti-HIV Compounds, J. Med. Chem. **2023**, *66*, 12163.
- [135] Sargent, M., editor. *Guide to Achieving Reliable Quantitative LC-MS Measurements*. RSC Analytical Methods Committee, **2013**.
- [136] Jia, Xiao. Membrane-Permeable Nucleoside Triphosphate Prodrugs of Anti-HIV Active Nucleoside Analogues: y-(Phosphate or Phosphonate)-Modified Nucleotide Analogues. PhD diss., Universität Hamburg, **2020**.
- [137] T. Sowa and S. Ouchi, The Facile Synthesis of 5'-Nucleotides by the Selective Phosphorylation of a Primary Hydroxyl Group of Nucleosides with Phosphoryl Chloride, BCSJ **1975**, *48*, 2084.
- [138] M. Yoshikawa, T. Kato and T. Takenishi, A novel method for phosphorylation of nucleosides to 5'-nucleotides, TETL **1967**, *50*, 5065.
- [139] Weinschenk, Lina. *DiPPro-Nucleotide mit asymmetrischer Maskierung der Pyrophosphateinheit*. PhD diss., Universität Hamburg, **2015**.
- [140] S. Mohamady and D. L. Jakeman, An improved method for the synthesis of nucleoside triphosphate analogues, J. Org. Chem. **2005**, *70*, 10588.
- [141] Jeschik, Nils. *Synthese und Untersuchung diverser photocaged Adenosinverbindungen*. PhD diss., Universität Hamburg, **2020**.

- [142] H. Nageh, L. Zhao, A. Nakayama, J.-Y. Hasegawa, Y. Wang and T. Nakano, Photo-induced β-elimination of 9-fluorenylmethanol leading to dibenzofulvene, Chem. Comm. **2017**, *53*, 8431.
- [143] P. H. G. Egelund, S. Jadhav, V. Martin, H. Johansson Castro, F. Richner, S. T. Le Quement, F. Dettner, C. Lechner, R. Schoenleber and D. Sejer Pedersen, Fmoc-Removal with Pyrrolidine Expands the Available Solvent Space in Green Solid-Phase Peptide Synthesis, ACS Sustainable Chem. Eng. **2021**, *9*, 14202.
- [144] L. A. Carpino and G. Y. Han, 9-Fluorenylmethoxycarbonyl amino-protecting group, J. Org. Chem **1972**, *37*, 3404.
- [145] Dekiert, Patrick. Synthese von membranpermeablen, chemisch stabilisierten NAADP-Derivaten. PhD diss., Universität Hamburg, **2021**.
- [146] H. Eckert and B. Forster, Triphosgene, a Crystalline Phosgene Substitute, Angew. Chem. Int. Ed. **1987**, *26*, 894.
- [147] R. S. Jansen, H. Rosing, J. H. M. Schellens and J. H. Beijnen, Mass spectrometry in the quantitative analysis of therapeutic intracellular nucleotide analogs, Mass Spectrom. Rev. **2011**, *30*, 321.
- [148] Walter, Thomas H., et al. A New Mixed-Mode Reversed-Phase/Anion-Exchange Stationary Phase Based on Hybrid Particles. Waters, **2020**.
- [149] A. Brookhart, M. Arora, M. McCullagh, I. D. Wilson, R. S. Plumb, J. P. Vissers and N. Tanna, Understanding mobile phase buffer composition and chemical structure effects on electrospray ionization mass spectrometry response, J. Chromatogr. A **2023**, *1696*, 463966.
- [150] J. Liigand, A. Laaniste and A. Kruve, pH Effects on Electrospray Ionization Efficiency, JASMS **2017**, *28*, 461.
- [151] I. Omari, P. Randhawa, J. Randhawa, J. Yu and J. S. McIndoe, Structure, Anion, and Solvent Effects on Cation Response in ESI-MS, JASMS **2019**, *30*, 1750.

- [152] S. Zhou and K. D. Cook, A mechanistic study of electrospray mass spectrometry: charge gradients within electrospray droplets and their influence on ion response, JASMS **2001**, *12*, 206.
- [153] M. H. Amad, N. B. Cech, G. S. Jackson and C. G. Enke, Importance of gasphase proton affinities in determining the electrospray ionization response for analytes and solvents, JMS **2000**, *35*, 784.
- [154] J. C. Heaton, J. J. Russell, T. Underwood, R. Boughtflower and D. V. McCalley, Comparison of peak shape in hydrophilic interaction chromatography using acidic salt buffers and simple acid solutions, J. Chromatogr. A **2014**, *1347*, 39.
- [155] L. Konermann, Addressing a Common Misconception: Ammonium Acetate as Neutral pH "Buffer" for Native Electrospray Mass Spectrometry, JASMS **2017**, *28*, 1827.
- [156] CRC Handbook of Chemistry and Physics: A Ready-Reference Book of Chemical and Physical Data. Edited by David R. Lide, 83rd ed., CRC Press, 2002.
- [157] X. Santarelli and C. Cabanne, Mixed Mode Chromatography: A Novel Way Toward New Selectivity, Curr. Protein Pept. Sci. **2019**, *20*, 14.
- [158] A. J. Alpert, Effect of salts on retention in hydrophilic interaction chromatography, J. Chromatogr. A **2018**, *1538*, 45.
- [159] N. C. Hughes, E. Y. K. Wong, J. Fan and N. Bajaj, Determination of carryover and contamination for mass spectrometry-based chromatographic assays, AAPS J. **2007**, *9*, E353-60.
- [160] D. Guillarme, S. Heinisch and J. L. Rocca, Effect of temperature in reversed phase liquid chromatography, J. Chromatogr. A **2004**, *1052*, 39.
- [161] D. Kumar, N. Gautam and Y. Alnouti, Analyte recovery in LC-MS/MS bioanalysis: An old issue revisited, Anal. Chim. Acta. **2022**, *1198*, 339512.

- [162] W. M. A. Niessen, P. Manini and R. Andreoli, Matrix effects in quantitative pesticide analysis using liquid chromatography-mass spectrometry, Mass Spectrom. Rev. **2006**, *25*, 881.
- [163] A. van Eeckhaut, K. Lanckmans, S. Sarre, I. Smolders and Y. Michotte, Validation of bioanalytical LC-MS/MS assays: evaluation of matrix effects, J. Chromatogr. B Analyt. Technol. Biomed. Life Sci. **2009**, *877*, 2198.
- [164] U.S. Food and Drug Administration. *Analytical Procedures and Methods Validation for Drugs and Biologics: Guidance for Industry.* **2015**.
- [165] Moosavi, Seyed Mojtaba, and Sussan Ghassabian. *Calibration and Validation of Analytical Methods: A Sampling of Current Approaches*. IntechOpen, **2018**.
- [166] J. C. Heaton and D. V. McCalley, Some factors that can lead to poor peak shape in hydrophilic interaction chromatography, and possibilities for their remediation, J. Chromatogr. A **2016**, *1427*, 37.
- [167] S. Guo, J. Duan, D. Qian, H. Wang, Y. Tang, Y. Qian, D. Wu, S. Su and E. Shang, Hydrophilic interaction ultra-high performance liquid chromatography coupled with triple quadrupole mass spectrometry for determination of nucleotides, nucleosides and nucleobases in Ziziphus plants, J. Chromatogr. A **2013**, *1301*, 147.
- [168] R. Zhang, D. G. Watson, L. Wang, G. D. Westrop, G. H. Coombs and T. Zhang, Evaluation of mobile phase characteristics on three zwitterionic columns in hydrophilic interaction liquid chromatography mode for liquid chromatography-high resolution mass spectrometry based untargeted metabolite profiling of Leishmania parasites, J. Chromatogr. A 2014, 1362, 168.
- [169] A. Wakamatsu, K. Morimoto, M. Shimizu and S. Kudoh, A severe peak tailing of phosphate compounds caused by interaction with stainless

- steel used for liquid chromatography and electrospray mass spectrometry, J. Sep. Sci. **2005**, *28*, 1823.
- [170] J. Heaton, M. D. Jones, C. Legido-Quigley, R. S. Plumb and N. W. Smith, Systematic evaluation of acetone and acetonitrile for use in hydrophilic interaction liquid chromatography coupled with electrospray ionization mass spectrometry of basic small molecules, RCM **2011**, *25*, 3666.
- [171] H. Sillén and N. Magnell, Screening ionisation and chromatography conditions for quantitative LC/MS methods, J. Chromatogr. B Analyt. Technol. Biomed. Life Sci. **2009**, *877*, 3581.
- [172] V. Czitrom, One-Factor-at-a-Time versus Designed Experiments, Am. Stat. **1999**, *53*, 126.
- [173] Montgomery, Douglas C. *Design and Analysis of Experiments*. John Wiley & Sons, Hoboken, NJ, **2013**.
- [174] G. Székely, B. Henriques, M. Gil, A. Ramos and C. Alvarez, Design of experiments as a tool for LC-MS/MS method development for the trace analysis of the potentially genotoxic 4-dimethylaminopyridine impurity in glucocorticoids, JPBA **2012**, *70*, 251.
- [175] K. Bheemanapally, M. M. H. Ibrahim and K. P. Briski, Optimization of Ultra-High-Performance Liquid Chromatography-Electrospray Ionization-Mass Spectrometry Detection of Glutamine-FMOC Ad-Hoc Derivative by Central Composite Design, Sci. Rep. **2020**, *10*, 7134.
- [176] A.-A. Golabchifar, M.-R. Rouini, B. Shafaghi, S. Rezaee, A. Foroumadi and M.-R. Khoshayand, Optimization of the simultaneous determination of imatinib and its major metabolite, CGP74588, in human plasma by a rapid HPLC method using D-optimal experimental design, Talanta **2011**, *85*, 2320.
- [177] E. S. Hecht, A. L. Oberg and D. C. Muddiman, Optimizing Mass Spectrometry Analyses: A Tailored Review on the Utility of Design of Experiments, JASMS **2016**, *27*, 767.

- [178] J. Bernal, A. M. Ares, J. Pól and S. K. Wiedmer, Hydrophilic interaction liquid chromatography in food analysis, J. Chromatogr. A **2011**, *1218*, 7438.
- [179] U. A. Thorsteinsdóttir and M. Thorsteinsdóttir, Design of experiments for development and optimization of a liquid chromatography coupled to tandem mass spectrometry bioanalytical assay, JMS **2021**, *56*, e4727.
- [180] P. Bhatt, M. Saquib Hasnain, A. K. Nayak, B. Hassan and S. Beg, Development and Validation of QbD-Driven Bioanalytical LC-MS/MS Method for the Quantification of Paracetamol and Diclofenac in Human Plasma, Anal. Chem. Lett. **2018**, *8*, 677.
- [181] P. A. Parker, S. M. Kowalski and G. G. Vining, Classes of Split-plot Response Surface Designs for Equivalent Estimation, Qual. Reliab. Eng. **2006**, *22*, 291.
- [182] Miller, J. N., and J. C. Miller. *Statistics and Chemometrics for Analytical Chemistry*. Prentice Hall, Harlow, England, **2000**.
- [183] D. V. McCalley, Influence of metals in the column or instrument on performance in hydrophilic interaction liquid chromatography, J. Chromatogr. A 2022, 1663, 462751.
- [184] B. K. Matuszewski, M. L. Constanzer and C. M. Chavez-Eng, Strategies for the assessment of matrix effect in quantitative bioanalytical methods based on HPLC-MS/MS, Anal. Chem. **2003**, *75*, 3019.
- [185] S. R. Rao, A. E. Snaith, D. Marino, X. Cheng, S. T. Lwin, I. R. Orriss, F. C. Hamdy and C. M. Edwards, Tumour-derived alkaline phosphatase regulates tumour growth, epithelial plasticity and disease-free survival in metastatic prostate cancer, Br. J. Cancer **2017**, *116*, 227.
- [186] V. Braun, H. Stuppner, L. Risch and C. Seger, Design and Validation of a Sensitive Multisteroid LC-MS/MS Assay for the Routine Clinical Use: One-Step Sample Preparation with Phospholipid Removal and Comparison to Immunoassays, Int. J. Mol. Sci. **2022**, *23*, 23.

- [187] M. C. Peoples, M. S. Halquist, O. Ismaiel, M. Y. El-Mammli, A. Shalaby and H. T. Karnes, Assessment of matrix effects and determination of niacin in human plasma using liquid-liquid extraction and liquid chromatography-tandem mass spectrometry, BMC **2008**, *22*, 1272.
- [188] R. Bargui, A. Solgadi, B. Prost, M. Chester, A. Ferreiro, J. Piquereau and M. Moulin, Phospholipids: Identification and Implication in Muscle Pathophysiology, Int. J. Mol. Sci. **2021**, *22*, 15.
- [189] G. Vale, S. A. Martin, M. A. Mitsche, B. M. Thompson, K. M. Eckert and J.
 G. McDonald, Three-phase liquid extraction: a simple and fast method for lipidomic workflows, J. Lipid Res. 2019, 60, 694.
- [190] F. Michopoulos, A. M. Edge, Y.-T. Hui, T. Liddicoat, G. Theodoridis and I. D. Wilson, Extraction methods for the removal of phospholipids and other endogenous material from a biological fluid, Bioanalysis **2011**, *3*, 2747.
- [191] V. Matyash, G. Liebisch, T. V. Kurzchalia, A. Shevchenko and D. Schwudke, Lipid extraction by methyl-tert-butyl ether for high-throughput lipidomics, J. Lipid Res. **2008**, *49*, 1137.
- [192] J. Folch, M. Lees and G. S. Stanley, A SIMPLE METHOD FOR THE ISOLATION AND PURIFICATION OF TOTAL LIPIDES FROM ANIMAL TISSUES, JBC **1957**, *226*, 497.
- [193] European Medicines Agency. *Guideline on Bioanalytical Method Validation*. **2012**.
- [194] Harris, Daniel C., G. Werner, and T. Werner. *Lehrbuch der Quantitativen Analyse*. Springer Berlin Heidelberg, Berlin, Heidelberg, **2014**.
- [195] X. Jia, D. Schols and C. Meier, Lipophilic Triphosphate Prodrugs of Various Nucleoside Analogues, J. Med. Chem. **2020**, *63*, 6991.

7 Appendix

7.1 List of hazards and precautionary statements

The following table (Table 7-1) shows all substances (reagents and solvents) used in this doctorate. Hazardous substances are classified according to GHS (CLP (Regulation (EC) 1272/2008)) and all corresponding GHS pictograms and H- and P-statements are indicated.

Table 7-1: List of hazards and precautionary statements for all substances used in this doctorate.

Substance	GHS pictograms	H-statement	P-statement
Acetic acid		226, 314	210, 280,
	~ ~		301+330+331,
			303+361+353
Acetic acid anhydride		226, 302, 331,	210, 260, 280,
	V V V	314, 335	303+361+353,
			305+351+338,
			312
Acetonitrile	<u>(4)</u>	225,	210, 280,
	V V	302+312+332,	301+312,
		319	303+361+353,
			304+340+312,
			305+351+338
Ammonia solution (25 %)	(!) (<u>*</u>)	314, 335, 410	261, 271, 273,
	V V V		280,
			303+361+353,
			305+351+338

Ammonium acetate	Not a hazardous substance according to CLP		
	(Regulation (EC) 1272/2008).		
Ammonium formate	<u>(1)</u>	319	264, 280,
	V		305+351+338,
			337+313
Ammonium hydrogen	<u>(!)</u>	302	301+312+330
carbonate	V		
tert-Butyl hydroperoxide		226, 242, 302,	210, 220, 280,
(5.5 M in <i>n</i> -decane)		311, 330, 314, 317,	301+330+331,
		341, 411	303+361+353,
			305+351+338,
			310
tert-Butyldimethylsilyl	W LE Y	228, 314, 411	210, 260, 273,
chloride	\Diamond		280,
			303+361+353,
			305+351+338,
			310
N-Chlorosuccinimide		290, 302, 314,	260, 273, 280,
	\vee \vee \vee	335, 410	301+312,
			303+361+353,
			305+351+338
Chloroform		302, 331, 315,	201, 273,
	V	319, 351, 361d,	301+312+330,
		336, 372, 412	302+352,
			304+340+311,
			308+313
Diazabicycloundecene		301, 314, 412,	273, 280,
	~ ~	290	301+310+330,
			301+330+331,
		250	·

			303+361+353,
			305+351+338
Dichloromethane		315, 319, 336, 351	201, 302+352,
	V V		305+351+338,
			308+313
4,5-Dicyanoimidazole		225,	210, 280,
(0.25 M in CH₃CN)	\triangleleft \vee \vee	302+312+332,	301+312,
		315, 318, 335	303+361+353,
			304+340+312,
			305+351+338
Dimethyl sulfoxide-d6	Not a hazard	ous substance acco	rding to CLP
	(Reg	ulation (EC) 1272/20	08).
<i>N,N</i> -Dimethylformamide	(N) (1) (2)	226, 312+332,	201, 210,
	\Rightarrow \checkmark	319, 360d	302+352,
			305+351+338,
			308+313
Diphenyl phosphite		302, 315, 318, 335	261, 264, 280,
	\vee \vee		301+312,
			302+352,
			305+351+338
DOWEX 50W X8	<u>(1)</u>	319	305+351+338
Ethyl acetate		225, 319, 336	210, 233, 240,
			241, 242,
			305+351+338
9-Fluorenemethanol	Not a hazard	ous substance acco	rding to CLP
	(Regulation (EC) 1272/2008).		
5-Fluoro-2'-deoxyuridine		301	264, 270,
			301+310, 405,
			501

Hydrochloric acid (37 %)		290, 314, 335	234, 261, 271,
	\vee		280,
			303+361+353,
			305+351+338
3-Hydroxypropionitrile	Not a hazard	ous substance acco	rding to CLP
	(Reg	ulation (EC) 1272/20	08).
Isopropanol	(N) (1)	225, 319, 336	210, 233, 240,
	\Rightarrow \checkmark		241, 242,
			305+351+338
Methanol		225,	210, 233, 280,
	\triangleleft \vee	301+311+331, 370	301+310,
			303+361+353,
			304+340+311
1-Methylimidazole		302, 311, 314,	202, 280,
	V V W	361d	301+312,
			303+361+353,
			304+340+310,
			305+351+338
Petroleum ether	(b) (1) (2)	224, 304, 315,	210, 233, 273,
(50-70)	◇ ◇ ◇	336, 411	301+310, 331,
	***		403+233
Pyridine	(N) (1)	225,	210, 280,
	\Rightarrow \checkmark	302+312+332,	301+312,
		315, 319	303+361+353,
			304+340+312,
			305+351+338
Pyridine trifluoroacetate		315, 319, 335	261, 264, 271,
	V		280, 302+352,
			305+351+338

Sodium sulfate	Not a bazard	ous substance asso	rding to CLD
Socium sunate	Not a hazardous substance according to CLP		
	(Regulation (EC) 1272/2008).		
Tetrabutylammonium	Not a hazardous substance according to CLP		
phosphate monobasic	(Regi	ulation (EC) 1272/20	008).
Tetrahydrofuran		225, 302, 319,	202, 210, 233,
	V V V	335, 336, 351	301+312,
			305+351+338,
			308+313
Toluene	(N) (1) (2)	225, 304, 315,	202, 210, 273,
	\triangleleft \vee \blacktriangleleft	336, 361d, 373,	301+310,
		412	303+361+353,
			331
Triethylamine		225, 302,	210, 280,
	\forall \vee \vee	311+331, 314, 335	301+312,
			303+361+353,
			304+340+310,
			305+351+338
Triethylamine		300+310+330,	260, 271, 280,
trihydrofluoride	V V	314	303+361+353,
			304+340+310,
			305+351+338
Trifluoroacetic anhydride		314, 332, 412	261, 273, 280,
	~ ~		303+361+353,
			304+340+310,
			305+351+338
Tris(tetrabutyl-		315, 319, 335	261, 264, 271,
ammonium) hydrogen	V		280, 302+352,
pyrophosphate			305+351+338

7.2 Supplementary data

The following subsections include all the data mentioned in chapter 4 (Results and discussion), but have been omitted as the data presented were comparable and sufficient for the purpose of discussion, or due to their excessive level of detail.

7.2.1 Measurements with the mixed-mode method

Table 7-2: Calibration standard (CS) samples for 5-FdU **10**, including corresponding concentrations in ng/mL, integrated peak areas of the duplicates including the resulting mean and the coefficient of variation (CV) in %.

Concentration	Analyte Peak Area 1	Analyte Peak Area 2	Mean Analyte	%CV
[ng/mL]	[counts]	[counts]	Peak Area [counts]	
2.5	1.10E+03	1.07E+03	1.09E+03	1.4
5.0	2.15E+03	9.95E+02	1.57E+03	37
10.0	3.32E+03	1.55E+03	2.44E+03	36
20.0	5.31E+03	5.56E+03	5.44E+03	2.3
40.0	9.19E+03	1.00E+04	9.60E+03	4.2
80.0	1.89E+04	1.88E+04	1.89E+04	0.3
160.0	3.78E+04	3.47E+04	3.63E+04	4.3
320.0	7.68E+04	7.21E+04	7.45E+04	3.2

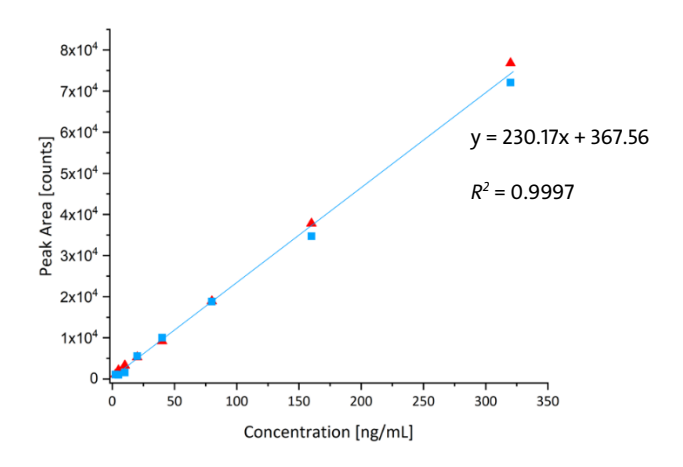


Figure 7-1: Calibration curve of 5-FdU 10 calculated from the mean values of peak area 1 and peak area 2 including linear regression equation and coefficient of determination R^2 .

7.2.2 Diagnostic graphs from the DoE validation

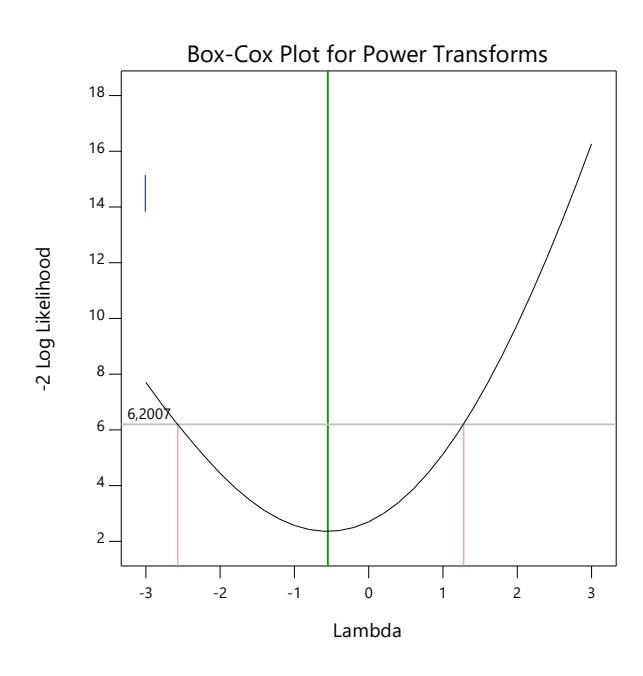


Figure 7-2: Box-cox plot for power transformations for 5-FdU-MP 9. The blue line indicates the parameter λ , which has a value of 1. The red lines denote the 95% confidence interval. Created with DesignExpert (version 11).

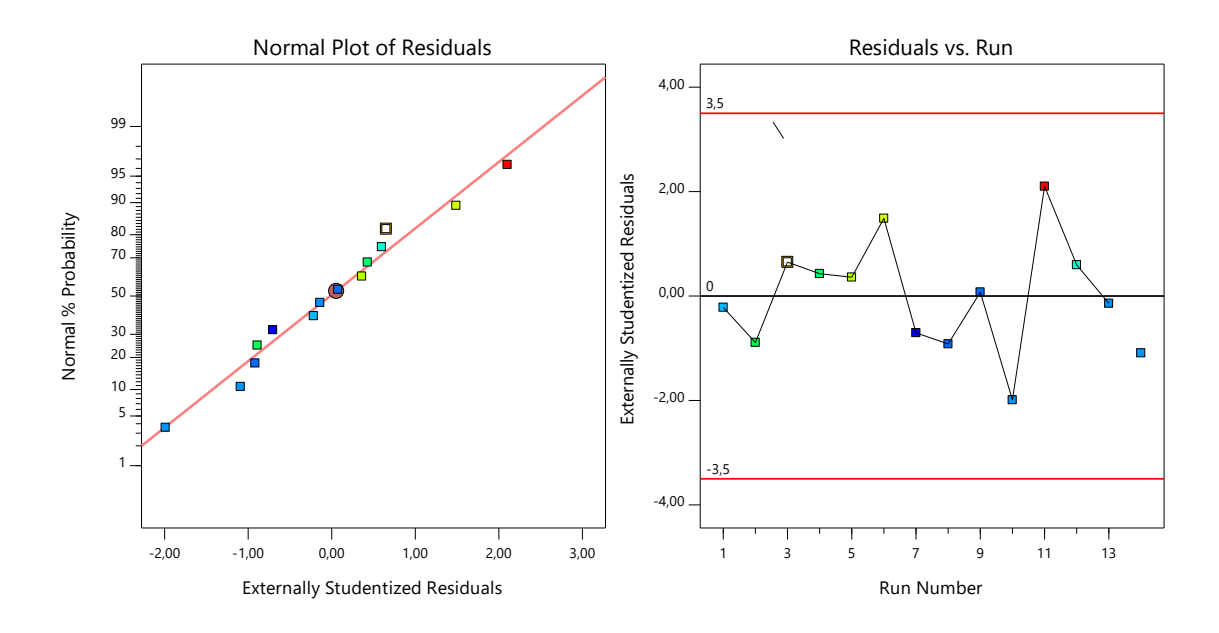


Figure 7-3: Normal Plot of Residuals (left) and Residuals vs. Run (right) for 5-FdU-MP **9**. Created with DesignExpert (version 11).

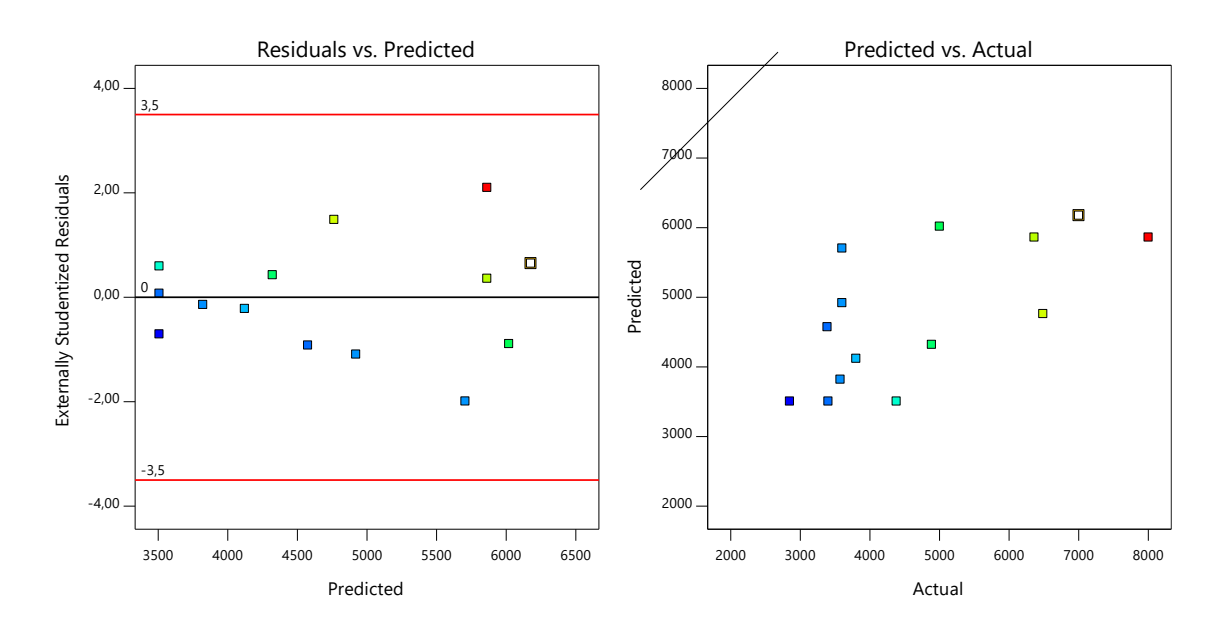


Figure 7-4: Residuals versus Predicted (left) and Predicted vs. Actual (right) for 5-FdU-MP **9**. Created with DesignExpert (version 11).

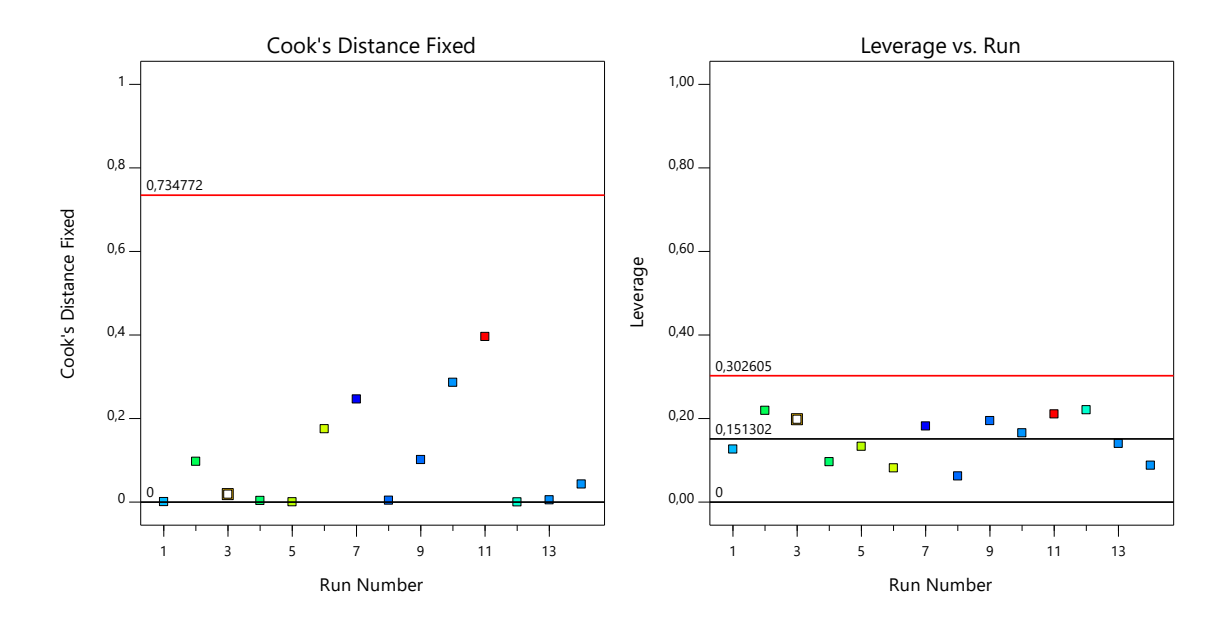


Figure 7-5: Cook's distance plot (left) and leverage versus run plot (right) for 5-FdU-MP **9**. Created in DesignExpert (version 11).

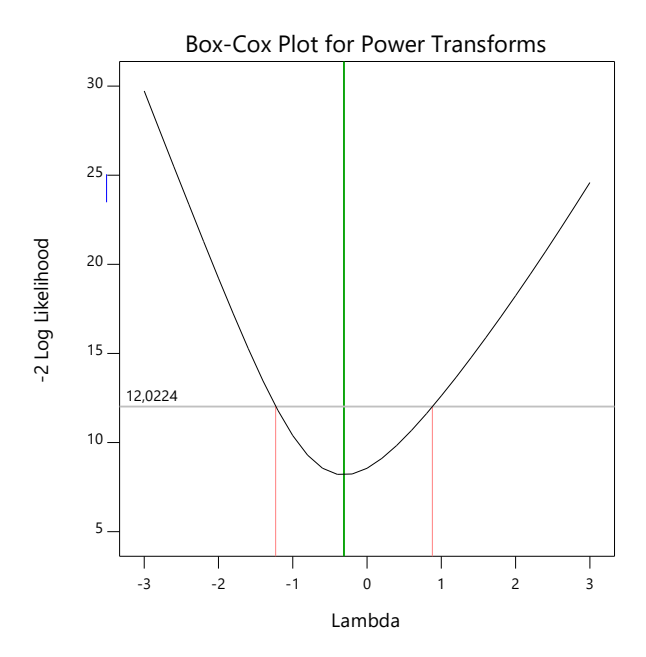


Figure 7-6: Box-cox plot for power transformations for 5-FdU-DP 8. The blue line indicates the parameter λ , which has a value of 1. The red lines denote the 95 % confidence interval. Created with DesignExpert (version 11).

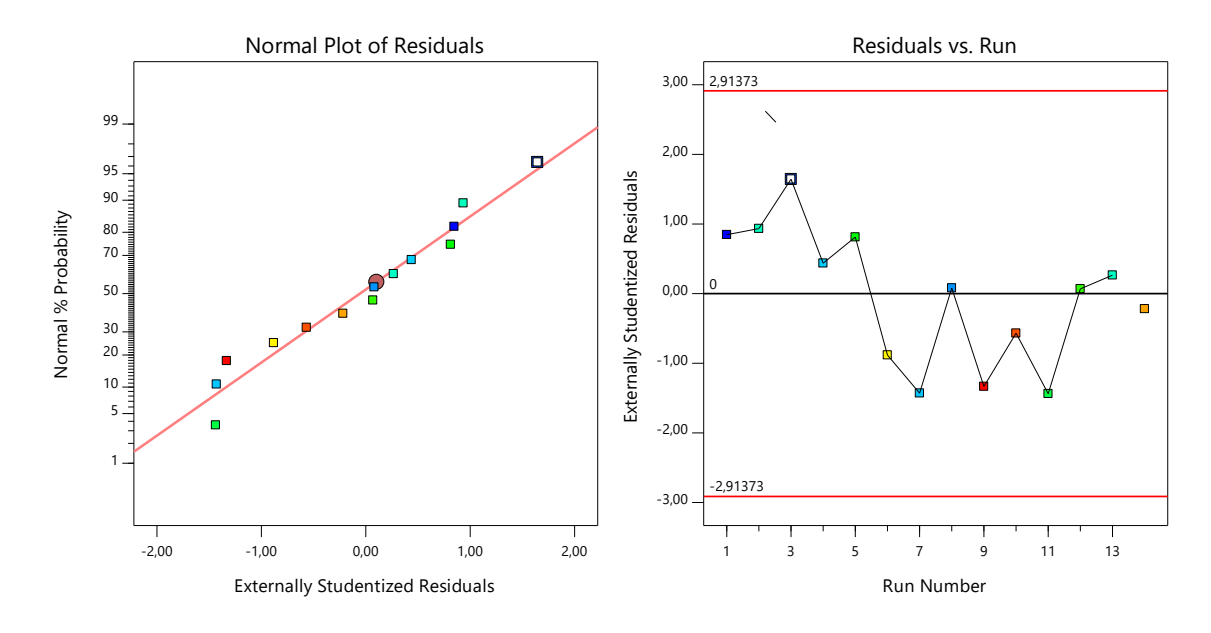


Figure 7-7: Normal Plot of Residuals (left) and Residuals vs. Run (right) for 5-FdU-DP **8**. Created with DesignExpert (version 11).

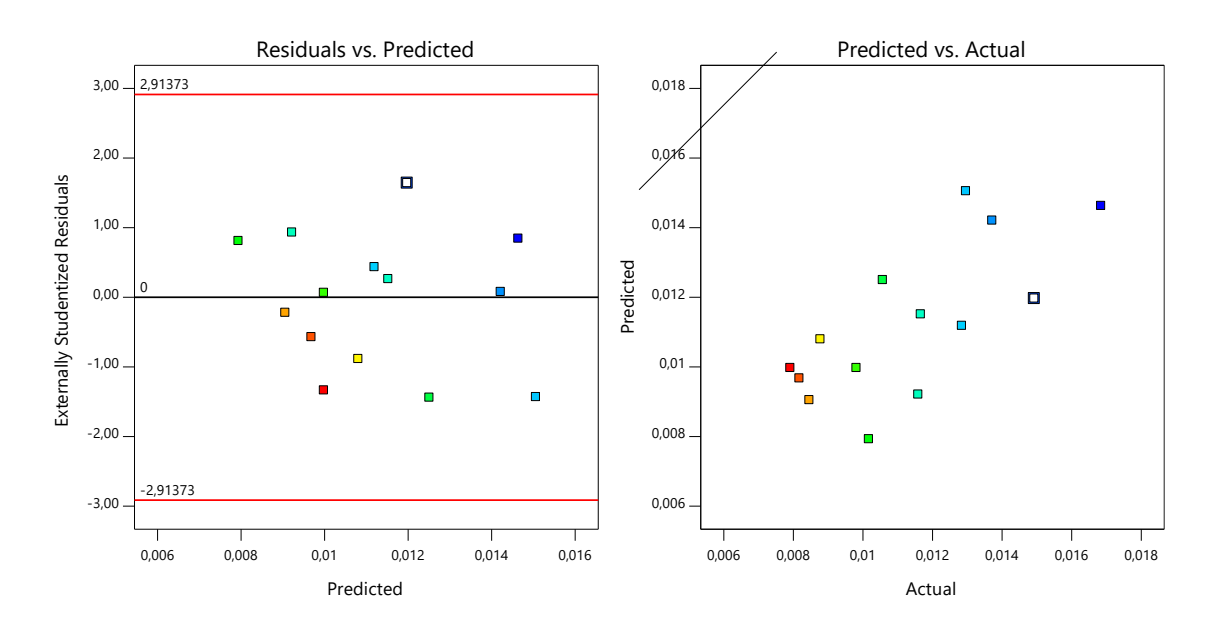


Figure 7-8: Residuals versus Predicted (left) and Predicted vs. Actual (right) for 5-FdU-DP **8**. Created with DesignExpert (version 11).

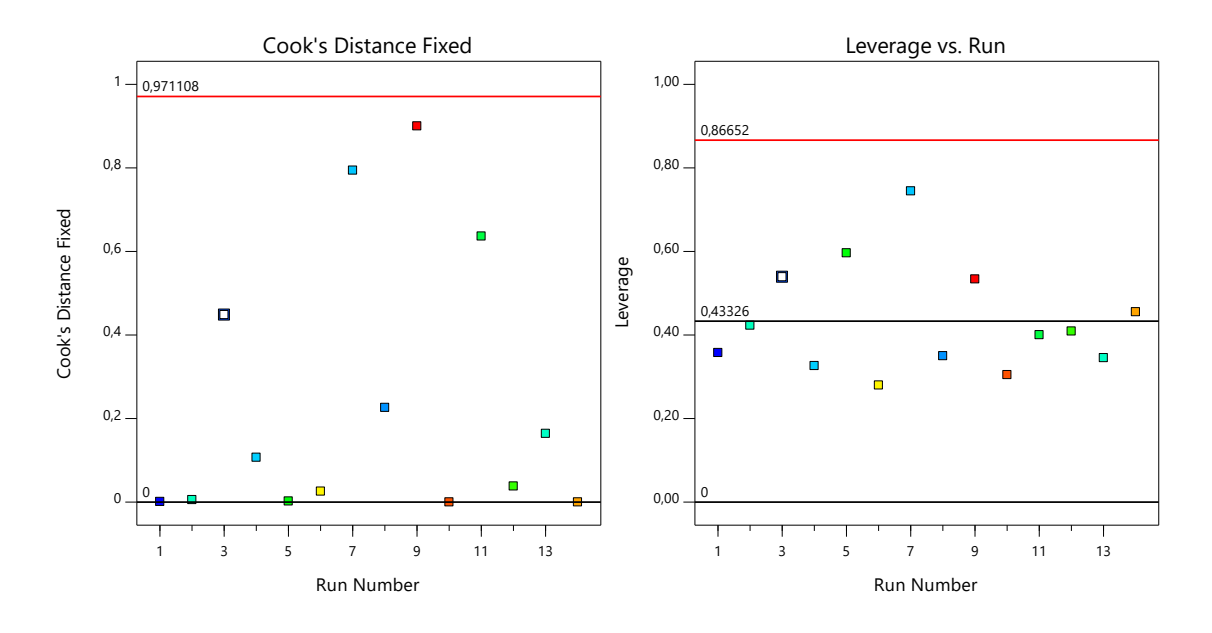


Figure 7-9: Cook's distance plot (left) and leverage versus run plot (right) for 5-FdU-DP **8**. Created in DesignExpert (version 11).

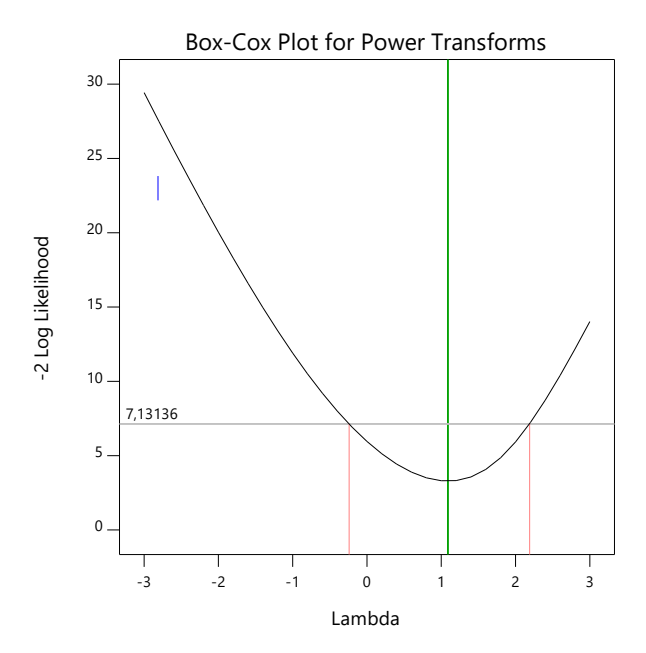


Figure 7-10: Box-cox plot for power transformations for 5-FdU-TP 7. The blue line indicates the parameter λ , which has a value of 1. The red lines denote the 95 % confidence interval. Created with DesignExpert (version 11).

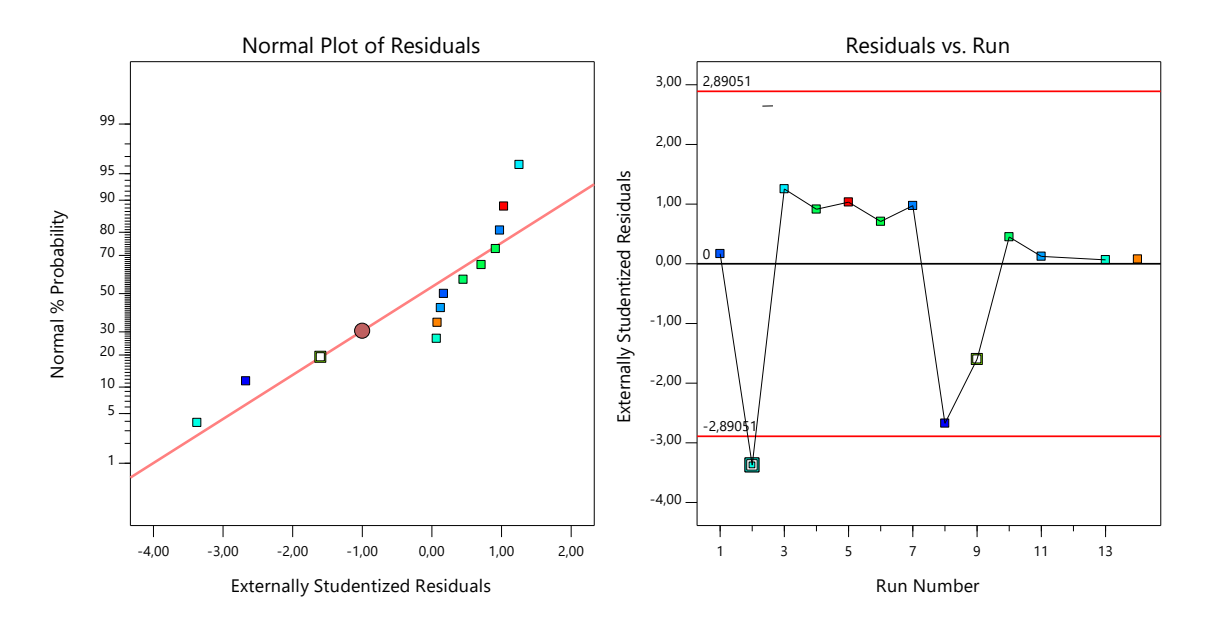


Figure 7-11: Normal Plot of Residuals (left) and Residuals vs. Run (right) for 5-FdU-TP **8**. Created with DesignExpert (version 11).

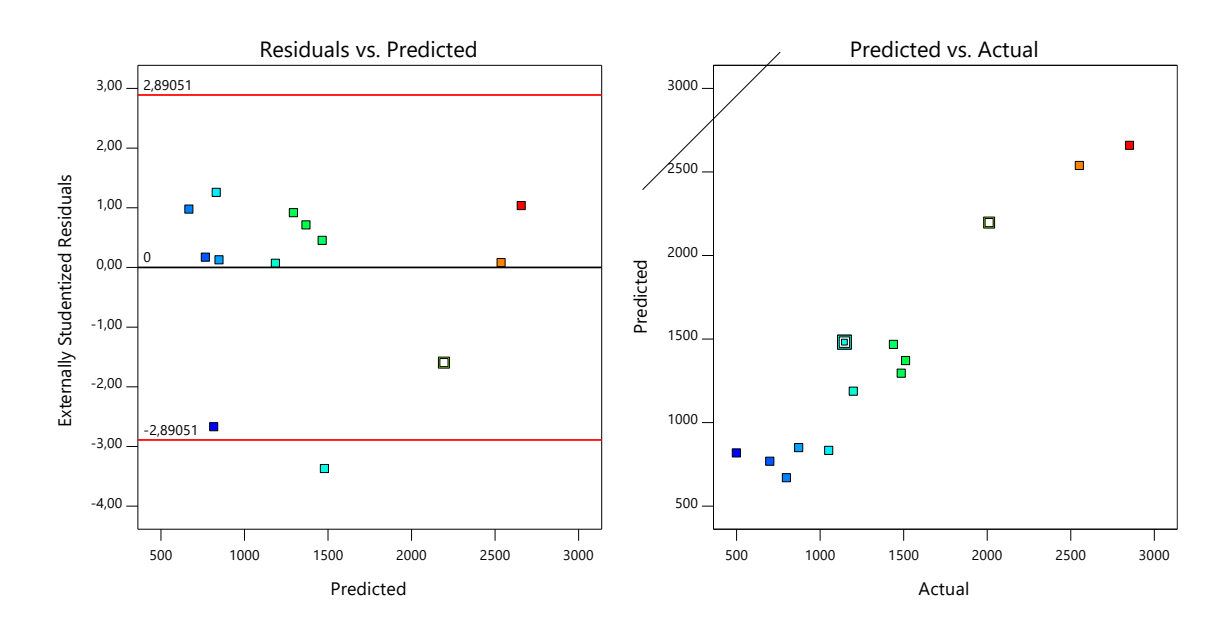


Figure 7-12: Residuals versus Predicted (left) and Predicted vs. Actual (right) for 5-FdU-TP **7**. Created with DesignExpert (version 11).

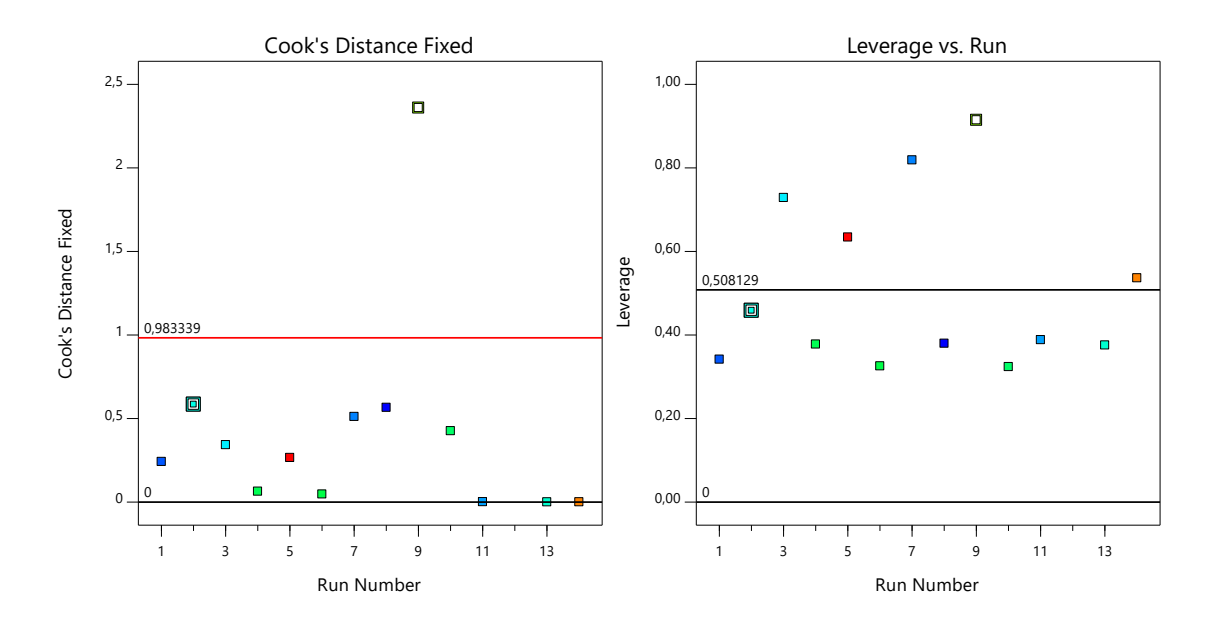


Figure 7-13: Cook's distance plot (left) and leverage versus run plot (right) for 5-FdU-TP **8**. Created in DesignExpert (version 11).

7.2.3 Raw data of the validation

The following tables (Table 7-3 –Table 7-26) summarize all underlying data for the validation experiments of each analyte in every matrix discussed in chapter 4.7.

Table 7-3: The mean values of the integrated analyte and internal standard (ISD) peak areas were used to determine the limit of detection (LOD) and limit of quantification (LOQ). Each analyte was measured at a concentration of 5 ng/mL in HT29 cell lysate (n = 5).

Analyte	Mean Analyte Peak Area [counts]	Mean Internal Standard Peak Area [counts]	Mean Analyte / ISD Peak Area
FdU 10	5.52E+04	1.46E+06	3.78E-02
Tri <i>PPP</i> ro 1	1.25E+04	1.90E+06	6.53E-03
TriPPPro 2	4.73E+03	1.12E+06	4.32E-03
Intermediate 5	1.35E+05	7.94E+06	1.73E-02
Intermediate 6	1.12E+05	2.90E+06	3.89E-02
FdU-MP 9	2.16E+05	1.39E+05	1.54E+00
FdU-DP 8	1.42E+05	2.69E+06	5.38E-02
FdU-TP 7	6.74E+04	2.69E+06	2.55E-02

Table 7-4: Determined mean integrated peak areas (as analyte peak area / ISD peak area) for low, mid and high QC samples (n = 2) including expected and calculated concentrations in ng/mL for the assessment of the accuracy in HT29 cell lysate.

Analyte	Expected concentration	Mean Analyte / ISD Peak	Calculated
Analyte	[ng/mL]	Area	concentration [ng/mL]
	50.0	1.05E-02	59.9
FdU 10	200	6.94E-01	197
	400	1.26E+00	358
TriPPPro-compound 1	50.0	1.35E-02	49.8
	200	9.23E-01	194
	400	1.70E+00	359
TriPPPro-compound 2	15.0	8.32E-04	17.1
	50.0	5.94E-02	50.4
	400	4.45E-01	430

Analyte	Expected concentration [ng/mL]	Mean Analyte / ISD Peak Area	Calculated concentration [ng/mL]
	35.0	6.20E-02	30.9
Intermediate 5	200	4.21E-01	197
	400	9.36E-01	436
	55.0	2.37E-02	62.8
Intermediate 6	150	2.21E-01	136
	400	6.40E-01	388
	80.0	2.12E+00	81.2
FdU-MP 9	250	1.09E+01	287
	450	2.05E+01	515
	65.0	8.04E-01	59.7
FdU-DP 8	100	1.31E+00	94.4
	800	1.18E+01	824
	150	1.06E-01	134
FdU-TP 7	300	5.06E-01	281
	800	1.72E+00	729

Table 7-5: Measurements of the intra- and inter-day precision runs for all analytes in HT29 cell lysate.

	FdU 10	TriPPPro-	TriPPPro-	Inter-	Inter-	FdU-MP 9	FdU-DP 8	FdU-TP 7
		compound	compound	mediate 5	mediate 6			
		1	2					
Day 1	6.94E+05	5.65E+04	2.15E+04	1.01E+05	6.55E+05	5.69E+04	2.07E+05	4.92E+04
(Analyte Peak	6.20E+05	5.42E+04	1.58E+04	1.27E+05	6.88E+05	1.07E+05	2.26E+05	6.37E+04
Area)	6.25E+05	5.15E+04	1.37E+04	1.31E+05	7.24E+05	1.17E+05	2.06E+05	5.58E+04
Mean 1	6.46E+05	5.41E+04	1.70E+04	1.20E+05	6.89E+05	9.36E+04	2.13E+05	5.62E+04
Day 2	4.80E+05	2.97E+05	1.46E+04	1.36E+05	5.41E+05	1.88E+05	1.73E+05	7.34E+04
(Analyte Peak	4.17E+05	1.59E+05	1.75E+04	1.18E+05	5.81E+05	2.03E+05	1.31E+05	6.54E+04
Area)	5.26E+05	1.19E+05	9.31E+03	1.28E+05	5.24E+05	2.56E+05	1.21E+05	6.35E+04
Mean 2	4.74E+05	1.39E+04	1.38E+04	1.27E+05	5.49E+05	2.16E+05	1.42E+05	6.74E+04
Day 3	5.26E+05	1.12E+05	1.69E+04	1.52E+05	5.87E+05	1.06E+05	1.70E+05	1.77E+04
(Analyte Peak	4.77E+05	8.07E+04	1.82E+04	1.61E+05	6.22E+05	1.76E+05	1.29E+05	5.01E+04
Area)	5.78E+05	7.73E+04	1.77E+04	1.60E+05	6.27E+05	1.91E+05	1.04E+05	5.92E+04
Mean 3	5.27E+05	9.00E+04	1.76E+04	1.58E+05	6.12E+05	1.58E+05	1.34E+05	4.23E+04

Table 7-6: Mean integrated peak areas for each analyte at different storage conditions (22 °C, 10 °C, -22°C including one freeze-thaw cycle) in HT29 cell lysate compared to a freshly spiked sample for assessing sample stability.

Sample type	FdU 10	TriPPPro- compound 1	TriPPPro- compound 2	Inter- mediate 5	Inter- mediate 6	FdU-MP 9	FdU-DP 8	FdU-TP 7
Benchtop storage (24 h, 22 °C)	8.72E+06	1.29E+05	6.33E+04	2.02E+06	3.49E+06	4.82E+05	6.04E+05	2.11E+05
Autosampler storage (24 h, 10°C)	1.06E+07	1.77E+05	5.80E+04	3.41E+06	6.64E+06	4.95E+05	7.09E+05	2.11E+05
Freezer storage (24 h, -22 °C)	8.60E+06	1.49E+05	5.24E+04	2.08E+06	2.92E+06	4.38E+05	7.50E+05	1.73E+05
Freshly spiked sample	1.12E+07	2.62E+05	1.02E+05	2.73E+06	5.25E+06	5.99E+05	9.88E+05	1.78E+05

Table 7-7: The mean values of the integrated analyte and internal standard (ISD) peak areas were used to determine the limit of detection (LOD) and limit of quantification (LOQ). Each analyte was measured at a concentration of 10 ng/mL in HT29 cell lysate (n = 5).

Analyte	Mean Analyte Peak Area [counts]	Mean Internal Standard Peak Area [counts]	Mean Analyte / ISD Peak Area
FdU 10	7.29E+05	6.55E+06	1.11E-01
TriPPPro- compound 1	1.43E+05	8.84E+05	1.62E-01
TriPPPro- compound 2	2.63E+04	1.17E+07	2.25E-03
Intermediate 5	1.20E+05	4.53E+06	2.68E-02
Intermediate 6	1.49E+05	5.81E+06	2.58E-02
FdU-MP 9	2.54E+04	5.54E+05	4.72E-02
FdU-DP 8	1.69E+05	2.52E+05	6.68E-01

Table 7-8: Determined mean integrated peak areas (as analyte peak area / ISD peak area) for low, mid and high QC samples (n = 2) including expected and calculated concentrations in ng/mL for the assessment of the accuracy in HT29 supernatant.

Analyte	Expected concentration	Mean Analyte / ISD Peak	Calculated concentration
Analyte	[ng/mL]	Area	[ng/mL]
	150	2.33E-01	171
FdU 10	200	3.31E-01	230
	400	6.84E-01	440
	30.0	3.75E-01	28.0
Tri <i>PPP</i> ro 1	150	2.35E+00	157
	250	3.88E+00	256
	1.00	1.93E-03	0.81
Tri <i>PPP</i> ro 2	150	1.29E-01	153
	350	2.62E-01	316
	40.0	2.67E-02	43.8
Intermediate 5	250	1.87E-01	285
	500	3.41E-01	520
	50.0	1.10E-01	60.0
Intermediate 6	250	4.74E-01	271
	400	8.05E-01	463
	30.0	1.75E-01	25.2
FdU-MP 9	400	2.20E+00	415
	600	1.58E+00	591
	100	1.88E-01	80.2
FdU-DP 8	200	4.38E-01	192
	400	1.04E+00	462

Table 7-9: Measurements of the intra- and inter-day precision runs for all analytes in HT29 supernatant.

	FdU 10	Tri <i>PPP</i> ro 1	Tri <i>PPP</i> ro 2	Inter-	Inter-	FdU-MP 9	FdU-DP 8	FdU-TP 7
				mediate 5	mediate 6			
Day 1	1.11E+06	1.41E+05	2.34E+04	1.37E+05	1.69E+05	2.08E+04	2.27E+05	4.64E+04
(Analyte Peak	1.10E+06	1.58E+05	2.66E+04	1.22E+05	2.30E+05	2.06E+04	1.55E+05	3.43E+04
Area)	1.09E+06	1.61E+05	2.37E+04	1.06E+05	1.74E+05	2.11E+04	1.50E+05	5.22E+04
	9.63E+05	1.62E+05	2.89E+04	1.10E+05	2.10E+05	1.85E+04	1.73E+05	4.43E+0
	9.68E+05	1.57E+05	2.90E+04	1.25E+05	2.06E+05	1.36E+04	1.44E+05	3.47E+0
Mean 1	1.05E+06	1.56E+05	2.63E+04	1.20E+05	1.98E+05	1.89E+04	1.70E+05	4.24E+0
Day 2	1.09E+06	1.24E+05	2.53E+04	9.05E+04	1.55E+05	3.34E+04	1.56E+05	2.49E+0
(Analyte Peak Area)	6.75E+05	9.46E+04	2.20E+04	8.04E+04	1.78E+05	2.80E+04	9.31E+04	4.42E+0
AICd)	7.52E+05	1.49E+05	2.18E+04	8.53E+04	1.81E+05	2.66E+04	1.81E+05	4.37E+0
	8.71E+05	1.07E+05	2.50E+04	1.18E+05	1.98E+05	1.99E+04	1.86E+05	5.67E+0

	FdU 10	Tri <i>PPP</i> ro 1	Tri <i>PPP</i> ro 2	Inter-	Inter-	FdU-MP 9	FdU-DP 8	FdU-TP 7
				mediate 5	mediate 6			
	8.09E+05	1.20E+05	3.16E+04	1.13E+05	1.98E+05	1.92E+04	1.25E+05	4.86E+04
Mean 2	8.39E+05	1.19E+05	2.51E+04	9.74E+04	1.82E+05	2.54E+04	1.48E+05	4.36E+04
Day 3	6.53E+05	1.23E+05	4.28E+04	8.13E+04	1.66E+05	3.30E+04	3.42E+05	6.84E+04
(Analyte Peak Area)	6.73E+05	1.20E+05	2.86E+04	7.86E+04	1.31E+05	1.81E+04	1.91E+05	3.74E+04
Aicaj	8.13E+05	1.62E+05	3.55E+04	1.11E+05	1.50E+05	1.69E+04	1.47E+05	3.77E+04
	7.82E+05	1.70E+05	4.05E+04	1.22E+05	1.62E+05	1.24E+04	1.48E+05	5.08E+04
	7.22E+05	1.41E+05	3.45E+04	1.20E+05	1.36E+05	1.38E+04	8.22E+04	3.94E+04
Mean 3	7.29E+05	1.43E+05	3.64E+04	1.03E+05	1.49E+05	1.88E+04	1.82E+05	4.67E+04

Table 7-10: Mean integrated peak areas for each analyte at different storage conditions (22 °C, 10 °C, -22°C including one freeze-thaw cycle) in HT29 supernatant compared to a freshly spiked sample for assessing sample stability.

Sample type	FdU 10	Tri <i>PPP</i> ro 1	Tri <i>PPP</i> ro 2	Inter- mediate 5	Inter- mediate 6	FdU-MP 9	FdU-DP 8
Benchtop storage (24 h, 22 °C)	1.10E+07	7.78E+06	1.11E+06	2.79E+06	3.26E+06	9.26E+04	0.00E+00
Autosampler storage (24 h, 10°C)	1.23E+07	9.57E+06	1.64E+06	3.55E+06	4.28E+06	8.42E+05	2.49E+04
Freezer storage (24 h, -22 °C)	1.12E+07	9.47E+06	1.44E+06	3.23E+06	3.88E+06	2.37E+05	0.00E+00
Freshly spiked sample	1.09E+07	6.99E+06	1.18E+06	3.59E+06	4.11E+06	9.95E+05	1.21E+05

Table 7-11: The mean values of the integrated analyte and internal standard (ISD) peak areas were used to determine the limit of detection (LOD) and limit of quantification (LOQ). Each analyte was measured at a concentration of 5 ng/mL in HT29 supernatant (n = 5).

Analyte	Mean Analyte Peak Area [counts]	Mean Internal Standard Peak Area [counts]	Mean Analyte / ISD Peak Area	
FdU 10	7.29E+05	6.55E+06	1.11E-01	
Tri <i>PPP</i> ro 1	1.43E+05	8.84E+05	1.62E-01	
Tri <i>PPP</i> ro 2	3.64E+04	1.17E+07	2.25E-03	
Intermediate 5	1.03E+05	2.29E+06	4.53E-02	
Intermediate 6	1.49E+05	5.81E+06	2.58E-02	

Analyte	Mean Analyte Peak Area [counts]	Mean Internal Standard Peak Area [counts]	Mean Analyte / ISD Peak Area
FdU-MP 9	1.88E+04	5.54E+05	4.72E-02
FdU-DP 8	1.69E+05	2.52E+05	6.68E-01

Table 7-12: Determined mean integrated peak areas (as analyte peak area / ISD peak area) for low, mid and high QC samples (n = 2) including expected and calculated concentrations in ng/mL for the assessment of the accuracy in SW620 cell lysate.

Analyte	Expected concentration	Mean Analyte / ISD Peak	Calculated
Analyte	[ng/mL]	Area	concentration [ng/mL]
	25.0	2.98E+01	26.5
FdU 10	50.0	6.14E+01	55.9
	400	4.22E+02	392
	0.50	2.06E-03	N/A
Tri <i>PPP</i> ro 1	50.0	1.80E-01	49.5
	400	1.21E+00	426
	10.0	3.80E-02	13.4
Tri <i>PPP</i> ro 2	50.0	1.50E-01	53.4
	400	9.46E-01	338
	55.0	2.07E-02	37.5
Intermediate 5	200	1.22E-01	187
	400	2.42E-01	364
	30.0	2.99E-02	25.5
Intermediate 6	200	2.50E-01	188
	400	5.66E-01	423
	0.50	1.60E-02	0.415
FdU-MP 9	50.0	7.23E-02	53.1
	400	4.78E-01	432
	150	4.81E+00	127
FdU-DP 8	450	1.65E+01	293
	800	4.35E+01	675
	150	2.21E+00	156
FdU-TP 7	450	5.95E+00	336
	800	1.48E+01	760

Table 7-13: Measurements of the intra- and inter-day precision runs for all analytes in SW620 cell lysate.

	FdU 10	Tri <i>PPP</i> ro 1	Tri <i>PPP</i> ro 2	Inter-	Inter-	FdU-MP 9	FdU-DP 8	FdU-TP 7
				mediate 5	mediate 6			
Day 1	6.39E+05	4.73E+05	7.32E+04	2.78E+05	3.45E+05	4.48E+04	2.80E+05	5.71E+04
(Analyte Peak	5.45E+05	1.16E+05	6.14E+04	2.63E+05	3.69E+05	4.78E+04	1.81E+05	3.83E+04
Area)	5.43E+05	9.21E+04	6.79E+04	2.52E+05	3.79E+05	4.30E+04	1.44E+05	2.48E+04
	6.55E+05	9.61E+04	7.11E+04	2.69E+05	3.21E+05	4.55E+04	1.21E+05	2.82E+04
	5.39E+05	1.00E+05	6.75E+04	2.70E+05	3.32E+05	4.27E+04	1.35E+05	3.10E+04
Mean 1	5.84E+05	1.75E+05	6.82E+04	2.66E+05	3.49E+05	4.48E+04	1.72E+05	3.59E+04
Day 2	4.80E+05	1.67E+05	7.52E+04	3.95E+05	3.02E+05	5.23E+04	1.75E+05	4.71E+04
(Analyte Peak	4.31E+05	1.50E+05	7.14E+04	4.57E+05	2.91E+05	4.92E+04	1.76E+05	5.07E+04
Area)	3.95E+05	2.29E+05	6.75E+04	3.41E+05	2.64E+05	3.95E+04	1.85E+05	3.77E+04
	4.33E+05	1.98E+05	6.78E+04	3.40E+05	2.96E+05	3.73E+04	1.51E+05	4.22E+04
	3.62E+05	1.84E+05	7.78E+04	4.06E+05	2.47E+05	3.48E+04	1.40E+05	1.76E+04
Mean 2	4.20E+05	1.86E+05	7.19E+04	3.88E+05	2.80E+05	4.26E+04	1.65E+05	3.91E+04
Day 3	3.43E+05	1.22E+05	8.83E+04	2.47E+05	3.56E+05	4.79E+04	3.31E+05	6.65E+04
(Analyte Peak	3.40E+05	1.11E+05	9.33E+04	2.50E+05	3.13E+05	4.10E+04	2.15E+05	2.61E+04
Area)	2.95E+05	1.09E+05	9.61E+04	2.81E+05	3.65E+05	4.59E+04	2.33E+05	5.24E+04
	3.29E+05	1.02E+05	9.21E+04	2.58E+05	3.69E+05	4.20E+04	1.28E+05	4.29E+04
	3.20E+05	1.99E+05	9.21E+04	2.34E+05	3.69E+05	3.40E+04	1.54E+05	4.03E+04
Mean 3	3.25E+05	1.29E+05	9.24E+04	2.54E+05	3.54E+05	4.22E+04	2.12E+05	4.56E+04

Table 7-14: Mean integrated peak areas for each analyte at different storage conditions (22 °C, 10 °C, -22°C including one freeze-thaw cycle) in SW620 cell lysate compared to a freshly spiked sample for assessing sample stability.

Sample type	FdU 10	Tri <i>PPP</i> ro 1	Tri <i>PPP</i> ro 2	Inter- mediate 5	Inter- mediate 6	FdU-MP 9	FdU-DP 8	FdU-TP 7
Benchtop storage (24 h, 22 °C)	1.53E+05	5.17E+05	1.51E+05	4.60E+05	5.43E+05	7.62E+04	3.20E+04	2.42E+04
Autosampler storage (24 h, 10°C)	1.29E+05	5.34E+05	1.89E+05	4.03E+05	5.76E+05	1.16E+05	3.60E+04	6.89E+03
Freezer storage (24 h, -22 °C)	1.52E+05	5.01E+05	1.43E+05	3.92E+05	4.97E+05	4.97E+04	9.97E+04	1.71E+04
Freshly spiked sample	2.81E+05	1.03E+06	4.14E+05	4.16E+05	7.43E+05	1.40E+05	2.07E+05	5.79E+04

Table 7-15: The mean values of the integrated analyte and internal standard (ISD) peak areas were used to determine the limit of detection (LOD) and limit of quantification (LOQ). Each analyte was measured at a concentration of 5 ng/mL in SW620 cell lysate(n = 5).

Analyte	Mean Analyte Peak Area [counts]	Mean Internal Standard Peak Area [counts]	Mean Analyte / ISD Peak Area		
FdU 10	5.84E+05	1.78E+06	3.32E-01		
Tri <i>PPP</i> ro 1	1.75E+05	2.38E+06	6.56E-02		
Tri <i>PPP</i> ro 2	6.82E+04	6.22E+06	1.10E-02		
Intermediate 5	2.66E+05	1.05E+07	2.58E-02		
Intermediate 6	3.49E+05	2.01E+07	1.74E-02		
FdU-MP 9	4.48E+04	1.20E+04	3.88E+00		
FdU-DP 8	1.72E+05	6.32E+05	2.78E-01		
FdU-TP 7	3.59E+04	6.32E+05	5.83E-02		

Table 7-16: Determined mean integrated peak areas (as analyte peak area / ISD peak area) for low, mid and high QC samples (n = 2) including expected and calculated concentrations in ng/mL for the assessment of the accuracy in SW620 supernatant.

Analyte	Expected concentration [ng/mL]	Mean Analyte / ISD Peak Area	Calculated concentration [ng/mL]
	15.0	1.00E-01	12.4
FdU 10	200	1.95E+00	224
	400	2.95E+00	340
	15.0	2.24E-01	13.6
Tri <i>PPP</i> ro 1	200	5.06E+00	312
	400	6.96E+00	429
	15.0	4.62E-03	17.4
Tri <i>PPP</i> ro 2	200	6.07E-02	215
	400	1.21E-01	428
	10.0	1.41E-02	9.06
Intermediate 5	250	2.99E-01	282
	400	4.78E-01	455
	15.0	6.81E-02	13.6
Intermediate 6	200	1.04E+00	204
	400	1.63E+00	321
	90.0	3.12E+00	76.0
FdU-MP 9	400	4.10E-01	16.0
	600	2.26E+01	505

Analyte	Expected concentration [ng/mL]	Mean Analyte / ISD Peak Area	Calculated concentration [ng/mL	
	90.0	3.04E+00	101	
FdU-DP 8	400	3.72E-01	13.0	
	600	2.16E+01	730	
	90.0	1.28E+00	89	
FdU-TP 7	400	9.56E-02	N/A	
	600	4.43E+00	679	

Table 7-17: Measurements of the intra- and inter-day precision runs for all analytes in SW620 supernatant.

	FdU 10	Tri <i>PPP</i> ro 1	Tri <i>PPP</i> ro 2	Inter-	Inter-	FdU-MP 9	FdU-DP 8	FdU-TP 7
				mediate 5	mediate 6			
Day 1	5.76E+04	1.85E+06	2.12E+05	4.26E+05	5.38E+05	1.04E+05	2.01E+05	4.65E+04
(Analyte Peak	3.68E+04	2.11E+06	1.95E+05	5.15E+05	5.40E+05	1.13E+05	2.16E+05	4.45E+04
Area)	4.18E+04	2.29E+06	2.14E+05	5.79E+05	5.31E+05	1.12E+05	2.13E+05	4.11E+04
	4.11E+04	1.98E+06	2.10E+05	5.06E+05	5.72E+05	1.12E+05	2.12E+05	3.33E+04
	3.48E+04	2.31E+06	2.01E+05	5.58E+05	5.01E+05	1.23E+05	2.72E+05	3.61E+04
Mean 1	4.24E+04	2.11E+06	2.06E+05	5.17E+05	5.36E+05	1.13E+05	2.23E+05	4.03E+04
Day 2	7.92E+04	1.26E+06	4.26E+05	2.03E+05	8.01E+05	8.19E+04	1.91E+05	2.89E+04
(Analyte Peak	5.74E+04	1.14E+06	3.58E+05	1.85E+05	6.27E+05	7.69E+04	2.53E+05	3.54E+04
Area)	6.74E+04	1.12E+06	4.11E+05	1.97E+05	6.17E+05	7.54E+04	2.15E+05	4.59E+04
	6.39E+04	1.06E+06	1.02E+02	2.11E+05	2.09E+03	7.71E+04	2.67E+05	3.70E+04
	3.59E+04	1.24E+06	3.59E+05	1.98E+05	8.67E+05	5.63E+04	2.61E+05	5.03E+04
Mean 2	6.08E+04	1.16E+06	3.89E+05	1.99E+05	5.83E+05	7.35E+04	2.37E+05	3.95E+04
Day 3	6.24E+04	3.94E+05	6.89E+04	1.69E+05	1.47E+05	4.77E+04	2.67E+05	4.74E+04
(Analyte Peak	5.13E+04	5.04E+05	7.05E+04	1.14E+05	1.25E+05	4.17E+04	2.22E+05	3.50E+04
Area)	5.90E+04	5.78E+05	6.99E+04	1.31E+05	1.33E+05	4.54E+04	2.02E+05	3.60E+04
	5.40E+04	6.96E+05	6.81E+04	1.34E+05	1.45E+05	4.48E+04	1.99E+05	2.73E+04
	5.45E+04	7.77E+05	1.06E+05	1.37E+05	1.51E+05	4.92E+04	1.68E+05	3.32E+04
Mean 3	5.62E+04	5.90E+05	7.67E+04	1.37E+05	1.40E+05	4.58E+04	2.12E+05	3.58E+04

Table 7-18: Mean integrated peak areas for each analyte at different storage conditions (22 °C, 10 °C, -22°C including one freeze-thaw cycle) in SW620 supernatant compared to a freshly spiked sample for assessing sample stability.

Sample type	FdU 10	Tri <i>PPP</i> ro 1	Tri <i>PPP</i> ro 2	Inter- mediate 5	Inter- mediate 6	FdU-MP 9	FdU-DP 8	FdU-TP 7
Benchtop storage (24 h, 22 °C)	1.51E+06	2.66E+07	1.56E+06	2.96E+06	3.16E+06	1.30E+06	6.15E+05	3.71E+04

Sample type	FdU 10	Tri <i>PPP</i> ro 1	Tri <i>PPP</i> ro 2	Inter- mediate 5	Inter- mediate 6	FdU-MP 9	FdU-DP 8	FdU-TP 7
Autosampler storage (24 h, 10°C)	1.48E+06	3.79E+07	2.20E+06	3.14E+06	3.56E+06	1.17E+06	6.83E+05	5.80E+04
Freezer storage (24 h, -22 °C)	1.23E+06	2.47E+07	1.62E+06	2.29E+06	2.63E+06	1.03E+06	4.87E+05	4.35E+04
Freshly spiked sample	1.24E+06	4.33E+07	3.13E+06	3.52E+06	3.80E+06	2.09E+06	6.91E+05	5.95E+04

Table 7-19: The mean values of the integrated analyte and internal standard (ISD) peak areas were used to determine the limit of detection (LOD) and limit of quantification (LOQ). Each analyte was measured at a concentration of 5 ng/mL in SW620 supernatant (n = 5).

Mean Analyte Peak Area [counts]	Mean Internal Standard Peak Area [counts]	Mean Analyte / ISD Peak Area		
4.24E+04	5.85E+06	7.22E-03		
1.16E+06	6.23E+06	1.88E-01		
7.67E+04	2.68E+07	2.85E-03		
5.17E+05	1.78E+07	2.91E-02		
5.36E+05	1.80E+07	2.98E-02		
1.13E+05	1.23E+06	9.18E-02		
2.23E+05	9.93E+05	2.29E-01		
4.03E+04	9.93E+05	4.14E-02		
	[counts] 4.24E+04 1.16E+06 7.67E+04 5.17E+05 5.36E+05 1.13E+05 2.23E+05	[counts] Peak Area [counts] 4.24E+04 5.85E+06 1.16E+06 6.23E+06 7.67E+04 2.68E+07 5.17E+05 1.78E+07 5.36E+05 1.80E+07 1.13E+05 1.23E+06 2.23E+05 9.93E+05		

Table 7-20: Determined mean integrated peak areas (as analyte peak area / ISD peak area) for low, mid and high QC samples (n = 2) including expected and calculated concentrations in ng/mL for the assessment of the accuracy in CEM/O cell lysate.

Analyte	Expected concentration	Mean Analyte / ISD Peak	Calculated	
Analyte	[ng/mL]	Area	concentration [ng/mL]	
	5.00	8.91E-04	6.00	
d4T 16	450	1.81E-02	405	
	750	3.34E-02	760	
	5.00	9.65E-02	4.61	
Tri <i>PPP</i> ro 3	450	8.50E+00	426	
	750	1.38E+01	692	

Analuta	Expected concentration	Mean Analyte / ISD Peak	Calculated
Analyte	[ng/mL]	Area	concentration [ng/mL]
	25.0	3.32E-02	69
Tri <i>PPP</i> ro 4	200	2.62E-01	200
	400	6.71E-01	434
	25.0	4.08E-02	25.0
Intermediate 11	200	4.21E-01	218
	400	8.01E-01	323
	30.0	3.46E-02	31.9
Intermediate 12	200	2.48E-01	176
	400	3.90E-01	272
	50.0	3.42E-02	54.0
d4T-MP 15	450	2.42E-01	392
	750	4.27E-01	693
	200	2.61E-01	225
d4T-DP 14	400	5.52E-01	410
	800	1.24E+00	845
	200	1.01E-01	193
d4T-TP 13	400	1.54E-01	405
	800	2.71E-01	875

Table 7-21: Measurements of the intra- and inter-day precision runs for all analytes in CEM/0 cell lysate.

	d4T 16	Tri <i>PPP</i> ro 3	Tri <i>PPP</i> ro 4	Inter-	Inter-	d4T-	d4T-	d4T-
				mediate 11	mediate 12	MP 15	DP 14	TP 13
Day 1	7.53E+03	2.54E+06	2.14E+06	3.23E+05	4.83E+05	1.38E+05	5.71E+04	2.62E+04
(Analyte Peak	6.14E+03	2.04E+06	2.39E+06	5.71E+05	4.54E+05	1.24E+05	3.97E+04	1.91E+04
Area)	5.30E+03	2.26E+06	3.13E+06	4.01E+05	4.72E+05	1.20E+05	3.64E+04	1.53E+04
	5.80E+03	2.91E+06	3.42E+06	2.13E+05	4.91E+05	1.31E+05	4.19E+04	1.81E+04
	7.18E+03	3.50E+06	3.07E+06	2.25E+05	4.56E+05	1.28E+05	2.96E+04	2.07E+04
Mean 1	6.39E+03	2.65E+06	2.83E+06	3.47E+05	4.71E+05	1.28E+05	4.09E+04	1.99E+04
Day 2	7.09E+03	5.45E+06	3.03E+06	2.63E+05	4.23E+05	1.67E+05	8.31E+04	2.59E+04
(Analyte Peak	6.31E+03	3.17E+06	4.11E+06	4.50E+05	4.11E+05	1.60E+05	6.35E+04	1.26E+04
Area)	4.91E+03	3.27E+06	3.47E+06	5.89E+05	3.32E+05	1.44E+05	4.17E+04	1.18E+04
	3.82E+03	3.22E+06	3.04E+06	6.00E+05	3.12E+05	1.49E+05	5.31E+04	1.52E+04
	4.68E+03	3.24E+06	2.61E+06	5.77E+05	3.02E+05	1.65E+05	6.48E+04	1.94E+04
Mean 2	5.36E+03	3.67E+06	3.25E+06	4.96E+05	3.56E+05	1.57E+05	6.12E+04	1.70E+04
Day 3	5.19E+03	2.32E+06	3.34E+06	5.75E+05	3.74E+05	1.46E+05	4.96E+04	1.21E+04
(Analyte Peak	3.73E+03	2.95E+06	1.98E+06	5.80E+05	3.22E+05	1.51E+05	4.55E+04	1.45E+04
Area)	3.30E+03	3.33E+06	1.93E+06	6.85E+05	3.50E+05	1.58E+05	5.46E+04	1.60E+04
	4.08E+03	3.57E+06	1.93E+06	6.67E+05	3.42E+05	1.87E+05	5.04E+04	1.38E+04

	d4T 16	Tri <i>PPP</i> ro 3	Tri <i>PPP</i> ro 4	Inter-	Inter-	d4T-	d4T-	d4T-
				mediate 11	mediate 12	MP 15	DP 14	TP 13
	5.30E+03	3.63E+06	2.06E+06	6.57E+05	3.67E+05	1.78E+05	5.95E+04	1.60E+04
Mean 3	4.32E+03	3.16E+06	2.25E+06	6.33E+05	3.51E+05	1.64E+05	5.19E+04	1.45E+04

Table 7-22: Mean integrated peak areas for each analyte at different storage conditions (22 °C, 10 °C, -22°C including one freeze-thaw cycle) in CEM/O cell lysate compared to a freshly spiked sample for assessing sample stability.

Sample type	d4T 16	Tri <i>PPP</i> ro 3	Tri <i>PPP</i> ro 4	Inter- mediate 11	Inter- mediate 12	d4T- MP 15	d4T- DP 14	d4T- TP 13
Benchtop storage (24 h, 22 °C)	7.94E+03	3.67E+07	1.15E+07	3.67E+07	8.70E+06	5.54E+05	1.71E+05	2.15E+04
Autosampler storage (24 h, 10°C)	1.09E+04	3.55E+07	1.20E+07	3.55E+07	6.72E+06	6.23E+05	2.52E+05	6.88E+04
Freezer storage (24 h, -22 °C)	8.42E+03	3.83E+07	1.21E+07	3.83E+07	6.78E+06	6.07E+05	1.30E+05	1.04E+04
Freshly spiked sample	1.30E+04	4.10E+07	1.17E+07	4.10E+07	6.59E+06	1.26E+06	4.40E+05	1.16E+05

Table 7-23: The mean values of the integrated analyte and internal standard (ISD) peak areas were used to determine the limit of detection (LOD) and limit of quantification (LOQ). Each analyte was measured at a concentration of 5 ng/mL in CEM/0 cell lysate (n = 5).

Analyte	Mean Analyte Peak Area [counts]	Mean Internal Standard Peak Area [counts]	Mean Analyte / ISD Peak Area
d4T 16	6.39E+03	1.96E+07	3.34E-04
Tri <i>PPP</i> ro 3	2.65E+06	1.60E+07	1.67E-01
Tri <i>PPP</i> ro 4	2.83E+06	1.60E+07	1.81E-01
Intermediate 11	6.33E+05	7.05E+06	8.97E-02
Intermediate 12	3.51E+05	7.05E+06	4.99E-02
d4T-MP 15	1.28E+05	1.89E+05	7.19E-01
d4T-DP 14	5.19E+04	1.25E+06	4.20E-02
d4T-TP 13	1.45E+04	1.25E+06	1.18E-02

Table 7-24: Determined mean integrated peak areas (as analyte peak area / ISD peak area) for low, mid and high QC samples (n = 2) including expected and calculated concentrations in ng/mL for the assessment of the accuracy in CEM/O supernatant.

Analyte	Expected concentration	Mean Analyte / ISD Peak	Calculated	
Analyte	[ng/mL]	Area	concentration [ng/mL]	
	25.0	1.47E-03	27.2	
d4T 16	200	7.94E-03	209	
	400	1.56E-02	424	
	25.0	6.09E-02	7.29	
Tri <i>PPP</i> ro 3	200	4.19E-01	234	
	400	7.81E-01	463	
	25.0	2.80E-02	24.3	
Tri <i>PPP</i> ro 4	200	2.02E-01	183	
	400	4.08E-01	371	
	25.0	1.98E-02	10.0	
Intermediate 11	200	2.05E-01	106	
	400	2.14E-01	110	
	30.0	2.98E-01	37.8	
Intermediate 12	200	2.05E+00	206	
	400	4.55E+00	446	
	25.0	2.30E-01	28.8	
d4T-MP 15	200	1.65E+00	177	
	400	3.41E+00	359	
	100	3.86E-02	93.7	
d4T-DP 14	450	3.08E-01	357	
	700	6.04E-01	649	
	100	4.33E-02	102	
d4T-TP 13	450	2.37E-01	392	
	700	4.00E-01	636	

Table 7-25: Measurements of the intra- and inter-day precision runs for all analytes in CEM/0 cell supernatant.

	d4T 16	Tri <i>PPP</i> ro 3	Tri <i>PPP</i> ro 4	Inter-	Inter-	d4T-	d4T-	d4T-
				mediate 11	mediate 12	MP 15	DP 14	TP 13
Day 1	6.09E+03	3.73E+06	2.99E+06	5.85E+05	5.13E+05	2.24E+05	1.82E+04	2.10E+04
(Analyte Peak	8.95E+03	4.48E+06	4.03E+06	6.05E+05	4.95E+05	2.22E+05	2.18E+04	1.19E+04
Area)	7.05E+03	5.04E+06	4.11E+06	5.67E+05	4.68E+05	2.30E+05	1.62E+04	1.27E+04
	5.98E+03	5.34E+06	3.56E+06	3.65E+05	5.75E+05	2.41E+05	1.33E+04	1.13E+04
	6.25E+03	5.21E+06	3.21E+06	3.37E+05	6.78E+05	2.34E+05	2.83E+04	1.28E+04
Mean 1	6.86E+03	4.76E+06	3.58E+06	4.92E+05	5.46E+05	2.30E+05	1.96E+04	1.39E+04

	d4T 16	Tri <i>PPP</i> ro 3	Tri <i>PPP</i> ro 4	Inter-	Inter-	d4T-	d4T-	d4T-
				mediate 11	mediate 12	MP 15	DP 14	TP 13
Day 2	6.62E+03	3.98E+06	2.61E+06	5.16E+05	5.19E+05	1.83E+05	2.15E+04	1.53E+0
(Analyte Peak	3.57E+03	3.85E+06	3.88E+06	3.91E+05	4.17E+05	1.77E+05	2.71E+04	1.84E+0
Area)	4.68E+03	4.96E+06	2.75E+06	2.78E+05	5.15E+05	1.75E+05	3.94E+04	2.43E+0
	2.43E+03	6.33E+06	3.55E+06	3.35E+05	5.67E+05	1.67E+05	1.84E+04	1.04E+
	3.13E+03	5.83E+06	4.68E+06	6.23E+05	5.43E+05	1.54E+05	2.83E+04	1.31E+0
Mean 2	4.09E+03	4.99E+06	3.49E+06	4.29E+05	5.12E+05	1.71E+05	2.69E+04	1.63E+0
Day 3	3.79E+03	2.33E+06	3.58E+06	4.05E+05	5.66E+05	1.46E+05	1.60E+04	1.23E+0
(Analyte Peak	4.53E+03	2.51E+06	3.01E+06	5.81E+05	4.49E+05	1.60E+05	1.98E+04	1.56E+
Area)	2.57E+03	2.55E+06	2.84E+06	4.52E+05	4.35E+05	1.60E+05	1.44E+04	1.05E+
	3.21E+03	2.88E+06	2.84E+06	4.31E+05	3.88E+05	1.57E+05	1.51E+04	1.04E+
	3.75E+03	2.98E+06	2.34E+06	3.51E+05	3.33E+05	1.74E+05	2.58E+04	8.62E+
Mean 3	3.57E+03	2.65E+06	2.92E+06	4.44E+05	4.34E+05	1.59E+05	1.82E+04	1.15E+0

Table 7-26: Mean integrated peak areas for each analyte at different storage conditions (22 °C, 10 °C, -22 °C including one freeze-thaw cycle) in CEM/O supernatant compared to a freshly spiked sample for assessing sample stability.

Sample type	d4T 16	Tri <i>PPP</i> ro 3	Tri <i>PPP</i> ro 4	Inter- mediate 11	Inter- mediate 12	d4T- MP 15	d4T- DP 14	d4T- TP 13
Benchtop storage (24 h, 22 °C)	2.94E+04	1.57E+07	1.50E+07	3.91E+06	3.82E+06	1.82E+06	2.73E+05	2.62E+05
Autosampler storage (24 h, 10°C)	4.26E+04	1.10E+07	1.78E+07	6.17E+06	5.03E+06	1.93E+06	2.77E+05	1.93E+05
Freezer storage (24 h, -22 °C)	3.27E+04	1.63E+07	1.59E+07	4.39E+06	3.55E+06	1.78E+06	2.80E+05	2.17E+05
Freshly spiked sample	2.41E+04	2.32E+07	2.43E+07	5.03E+06	4.08E+06	1.58E+06	2.74E+05	2.55E+05

Table 7-27: The mean values of the integrated analyte and internal standard (ISD) peak areas were used to determine the limit of detection (LOD) and limit of quantification (LOQ). Each analyte was measured at a concentration of 5 ng/mL in CEM/0 supernatant (n = 5).

Analyte	Mean Analyte Peak Area [counts]	Mean Internal Standard Peak Area [counts]	Mean Analyte / ISD Peak Area
d4T 16	3.57E+03	2.21E+07	1.62E-04
Tri <i>PPP</i> ro 3	2.65E+06	4.51E+07	5.92E-02

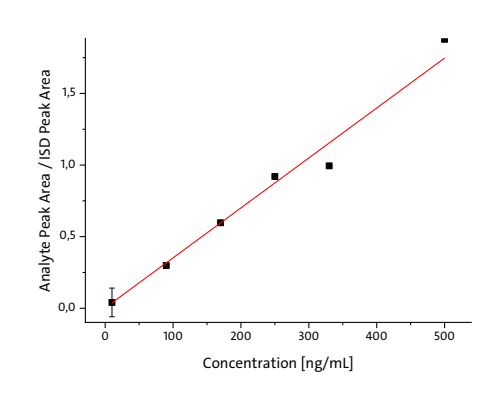
Tri <i>PPP</i> ro 4	2.92E+06	4.51E+07	6.46E-02
Intermediate 11	4.92E+05	6.93E+06	7.47E-02
Intermediate 12	4.34E+05	4.82E+06	1.05E-01
d4T-MP 15	2.30E+05	1.14E+06	2.03E-01
d4T-DP 14	1.96E+04	1.14E+06	1.73E-02
d4T-TP 13	1.39E+04	1.14E+06	1.22E-02

7.2.4 Calibration curves

7.2.4.1 HT29 cell lysate and supernatant

Table 7-28: Back-calculation of calibration levels for FdU **10** in HT29 cell lysate.

Concentration x [ng/mL]	Mean Analyte / ISD Peak Area y]	Calculated x [ng/mL]	%CV [%]	Accuracy [%]	Requirement fulfilled?
10.0	4.04E-02	10.7	9.0	107	True
90.0	2.98E-01	84.9	8.7	94	True
170	5.96E-01	170	10	100	True
250	9.20E-01	262	1.5	105	True
330	9.94E-01	286	11	87	True
500	1.88E+00	536	7.6	107	True



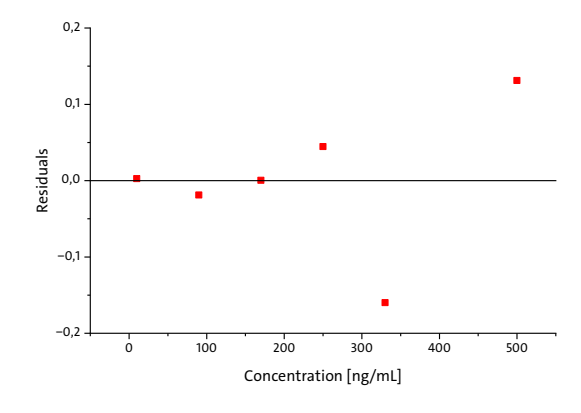
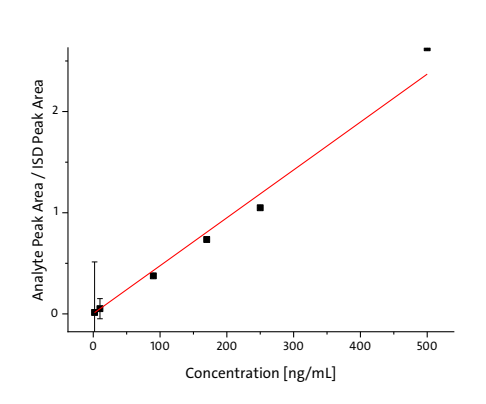


Figure 7-14: Calibration curve (left) and corresponding residual plot (right) for FdU **10** in HT29 cell lysate.

 Table 7-29: Back-calculation of calibration levels for TriPPPro-compound 1 in HT29 cell lysate.

Concentration x [ng/mL]	Mean Analyte / ISD Peak Area y]	Calculated x [ng/mL]	Accuracy [%]	Deviation [%]	Requirement fulfilled?
2.00	1.41E-02	2.37	118	18	True
10.0	5.15E-02	10.3	103	3	True
90.0	3.76E-01	79.5	88	12	True
170	7.35E-01	155	91	8	True
250	1.05E+00	220	88	12	True
500	2.63E+00	554	111	11	True



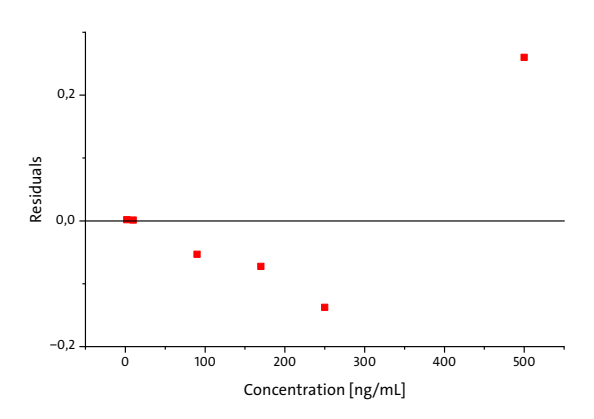
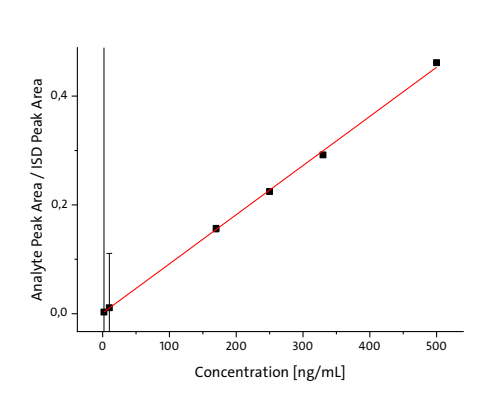


Figure 7-15: Calibration curve (left) and corresponding residual plot (right) for Tri*PPP*ro-compound **1** in HT29 cell lysate.

Table 7-30: Back-calculation of calibration levels for TriPPPro-compound 2 in HT29 cell lysate.

Concentration x [ng/mL]	Mean Analyte / ISD Peak Area y]	Calculated x [ng/mL]	Accuracy [%]	Deviation [%]	Requirement fulfilled?
10.0	1.75E-02	8.00	80	20	True
25.0	3.78E-02	29.0	115	15	True
45.0	6.13E-02	52.1	115	15	True
80.0	8.08E-02	72.3	90	10	True
200	2.04E-01	194	97	3	True
500	5.20E-01	505	101	1	True



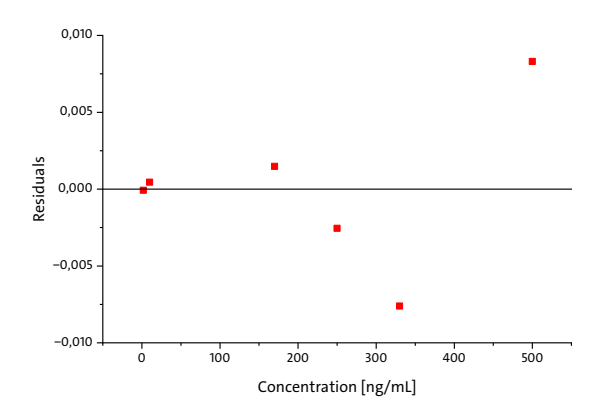
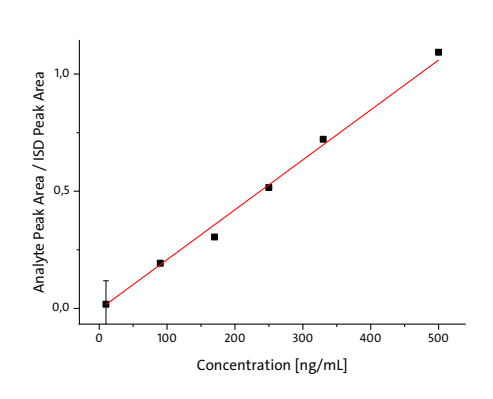


Figure 7-16: Calibration curve (left) and corresponding residual plot (right) for Tri*PPP*ro-compound **2** in HT29 cell lysate.

Table 7-31: Back-calculation of calibration levels for intermediate **5** in HT29 cell lysate.

Concentration x [ng/mL]	Mean Analyte / ISD Peak Area y]	Calculated x [ng/mL]	Accuracy [%]	Deviation [%]	Requirement fulfilled?
10.0	1.81E-02	10.6	106	6	True
90.0	1.93E-01	91.9	102	2	True
170	3.05E-01	147	87	13	True
250	5.15E-01	251	100	0	True
330	7.22E-01	340	103	3	True
500	1.09E+00	510	102	2	True



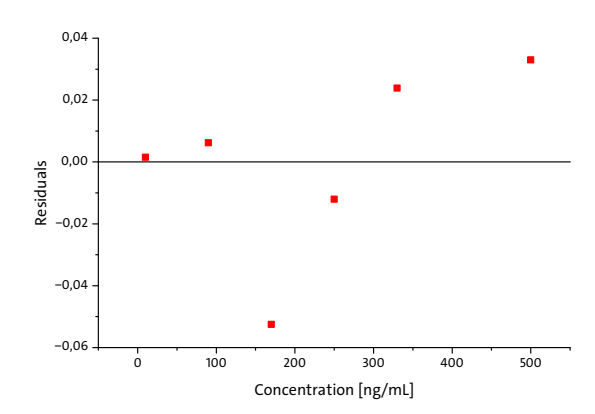
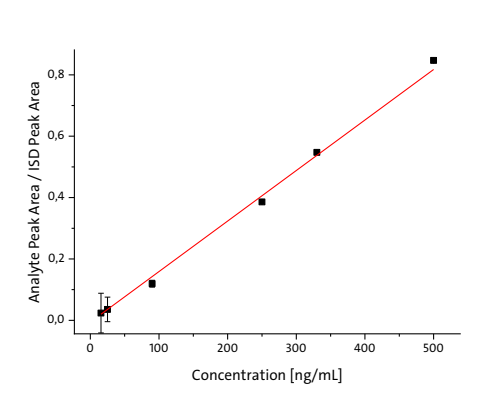


Figure 7-17: Calibration curve (left) and corresponding residual plot (right) for intermediate **5** in HT29 cell lysate.

Table 7-32: Back-calculation of calibration levels for intermediate **6** in HT29 cell lysate.

Concentration x [ng/mL]	Mean Analyte / ISD Peak Area y]	Calculated x [ng/mL]	Accuracy [%]	Deviation [%]	Requirement fulfilled?
15.5	2.37E-02	17.5	113	13	True
25.0	3.56E-02	24.7	99	1	True
90.0	1.19E-01	80.2	89	11	True
250	3.86E-01	235	94	6	True
330	5.47E-01	332	101	1	True
500	8.47E-01	521	104	4	True



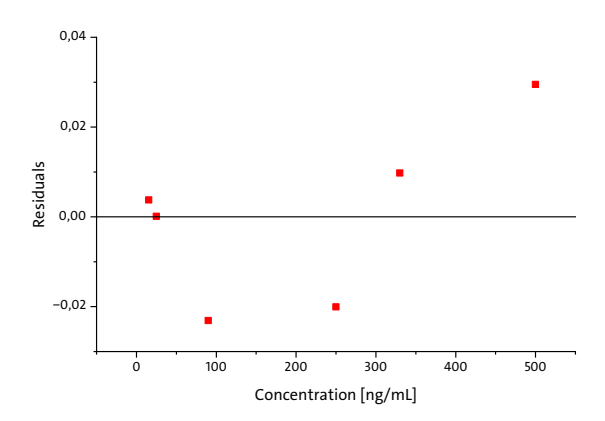
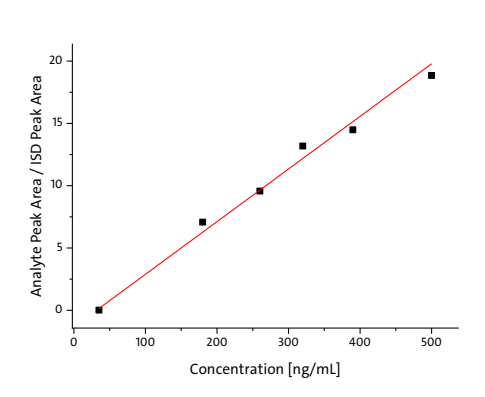


Figure 7-18: Calibration curve (left) and corresponding residual plot (right) for intermediate **6** in HT29 cell lysate.

Table 7-33: Back-calculation of calibration levels for 5-FdU-MP **9** in HT29 cell lysate.

Concentration x [ng/mL]	Mean Analyte / ISD Peak Area y]	Calculated x [ng/mL]	Accuracy [%]	Deviation [%]	Requirement fulfilled?
35.0	1.73E-02	31.8	91	9	True
180	7.07E+00	200.0	111	11	True
260	9.57E+00	258	99	1	True
320	1.32E+01	344	107	7	True
390	1.45E+01	376	96	4	True
500	1.88E+01	476	95	5	True



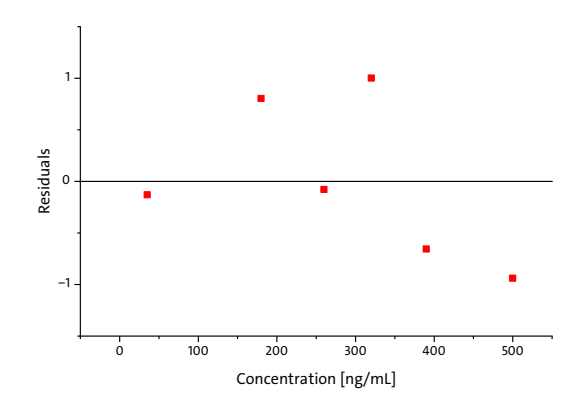
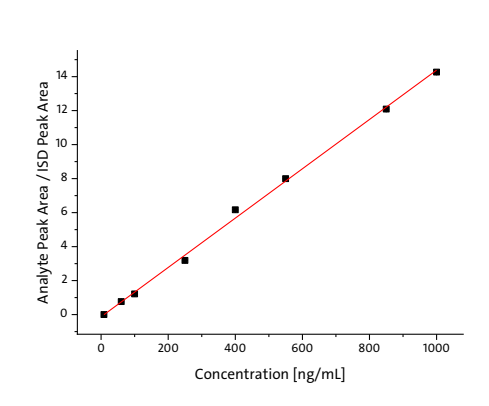


Figure 7-19: Calibration curve (left) and corresponding residual plot (right) for 5-FdU-MP **9** in HT29 cell lysate.

Table 7-34: Back-calculation of calibration levels for 5-FdU-DP **8** in HT29 cell lysate.

Concentration x [ng/mL]	Mean Analyte / ISD Peak Area y]	Calculated x [ng/mL]	Accuracy [%]	Deviation [%]	Requirement fulfilled?
8.500	3.11E-03	9.986	117	17	True
60.00	7.64E-01	56.95	95	5	True
100.0	1.21E+00	88.21	88	12	True
250.0	3.19E+00	225.0	90	10	True
400.0	6.16E+00	432.2	108	8	True
550.0	7.99E+00	559.5	102	2	True
850.0	1.21E+01	847.1	100	0	True
1000	1.43E+01	1000	100	0	True



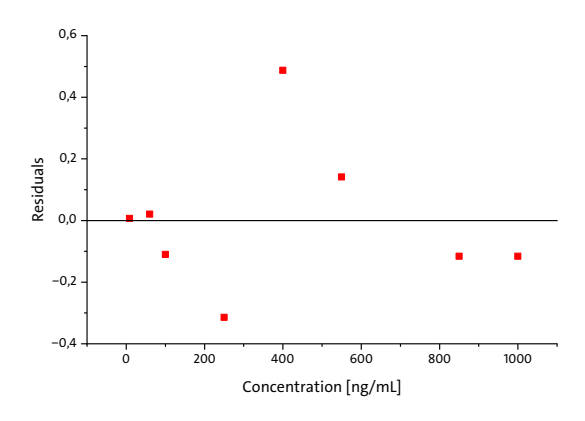
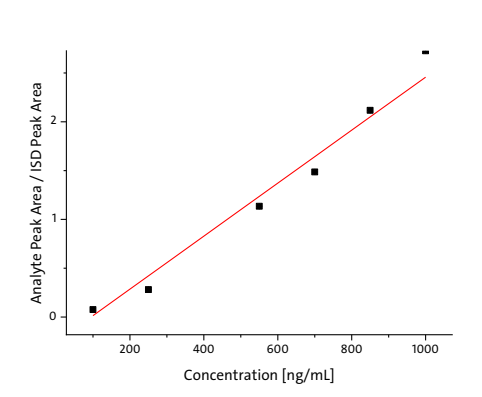


Figure 7-20: Calibration curve (left) and corresponding residual plot (right) for 5-FdU-DP **8** in HT29 cell lysate.

Table 7-35: Back-calculation of calibration levels for 5-FdU-TP **7** in HT29 cell lysate.

Concentration x [ng/mL]	Mean Analyte / ISD Peak Area y]	Calculated x [ng/mL]	Accuracy [%]	Deviation [%]	Requirement fulfilled?
100.0	7.64E-02	119.9	120	20	True
250.0	2.81E-01	198.1	79	21	False
550.0	1.13E+00	512.8	93	7	True
700.0	1.49E+00	642.2	92	8	True
850.0	2.12E+00	874.4	103	3	True
1000	2.73E+00	1100	110	10	True



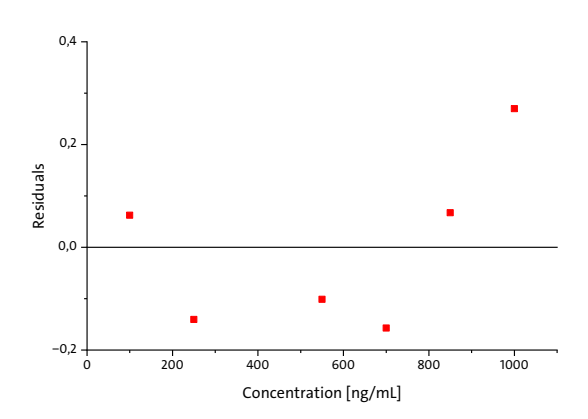
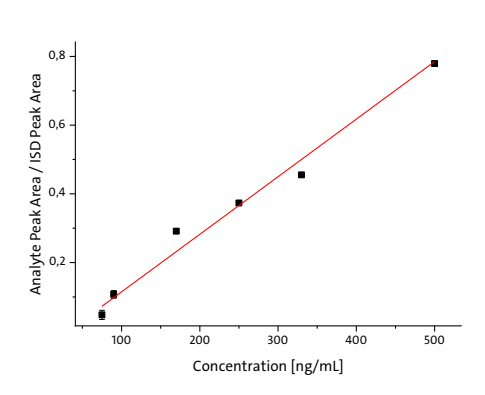


Figure 7-21: Calibration curve (left) and corresponding residual plot (right) for 5-FdU-TP **7** in HT29 cell lysate.

Table 7-36: Back-calculation of calibration levels for FdU 10 in HT29 supernatant.

Concentration x [ng/mL]	Mean Analyte / ISD Peak Area y]	Calculated x [ng/mL]	Accuracy [%]	Deviation [%]	Requirement fulfilled?
75.0	4.76E-02	59.7	80	20	True
90.0	1.07E-01	95.9	107	7	True
170	2.91E-01	206	121	21	False
250	3.73E-01	254	102	2	True
330	4.55E-01	303	92	8	True
500	7.79E-01	496	99	1	True



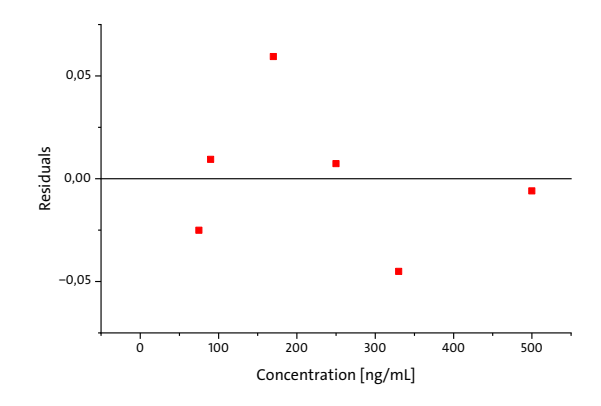
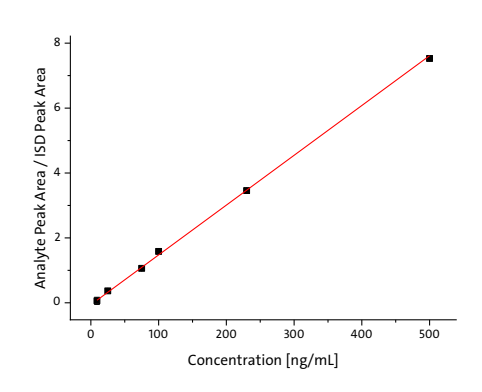


Figure 7-22: Calibration curve (left) and corresponding residual plot (right) for FdU **10** in HT29 supernatant.

Table 7-37: Back-calculation of calibration levels for Tri*PPP*ro-compound 1 in HT29 supernatant.

Concentration x [ng/mL]	Mean Analyte Peak Area y [counts]	Calculated x [ng/mL]	Accuracy [%]	Deviation [%]	Requirement fulfilled?
9.00	6.06E-02	7.63	85	15	True
25.0	3.70E-01	27.8	111	11	True
75.0	1.07E+00	73.6	98	2	True
100	1.60E+00	108	108	8	True
230	3.46E+00	229	100	0	True
500	7.52E+00	493	99	1	True



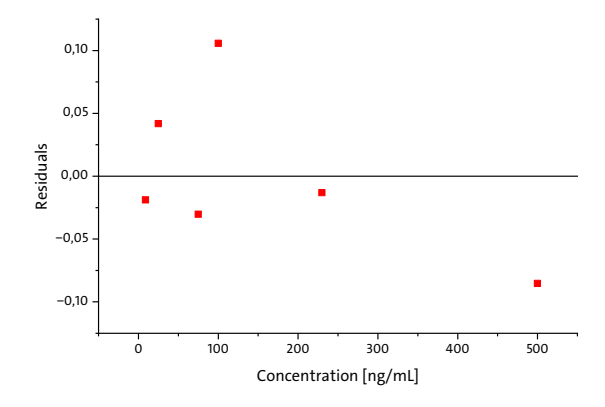
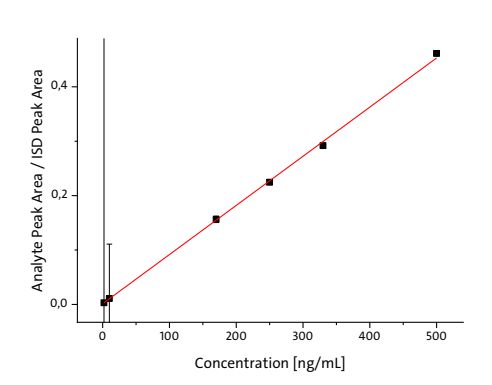


Figure 7-23: Calibration curve (left) and corresponding residual plot (right) for Tri*PPP*ro-compound 1 in HT29 supernatant.

 Table 7-38: Back-calculation of calibration levels for TriPPPro-compound 2 in HT29 supernatant.

Concentration x	Mean Analyte Peak	Calculated x	Accuracy [%]	Deviation [%]	Requirement fulfilled?
[ng/mL]	Area y [counts]	[ng/mL]			
2.00	3.06E-03	1.92	96	4	True
10.0	1.08E-02	10.5	105	5	True
170	1.56E-01	171	101	1	True
250	2.25E-01	247	99	1	True
330	2.92E-01	321	97	3	True
500	4.62E-01	510	102	2	True



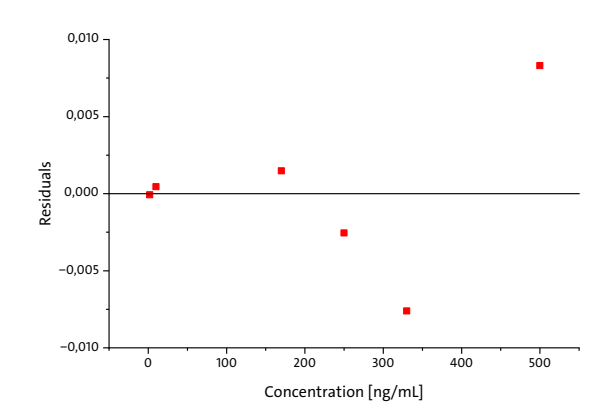
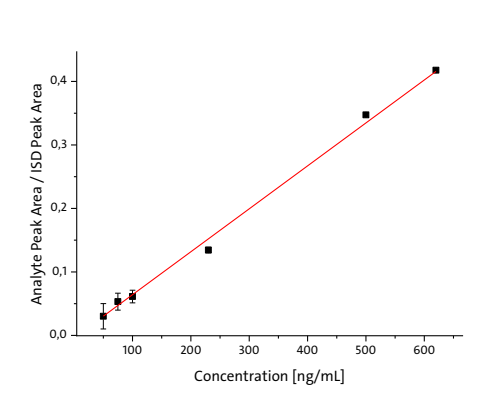


Figure 7-24: Calibration curve (left) and corresponding residual plot (right) for Tri*PPP*ro-compound **2** in HT29 supernatant.

Table 7-39: Back-calculation of calibration levels for intermediate 5 in HT29 supernatant.

Concentration x [ng/mL]	Mean Analyte Peak Area y [counts]	Calculated x [ng/mL]	Accuracy [%]	Deviation [%]	Requirement fulfilled?
50.0	3.03E-02	50.0	100	0	True
75.0	5.35E-02	84.1	112	12	True
100	6.11E-02	95.2	95	5	True
230	1.34E-01	202	88	12	True
500	3.53E-01	522	104	4	True
620	4.21E-01	621	100	0	True



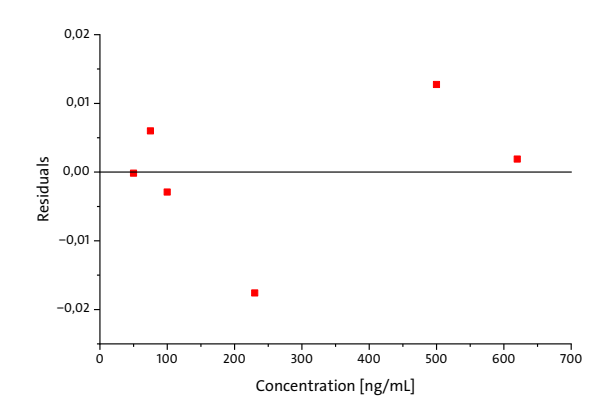
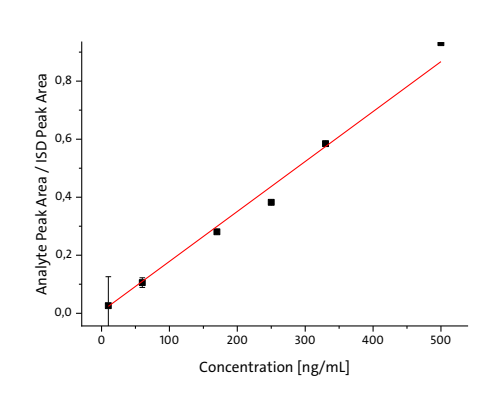


Figure 7-25: Calibration curve (left) and corresponding residual plot (right) for intermediate **5** in HT29 supernatant.

Table 7-40: Back-calculation of calibration levels for intermediate **6** in HT29 supernatant.

Concentration x [ng/mL]	Mean Analyte Peak Area y [counts]	Calculated x [ng/mL]	Accuracy [%]	Deviation [%]	Requirement fulfilled?
10.0	2.62E-02	11.3	113	13	True
60.0	1.06E-01	57.2	95	5	True
170	2.88E-01	162.5	96	4	True
250	3.82E-01	217	87	13	True
330	5.85E-01	334	101	1	True
500	9.32E-01	535	107	7	True



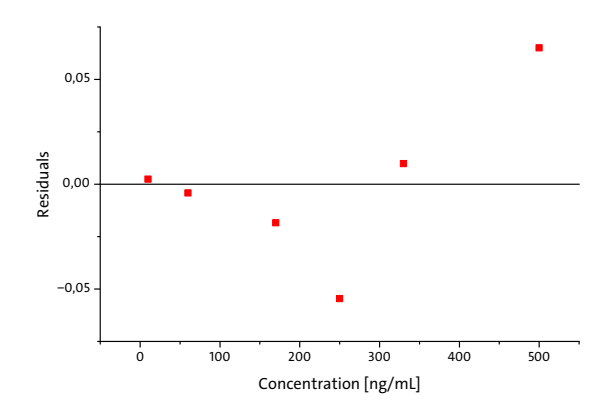
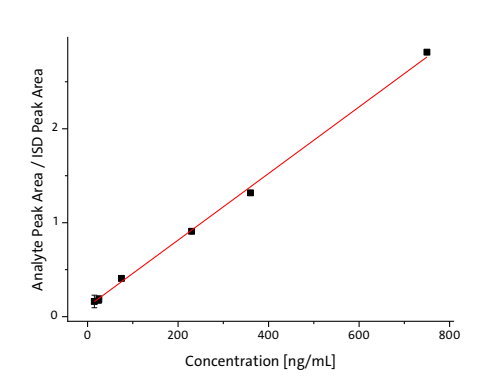


Figure 7-26: Calibration curve (left) and corresponding residual plot (right) for intermediate **6** in HT29 supernatant.

Table 7-41: Back-calculation of calibration levels for FdU-MP **9** in HT29 supernatant.

Concentration x [ng/mL]	Mean Analyte Peak Area y [counts]	Calculated x [ng/mL]	Accuracy [%]	Deviation [%]	Requirement fulfilled?
15.0	1.61E-01	17.8	118	18	True
25.0	1.83E-01	25.6	102	2	True
75.0	4.07E-01	81.4	108	8	True
230	9.09E-01	230	100	0	True
360	1.32E+00	343	95	5	True
750	2.81E+00	758	101	1	True



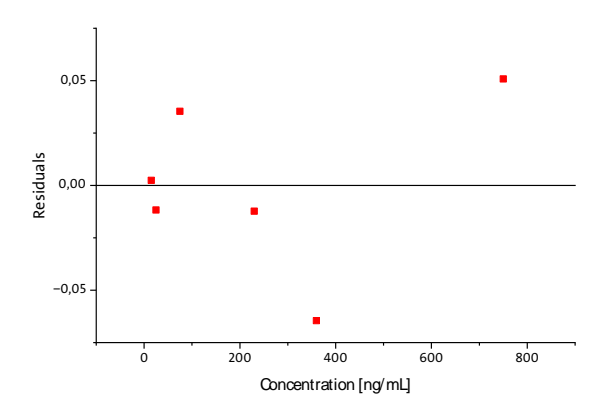
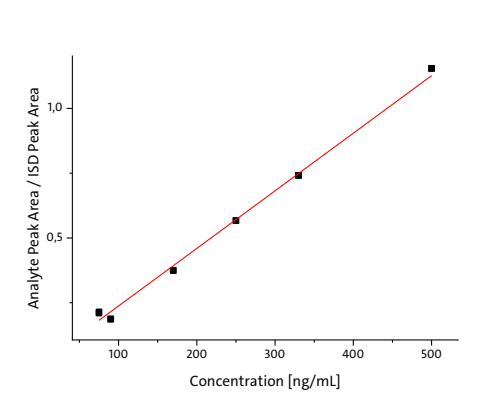


Figure 7-27: Calibration curve (left) and corresponding residual plot (right) for 5-FdU-MP **9** in HT29 supernatant.

Table 7-42: Back-calculation of calibration levels for FdU-DP **8** in HT29 supernatant.

Concentration x [ng/mL]	Mean Analyte Peak Area y [counts]	Calculated x [ng/mL]	Accuracy [%]	Deviation [%]	Requirement fulfilled?
75.0	2.12E-01	87.1	116	16	True
90.0	1.87E-01	79.3	88	12	True
170	3.75E-01	161	95	5	True
250	5.67E-01	249	99	1	True
330	7.41E-01	327	99	1	True
500	1.15E+00	512	102	2	True



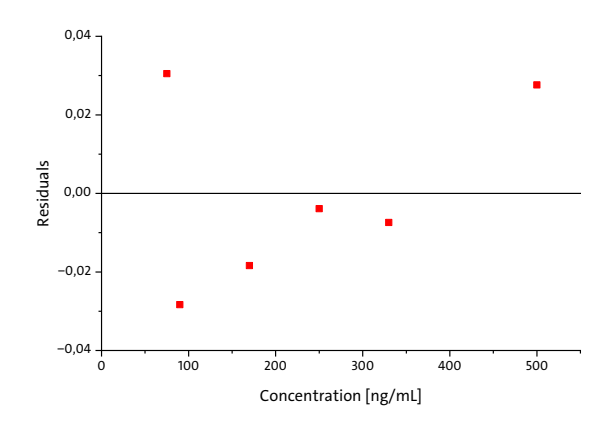
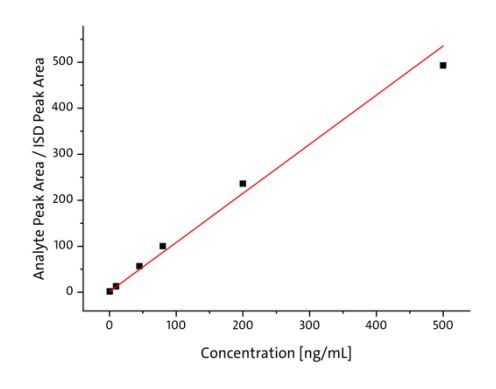


Figure 7-28: Calibration curve (left) and corresponding residual plot (right) for 5-FdU-DP **8** in HT29 supernatant.

7.2.4.2 SW620 cell lysate and supernatant

Table 7-43: Back-calculation of calibration levels for FdU 10 in SW620 cell lysate.

Concentration x [ng/mL]	Mean Analyte Peak Area y [counts]	Calculated x [ng/mL]	Accuracy [%]	Deviation [%]	Requirement fulfilled?
0.50	1.79E+00	0.30	61	39	False
10.0	1.30E+01	10.8	107	7	True
45.0	5.67E+01	51.6	115	15	True
80.0	1.00E+02	92.2	115	15	True
200	2.36E+02	219	109	9	True
500	4.96E+02	462	92	8	True



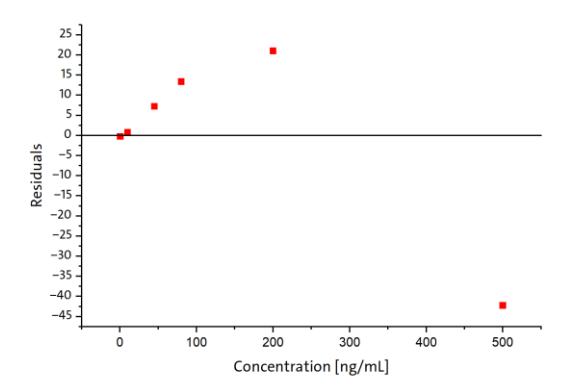
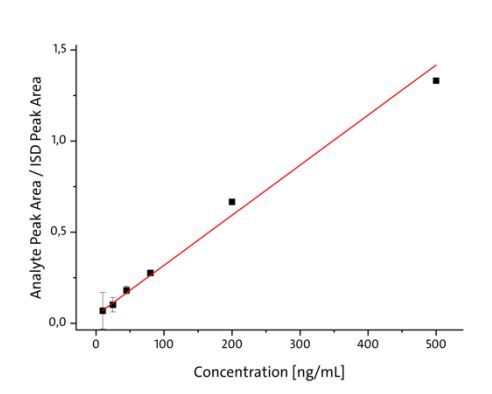


Figure 7-29: Calibration curve (left) and corresponding residual plot (right) for FdU **10** in SW620 cell lysate.

Table 7-44: Back-calculation of calibration levels for Tri*PPP*ro-compound **1** in SW620 cell lysate.

Concentration x [ng/mL]	Mean Analyte Peak Area y [counts]	Calculated x [ng/mL]	Accuracy [%]	Deviation [%]	Requirement fulfilled?
10.0	6.91E-02	9.03	90	10	True
25.0	1.03E-01	21.3	85	15	True
45.0	1.81E-01	50.0	111	11	True
80.0	2.77E-01	85.0	106	6	True
200	6.65E-01	226	113	13	True
500	1.33E+00	468	94	6	True



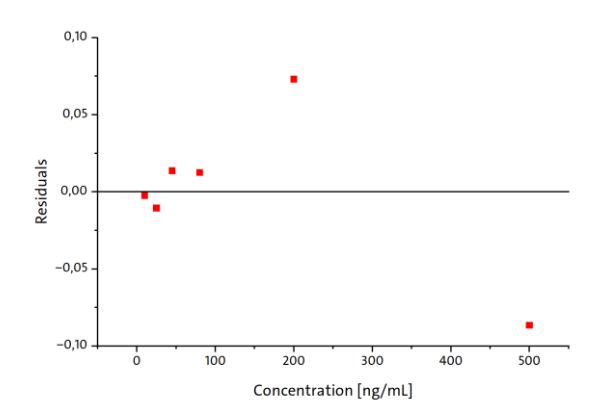
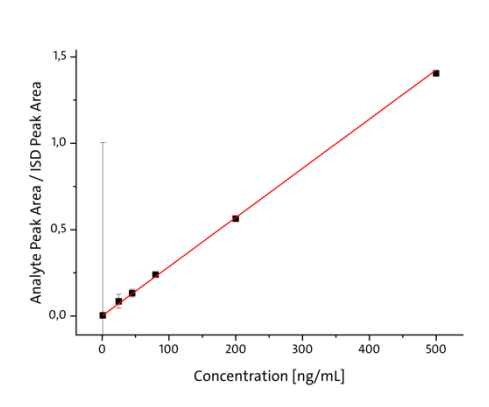


Figure 7-30: Calibration curve (left) and corresponding residual plot (right) for Tri*PPP*ro-compound 1 in SW620 cell lysate.

Table 7-45: Back-calculation of calibration levels for Tri*PPP*ro-compound **2** in SW620 cell lysate.

Concentration x [ng/mL]	Mean Analyte Peak Area y [counts]	Calculated x [ng/mL]	Accuracy [%]	Deviation [%]	Requirement fulfilled?
1.00	3.61E-03	1.13	113	13	True
25.0	6.46E-02	22.9	92	8	True
45.0	1.12E-01	39.7	88	12	True
80.0	2.40E-01	85.6	107	7	True
200	5.63E-01	201	100	0	True
500	1.40E+00	501	100	0	True



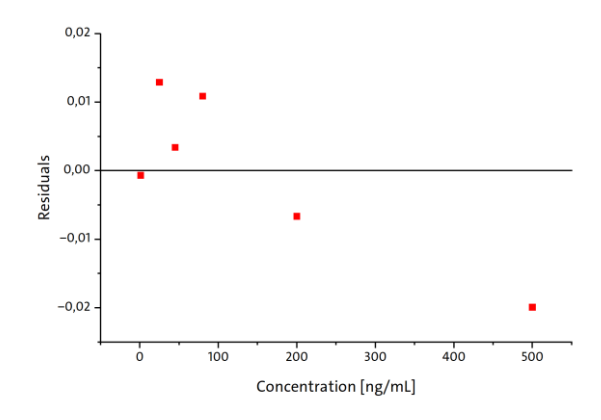
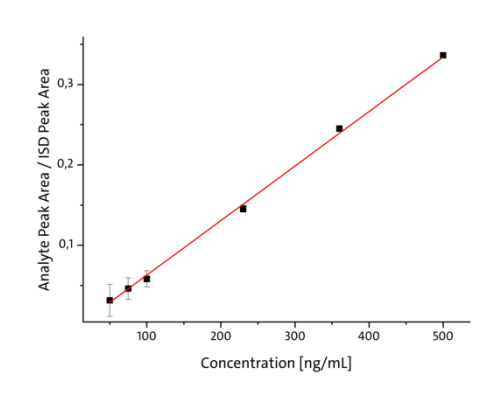


Figure 7-31: Calibration curve (left) and corresponding residual plot (right) for Tri*PPP*ro-compound **2** in SW620 cell lysate.

Table 7-46: Back-calculation of calibration levels for intermediate **5** in SW620 cell lysate.

Concentration x [ng/mL]	Mean Analyte Peak Area y [counts]	Calculated x [ng/mL]	Accuracy [%]	Deviation [%]	Requirement fulfilled?
50.0	3.15E-02	53.5	107	7	True
75.0	4.63E-02	75.4	100	0	True
100	5.82E-02	93.0	93	7	True
230	1.45E-01	222	97	3	True
360	2.45E-01	369	103	3	True
500	3.35E-01	502	100	0	True



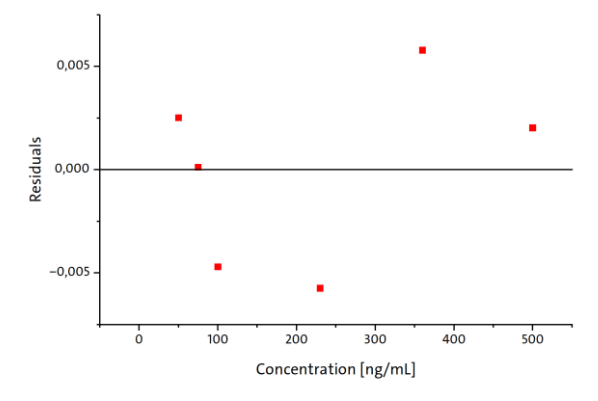
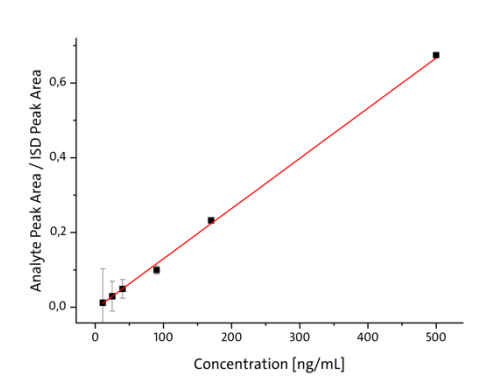


Figure 7-32: Calibration curve (left) and corresponding residual plot (right) for intermediate **5** in SW620 cell lysate.

Table 7-47: Back-calculation of calibration levels for intermediate **6** in SW620 cell lysate.

Concentration x [ng/mL]	Mean Analyte Peak Area y [counts]	Calculated x [ng/mL]	Accuracy [%]	Deviation [%]	Requirement fulfilled?
11.0	1.18E-02	12.0	109	9	True
25.0	2.92E-02	24.9	100	0	True
40.0	4.94E-02	39.9	100	0	True
90.0	9.91E-02	76.7	85	15	True
170	2.35E-01	177	104	4	True
500	6.76E-01	504	101	1	True



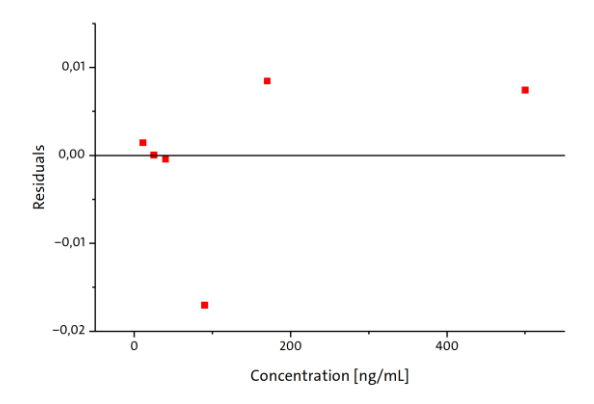
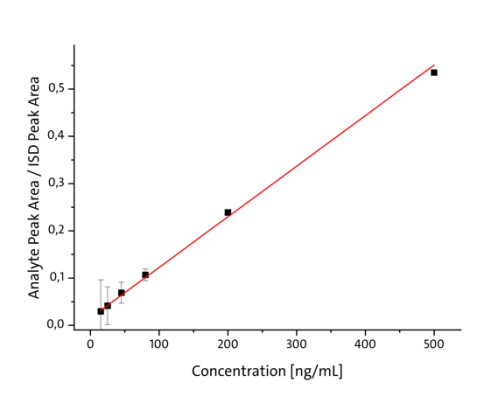


Figure 7-33: Calibration curve (left) and corresponding residual plot (right) for intermediate **6** in SW620 cell lysate.

Table 7-48: Back-calculation of calibration levels for 5-FdU-MP **9** in SW620 cell lysate.

Concentration x [ng/mL]	Mean Analyte Peak Area y [counts]	Calculated x [ng/mL]	Accuracy [%]	Deviation [%]	Requirement fulfilled?
15.0	2.92E-02	12.8	85	15	True
25.0	4.13E-02	24.2	97	3	True
45.0	6.90E-02	50.1	111	11	True
80.0	1.06E-01	84.9	106	6	True
200	2.39E-01	209	104	4	True
500	5.35E-01	486	97	3	True



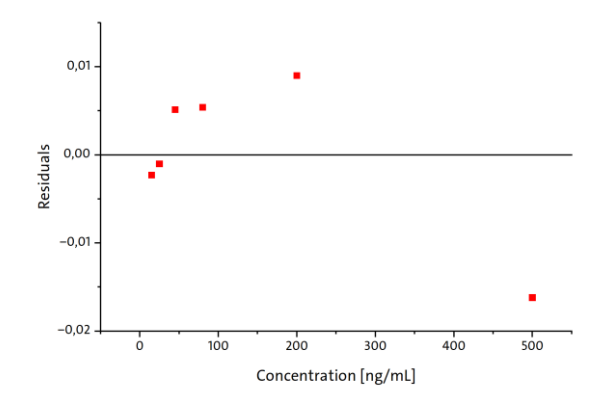
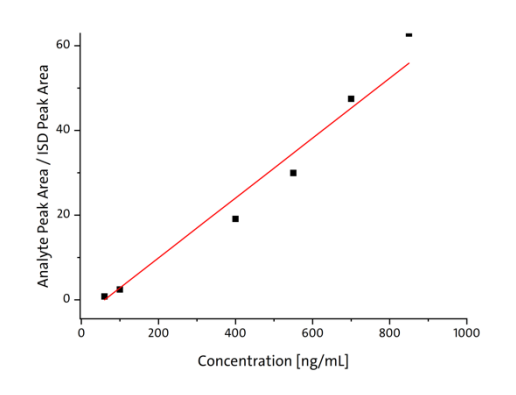


Figure 7-34: Calibration curve (left) and corresponding residual plot (right) for 5-FdU-MP **9** in SW620 cell lysate.

Table 7-49: Back-calculation of calibration levels for 5-FdU-DP **8** in SW620 cell lysate.

Concentration x [ng/mL]	Mean Analyte Peak Area y [counts]	Calculated x [ng/mL]	Accuracy [%]	Deviation [%]	Requirement fulfilled?
60.0	8.13E-01	69.8	116	16	True
100	2.67E+00	96.1	96	4	True
400	2.02E+01	344	86	14	True
550	2.93E+01	473	86	14	True
700	4.72E+01	728	104	4	True
850	6.29E+01	949	112	12	True



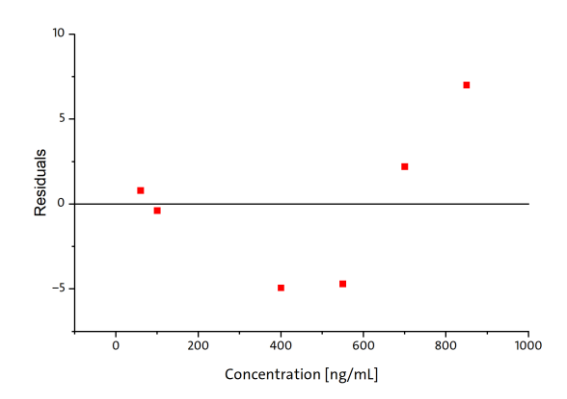
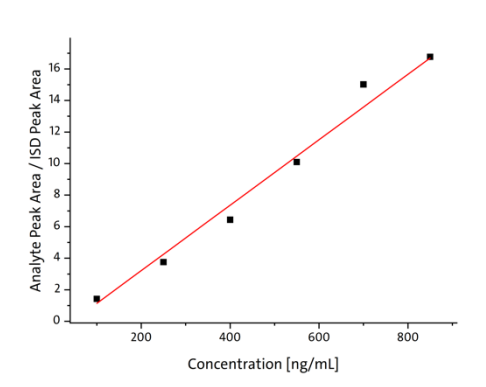


Figure 7-35: Calibration curve (left) and corresponding residual plot for 5-FdU-DP **8** in SW620 cell lysate.

Table 7-50: Back-calculation of calibration levels for 5-FdU-TP **7** in SW620 cell lysate.

Concentration x [ng/mL]	Mean Analyte Peak Area y [counts]	Calculated x [ng/mL]	Accuracy [%]	Deviation [%]	Requirement fulfilled?
100	1.38E+00	116	116	16	True
250 400	3.48E+00 6.39E+00	356	87 89	13	True True
550	1.01E+01	537	98	2	True
700	1.50E+01	770	110	10	True
850	1.67E+01	853	100	0	True



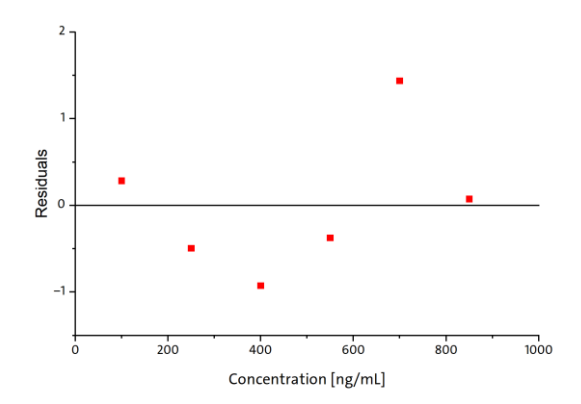
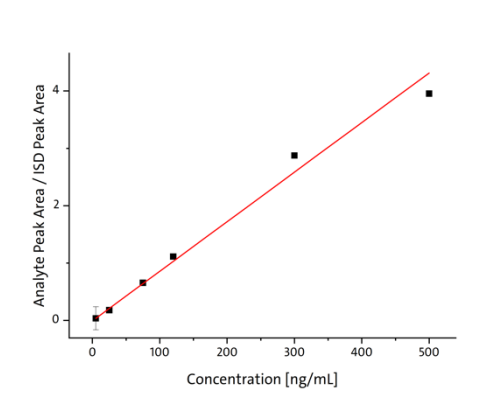


Figure 7-36: Calibration curve (left) and corresponding residual plot (right) for 5-FdU-TP **7** in SW620 cell lysate.

 Table 7-51: Back-calculation of calibration levels for FdU 10 in SW620 supernatant.

Concentration x [ng/mL]	Mean Analyte Peak Area y [counts]	Calculated x [ng/mL]	Accuracy [%]	Deviation [%]	Requirement fulfilled?
5.00	3.60E-02	5.03	101	1	True
25.0	1.84E-01	22.0	88	12	True
75.0	6.57E-01	76.4	102	2	True
120	1.11E+00	128	107	7	True
300	2.87E+00	331	110	10	True
500	4.02E+00	463	93	7	True



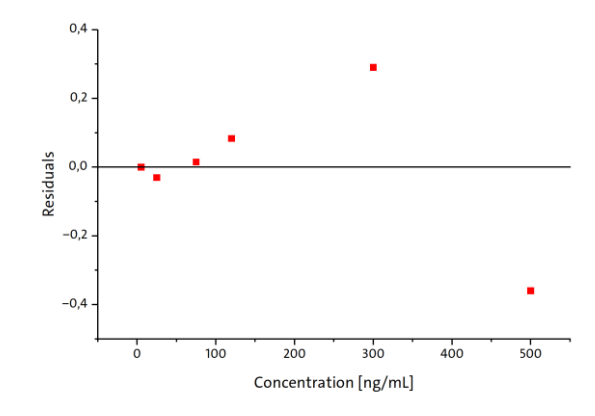
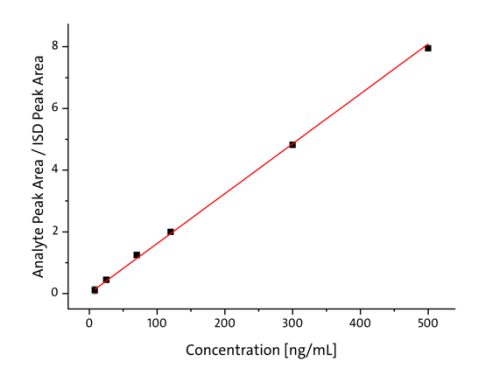


Figure 7-37: Calibration curve (left) and corresponding residual plot (right) for FdU **10** in SW620 supernatant.

Table 7-52: Back-calculation of calibration levels for TriPPPro-compound 1 in SW620 supernatant.

Concentration x [ng/mL]	Mean Analyte Peak Area y [counts]	Calculated x [ng/mL]	Accuracy [%]	Deviation [%]	Requirement fulfilled?
8.00	1.12E-01	6.58	82	18	True
25.0	4.42E-01	27.0	108	8	True
70.0	1.25E+00	76.9	110	10	True
120	1.99E+00	123	102	2	True
300	4.85E+00	299	100	0	True
500	7.96E+00	491	98	2	True



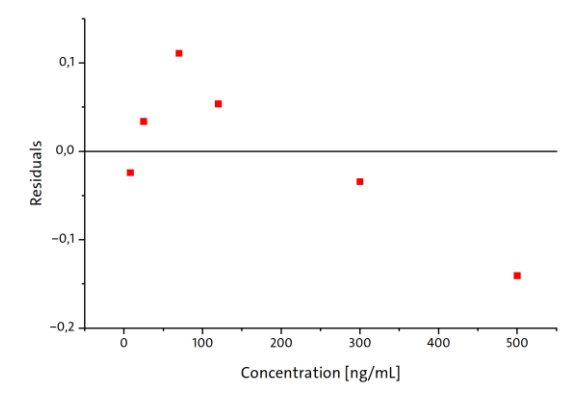
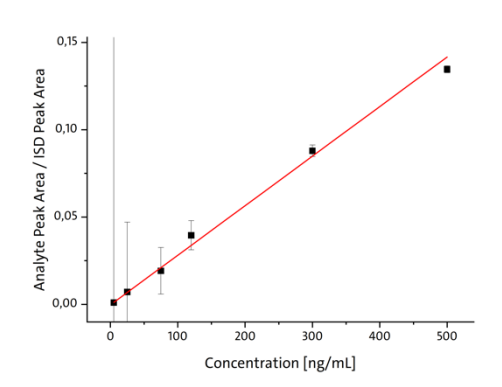


Figure 7-38: Calibration curve (left) and corresponding residual plot (right) for Tri*PPP*ro-compound 1 in SW620 supernatant.

 Table 7-53: Back-calculation of calibration levels for TriPPPro-compound 2 in SW620 supernatant.

Concentration x [ng/mL]	Mean Analyte Peak Area y [counts]	Calculated x [ng/mL]	Accuracy [%]	Deviation [%]	Requirement fulfilled?
5.00	9.71E-04	4.62	92	8	True
25.0	6.80E-03	25.1	100	0	True
75.0	1.92E-02	68.6	91	9	True
120	3.97E-02	141	117	17	False
300	8.78E-02	310	103	3	True
500	1.35E-01	477	95	5	True



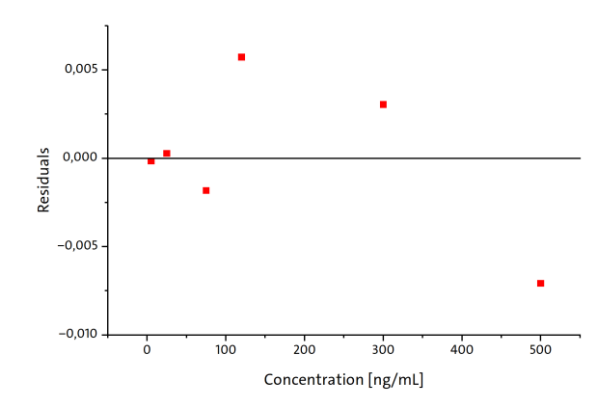
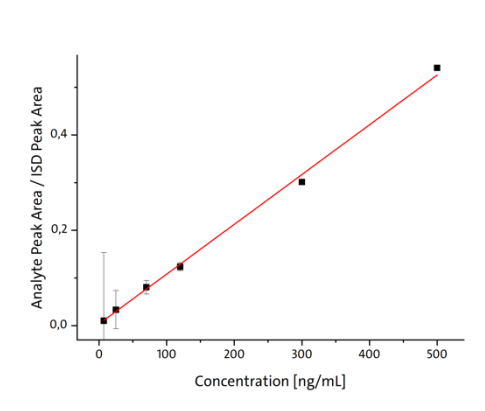


Figure 7-39: Calibration curve (left) and corresponding residual plot (right) for Tri*PPP*ro-compound **2** in SW620 supernatant.

Table 7-54: Back-calculation of calibration levels for intermediate **5** in SW620 supernatant.

Concentration x [ng/mL]	Mean Analyte Peak Area y [counts]	Calculated x [ng/mL]	Accuracy [%]	Deviation [%]	Requirement fulfilled?
7.00	1.12E-02	6.24	89	11	True
25.0	3.34E-02	27.6	110	10	True
70.0	8.25E-02	74.8	107	7	True
120	1.23E-01	114.2	95	5	True
300	3.02E-01	286	95	5	True
500	5.38E-01	512	102	2	True



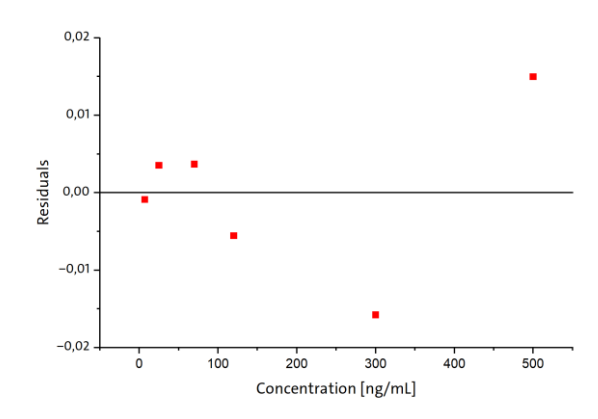
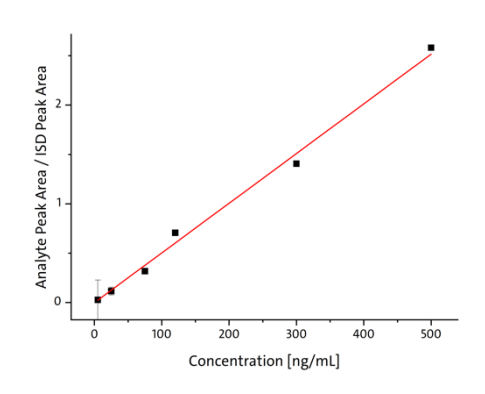


Figure 7-40: Calibration curve (left) and corresponding residual plot (right) for intermediate **5** in SW620 supernatant.

Table 7-55: Back-calculation of calibration levels for intermediate **6** in SW620 supernatant.

Concentration x [ng/mL]	Mean Analyte Peak Area y [counts]	Calculated x [ng/mL]	Accuracy [%]	Deviation [%]	Requirement fulfilled?
5.00	2.73E-02	5.65	113	13	True
25.0	1.16E-01	23.0	92	8	True
75.0	3.20E-01	63.0	84	16	False
120	7.02E-01	138.0	115	15	True
300	1.41E+00	277	92	8	True
500	2.64E+00	518	104	4	True



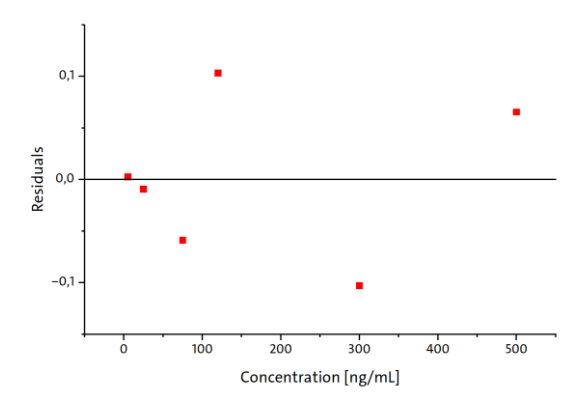
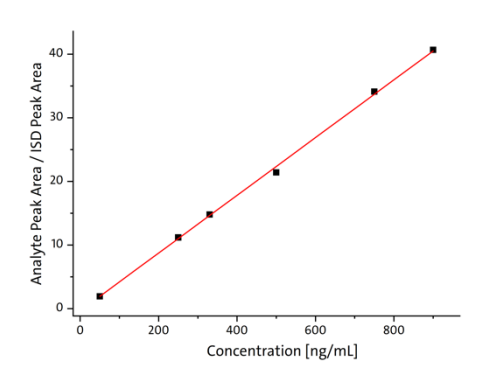


Figure 7-41: Calibration curve (left) and corresponding residual plot (right) for intermediate **6** in SW620 supernatant.

Table 7-56: Back-calculation of calibration levels for 5-FdU-MP **9** in SW620 supernatant.

Concentration x [ng/mL]	Mean Analyte Peak Area y [counts]	Calculated x [ng/mL]	Accuracy [%]	Deviation [%]	Requirement fulfilled?
50.0	1.91E+00	47.1	94	6	True
250	1.13E+01	253	101	1	True
300	1.49E+01	331	110	10	True
500	2.14E+01	473	95	5	True
750	3.41E+01	751	100	0	True
900	4.07E+01	895	99	1	True



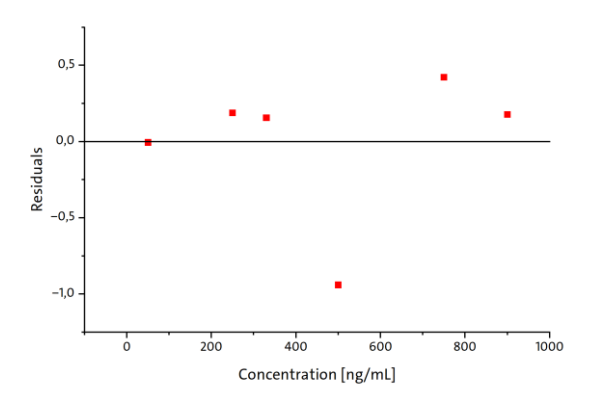
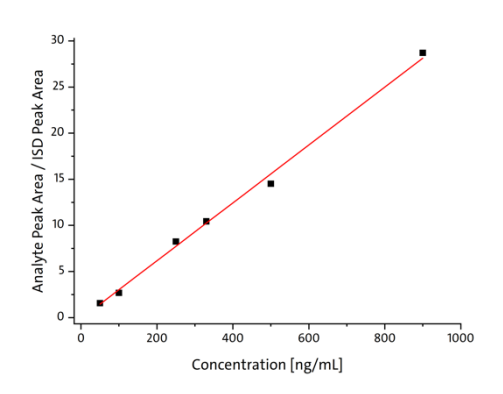


Figure 7-42: Calibration curve (left) and corresponding residual plot (right) for 5-FdU-MP **9** in SW620 supernatant.

Table 7-57: Back-calculation of calibration levels for 5-FdU-DP 8 in SW620 supernatant.

Concentration x [ng/mL]	Mean Analyte Peak Area y [counts]	Calculated x [ng/mL]	Accuracy [%]	Deviation [%]	Requirement fulfilled?
50.0	1.57E+00	53.5	107.0	7	True
100	2.68E+00	89	89	11	True
250	8.33E+00	269	107	7	True
330	1.04E+01	334	101	1	True
500	1.45E+01	466	93	7	True
900	2.87E+01	919	102	2	True



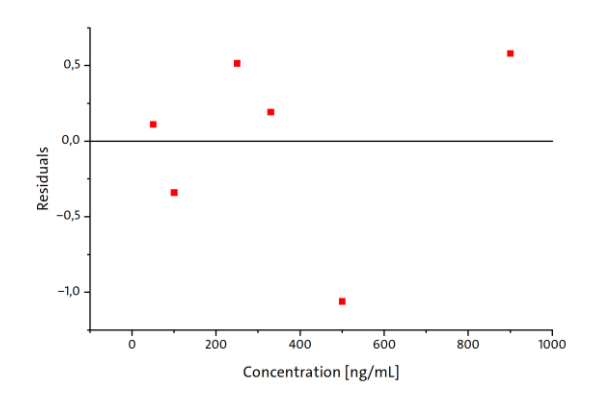
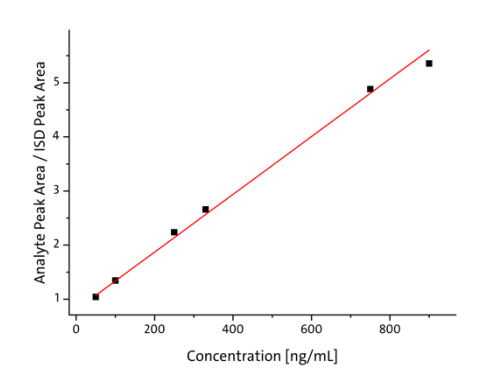


Figure 7-43: Calibration curve (left) and corresponding residual plot (right) for 5-FdU-DP **8** in SW620 supernatant.

Table 7-58: Back-calculation of calibration levels for 5-FdU-TP **7** in SW620 supernatant.

Concentration x [ng/mL]	Mean Analyte Peak Area y [counts]	Calculated x [ng/mL]	Accuracy [%]	Deviation [%]	Requirement fulfilled?
50.0	1.04E+00	44.6	89	11	True
100	1.34E+00	102	102	2	True
250	2.24E+00	269	108	8	True
330	2.65E+00	346	105	5	True
500	4.90E+00	767	102	2	True
900	5.36E+00	853	95	5	True



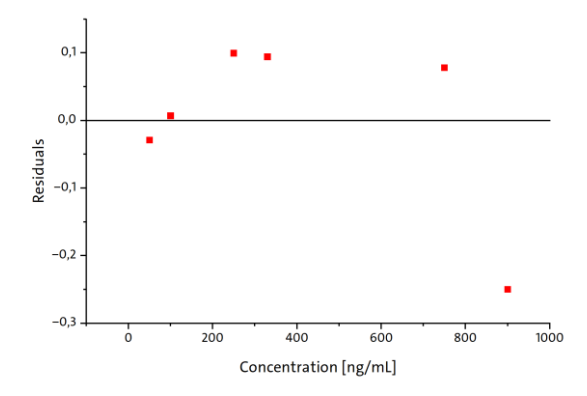


Figure 7-44: Calibration curve (left) and corresponding residual plot (right) for 5-FdU-TP **7** in SW620 supernatant.

7.2.4.3 CEM/0 cell lysate and supernatant

Table 7-59: Back-calculation of calibration levels for d4T **16** in CEM/O cell lysate.

Concentration x [ng/mL]	Mean Analyte Peak Area y [counts]	Calculated x [ng/mL]	Accuracy [%]	Deviation [%]	Requirement fulfilled?
10.0	1.04E-03	9.9	99	1	True
90.0	4.63E-03	93.6	104	4	True
250	1.15E-02	255	102	2	True
330	1.57E-02	350	106	6	True
500	2.05E-02	464	93	7	True
1000	4.42E-02	1014	101	1	True

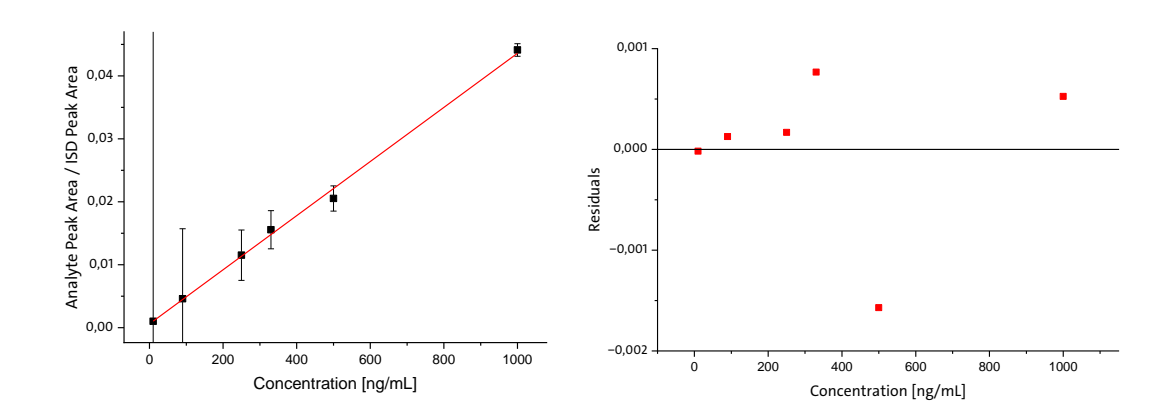
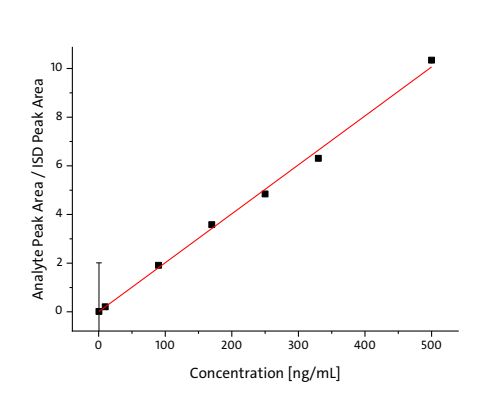


Figure 7-45: Calibration curve (left) and corresponding residual plot (right) for d4T **16** in CEM/0 cell lysate.

Table 7-60: Back-calculation of calibration levels for Tri*PPP*ro-compound **3** in CEM/0 cell lysate.

Concentration x [ng/mL]	Mean Analyte Peak Area y [counts]	Calculated x [ng/mL]	Accuracy [%]	Deviation [%]	Requirement fulfilled?
0.50	1.43E-02	0.48	96	4	True
10.0	2.07E-01	10.1	101	1	True
90.0	1.91E+00	94.8	105	5	True
170	3.29E+00	163	96	4	True
250	4.84E+00	240	96	4	True
330	6.30E+00	313	95	5	True



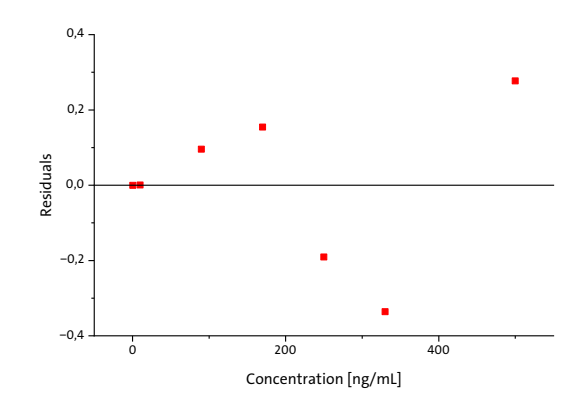
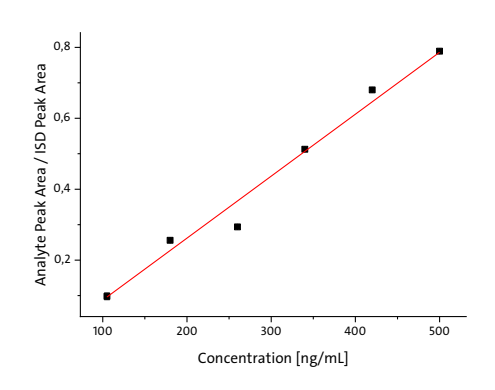


Figure 7-46: Calibration curve (left) and corresponding residual plot (right) for Tri*PPP*ro-compound **3** in CEM/0 cell lysate.

Table 7-61: Back-calculation of calibration levels for TriPPPro-compound 4 in CEM/0 cell lysate.

Concentration x [ng/mL]	Mean Analyte Peak Area y [counts]	Calculated x [ng/mL]	Accuracy [%]	Deviation [%]	Requirement fulfilled?
105	9.79E-02	106	101	1	True
180	2.55E-01	196	109	9	True
260	2.92E-01	217	83	17	True
340	5.10E-01	342	100	0	True
420	6.82E-01	440	105	5	True
500	7.88E-01	500	100	0	True



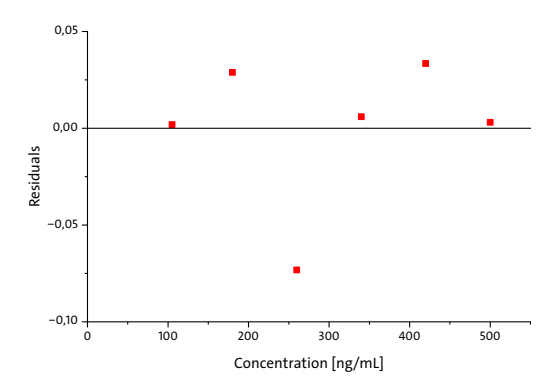
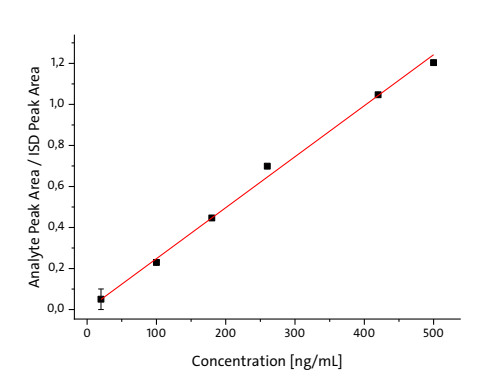


Figure 7-47: Calibration curve (left) and corresponding residual plot (right) for Tri*PPP*ro-compound **4** in CEM/0 cell lysate.

 Table 7-62: Back-calculation of calibration levels for intermediate 11 in CEM/O cell lysate.

Concentration x [ng/mL]	Mean Analyte Peak Area y [counts]	Calculated x [ng/mL]	Accuracy [%]	Deviation [%]	Requirement fulfilled?
20.0	5.03E-02	20.4	102	2	True
100	2.30E-01	92.4	92	8	True
180	4.46E-01	179	100	0	True
260	6.99E-01	281	108	8	True
420	1.05E+00	421	100	0	True
500	1.20E+00	483	97	3	True



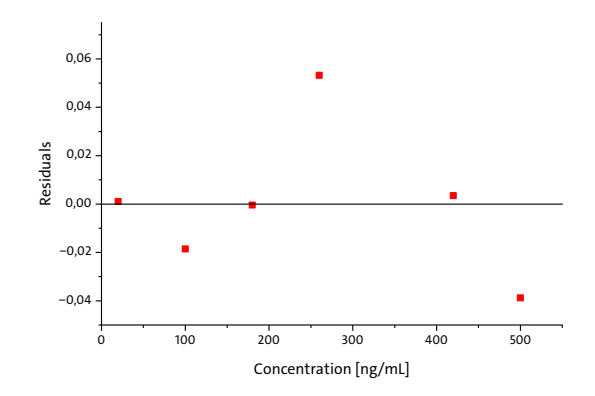
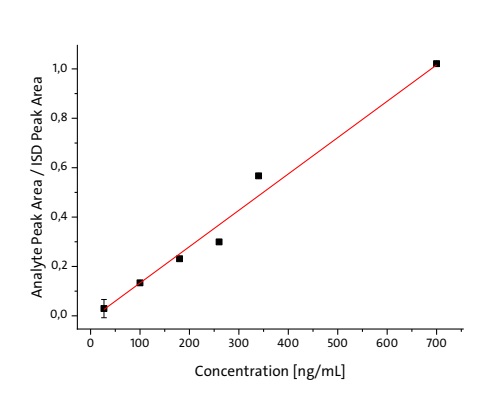


Figure 7-48: Calibration curve (left) and corresponding residual plot (right) for intermediate **11** in CEM/0 cell lysate.

Table 7-63: Back-calculation of calibration levels for intermediate 12 in CEM/O cell lysate.

Concentration x [ng/mL]	Mean Analyte Peak Area y [counts]	Calculated x [ng/mL]	Accuracy [%]	Deviation [%]	Requirement fulfilled?
27.0	3.13E-02	30.9	114	14	True
100	1.35E-01	101	101	1	True
180	2.36E-01	170	94	6	True
260	2.99E-01	213	82	18	False
340	5.67E-01	392	115	15	True
700	1.03E+00	713	102	2	True



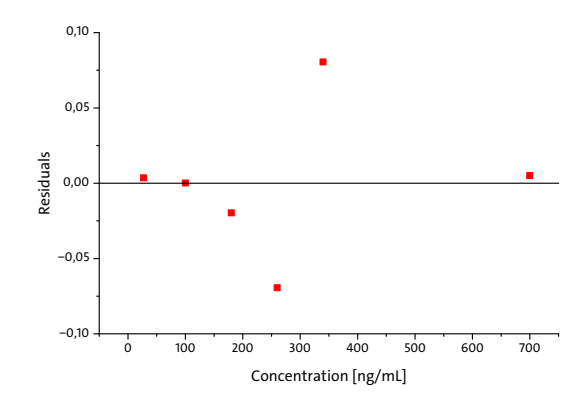
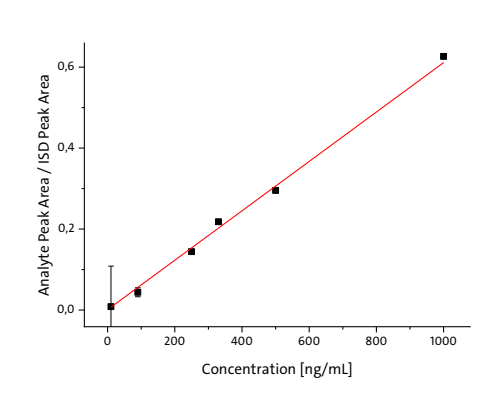


Figure 7-49: Calibration curve (left) and corresponding residual plot (right) for intermediate **12** in CEM/0 cell lysate.

Table 7-64: Back-calculation of calibration levels for d4T-MP 15 in CEM/O cell lysate.

Concentration x [ng/mL]	Mean Analyte Peak Area y [counts]	Calculated x [ng/mL]	Accuracy [%]	Deviation [%]	Requirement fulfilled?
10.0	8.62E-03	12.5	125	25	False
90.0	4.41E-02	70.5	78	22	False
250	1.50E-01	244	97	3	True
330	2.20E-01	358	109	9	True
500	2.95E-01	482	96	4	True
1000	6.27E-01	1025	103	3	True



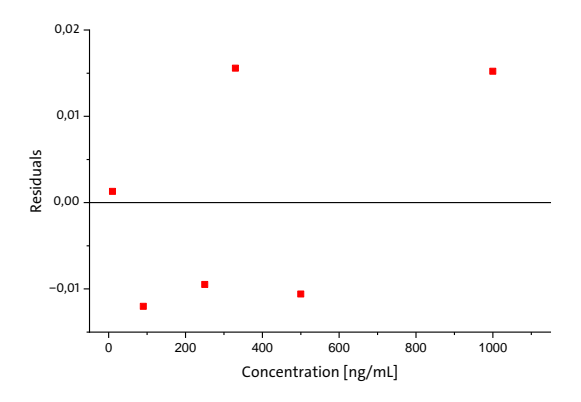
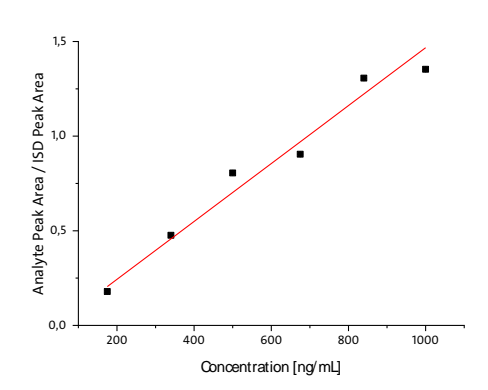


Figure 7-50: Calibration curve (left) and corresponding residual plot (right) for d4T-MP **15** in CEM/0 cell lysate.

Table 7-65: Back-calculation of calibration levels for d4T-DP **14** in CEM/0 cell lysate.

Concentration x [ng/mL]	Mean Analyte Peak Area y [counts]	Calculated x [ng/mL]	Accuracy [%]	Deviation [%]	Requirement fulfilled?
175	1.75E-01	155	89	11	True
340	4.41E-01	329	97	3	True
500	7.41E-01	525	105	5	True
675	9.49E-01	661	98	2	True
840	1.24E+00	852	101	1	True
1000	1.45E+00	990	99	1	True



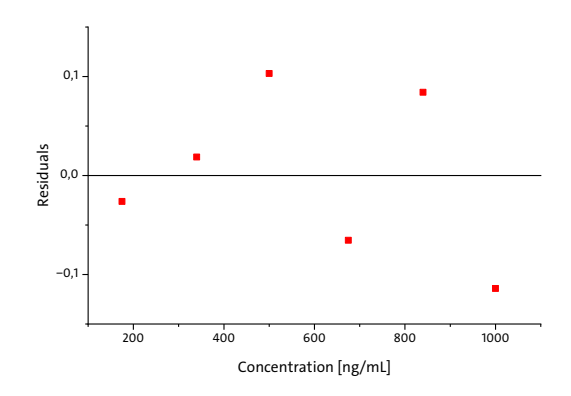
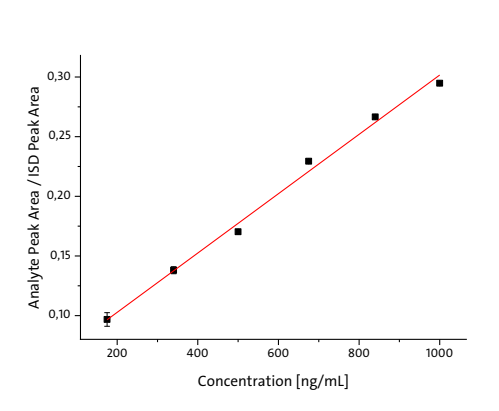


Figure 7-51: Calibration curve (left) and corresponding residual plot for d4T-DP **14** in CEM/0 cell lysate.

Table 7-66: Back-calculation of calibration levels for d4T-TP **13** in CEM/O cell lysate.

Concentration x [ng/mL]	Mean Analyte Peak Area y [counts]	Calculated x [ng/mL]	Accuracy [%]	Deviation [%]	Requirement fulfilled?
175	9.68E-02	176	101	1	True
340	1.38E-01	342	101	1	True
500	1.71E-01	473	95	5	True
675	2.30E-01	713	106	6	True
840	2.66E-01	857	102	2	True
1000	2.96E-01	975	98	2	True



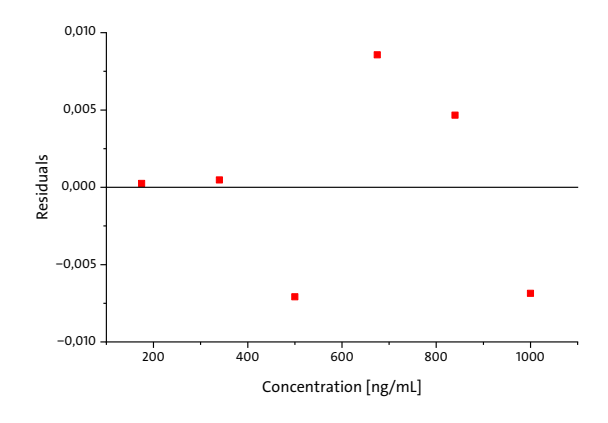
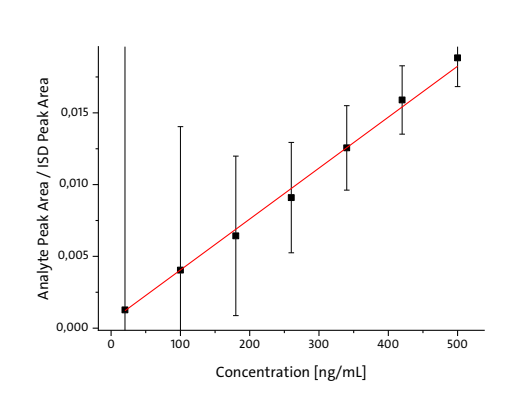


Figure 7-52: Calibration curve (left) and corresponding residual plot for d4T-TP 13 in CEM/O cell lysate.

Table 7-67: Back-calculation of calibration levels for d4T **16** in CEM/0 cell lysate.

Concentration x [ng/mL]	Mean Analyte Peak Area y [counts]	Calculated x [ng/mL]	Accuracy [%]	Deviation [%]	Requirement fulfilled?
20.0	1.27E-03	21.6	108	8	True
100	4.05E-03	100	100	0	True
180	6.43E-03	167	93	7	True
260	9.13E-03	243	93	7	True
340	1.26E-02	341	100	0	True
420	1.59E-02	434	103	3	True



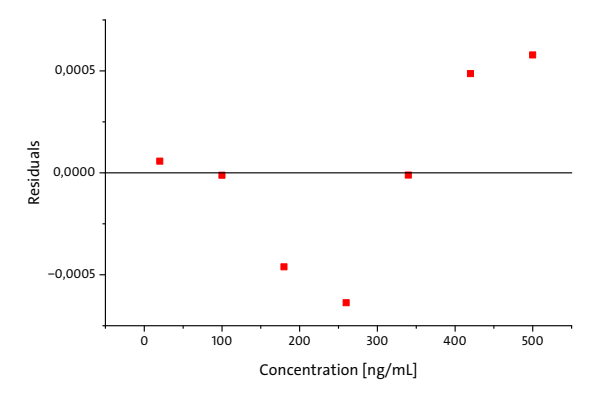
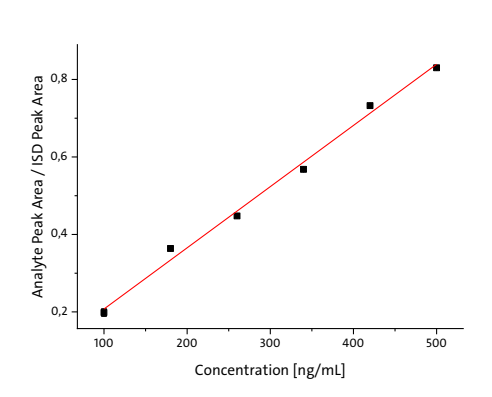


Figure 7-53: Calibration curve (left) and corresponding residual plot for d4T **16** in CEM/0 supernatant.

Table 7-68: Back-calculation of calibration levels for Tri*PPP*ro-compound **3** in CEM/0 cell lysate.

Concentration x [ng/mL]	Mean Analyte Peak Area y [counts]	Calculated x [ng/mL]	Accuracy [%]	Deviation [%]	Requirement fulfilled?
100	1.98E-01	94.1	94	6	True
180	3.63E-01	199	110	10	True
260	4.46E-01	251	97	3	True
340	5.68E-01	328	97	3	True
420	7.33E-01	432	103	3	True
500	8.30E-01	494	99	1	True



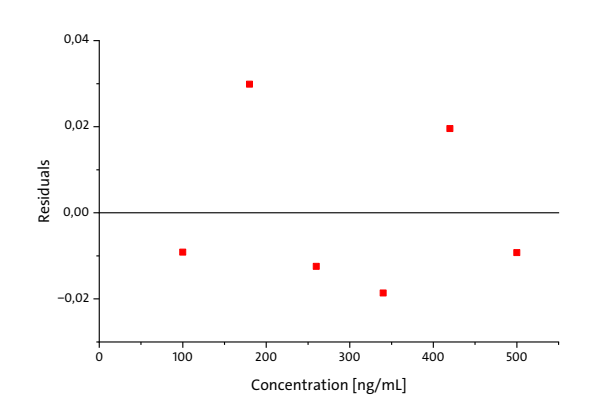
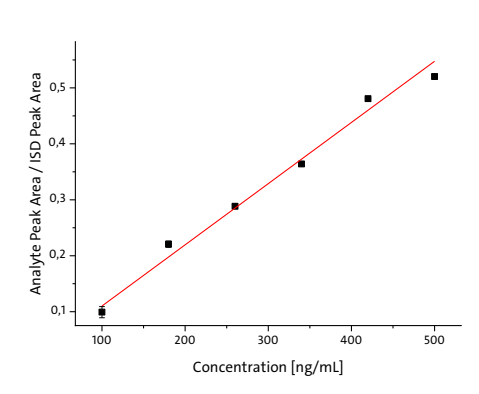


Figure 7-54: Calibration curve (left) and corresponding residual plot for Tri*PPP*ro-compound **3** in CEM/0 supernatant.

Table 7-69: Back-calculation of calibration levels for Tri*PPP*ro-compound **4** in CEM/0 cell lysate.

Concentration x [ng/mL]	Mean Analyte Peak Area y [counts]	Calculated x [ng/mL]	Accuracy [%]	Deviation [%]	Requirement fulfilled?
100	9.92E-02	90.3	90	10	True
180	2.21E-01	202	112	12	True
260	2.93E-01	268	103	3	True
340	3.64E-01	333	98	2	True
420	4.81E-01	440	105	5	True
500	5.20E-01	476	95	5	True



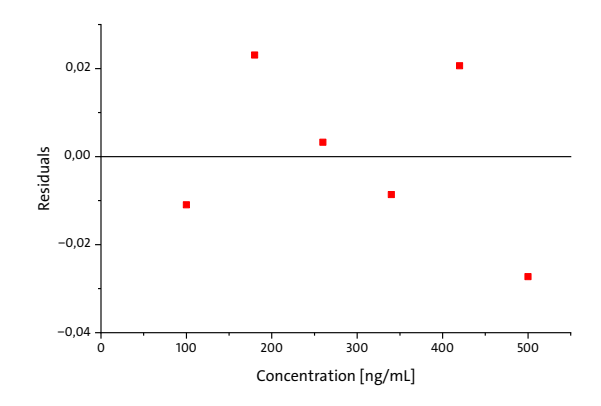
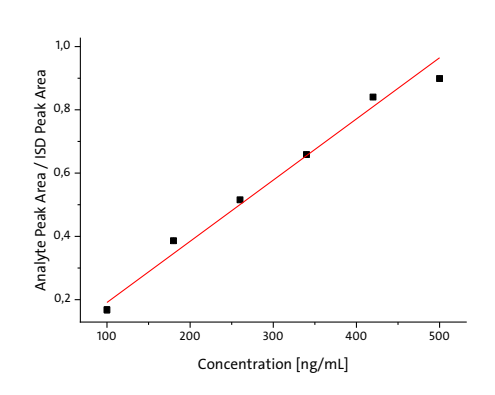


Figure 7-55: Calibration curve (left) and corresponding residual plot for Tri*PPP*ro-compound **4** in CEM/0 supernatant.

 Table 7-70: Back-calculation of calibration levels for intermediate 11 in CEM/0 cell lysate.

Concentration x [ng/mL]	Mean Analyte Peak Area y [counts]	Calculated x [ng/mL]	Accuracy [%]	Deviation [%]	Requirement fulfilled?
100	1.70E-01	89.5	89	11	True
180	3.88E-01	202	112	12	True
260	5.16E-01	269	103	3	True
340	6.58E-01	342	101	1	True
420	8.49E-01	441	105	5	True
500	8.98E-01	466	93	7	True



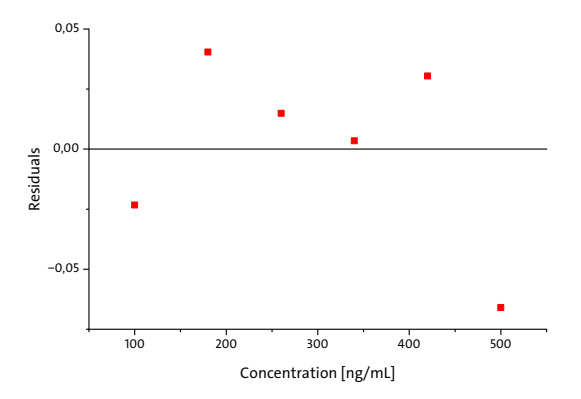
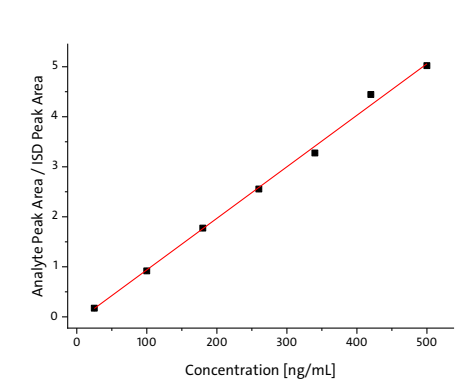


Figure 7-56: Calibration curve (left) and corresponding residual plot for intermediate **11** in CEM/0 supernatant.

Table 7-71: Back-calculation of calibration levels for intermediate 12 in CEM/O cell lysate.

Concentration x [ng/mL]	Mean Analyte Peak Area y [counts]	Calculated x [ng/mL]	Accuracy [%]	Deviation [%]	Requirement fulfilled?
25.0	1.73E-01	25.6	103	3	True
100	9.26E-01	98.7	99	1	True
180	1.77E+00	181	100	0	True
260	2.56E+00	258	99	1	True
340	3.29E+00	329	97	3	True
420	4.50E+00	445	106	6	True



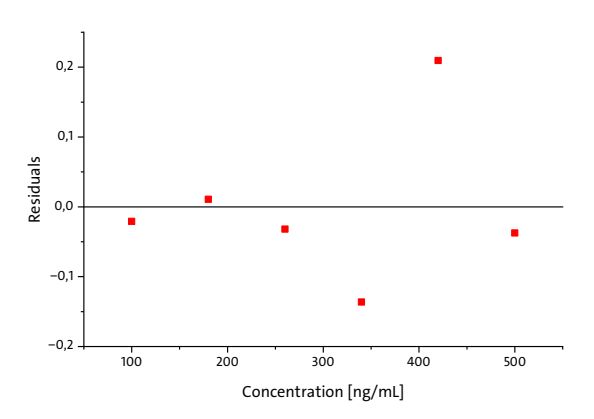
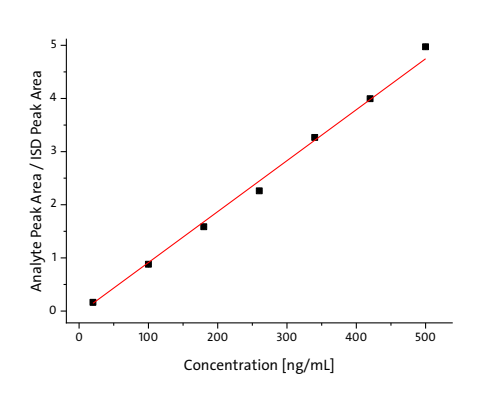


Figure 7-57: Calibration curve (left) and corresponding residual plot for intermediate **12** in CEM/0 supernatant.

Table 7-72: Back-calculation of calibration levels for d4T-MP **15** in CEM/O cell lysate.

Concentration x [ng/mL]	Mean Analyte Peak Area y [counts]	Calculated x [ng/mL]	Accuracy [%]	Deviation [%]	Requirement fulfilled?
20.0	1.64E-01	21.9	110	10	True
100	8.76E-01	96.2	96	4	True
180	1.61E+00	173	96	4	True
260	2.26E+00	241	93	7	True
340	3.27E+00	345	102	2	True
420	4.00E+00	422	100	0	True
500	4.97E+00	523	105	5	True



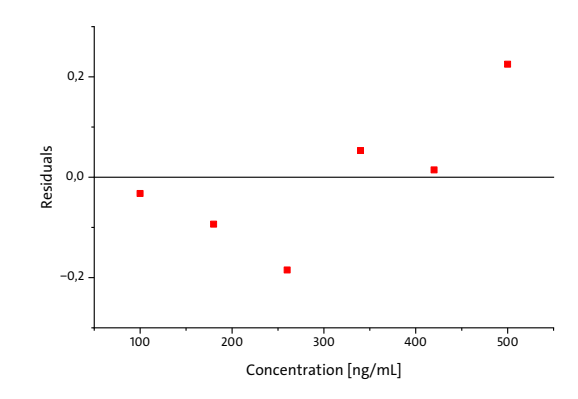
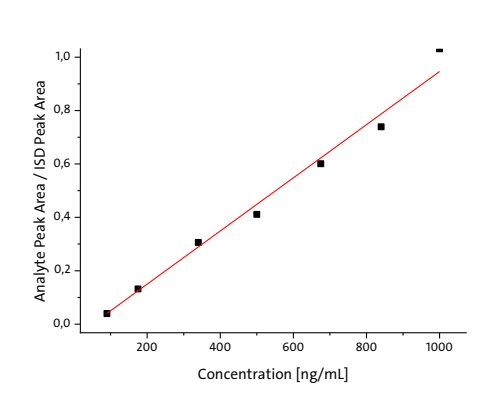


Figure 7-58: Calibration curve (left) and corresponding residual plot for d4T-MP **15** in CEM/0 supernatant.

Table 7-73: Back-calculation of calibration levels for d4T-DP **14** in CEM/0 cell lysate.

Concentration x [ng/mL]	Mean Analyte Peak Area y [counts]	Calculated x [ng/mL]	Accuracy [%]	Deviation [%]	Requirement fulfilled?
90.0	4.61E-02	96.0	107	7	True
175	1.11E-01	161	92	8	True
340	2.91E-01	342	101	1	True
500	4.10E-01	461	92	8	True
675	6.16E-01	669	99	1	True
840	7.92E-01	845	101	1	True
1000	1.03E+00	1082	108	8	True



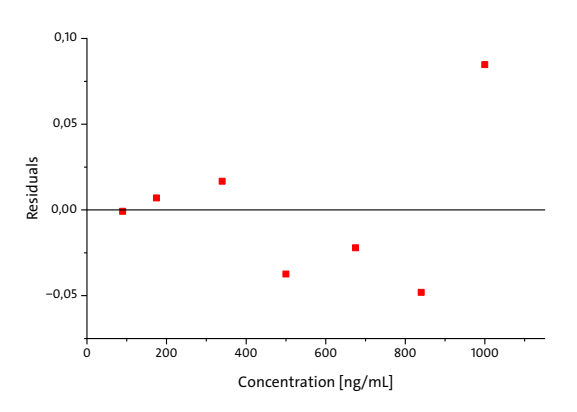
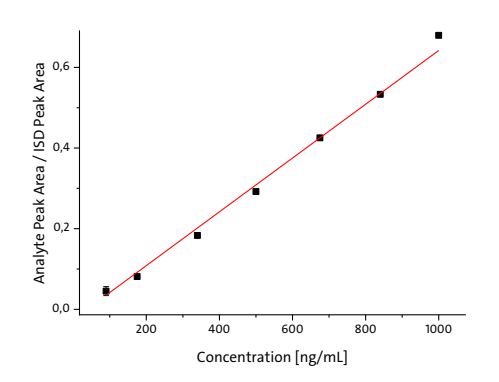


Figure 7-59: Calibration curve (left) and corresponding residual plot for d4T-DP **14** in CEM/0 supernatant.

 Table 7-74: Back-calculation of calibration levels for d4T-TP 13 in CEM/0 cell lysate.

Concentration x [ng/mL]	Mean Analyte Peak Area y [counts]	Calculated x [ng/mL]	Accuracy [%]	Deviation [%]	Requirement fulfilled?
90.0	4.46E-02	104	116	16	False
175	8.15E-02	160	91	9	True
340	1.88E-01	319	94	6	True
500	2.94E-01	478	96	4	True
675	4.26E-01	677	100	0	True
840	5.33E-01	837	100	0	True
1000	6.78E-01	1054	105	5	True



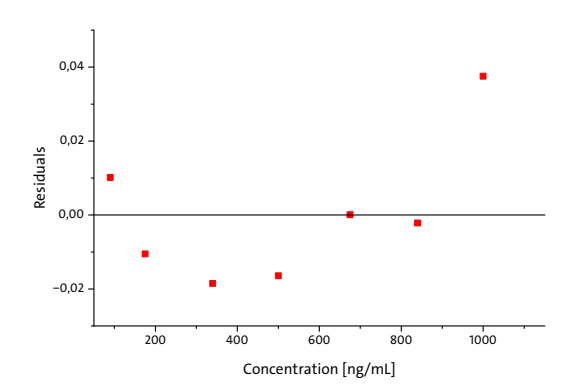


Figure 7-60: Calibration curve (left) and corresponding residual plot for d4T-TP **13** in CEM/0 supernatant.

8 Acknowledgement

ICH DANKE...

Herrn Prof. Dr. Chris Meier dafür, dass ich dieses interessante und herausfordernde Thema unter seiner Betreuung durchführen konnte; für den wissenschaftlichen Freiraum, der mir bei der Bearbeitung gewährt wurde; sowie die fachlichen Anregungen, die dazu beigetragen haben, diese Arbeit anzufertigen.

Herrn Prof. Dr. Ralph Holl für die freundliche Übernahme des Zweitgutachtens.

Den Mitarbeiter:innen, besonders Frau Maike Märker aus der ehemaligen Arbeitsgruppe von Prof. Dr. Udo Schumacher am UKE sowie Frau Tina Meyer aus der Arbeitsgruppe von Prof. Dr. Stephanie Pfänder des LIV für die großartige Arbeit beim Anfertigen zahlreicher Zellaufnahmestudien und Mock-Samples.

Dem technischen Personal der NMR-Abteilung unter der Leitung von Herrn Dr. Thomas Hackl, sowie der MS-Abteilung unter der Leitung von Frau Dr. Jennifer Menzel. Dabei gilt mein ganz besonderer Dank Frau Gaby Graack, die mich seit Beginn meiner Masterarbeit an der QTRAP unterstützt hat, wo sie nur konnte.

Celine, Iven und Nils für das sorgfältige Korrekturlesen und Auseinandersetzen mit dieser Arbeit. Ganz besonders möchte ich an dieser Stelle Dr. Maria Riedner danken, die mich sowohl bei den praktischen Arbeiten als auch beim Schreiben dieser Arbeit unterstützt hat und durch ihre kritische Durchsicht zur Qualität dieses Schriftstücks beigetragen hat.

Meinen Praktikantinnen für ihre Arbeit und Beiträge zu meiner Arbeit.

Dem gesamten AK-Meier, ehemaligen und aktuellen Mitgliedern, für die großartige Arbeitsatmosphäre, jede Kaffeepause, zahlreiche anregende Gespräche, heiß diskutierte Themen, alle schönen Boßeltouren; kurzum: für alle tollen Erinnerungen, die ihr geschaffen habt! Besonders erwähnen möchte ich meinen Stockwerk- und Boßelpartner Iven. Außerdem bedanke ich mich sehr bei Dr. Julian Witt, der mir vieles über Phosphatchemie beigebracht hat.

Dr. Brita Werner für eine schöne Zeit im OCP und alle aufbauenden Gespräche.

Stephi für die wunderbare Freundschaft und die vielen schönen Momente während unseres Studiums. Ebenso möchte ich mich an dieser Stelle bei Chris und Andi bedanken.

Meiner Mama, meinen Brüdern und Muriel, die sehr lange auf mich und diese Arbeit gewartet haben. Ich danke euch für euren Rückhalt, euren Zuspruch und dafür, dass ihr immer an mich geglaubt habt!

Nils. Für dein Zen-Sein.

9 Declaration on Oath

I hereby declare on oath that I have written this dissertation myself and have not

used any sources and aids other than those specified. If electronic resources based

on generative artificial intelligence (gKI) were used in the course of writing this

dissertation, I declare that my own work was the main focus and that all resources

used are fully documented in accordance with good scientific practice. I am

responsible for any erroneous or distorted content, incorrect references, violations

of data protection and copyright law or plagiarism that may have been generated by

the CCI.

Hiermit versichere ich an Eides statt, die vorliegende Dissertationsschrift selbst

verfasst und keine anderen als die angegebenen Quellen und Hilfsmittel benutzt zu

haben. Sofern im Zuge der Erstellung der vorliegenden Dissertationsschrift

generative Künstliche Intelligenz (gKI) basierte elektronische Hilfsmittel verwendet

wurden, versichere ich, dass meine eigene Leistung im Vordergrund stand und dass

eine vollständige Dokumentation aller verwendeten Hilfsmittel gemäß der Guten

wissenschaftlichen Praxis vorliegt. Ich trage die Verantwortung für eventuell durch

die gKI generierte fehlerhafte oder verzerrte Inhalte, fehlerhafte Referenzen,

Verstöße gegen das Datenschutz- und Urheberrecht oder Plagiate.

Hamburg, den 30.10.2025

Place, Date

Michelle Vogts, M.Sc.

314